acta mechanica et automatica

vol. 6, no. 1 (19)

CONTENTS

DESIGN, ANALYSIS AND PERFORMANCE EVALUATION
OF THE LINEAR, MAGNETORHEOLOGICAL DAMPER

Jacek Mateusz BAJKOWSKI[*]

[*]The Faculty of Automotive and Construction Machinery Engineering, Institute of Vehicles, Warsaw University of Technology,
ul. Narbutta 84, 00-524 Warsaw, Poland

jm.bajkowski@gmail.com

Abstract: The paper issues the design and analysis of the linear, magnetorheological damper. Basic information concerning the characteristics of the typical magnetorheological fluid and the damper incorporating it, were presented with the short description of the applied fluid MRF-132 DG. Basing on the computations, the prototype damper T-MR SIMR 132 DG was designed, manufactured, and tested under different operating conditions. Presented calculations were verified with the experimental results and their accuracy was evaluated. The conclusions and observations from the research were compiled in the summary.

Key words: Vibration, Damping, Magnetorheological Fluid, MRF

1. INTRODUCTION

The recently observed increase of the interest in the field of smart fluids by the industrial centres, academic and research institutes, unfortunately does not translate into their popularisation in the engineering applications.

The number of solutions utilizing smart materials like magnetorheological (MR) fluids still persists in the number of applications supported with the typical, hydraulic and pneumatic systems. What holds back the application engineers from mass deployment of such devices might be the poor range of proposed and evaluated solutions incorporating the MR fluids. Another important element is the constantly high price of the fluids, provided mainly by the LORD Corporation, which dominated the market. The difficult access to the high-quality MR fluids also did not encourage constructors to design new solutions. The evolutionary devices are mainly prototype units, designed at the academic and research centres, and they are still in the experimental phase.

2. DESIGN OF THE PROTOTYPE DAMPER

The better market access to other manufacturers' fluids, as well as their improved parameters and quality, stimulates and encourages to creating, and modifying the shock absorbers, clutches, brakes and other devices.

Therefore there is a need to develop, a comprehensive algorithm for designing devices utilizing the unique properties of the magnetorheological fluids. The presented paper is a proposition of such an algorithm, and its experimental verification.

The linear damper prototype is presented as a blueprint in Fig. 1. The photo of the device, and the cross-section view of the annular flow gap, is presented in Fig. 2.

The typical magnetorheological fluid named MRF-132 DG manufactured by Lord Co., was used in the prototype. The fluid is a suspension of a 10 μm diameter sized, magnetically susceptible particles, in a carrier, hydrocarbon fluid. According to the

datasheet, the density of the liquid is around 3 g/cm^3 and viscosity of a 0.09 Pa·s. The maximum yield stress value is 50 kPa and it is achieved with the magnetic induction of 1.5 T.
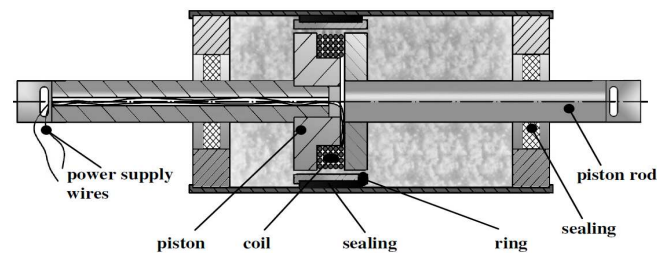

Fig. 1. Linear magnetorheological damper prototype,
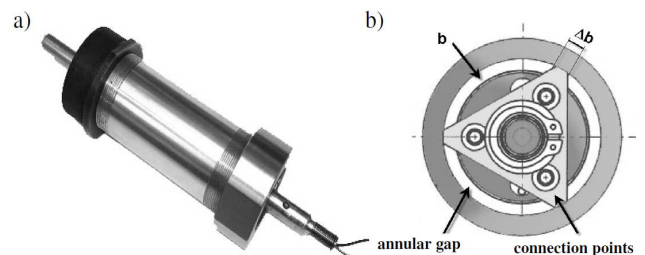with its basic assemblies

Fig. 2. a) Prototype of the T-MR SiMR 132 DG damper;
b) cross- section view of the annular flow gap and the mount
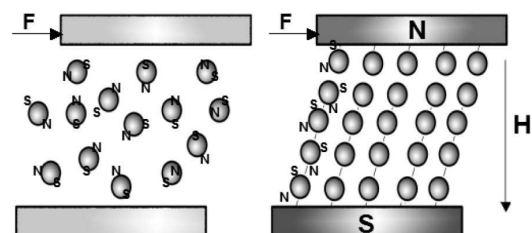

Fig. 3. The magnetorheological particle chains assemblies,
in the presence of the magnetic field

When exposed to a magnetic field, the rheology of the fluid reversibly and instantaneously changes from a free-flowing liquid to a semi-solid state, with the controllable yield strength, as a consequence of the sudden change in the particles arrangement. Upon application of the magnetic field, particles align with the direction of the flux lines (Fig. 3), in a chain-like combination, thereby restricting the fluid's movement within the gap, in proportion to the strength of the magnetic field.

2.1. Major Simplifying Assumptions Concerning the Magnetorheological Fluid

Simplifications concerning the magnetorheological fluid behaviour were assumed prior to the experiments. The fluid features include the fast response time, and high yield strength in the presence of the magnetic flux, and very low yield strength in the absence of it, which allows for a wide range of controllability. The fluid also provides hard settling resistance, and it does not abrade the devices.

In further analysis it was assumed that the liquid properties would be described by the phenomenological, viscoplastic Bingham model. The properties of this model are illustrated in Fig. 4.
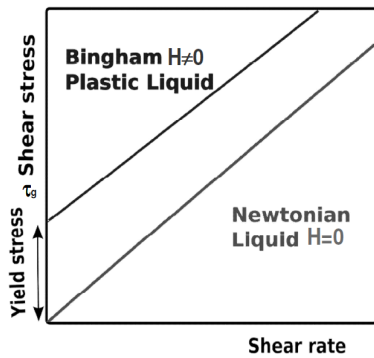

Fig. 4. Shear stress vs. shear rate in Bingham model for different liquid states, activated by the magnetic field

2.2. Simplifications concerning damper performance

The work regime of the MR fluid inside the damper is called the valve mode. In the valve mode, the fluid flows through an orifice, as presented in Fig. 5. In this model the annular flow is treated as a flow between two, parallel, still plates. The principle of operation resembles throttling (Kim et al, 2001). The resistance to flow of a liquid through the narrow gap is controlled by the changes in the magnetic field H, which vector is normal to the direction of the flow. The adjustment of the magnetic field is performed by the change of the current in the coil winding, mounted on the piston.

Further simplifications which were crucial for the computation of the damper's performance were:
- the damping force acts linear;
- the flow gap is formed by the stationary walls;
- the height of the gap is much smaller then its length and the width, therefore the flow is considered as a flow between parallel plates, thus the valve mode simplification is reasonable;
- stress value is constant along the gap, and it depends only

on the value of the magnetic flux in the gap (Mukhlis et al, 2006).
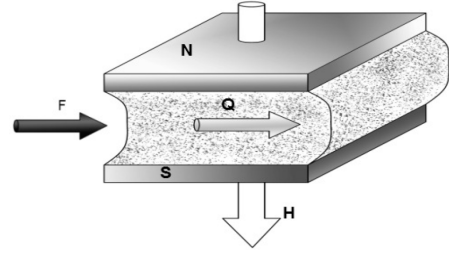
Fig. 5. The valve mode of the flow - the throttled flow through the gap

2.3. The Device Parameters Calculation

The prototype basic geometrical dimensions and the desired maximum damping force value were imposed. The gap view, with the basic parameters denotation is presented in Fig. 6.
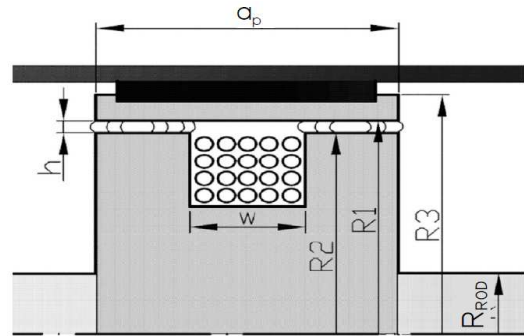
Fig. 6. View of the flow gap and the basic parameters denotation: R_1, R_2 – outer and inner gap radius; R_3 – piston radius; R_{rod} – piston rod radius; h – gap height; w – coil width; a_p – piston length

Proposing the approximate diameters of the piston and the rod, the effective circumference of the flow gap, decreased by the length of the connection points Δb, which are covering the gap (Fig. 2 b), may be expressed as:

$$b = \pi(R_1 + R_2) - 3 \cdot \Delta b \qquad (1)$$

The effective area of the flow gap is equal to:

$$A_{gap} = b \cdot h \qquad (2)$$

where: $h = R_1 - R_2$ is the gap height.

The total linear damping force may be expressed as a sum of the particular forces (Gavin et al., 2001):

$$F_{damp} = F_\tau + F_{ns} = F_\tau + F_\mu + F_f \qquad (3)$$

where: F_τ – controlled force, related to the actual yield stress of the MR fluid, F_{ns} – non controlled damping force, related to the viscosity and friction, F_μ – viscotic resistance force, F_f – friction force between piston and the cylinder.

For the axisymmetric flow, the equations describing the pressure gradient in the flow gap, simplified by the parallel plates model, for the Bingham characteristics, reduce to the 5th degree

equation (Phillips, 1969). This equation can be used for all type of the viscotic dampers with the parallel plates type of a gap:

$$3(\chi - 2\sigma)^2[\chi^3 - (1+3\sigma - \upsilon)\chi^2 + 4\sigma^3] + \sigma\upsilon^2\chi^2 = 0 \tag{4}$$

where: χ – dimensionless pressure gradient, σ – dimensionless stress gradient.

The value of the dimensionless velocity is expressed as:

$$\upsilon = \frac{bh\nu}{2Q} \tag{5}$$

where ν – velocity of the piston.

The volumetric flow rate of the MR fluid through the gap can be calculated as:

$$Q = \nu \cdot A_p \tag{6}$$

where in the formula above, the surface area of the piston, denoted as A_p is calculated as

$$A_p = \pi R_3^2 - A_{gap} - \pi R_{rod}^2 \tag{7}$$

The pressure gradient χ and the stress gradient σ are described by the formula (Milecki, 2010):

$$\chi = \frac{bh^3 \Delta p}{12 \cdot Q\mu a_p} \tag{8}$$

$$\sigma = \frac{bh^2 \tau_0}{12Q\mu} \tag{9}$$

Parameter denoted as a is the length of the area, in which the magnetic flux influences the MR fluid:

$$a = a_p - w \tag{10}$$

In the absence of the magnetic field the dimensionless stress $\sigma = 0$, therefore the equation (4) simplifies to a form:

$$\chi = 1 - \upsilon = 1 - \frac{bh\nu}{2Q} \tag{11}$$

From the equation (8) we can state, that the pressure drop cased by the Newtonian fluid viscotic flow, can be expressed as:

$$\Delta p_\mu = \frac{12A_p a_p \nu\mu\chi}{bh^3} \tag{12}$$

The damping force related only to the viscosity of the fluid is equal to:

$$F_\mu = \Delta p_\mu A_p \tag{13}$$

Substituting the relation (12) to (13):

$$F_\mu = \frac{12A_p^2 a_p \nu\mu\chi}{bh^3} \tag{14}$$

Combining the (11) and (14) the equation, the total viscotic force value is obtained:

$$F_\mu = \left(1 - \frac{bh\nu}{2Q}\right)\frac{12A_p a_p Q\mu}{bh^3} \tag{15}$$

Including the previous equations, and utilizing the simplifying formula ($A_p \gg b$), the equation above can be transformed into:

$$F_\mu = \frac{12A_p^2 a_p \nu\mu}{\pi(R_1 + R_2)h^3} \tag{16}$$

Using the approximate solution of (4) we obtain:

$$\chi(\sigma, \upsilon) = 1 + 2{,}07\sigma - \upsilon + \frac{\sigma}{1 + 0{.}4\sigma} \tag{17}$$

The decrease of the pressure along the gap, caused by the non-zero yield stress value is given by the equation (Kęsy, 2008):

$$\Delta p_\tau = c\frac{\tau_0(B)a}{h} \tag{18}$$

The constant value c, which is related to the geometrical dimensions of the damper and the damping force, can be approximated with the accuracy of 3% by the relation below (Poynor, 2010):

$$c = 2{,}07 + \frac{1}{1 + 0{,}4\sigma} \tag{19}$$

Taking into consideration the simplifying assumptions, we can determine the value of the damping force, controlled with the magnetic field:

$$F_\tau = k_p \Delta p_\tau A_p \tag{20}$$

where: k_p – constant, correction factor, related to the roundness of the magnetic field lines that are increasing the magnetic field area.

The final form of the sum of the forces is then as follows:

$$F_{damp} = k_p c\frac{\tau_{0B}(B)aA_p}{h} + \frac{12A_p^2 a_p \nu\mu}{\pi(R_1 + R_2)h^3} + F_f \tag{21}$$

The value of the friction force F_f depends on the type of the used sealing, construction materials, type of their machining, piston velocity, duration of the piston rest time and other.

In the discussed example of the calculations for the prototype device, the friction force value was preliminarily estimated on the basis of the experimental data. From the equation (16) and (20), it can be concluded, that by reducing the height of the flow gap, the maximum damping force of the device can be increased. The increase of the non-controlled visco-elastic force is in proportion to the third power of the gap height. The value of the controlled force increases slower than the value of the uncontrolled force. It is caused by the fact that the height of the gap in equation (20) is in the first power.

The presented order of calculation allows determining most of the parameters which are crucial for the proper design of the linear damper with MR fluid. Additionally, it is necessary to determine the maximum value of the energy dissipated by the damper. The value of the energy corresponds to the value of the work, which is done by the non-Newtonian fluid during its movement through the flow gap, and it can be calculated as:

$$W = Q(\Delta p_\tau + \Delta p_\mu) \tag{22}$$

Another important parameter is the controlled force range, which is the ratio of the controllable force to the non controllable one:

$$D = \frac{F_\tau}{F_\mu + F_f} = \frac{c\tau_{0B}(B)bh^2 \Delta p}{12W\mu + F_f} \tag{23}$$

To achieve the widest possible range of the controlled damping force, the value of this parameter should be maximized.

3. REASERCH OF THE T-MR SIMR 132 DG DAMPER

Three different gap heights were considered in the experiments: $h = 5 \cdot 10^{-4}$ m, $7 \cdot 10^{-4}$ m and 10^{-3} m. Utilizing the equations presented in Chapter 2, the damper research data was expected to match the parameters summarized in Tab. 1. Also, the comparison between experimental results and computational ones was attached.

Tab. 1. Comparison of the maximum damping force, obtained computationally and experimentally for different operating conditions

DESIGN PARAMETERS									
Dynamic viscosity of the fluid $\mu = 0.092$ Pa · s									
Maximum Yield stress $\tau_0 = 48 \cdot 103$ Pa									
Flow gap height h [m]	$5 \cdot 10^{-4}$			$7 \cdot 10^{-4}$			10^{-3}		
CALCULATED DAMPING FORCE F_{damp} [N]									
I [A]	0.1	0.2	0.4	0.5	1.0	2.0	0.5	1.0	2.0
Velocity v [10^{-3} m/s] 17	755	1110	1395	820	900	1095	400	465	500
33	790	1145	1430	830	915	1105	405	470	505
50	825	1180	1465	842	925	1075	410	475	510
EXPERIMENTAL DAMPING FORCE F_{damp} [N]									
Velocity v [10^{-3} m/s] 17	730	980	1165	830	930	1100	500	565	630
33	800	1130	1370	930	1065	1230	530	620	700
50	870	1200	1420	1050	1150	1290	560	675	740

Tab. 2. Comparison of the obtained relative errors of the damping force for different operating conditions

COMPUTATIONAL RELATIVE ERROR F_{damp} [%]									
Flow gap height h [m]	$5 \cdot 10^{-4}$			$7 \cdot 10^{-4}$			10^{-3}		
I [A]	0.1	0.2	0.4	0,5	1,0	2,0	0,5	1,0	2,0
Velocity [10^{-3} m/s] 17	3	13	19	1	3	1	20	18	20
33	2	2	4	11	14	10	24	24	28
50	5	2	3	19	19	16	27	29	31
AVERAGE ERROR OF F_{damp} [%] over a piston velocity									
$\delta_{avg}(v)$	3	6	9	10	12	9	24	24	26
AVERAGE ERROR OF F_{damp} [%] over a coil current									
$\delta_{avg}(I)$ 17	11			2			19		
33	3			12			25		
50	3			18			29		
TOTAL AVERAGE ERROR OF F_{damp} [%]									
$\delta_{total}(v. I)$	6			11			25		

The percentage error of the value of the damping force for different operating conditions is presented in Tab. 2. Sample results of the $F(x)$ relation, obtained for different piston velocities and several coil current values, are presented in Fig. 7.

The results show a relevance of the applied equations for determining the parameters of the designed damper with MR fluid. The smallest error values relating to the damping force are obtained for the narrowest gap. Depending on the coil current, the average error over piston velocity ranged from 3% to 6%. The value of the error over coil current ranged from 3% to 11%.

The increase of the gap height enhanced the disparity between the computational and the experimental values. By analysing the average error over the piston velocity, it can be stated, that the increase of the piston velocity amplifies an error of the damping force estimation. This error is greater, as the height of the flow gap increases. This effect may be related to the simplifications in calculation of the pressure drop.
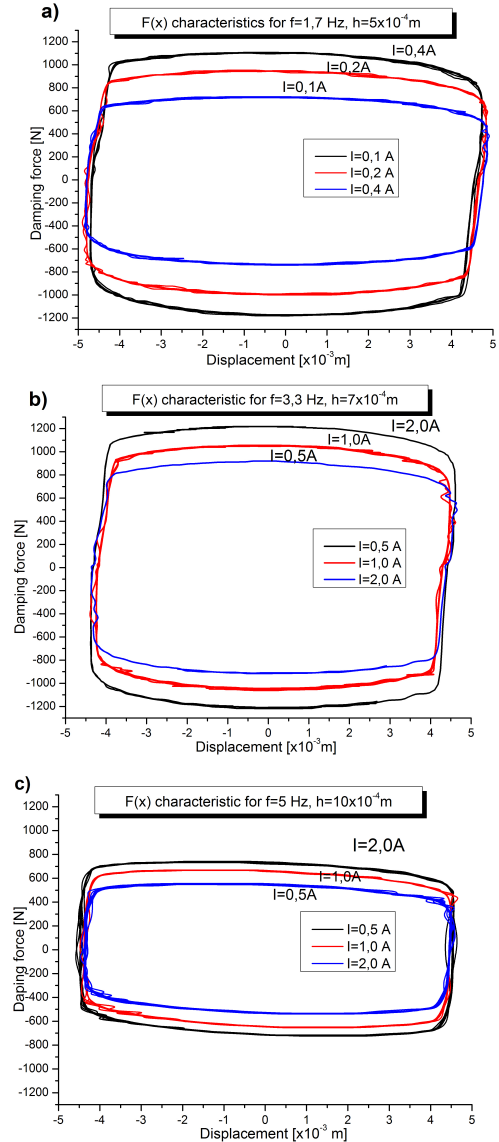
Fig. 7. Experimental characteristics of the F(x) relation for: a) gap height $5 \cdot 10^{-4}$ m and frequency 1,7 Hz; b) gap $7 \cdot 10^{-4}$ and frequency 3,3 Hz; c) gap $10 \cdot 10^{-4}$ and frequency 5 Hz

Increasing the current in the device's coil enlarges the magnetic field flux and thus, increases the yield stress denoted as $\tau_0(B)$. Precise computations of the magnetic induction are complicated, while the accurate experimental research is time and effort consuming. The $\tau_0(B)$ function provided by the manufacturer of the fluid, is usually only approximate and imprecise,

which negatively influences the accuracy of the computations. It is caused by the fact that the maximum damping force linearly depends on the value of the yield stress. Difficulties in determining the magnetic induction value explain the high value of the $\delta_{avg}(I)$ error.

The continuous line in Fig. 8 shows the experimental data for the maximum force F_{damp} for the highest coil current. It was compared with the computational results marked as the dotted line. For the gap height of $5 \cdot 10^{-4}$, the calculated values tend to the experimental ones, as the velocity of the piston v increases. For the other gap heights, the results diverge.
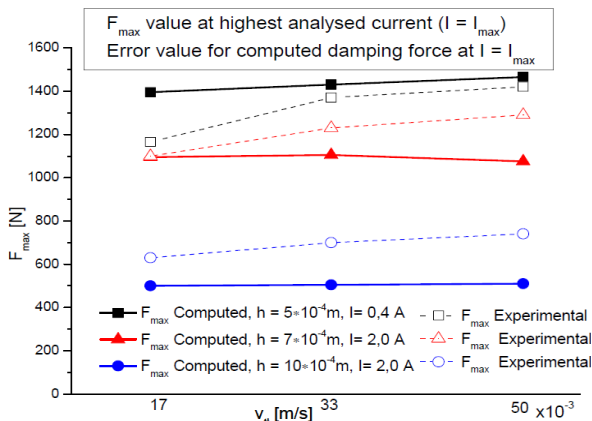
Fig. 8. Comparison of the theoretical and experimental data

Fig. 9 presents the dependence of the relative error of the maximum damping force as a function of the piston velocity, for the highest current values studied.
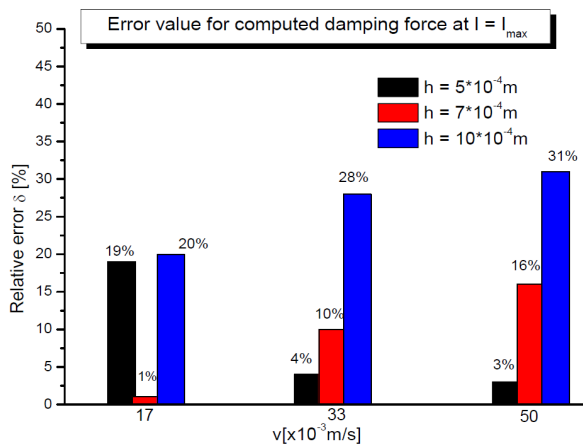
Fig. 9. Error of the damping force value calculation over velocity of the piston, for the highest coil current values

For the gap values $7 \cdot 10^{-4}$ m and 10^{-3} m, with the increase of the velocity, the total error of force estimation also increases. The greater the annular gap is the higher the inaccuracy caused by the simplification of the parallel plate flow model gets.

For these values of the gap height, the value of the error is associated with imprecise determination of the magnetic induction in the gap. With the increase of the gap height, the magnetic flux lines distorts, which leads to extending of the zone in which the fluid is in the active state. This may explain the fact of the

undervaluation of the computed damping force for the gap of height $7 \cdot 10^{-4}$ m, and 10^{-3} m compared to the experimental results.

4. FINAL CONCLUSIONS

The ramification of this paper is a numerical tool that allows to initially calculate the damping force value of the linear, magnetorheological damper. The manufactured prototype allowed verifying the theoretical equations with the experimental results. The assumed simplifications of the phenomena connected with the operation of the device, revealed a major influence on the computational inaccuracies.

It can be concluded that the most accurate calculations can be obtained for the smallest gap height, due to the possibility of the precise determination of the magnetic field, and the small error of the simplified model of the flow between parallel plates.

The analysis suggests the need to develop more precise tools supporting the design process of the devices with MR fluids. It seems reasonable to create a reverse algorithm that will allow estimating the geometry of the device, basing on the desired value of the dissipated energy. In addition, it is necessary to determine more accurately the value of the magnetic induction in the flow gap of the MR device. It would be also interesting to define the influence of the temperature on the viscosity and the yield stress, as well as to take this influence into account for the theoretical calculations.

REFERENCES

1. **Gavin H., Hoagg J., Dobossy M.** (2001), *Optimal Design of MR Device, Proc. U.S.-Japan Workshop on Smart Structures for Improved Seismic Performance in Urban Regions*, Seattle, 225-236.
2. **Kęsy Z.** (2008), *Sprzęgła z cieczami elektro- i magnetoreologicznymi*, wyd. Politechnika Radomska, Radom
3. **Kim J.-H., Lee Ch.-W., Jung B.-B., Park Y.** (2001), Design of Magneto-Rheological Fluid Based Device, *KSME International Journal*, Vol. 15 No. 11, pp. 1517-1523.
4. **Milecki A.** (2010), *Electro- and magneto-rheological fluids and their application in technique (in Polish)*, wyd. II, wyd. Politechniki Poznańskiej, Poznań, 42-60.
5. **Mukhlis R. Z., Mohamed N., Mohd Nor M. J.** (2006), The design and simulation of flow mode electrorheological damper, *Jurnal Teknologi*, University of Technology Malaysia , 44(A) Jun 2006, 115–125.
6. **Poynor J. C.** (2001), *Innovative Designs for Magneto- Rheological Dampers*, Master of Science in Mechanical Engineering degree thesis, Mehdi A., Virginia Polytechnic.
7. **Phillips R.** (1969), *Engineering applications of fluids with a variable yield stress*, Ph.D. Thesis, University of California, Berkeley.

NUMERICAL ANALYSIS OF IED DETONATION EFFECT ON STEEL PLATE

Wiesław BARNAT[*], Robert PANOWICZ[*], Tadeusz NIEZGODA[*], Paweł DYBCIO[*]

[*]Department of Mechanics and Applied Computer Science, Faculty of Mechanical Engineering, Military University of Technology,
ul. Kaliskiego 2, 00-908 Warszawa, Poland

wbarnat@wat.edu.pl, rpanowicz@wat.edu.pl, t.niezgoda@wme.wat.edu.pl, pdybcio@wat.edu.pl

Abstract: The article presents the results of initial works on protection of vehicles crews against improvised explosive mechanisms (charges) IED. The presented coupled problem of explosion and interaction of pressure impulse coming from detonation was described in available standard documents. The presented results are the introduction to works on composed protective layers applied in vehicles.

Key words: Blast Wave, IED, Improvised Explosive Device, FEM, Finite Element Method

1. INTRODUCTION

Vehicles resistance to impact of a shrapnel is widely discussed in numerous articles and standard documents concerning bulletproof objects. Contemporary armed conflicts confirm that real threats of soldiers are connected to a great extend with IED charges with a special recognition of shrapnels.

The paper describes the initial results of numerical simulation of coupled phenomena of interaction of explosion and shrapnel on a steel plate. The shape of a shrapnel was assumed on the base of STANAG 4569. Test shrapnels are made of steel bullets of 0.4 g mass. The explosive charge interacting on the plate was of 0.3 kg mass. In such case, explosive material interacts on the shrapnel (bullet) powering it. Additionally, it is interesting that the pressure impulse moving with velocity approximated to sound velocity reaches the plate earlier than the shrapnel – changing its material characteristics.

To conduct the simulation, there was applied a finite element method (FEM) implemented in MSC Dytran software. Numerical calculations were carried out in explicit option. Material data required for constructing a model, especially for a steel plate prepared from St3S steel, were taken from the available literature and on the base of experiments performed in the Department of Mechanics and Applied Computer Science MUT. For example, to describe the material of a steel plate it was applied the Johnson Cook model of kinetic reinforcement. The Johnson Cook model (YLDJC) (MSC Dytran Theory Manual) describes the plasticity boundary. It is applied at deformation high rates. The plasticizing stress depends, in this equation, on deformation, deformation rate and temperature.

$$\sigma_y = (A + \varepsilon_p^n (1 + C\ln\left(\frac{\dot{\varepsilon}}{\dot{\varepsilon_0}}\right))(1 - T^{*m}) \tag{1}$$

$$T^* = \frac{(T - T_r)}{(T_m - T_r)} \tag{2}$$

where: σ – plasticity boundary, ε_p – intensity of plastic deformation, $\dot{\varepsilon}$ – velocity of changes of plastic deformation intensity (de-

formations rate), $\dot{\varepsilon_0}$ – deformations rate (reference), T – temperature, T_r – room temperature, T_m – (melt temperature), A, B, n, C, m – constants.

The conditions for Euler elements modelling the charge determined density, inner energy and the shape. For the explosive material, there was assumed density 1600 kg/m3, density of inner energy 4.2 MJ/kg and volume corresponding to the 300 g of TNT charge mass.

The Euler area was a cuboid. The air was described with the state equation:

$$P = c_o + c_1\mu + c_2\mu + c_3\mu + (c_4 + c_5\mu + c_6\mu)E_0 \tag{3}$$

where: $c_0 = 5.4855E{-}5$; $c_1 = 0.0002$; $c_2 = -4.6904E{-}6$; $c_3 = 1.3457E{-}7$; $c_4 = 0.2057$; $c_5 = 0.0015$; $c_6 = -2.822E{-}5$; $E_0 = 0.000271$ GPa. Air density $\rho_o = 1.2$ kg/m3.

1.1. Description of numerical model of coupled system

As it was already mentioned, the numerical analysis was carried out with the use of MSC Dytran software using a method of explicit integration after time. This method is based on a dynamics equation presented below.

In implicit algorithms applied in MSC.Dytran (MSC Dytran Theory Manual) and LS–Dyna (Hallquist, 1998) software, equation (4) is solved through direct integration after time. These equations exist in the coupled form, what is connected with a significant numerical cost of their solution and with great requirement for memory during calculations.

Due to relatively short duration time of the phenomena, there is a possibility of ignoring the damping.

$$[M]\{\ddot{x}\}_n = \{F\}_n - \{F_{int}\}_{n'} \tag{4}$$

where: $[M]$ – masses matrix, $\{F\}$ – external forces matrix, $\{F_{int}\}$ – internal forces matrix

Assuming that masses matrix exists in diagonal form, equations of motion can be solved with an explicit Euler method. In this case, a vector of nodal accelerations can be determined from the

following formulae:

$$\{\ddot{x}\}_n = [M]^{-1}(\{F\}_n - \{F_{int}\})_n \tag{5}$$

In equation (2) there can be also considered the damping, however, only in the form of a diagonal matrix.

Velocity (velocities) vectors $\{\dot{x}\}_{n+1/2}$ as well as displacements vectors $\{x\}_{n+1}$ on the subsequent time steps are obtained by integration after time with the use of the method of central finite differences:

$$\{\dot{x}\}_{n+1/2} = \{\dot{x}\}_{n-1/2} + \{x\}_n \Delta t_n$$
$$\{\dot{x}\}_{n+1} = \{\dot{x}\}_n + \{\dot{x}\}_{n+1/2} \Delta t_{n+1/2} \tag{6}$$

Unfortunately, this method is not conditionally stable. In order to assure the stability it is necesary to limit the lehgth of integration step (5):

$$\Delta T \le 2/\omega_{max} \tag{7}$$

where ω_{max} is the highest frequency of own undamped vibrations of a discrete model.

That means that the step must be shorter than time of wave propagation through the smallest element in the calculation model. It results in the fact that the more accurate the model (small elements) is, the shorter integration step is and the calculations time is longer. Simultaneously, the problem of length selection disappears.
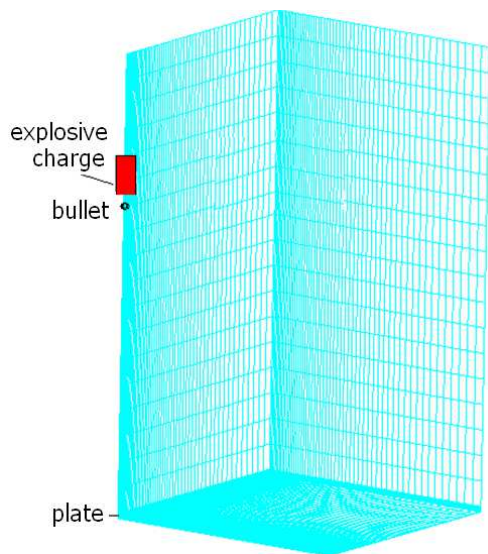

Fig. 1. Numerical model diagram

The analysed model, presented in Fig. 1, consisted of Euler area describing the air and a steel plate of dimensions 0.5x0.5 m and thickness of 5 mm (with a division of 5 elements on thickness). Due to a complicated character of the problem, the mesh of division of finite elements was not uniform. The thickest division was applied to the area of impact of the bullet into the plate. The plate was modelled as ¼ due to the symmetry and the extent of the task. The plate was fixed on the external edges, however, the edges of symmetry were deprived of specific degrees of freedom – allowing the obtainment of the symmetry system.

The plate manufactured from St3S steel was described with the use of Johnson-Cook material model using kinematic model of material reinforcement considering the change of plasticity boundary values.

A cylinder explosive charge of 0.3 kg mass was placed in the distance of 0.3 m from the plate. Explosive material was described as energy with an accurately selected shape and value (Barnat, 2010).

The bullet describing the shrapnel moved at the initial velocity of 1200 m/s. ALE coupling was used to connect the Euler and Lagrange areas. General coupling was used to model the interaction of the bullet-explosive charge-plate system.

2. NUMERICAL ANALYSIS RESULTS

As a result of numerical analysis of the described system, it was confirmed that there occurred a puncture (penetration) of the examined plate.
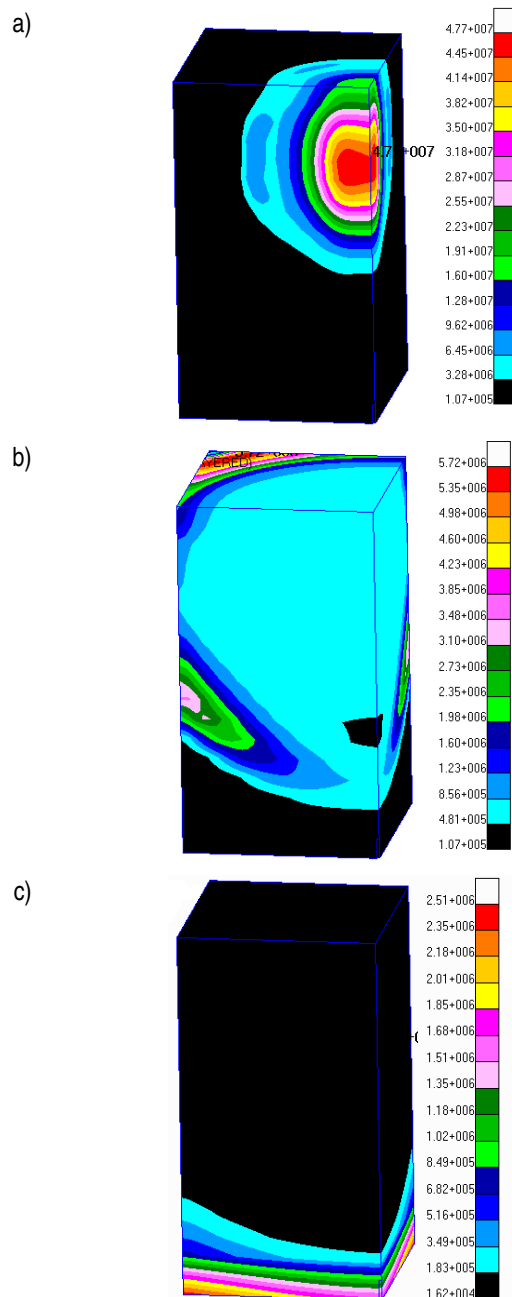

Fig. 2. Dispersion of pressure way in different time moments:
a) 3.395E-5 s, b) 9.377E-5 s, c) 0.00021341 s

It is interesting that in the first stage of the numerical analysis, the pressure wave reached the plate before the shrapnel. Reaching of the pressure wave took place for time of approximately 3.395E-5 s. Dispersion of the pressure wave in different time moments is presented in Fig. 2.

The change of velocity is interesting. For time of approximately 0.00025. A general diagram of position of a bullet before and after penetration is presented in Fig. 3. The bullet (according to standards) was placed in the distance of approximately 0.3 m from the plate and was moving at the initial velocity of 1230 m/s.

According to predictions and literature examinations, the presented plate manufactured from St3S steel (with the plasticity boundary Re=220 MPa (Poradnik Mechanika, 1982)) was not able to stop the bullet. As a result of the interaction of the bullet on the plate, penetration of the plate occurred.

Fig. 4 presents contour lines of plate deflection resulted from detonation interaction. It is worth noticing that pressure impulse reaches the plate before the bullet. As a result of interaction of pressure impulse on the steel plate, the plate deformed permanently by 2.17E-4 m. Permanent deformation of the plate took place for time t=0.000238 s and was caused by the pressure impulse from detonation of approximately 0.3 kg TNT interacted on it.
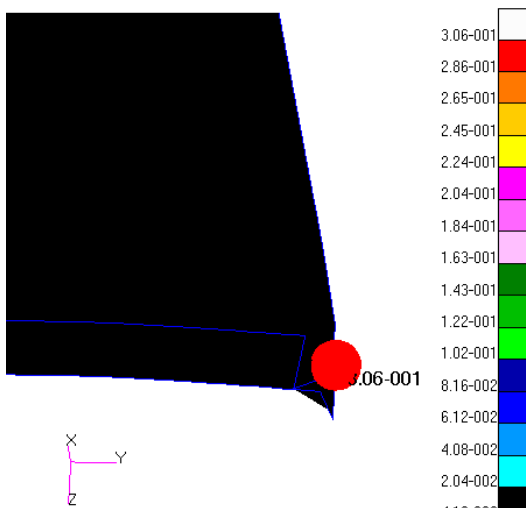
For time 0.00024 s, interaction of the bullet on the plate caused by the contact of both these bodies occurred. The intersection of two curves clearly verified penetration of the plate by the bullet.

3. CONCLUSION

The article presents the initial results of the works on the phenomenon of shrapnel resistance against improvised explosive devices. These examinations are aimed at increasing the protection of military vehicles crews against IED widely applied in asymmetrical conflicts. The described phenomena has a complex character. The hitherto numerical works treated them as a separate problem (expanded). Such an attitude is easier, however, it causes a kind of ratification of results. Inaccuracy of the results from neglecting the changes of material properties under an influence of high velocity of deformation. An experimental connection of explosion and a shrapnel will be the next challenge in shrapnel resistance examinations.

The nest stage of investigations will deal with conducting an experiment in order to validate the presented problem. The problem of physical nature lies in the fact that the pressure impulse (moving in the air at velocity higher than sound velocity) reaches the obstacle the first (before the bullet). This impulse causes deformations occurring with high velocities. As a result of high velocities of deformation, the material characteristic changes (due to dynamic reinforcement). In such a case, a shrapnel impacts into a completely different material than initially expected. In this respect, there is a necessity of using constitutive equations, describing the material, which would take into consideration the dynamic reinforcement. To describe the material of the steel plate, the coating elements taking into account Johnson Cook kinematic reinforcement model was applied.

REFERENCES

1. **Barnat W.** (2010), *Wybrane problemy energochłonności nowych typów paneli ochronnych obciążonych falą wybuchu*, BEL Studio, Warszawa.
2. **Hallquist JO.** (1998), *LS–Dyna. Theoretical manual*, California Livermore Software Technology Corporation.
3. *MSC Dytran Theory Manual*, (2005), MSC.Software C.O.
4. *Mechanical engineering handbook (in Polish)* (1982), Wydawnictwa Naukowo Techniczne, Warszawa.

Fig. 3. Scheme of penetration of plate with bullet
(positions of bullet before and after interaction on the plate)

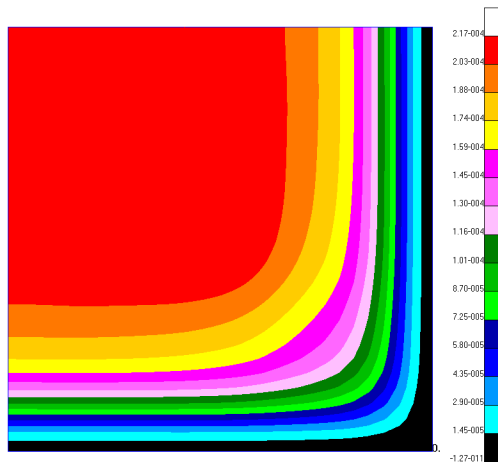**Fig. 4.** Contour lines of deflection of steel plate [m] for time 0.000238 s under the influence of pressure impulse

NUMERICAL AND EXPERIMENTAL COMPARISON OF COMBINED MULTILAYER PROTECTIVE PANELS

Wiesław BARNAT*, Robert PANOWICZ*, Tadeusz NIEZGODA*,

*Department of Mechanics and Applied Computer Science, Faculty of Mechanical Engineering, Military University of Technology,
ul. Kaliskiego 2, 00-908 Warszawa, Poland

wbarnat@wat.edu.pl, rpanowicz@wat.edu.pl, tniezgoda@wat.edu.pl

Abstract: The paper presents numerical and experimental analysis of combined multilayer protective panels. The developed structures are prospective solutions for enhancing protection of military vehicles and crucial elements of pipelines especially in places like river crossings.

Key words: FEM, Blast Wave, Fluid Structure Interaction, Elastomer, Protective Panel

1. INTRODUCTION

Asymmetric actions used by terrorist formations are directed against the most important elements of infrastructure and human lives. Crews of combat vehicles and industrial installations of oil and gas are mainly subjected to such actions. Counteraction to terrorist attacks is increasing of impact resistance of the construction to short-time loads coming from explosions (Trzciński et al., 2005; Krzewiński and Rekrucki, 2005). The paper describes one of the possible methods of increasing the impact resistance through application of hyperelastic elastomer material as an energy absorbing layer. Layers of this type are widely applied in contemporary mechanics. They are mainly used to disperse energy generated as a result of interaction of pressure, caused, for example, by explosion, on the construction (Thornton and Jeryan, 1988; Babul, 1980; Włodarczyk, 1994). In the considered case, a layer of elastomer was placed on the steel base plate (protected) creating a simple construction. The construction was subjected to dynamic load in the form of pressure wave coming from detonation of explosive material.

The further part of the paper presents various numerical analyses of the developed construction accompanied by experimental verification of the carried out calculations.

In order to perform numerical analyses, implementation of a finite elements method included in MSC.Dytran software was applied.

The results from the conducted analyses will be applied to further validating and optimizing examinations aimed at absorbing or dispersion of maximum significant value of energy interacting on the energy absorbing panel utilized in constructing of armoured vehicles and protective elements of stationary constructions of strategic importance.

2. DESCRIPTION OF EXAMINED OBJECTS

A square steel plate (500 x 500 mm) made of ST3 steel of 2 mm thickness with elastomer layer of 9 mm thickness was subjected to numerical investigations with experimental verification.

The model was loaded with a pressure impulse wave coming from detonation of a 100 g TNT explosive charge in the shape of cylinder is presented in Fig. 1. The obtained numerical results were compared with own experimental data.
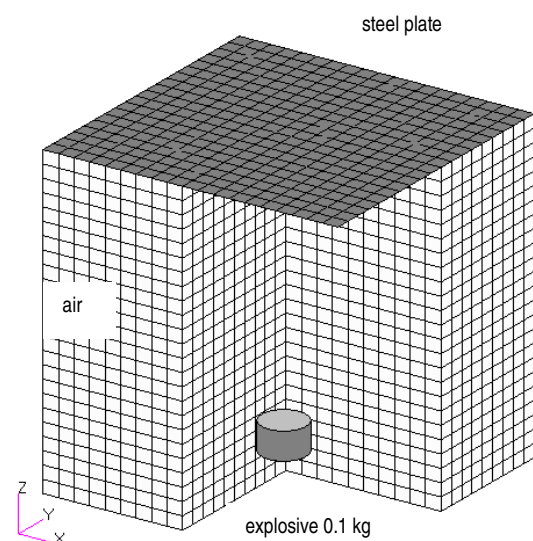
Fig. 1. General view of numerical model

The metal plates were covered with PNMU elastomer. Elastomer has linear build of macroparticules. It is built of elastic and stiff segments, consisting of flexible and stiff mers. This polymer is self-extinguishing, it shows low water absorption and high hydrolytic resistance. Thanks to these properties, elements made of such polymers can work a long time in water environment. They exhibit also high wear resistance. So far, the industrial applications of such polymers include a wide range of parts, especially those working in raw materials processing, e.g. in mining.

The PNMUs remain in the high-elastic state, which means that the energy of thermal vibrations is higher than the energy barrier to rotations about the bonds and, as a result of that, even under a small loading they exhibit considerable elastic deformation, which can be easily and quickly reversed under the influence of the loading.

The elastomer is characterized by density at the range of 1.23 kg/dm^3, linear thermal expansion coefficient 2.4 10^{-4} 1/Co, hardness 70 oShA, resiliency equal to 47% and abrasive wear at the range of approximately 30 mm^3 (determined with Schopper-Schlobach method). Usage temperature PNMU should not exceed 160°C.

3. RESULTS OF NUMERICAL ANALYSIS

The previous works (Krzewiński and Rekrucki, 2005; Babul, 1980; Barnat, 2010; Dytran Theory Manual, LS-DYNA Theoretical Manual) presented the results of investigations concerning, among others: the influence of Euler elements mesh parameters, values of initial energies of explosive material and selection of coupling between Euler and Lagrange domains on the results of analyses considered in constructions. Based on the obtained experiences, the models used in present considerations were built.
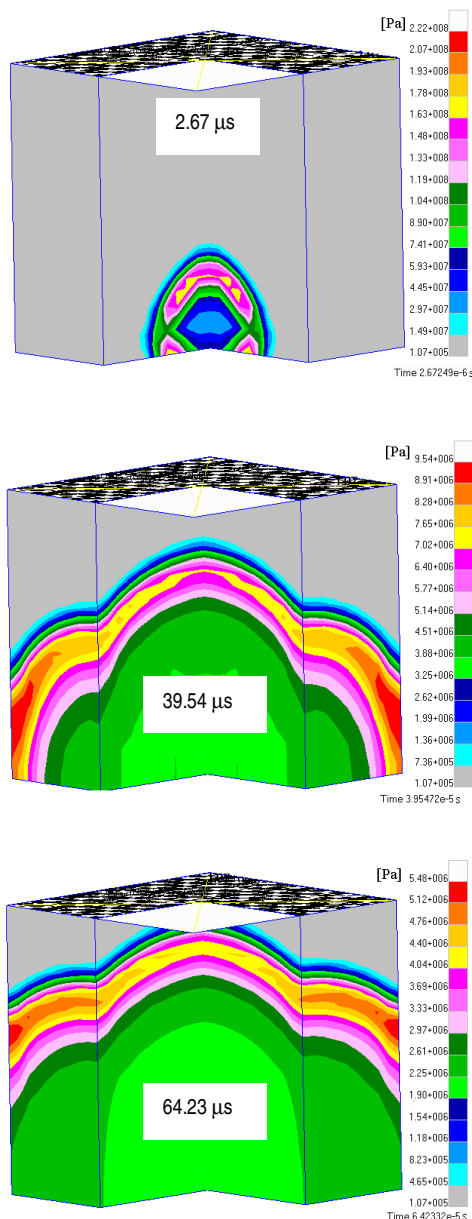

Fig. 2. View of pressure wave for three time moments

The objects were subjected to a pressure wave coming from detonation of 0.1 kg explosive charge in the shape of cylinder made of TNT. Dispersion of a pressure impulse coming from detonation of this charge in Euler area is presented in Fig. 2.

To estimate the results, the estimation of displacement of the plate central node located in the planes of symmetry and reaction coming from the ground was applied.

Fig. 3 presentS the final form of steel plates deformation obtained through numerical calculation with the use of explicit implementation of the finite element method.

At the initial time of approximately 39.54 μs the wave reached the objects without any displacements. The pressure impulse duration time is relatively short as compared to the time of displacement increasing, which is significantly longer and equals to approximately 750 μs. In the case of a model of a single examined plate, the level of displacements stabilizes around the value of 32 mm. A similar course of displacements of the central point was observed for a model of the plate with elastomer layer, however, in this case, the amplitude of vibrations was significantly greater. The final displacement of the central node was equal to 27 mm.
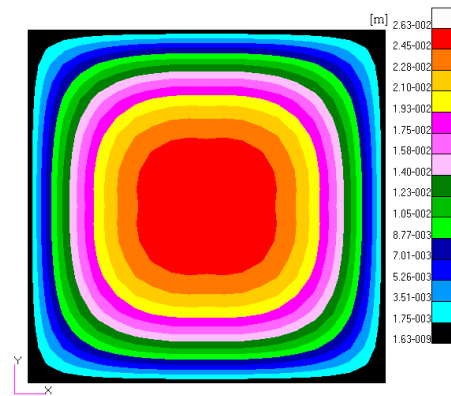
Fig. 3. The final form of deformation of plate with elastomer layer (pressure values in MPa)
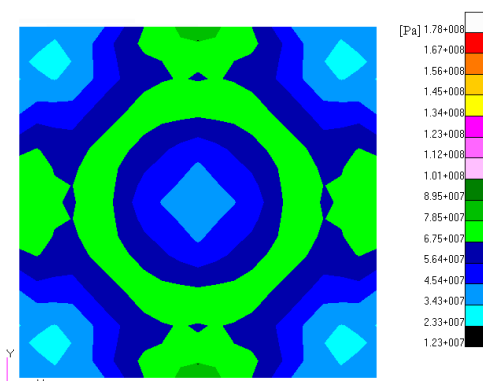
Fig. 4. Strain maps for steel plate with elastomer layer

In the case of application of the elastomer layer, the final form of deformation of the plate is flat. Such character of deformation takes place owing to the elastomer layer increasing stiffness of the system, thus causing distribution of load on the greater surface of the considered system.

The applied layer influences also maximum acceleration which amounted to 700 000 m/s^2. Along with decaying of external

forces, in the further part of the analysis, the decreasing values of acceleration oscillation of the base layer occur. The values of strains, presented in Fig. 4, equal 178MPa.

4. EQUIPMENT APPLIED IN INVESTIGATIONS

Experimental investigations of energy absorption were carried out in the Military University of Technology on the authorial testing stand for measurement of force interacting on the examined panel. The testing stand was designed and constructed in the Department of Mechanics and Applied Computer Science Military University of Technology. The stand allows measurement of forces induced by dynamic processes such as even interaction of a pressure wave coming from detonation of explosive material. Photo 5 presents the testing stand with the system for measuring the forces used in the tests.

In the system of signals processing, there is applied a tensometric amplifier MS 1001, produced by INFEL company from Świdnik, for intensification of signals coming from tensors. The recording of signals was conducted with the use of a measurement card – model NI-USB 6251, produced by National Instruments company, including a fast analogous-digital converter (sampling 1.25 MHz on each of the channels), a portable computer TOSHIBA Satellite and a software for maintenance of a measurement card.
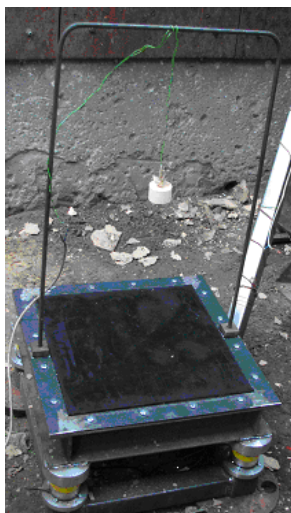

Fig. 5. Force measurement system utilized in tests

5. RESULTS OF EXPERIMENTAL INVESTIGATIONS

After carrying out the tests on the testing stand, the obtained electric signals were subjected to calibration in order to prepare the graphs of changes of force in the function of time. Due to difficulties in measuring during experimental research, it was limited to reading force interacted on the frame and the value of final deformation of the deformation of the system centre.

Fig. 6 presents photos of the plate with an additional elastomer layer.

The measured permanent displacement of the central node of the steel plate was equal to 32 mm. Application of a protective layer reduced the value of this displacement by 30% (displacement amounted to 22 mm). Additionally, based on the recorded courses, there were determined the maximum values of forces

(Fig. 7 and 8) interacting on the measuring system for individual objects
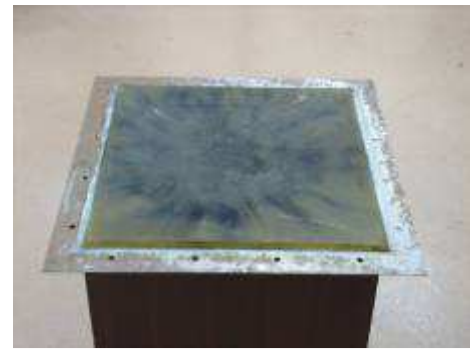
Fig. 6. 2 mm thick plate with elastomer layer (deformation obtained from the experiment)
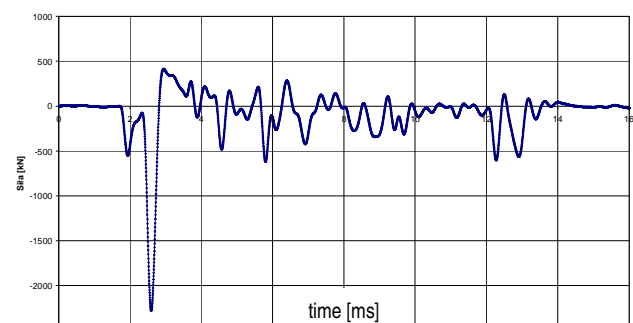
Fig. 7. The course of changes of loading the panel made of steel plate
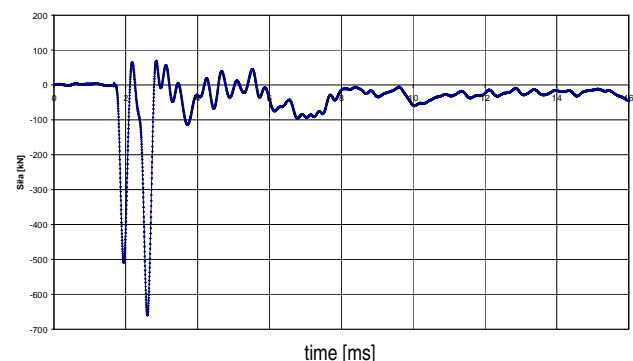
Fig. 8. The course of changes of loading the panel made of steel plate with elastomer layer

6. CONCLUSIONS

Constructions, which can be subjected to damages resulted from different kind of fast-changing constraints such as impacts, or influence of a pressure wave coming from detonation of explosive materials, should have the structure enabling absorption of possibly the greatest part of constraint energy which influences on it. The energy absorbing elements are mainly built in the form of sandwich layers which core is a specially selected material. One of the interesting types of materials, which can be used here, is elastomer. These materials, capable of absorbing energy of a blast wave coming from detonation, enable significant increasing of a protection level. Application of these materials causes reducing of vibrations frequency of the system loaded with a pressure impulse.

The maximum displacements of the protected plate were obtained for model 1. The minimum displacement of the central node was observed for model 2, in which an elastomer layer was applied. The experimental studies verifies also that elastomer layers absorb and disperse well the energy of impact protecting the object against the effects of influence of a pressure wave coming from detonation of explosive materials.

The authors presented the fragment of investigations carried out at the Department of Mechanics and Applied Computer Science, Military University of Technology.

REFERENCES

1. **Babul W.** (1980), *Metals deformation with the force of explosion (in polish)*, WNT Warszawa.
2. **Barnat W.** (2010), *Numeryczno doświadczalna analiza złożonych warstw ochronnych obciążonych falą uderzeniową wybuchu*, Bell Studio, Warszawa.
3. **Dobrociński S.** (2000), *Stability solutions for resistance construction (in polish),* AMW Gdynia.
4. Dytran Theory Manual, (2004).
5. **Krzewiński R., Rekrucki R.** (2005), *Construction works with explosives (in polish),* Polcen.
6. LS-DYNA theoretical manual, (1998).
7. **Thornton P. H., Jeryan R. A.** (1988) Crash Energy Management in Composite Automotive Structures, *International Journal of Impact Engineering*, Vol. 7, No 2.
8. **Trzciński W., Trębiński R., Cudziło S.** (2005), *Investigation of the Behaviour of Steel and Laminated Fabric Plates Under Blast Wave Load,* Part I: Experimental Approach, V International Armament Conference, Waplewo.
9. **Włodarczyk E.** (1994), *Mechanics of explosion (in Polish),* PWN Warszawa.

FRACTOGRAPHY AND DAMAGE ANALYSIS OF CARBON/EPOXY COMPOSITES UNDER STATIC AND DYNAMIC LOADS AT ELEVATED TEMPERATURES

Jarosław BIENIAŚ*, Monika OSTAPIUK*, Barbara SUROWSKA*

*Material Engineering Department, Mechanical Engineering Faculty, Lublin University of Technology
ul. Nadbystrzycka 36, 20-618 Lublin, Poland

j.bienias@pollub.pl, m.ostapiuk@pollub.pl, b.surowska@pollub.pl

Abstract: This paper presents the microstructural and fractographic analysis of damage in carbon/epoxy composites after static and fatigue strength (shear) tests at elevated temperature. The microstructural tests and fractographic analysis confirmed the complexity of degradation process and degradation mechanisms in composite structure. Multiple cracks, delaminations and interface degradation between fibre and matrix have been observed. The fracture analysis indicate the occurrence of characteristic failure area: matrix river lines, matrix rollers, fractures and reinforcing fibres imprints. The interface, except of the type of components and their features, is the principal factor determining the properties of composite material. The quality of the bonding between the reinforcing phase and matrix, mechanism of composite cracking as a whole as well as cracks of individual components are directly affected by the interface.

Key words: Carbon Fibre Reinforced Polymer, Microstructure, Damage, Fractography, Shear, Mechanical Tests

1. INTRODUCTION

Nowadays, the fibre reinforced polymeric composites belong to the materials groups used in technical applications with the highest development potential in the years to come owing to favourable combination of their properties e.g. high strength and rigidity versus low density, fatigue characteristics and chemical resistance. Therefore these materials are widely used mainly in the aircraft and automotive industries as well as in sporting goods sector (Morgan, 2005; Chung, 1994).

At the moment, the carbon fibre reinforced composites are particularly interesting part of the wide group of composite materials. High strength properties, fault tolerance (impact resistance), dimensional stability and high fatigue strength are required in case of carbon composites (Chung, 1994; Freeman, 1993).

Therefore the damage mechanisms in carbon composites are an important aspect to be considered in the designing and manufacturing process as well as in the service life of composite structures. The degradation processes in composite materials are more complex than in case of metal materials. The damages of reinforcing fibres and matrix, delaminations as well as degradation of fibre/matrix interface are observed (Gamstedt et al., 2009; Wu et al., 2010)

Particularly important are the static and fatigue strength tests under the influence of shear stress and the determining role of matrix which may lead to significant reduction of strength properties of composite materials (Hodgkinson, 2000).

In many cases, the optimization of composite materials is possible as a compromise between the achievement of high mechanical properties and high shear strength of composites (Hodgkinson, 2000).

Furthermore accelerated degradation of mechanical properties in composites is possible in case of an intensive impact of environment conditions i.e. humidity and increased tempera-

tures. Therefore the evaluation of damage mechanisms may become more complex (Jen et al., 2008).

The damage process in composite materials can be associated with structure designing phase, applied materials and manufacturing technology or elements operation. Valuable information about damage processes is obtained from fractographic tests, particularly about the reasons leading to damages of individual components, damage - cracking initiation, errors in manufacturing process or defects in materials. The fractographic tests make it possible to understand more deeply the damage process and its interpretation contributing to further development, among others in the scope of damage criteria (Greenhalgh, 2009).

The evaluation of damage character is the essential question in the carbon fibre reinforced composites (as state of art engineering materials) often exposed to the influence of increased temperatures and shear stresses (in static and dynamic processes).

In the present study, the authors described microstructural and fractographic analysis of damage in carbon/ epoxy composites after the static and fatigue tests (shear test, configuration [±45]) at increased temperatures.

2. MATERIAL AND METHODS

The carbon/ epoxy composites made of unidirectional prepreg tape in HexPly system (Hexcel, USA) in configuration $[\pm45]_8$. Epoxy resin has been used as composite matrix and carbon fibres have been applied as high strength reinforcing. Nominal percentage (v/v) of reinforcing fibres in composite was equal to about 60%. The composite materials have been produced using autoclave technique in the Material Engineering Department in Lublin University of Technology.

The fractographic analysis has been performed on the materials after the following tests:

– static shear strength (temp. +85ºC);

- fatigue shear strength (temp. +50 ºC *tension-tension* method);
- specimen after the highest number of cycles.

The tests for strength and fatigue properties have been performed in accordance with relevant standards applicable to this type of materials (ISO, ASTM).

The microstructural and fractographic analysis has been carried out using the optical microscopic equipment (Nikon MA200, Japan) and Scanning Electron Microscope (SEM) (Zeiss Ultra, Germany).

3. RESULTS AND DISCUSSION

Fig. 1 illustrates the macroscopic image of carbon/epoxy composites after (static and fatigue) shear test. In both cases, the damage occurred in the central part of the material in the form of complete damage of reinforcing fibres and matrix as well as delamination in interlayer planes.

Fig. 1. Specimens of carbon/ epoxy composites after shear test:
a) static test; b) fatigue test

The microstructure of carbon/ epoxy composite after the static shear test is illustrated in Fig. 2a.

The delaminations between successive layers and lateral cracks connected to each other are visible along fibre/matrix boundaries.
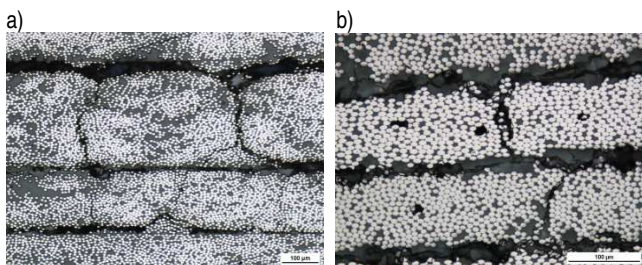

Fig. 2. The microstructure of carbon/epoxy composite after the shear tests: a) static test; b) fatigue test (cross- section)

In case of carbon/epoxy composite after the fatigue shear test (Fig. 2b), the presence of delaminations is found between layers and lateral cracks across the composite layers. Multiple porosities have been observed, particularly within interlayer spaces. Individual cracks combine with porosities forming the grid of cracks.

The process of porosities forming in carbon/epoxy laminate occurred probably in course of manufacturing i.e. polymerization process (loss of vacuum bag tightness). Occurred porosities may affect not only the quality of composite structure but also may lead to the reduction of strength and fatigue properties of the material.

The mechanism of crack propagation process along the fibre/matrix boundaries with visible degradation of interface has been illustrated in Fig. 3. Multiple areas of initiation and cracks are visible (loss of adhesion) and may combine together easily leading to the damage of composite.
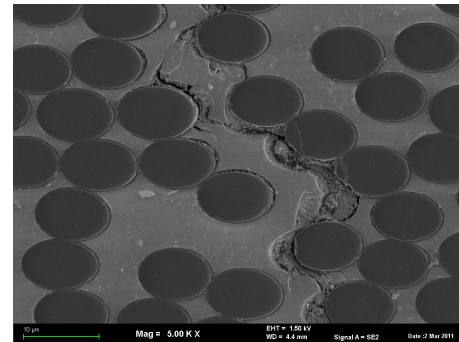
Fig. 3. Cracks and degradation of fibre/matrix interface (cross- section); SEM

The fractography of fractures is applied as one of principal methods as well as interpretation of the results obtained in strength and fatigue tests.

Essential data on composites behaviour relating to the fractographic analysis of damage in composite structures are contained in the studies elaborated by Clements and Purslow (Greenhalgh, 2009). Owing to the differences occurring in composites damage morphology, two damage regions have been indicated by Clements i.e. high energy region and low energy region. Fig. 4 illustrates the fracture surface obtained in performed tests.
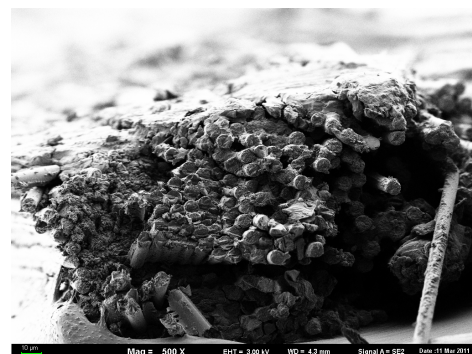
Fig. 4. Fracture surface in examined composites after static and fatigue tests. Damage region is typical for high energies; SEM

In case of low energies, the surface on fibres fracture is smooth and the fibres are arranged in an uniform manner. Their location on the same level is the symptom of low energy level occurring at the time of structure damage. However in case of the damage characterized by the high energy level and observed also in materials under analysis, the surface of fracture is non-uniform and the reinforcing fibres are located on various levels (Greenhalgh, 2009).

No significant differences appeared from the analysis of damage fractures after static and dynamic tests. Fig. 5 illustrates the fractures of reinforcing fibres.

a)

b)
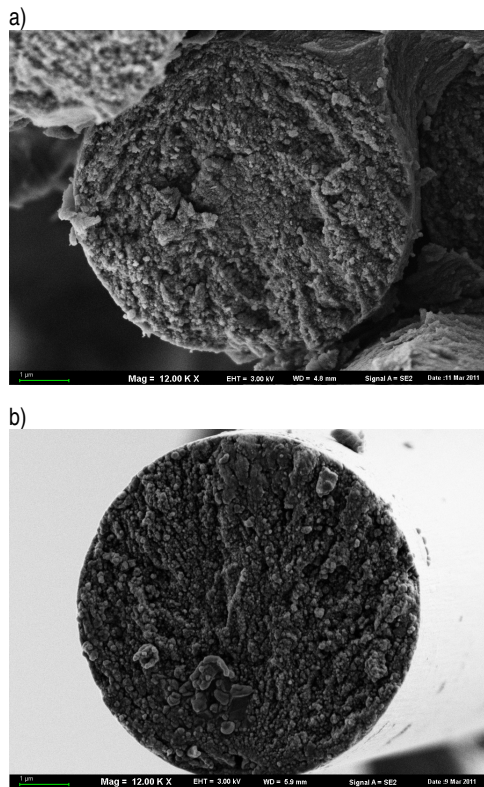
Rys. 5. Fractures of carbon fibres after shear strength tests:
a) static test; b) fatigue test

A characteristic crack initiation zone (source) has been observed in both cases. Radially propagating crack growth direction lines are the symptoms of brittle cracking phenomenon occurred in fibres in course of structure damage. This phenomenon has been confirmed by observations of Greenhalgh (2009).

The surface of matrix after performed static shear tests has been illustrated in Fig. 6.
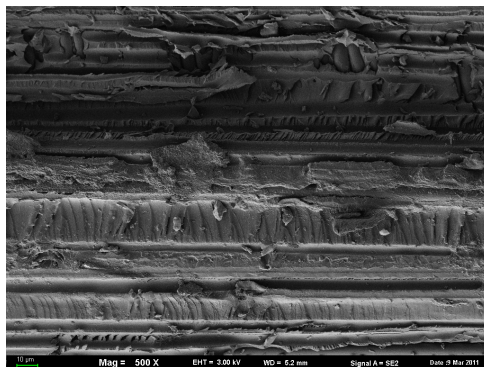
Fig. 6. Surface of matrix fracture after performed static shear tests; SEM

The figure illustrates visible characteristic matrix flow lateral lines indicating the structure damage growth direction lines which are situated between adjacent fibres or their imprints.

Fig. 7 illustrates a characteristic morphology of matrix rolling and the creation of resin "flakes" inclined to surface. This effect is characteristic for damage as a result of fatigue processes with high number of cycles and under the impact of shear forces. The dimension and distribution depends on the space between the matrix and fibre. The number of cycles and the strength of fibre/matrix bonding are the factors affecting such behaviour of the matrix material. Under fatigue loads, the matrix plasticity is increased and its deformation takes place (Fig. 7). The damages are initiated locally in the matrix. There the micro-damages propagate along fibre/matrix boundary in the initial phase and grow until the interface degradation is achieved and the fibre – matrix bonding is lost (Greenhalgh, 2009).
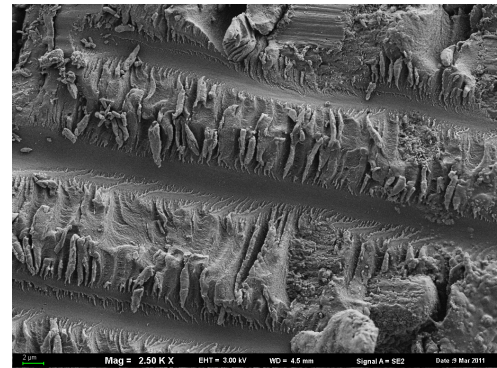
Fig. 7. Morphology of matrix fracture surface in carbon/ epoxy composite after fatigue shear strength test; SEM

In both cases, characteristic imprints of reinforcing fibres have been observed on damage surface (Fig. 8); the fibres have been completely separated from the matrix (Greenhalgh, 2009).
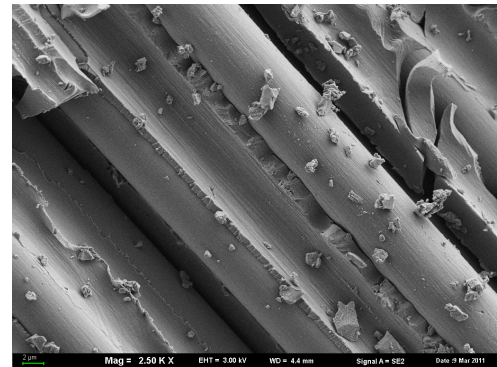
Fig. 8. Characteristic imprints of reinforcing fibres on damage surface; SEM
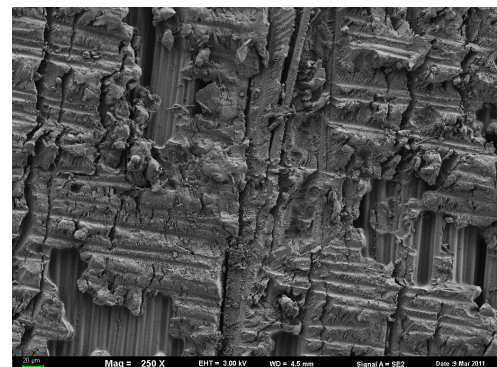
Fig. 9. Surface of carbon/ epoxy composite fracture with visible fracture layer and fibres after performed fatigue shear tests

Fig. 9 illustrates the surface of matrix material after fatigue shear strength tests with visible traces of arrangement of individual fibres. There are multiple cracks and deep furrows in matrix, parallel to each other, oriented in the direction perpendicular to the previous direction of fibres (Greenhalgh, 2009).

The analysis of fractures, surfaces of fibres and composites subjected to cyclic loads makes it possible to determine the type of damage, with consideration of components bonding; the analysis depends on the type of fibres, their arrangement, type of matrix, bonding between phases and the type of applied load (Hartwig et al., 1998).

The damage mechanism in polymeric composites subjected to diversified loads significantly differs from conventional materials. The growth of cracks, degradation of fibres and matrix as a result of the impact of high stresses lead to the complete damage of material (Tai et al., 1995). The damage of fibres as a result of the impact of low stresses can be caused by the loss of bonding on fibre/matrix interface and degradation of reinforcing fibres is possible before the complete damage of composite (Tai et al., 1995).

Cracks growth in polymeric composites reinforced with unidirectional fibres arranged in ±45 direction may depend on the occurrence of structural discontinuities (porosities) and microdamages of high values of shear stresses occurring between the layers (Putic S. et al., 2003).

4. SUMMARY

The microstructural tests and fractographic analysis for composites with epoxy matrix reinforced with carbon fibres demonstrated the complexity of degradation process and its mechanisms in composite structure. The presence of multiple cracks (laterally oriented) and delaminations has been observed in composites microstructure in both cases (in static and dynamic conditions).

Any significant differences in fractures morphology (brittle cracks of reinforcing fibres) have been not demonstrated in course of fractographic analysis of individual reinforcing fibres. Some characteristic zones have been found on the fractures surface, among others matrix river lines (static tests), matrix rolling (fatigue tests), cracks and imprints of reinforcing fibres. The character of fractures surface is associated with high damage energies.

The damage process in composite materials is associated mainly with fibre/matrix interface and with the properties of matrix material. Multiple degradation areas have been observed on fibre/matrix boundary: initiation sources, loss of adhesion, cracks propagating along fibre / matrix boundaries.

In summary it can be concluded that the interface except of the type of components and their features, is the principal factor determining the properties of composite material. The quality of the bonding between the reinforcing phase and matrix, mechanism of composite cracking as whole as well as cracks of individual components are directly affected by the interface.

REFERENCES

1. **Chung D. D. L.** (1994), *Carbon fiber composites*, Butterworth-Heinemann, Boston.
2. **Freeman W. T.** (1993), The Use of Composites in Aircraft Primary Structure, *Composites Engineering*, Vol. 3, 767–775
3. **Gamstedt E. K., Talreja R. (1999),** Fatigue damage mechanisms in unidirectional carbon-fibrereinforced plastics, *Journal of Materials Science*, Vol. 34, 2535-2546.
4. **Greenhalgh E. S.** (2009), *Failure analysis and fractography of polymer composites*, Woodhead Publishing in Materials, CRC.
5. **Harris B.** (2000), *Fatigue in composites*, CRC Press, Boca Raton.
6. **Hartwig G., Hubner R., Knaak S., Pannkoke C.** (1998), Fatigue behaviour of composites, *Cryogenics*, 38, 75-78.
7. **Hodgkinson J.M.** (2000), *Mechanical testing of advanced fibre composites*, CRC Press, Cambridge.
8. **Jen M-H. R., Tseng Y-Ch., Kung H-K., Haung J. C.** (2008), Fatigue response of APC-2 composite laminates at elevated temperatures, *Composites: Part B*, Vol. 39, 1142-1146.
9. **Morgan P.** (2005), *Carbon fibers and their composites*, Taylor and Francis Group, New York.
10. **Putic S., Uskokovic P. S., Aleksic R.** (2003), Analysis of fatigue and crack growth in carbon- fiber epoxy matrix composite laminates, *Strength of Materials*, Vol.35, 500-507.
11. **Tai N. H., Ma C. C. M., Wu S. H.** (1995), Fatigue behaviour of carbon fibre/PEEK laminate composites, *Composites*, 26, 551-559.
12. **Wu F., Yao W.** (2010), A fatigue damage model of composite materials, *International Journal of Fatigue*, Vol. 32, 134-138.

NUMERICAL-EXPERIMENTAL ANALYSIS OF PLASTIC FLOW BEGINNING PHASE ROUND THE HOLE IN THE THIN SHIELD UNDER TENSION

Stefan BUĆKO*, Henryk JODŁOWSKI*, Marcin TRZEBICKI**

*Institute of Applied Mechanics, Cracow University of Technology, al. Jana Pawła II 37, 30 -864 Kraków, Poland
**Institute of Machine Design, Cracow University of Technology, al. Jana Pawła II 37, 30 -864 Kraków, Poland

s_bucko@mech.pk.edu.pl, abies@mech.pk.edu.pl, mtrzeb@mech.pk.edu.pl

Abstract: The method of recognition of plastic strains with the use of optical interference was characterized in the work. The idea of the method was shown on the example test for 15HM steel tension. The results of experimental testing of plastic strains initiation in the thin shield with opening of Ø20 diameter under tension, especially considering round the hole zone were presented in further part of the work. The experiment was carried out with the use of method mentioned above. In the experiment the stresses initializing plastic deformations and the shape of plastic zone were determined. The stress state analysis in the hole zone in the specimen under tension was realized with the use of finite element method. The calculations were done for two significantly different hole diameters. The results of FEM calculations allow for certification that for the holes of diameters significantly bigger than the shield thickness round the hole plane stress state occurs.

Key words: Plastic Strains Identification, Optical Interference, Stress Concentration, Experimental Research, FEM Analysis

1. INTRODUCTION

The problem of concern is the quantitative description and the experimentally verified interpretation of the initial formation phase of macroscopic plastic deformations in zones with a stress gradient for materials with material unstableness. In materials with a distinct yield point the smallest plastic deformation can be significantly larger than the strains associated to the elastic limit (upper yield point). Occurrence of plastic deformation at the point of maximal effort is not possible at the time of fulfillment in this one point the condition of plasticity, as in the neighboring points stresses are smaller than the yield strength. Occurrence of plastic deformation in the form of plastic slips requires the assembly of a portion of elastic energy required to run the slip, and therefore requires a large elastic deformation in grains around this point. In the scientific literature so far no convincing answer to the question: how and when the plastic deformation in such cases begins.

The common practice of experimental research into elastic-plastic state under conditions of stress gradient i.e. in the vicinity such as holes in the discs or in areas of other notches, depended mostly on the measurement of displacement, strain calculation and use of the yield condition (Durelli and Parks 1970, Theocaris, Marketos 1964) or the use of optically active layer and the condition of plasticity, which is not always synonymous with the start of plastic deformation. Further analysis has usually been conducted by solving the classical equations of the plasticity theory. As a result, the shape of plastic zone depend on the results of measurements and the adopted conditions of plasticity, which has not been the result of the experiment any more.

In that method, it is assumed that the launch of the plastic slides in the homogeneous stress state (pure tensile strength) and in conditions of stress gradient occurs at the same stress level, which assumption is dubious, considering the literature (Brzoska, 1972; Malinin and Rżysko, 1981).

The purpose of this paper is to further verify the effectiveness of previously developed methods for identifying plastic macro-strains in the active process of loading, in steels of material insta-

bility, based on the use of optical interference phenomenon (Bucko and Jodłowski, 2006; Jodłowski, 2007) and attempt to estimate the value of the yield strength i.e. at which begins the process of plastic flow - what respond to physical phenomena accompanying the yield strength is pronounced in the static tensile experiment. An important element is the attempt to explain the mechanisms of launching of plastic slips - regarding the plane of maximum shear stress action.

2. CHARACTERISTICS OF EXPERIMENTAL RESEARCH

The method of plastic macro-strains identifying in the active process of loading in the active process utilizing known phenomenon of optical interference has been discussed in detail and justified in the previously mentioned works (Bucko and Jodłowski, 2006, 2009; Jodłowski, 2007). A shortened description of the research method is presented below but in the next section the examples of research of verifying correctness and effectiveness of this method in the static tensile test are discussed. The idea of this method of research is as follows:

Disappearance of interference fringes observed previously in the active process of loading shows that plastic deformation occurred.

"Occurrence of interference fringes that means the polished surface ability to reflect light, may in fact occur only on the surface of these grains, in which there was no slip yet malleable, which is in a state of elastic".

The test method is based on the principle formulated above can probably detect only a plastic macro-strains in the scale occurring when the yield stress is pronounced in the static tensile experiment, but it is possible to observe their formation in the active process of loading. The method therefore does not require termination of the experiment in order to perform microscopic observation or realising of the unloading process just to verify the nature of the deformation. The proposed method is not sensitive to the possible displacement of the observed sample surface

because the interference fringes number is not important (confirms only a distance between the interference strainer and sample), significant is merely the presence or disappearance of optical interference phenomenon. An important advantage of optical interference method is also possibility to visualize the process of formation and propagation of plastic deformation.
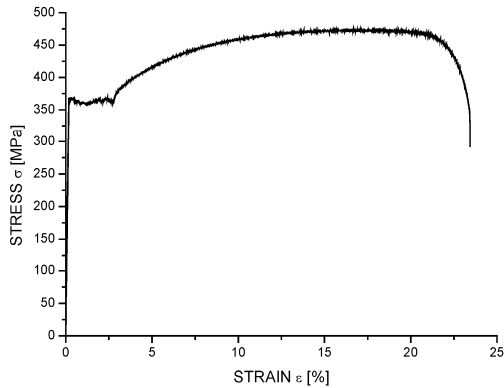

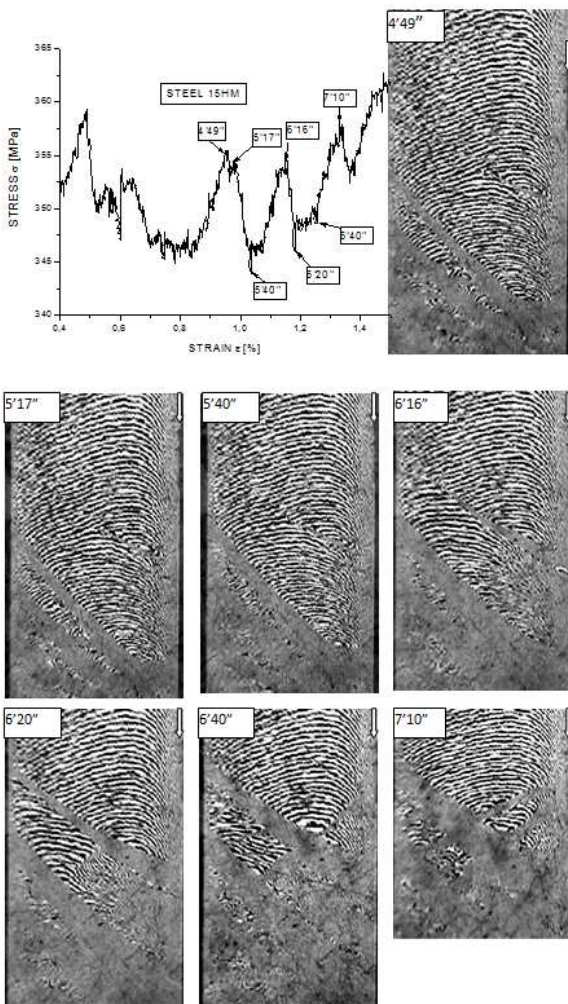**Fig. 1.** 15HM steel tensile test diagram

Fig. 2. 15HM steel. A part of the plastic platform of tensile test diagram. Marked points correspond to the times of phenomena occurrence on the video film

In order to illustrate the effects occurred in plastic deformation identification with the use of optical interference method,

the interference fringes images are showed below. The images were recorded during the static tensile test of specimen made of 15HM steel. From the same material the next specimen with the central hole was prepared for the test described in the further part of the work.

Fig. 1 shows a graph of that stretch of steel in a classic form, while Fig. 2 shows an accurate (zoomed) picture of the plastic platform with the registered moments in time attached to the set of pictures interferential fringes registered in the same moments of time. During the study the principle of full synchronization of recording of all parameters and images was adhered.

According to the described above method disappearance of interference fringes means that plastic slips took place. The diagonal bands slopped to the axis of the sample where the interference fringes disappeared are visible on the photographs shown in Fig. 2. Next such bands appear following the development of plastic deformations. In the zones among these bands where the interference fringes are still visible slow disappearance of the fringes is observed.

3. EXPERIMENTAL RESEARCH ON DISC WITH AN APERTURE

Experimental studies were carried out for the thin plate of dimensions 550x98.8x4.7 [mm] under tension with symmetric aperture with a diameter of 20 [mm] made of 15HM steel with pronounced yield point , tensile diagram of this steel is shown in Fig. 1 in section 2 of work. Shape of the test plate is shown in Fig. 3.
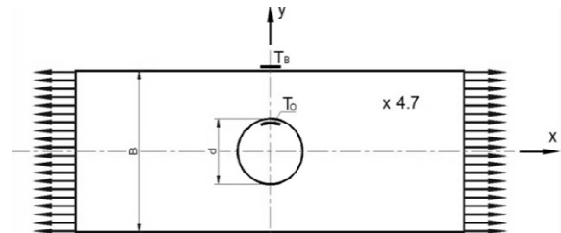
Fig. 3. Scheme of the shield with strain gauges T_O i T_B

To verify the correctness of the indications of optical interference method in place of extreme stress on the lateral surface of aperture electrical resistance strain gauge T_O was glued, second T_B strain gauge was glued to the side surface of the shield.

The interference fringes images were recorded with the use of camera as well as changes of tensile force and the resistance strain gauge T_O indications have being registered during the experiment. All these parameters were recorded synchronously on a common timeline. Applied method of registration of characteristic experiment parameters allowed for unambiguous assignment of nominal stresses and maximal strains, strains and stresses calculated according to two methods (analytical and numerical-FEM) to corresponding interference fringes images.

The first signs indicating the occurrence of plastic slip in the disc loading process revealed in the film by a step change of the interference fringes distribution at the opening in the form of a pulse sent to the outer surface of the shield, and by rapid increase of the strain gauge indications placed on the hole side surface - Fig. 3.

One possible and reliable ways to verify the correctness of the method of optical interference in the use to identification of plastic macro-strains is to compare changes in the measured stress value to the maximum stress value calculated for corresponding loads from Howland formula and to the stress calculated by finite element method assuming a linear elasticity.

The maximum value of stress on the hole lateral surface as the first plastic slip was observed calculated from the strain gauge TO indication and the real material Young's modulus value was $\sigma_{mo} = 1.462R_{eH}$. Impulse interference fringes on the image appeared in the axis of symmetry perpendicular to the direction of stretching, and plastic zone (disappearance fringes at the surface) was shifted close to half of the thickness of the disc and develop in a direction coinciding with the direction of symmetry axis. This indicates that the initiation of slip occurred in the mid-surface zone of the blade.
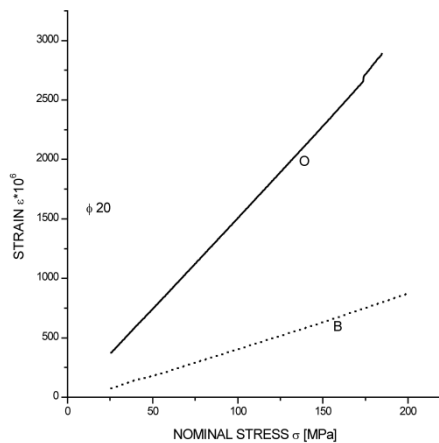

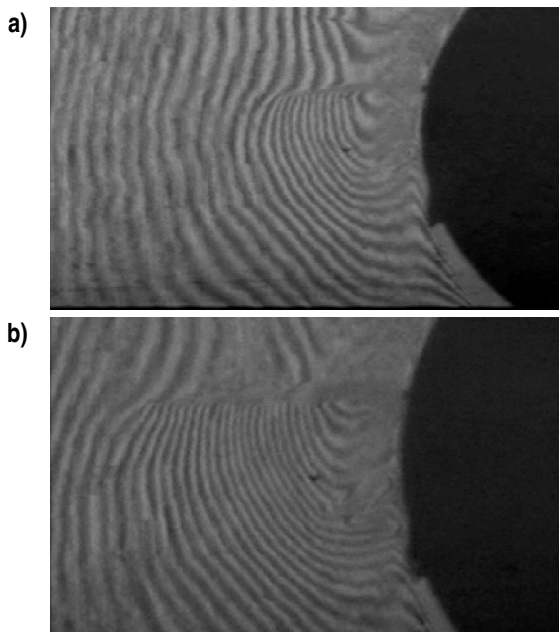**Fig. 4.** Diagram of strains indicated by resistance strain gauges T_O i T_B

Fig. 5. View of the plastic zone interference fringes in the ⌀20 hole neighborhood: a) beginning phase of plastic strains; b) developed phase of plastic strains

Fig. 4 shows the deformation diagrams on the side surface of the hole (T_O) and at the lateral surface of the disc (T_B). At the graph of the T_O strain gauge indication the dramatic increase in deformation display is visible. This corresponds to the impulse mentioned above what is visible on the interference fringes image.

Two images of plastic zones in various stages of increase are shown in Figs 5a and 5b. To show the pulse starting slipping on the photograph is not possible, because requires the continuous observation of phenomena such as the movie. Plastic zone, visible on the shield surface in the shape of a narrow wedge develops in the direction of the side surface of the plate as shown in the work (Bucko and Jodłowski, 2009) for a disk with a hole of larger diameter. Interference fringes systems on both sides of the plastic zone differ significantly with their density and shape and therefore exhibit a discontinuity. Interference fringes discontinuity indicate on displacement discontinuity on the shield surface, which may indicate the opposite directions of displacements of the surfaces. The fringes are in fact in some ways contour lines of gap size between the mirror and observed shield surface.

4. ANALYSIS OF STRESS AND STRAIN STATE IN THE HOLE ZONE

Analytical solutions of the problem of stress distribution around the hole in the thin disk are known for a long time. Theoretical studies of this problem stemmed from the computing needs for riveted connections. For a small hole in an infinite shield is the Kirsch solution of 1898, while for holes of any diameter compared to the shield width the solution has been obtained by Howland (Howland, 1930). Both of the above-mentioned analytical solutions are based on the assumption of plane state of stress and the linear elasticity. Both of the above-mentioned analytical solutions are based on the assumption plane stress state and the linear elasticity obviously. Especially the latter approach became the basis for developing charts of stress concentration factors around holes in thin shields, commonly used in the calculation of fatigue strength. In later years he also obtained a solution based on the equations of the theory of plasticity and also on the assumption of plane stress (Durelli and Parks, 1970; Theocaris and Marketos, 1964). Observations of schemas of plasticising of shields with holes diameters of which were close to the shields thickness suggest that there is significant derogation from the plane stress state in the discs whose thickness is much smaller than the width, which is normally considered to be thin. Analytical solution of the problem of stress state around the hole, taking into account the spatial state of stress is very complex and unlikely to bring success. The work thus takes the concept to analyze the state of stress around the hole using the finite element method allowing for taking into account triaxial stress state in the zone of the hole. Finite element method as an approximate method of calculation provides a number of computational problems especially in boundary zones. These difficulties can be at least partially overcome by using a suitable discretization and a calculation result sufficiently close to a strict solution can be obtained.

For the analysed shield FEM calculations were performed using ALGOR system. In order to show the impact of hole diameter relative to the thickness of the disc at a fixed width below shows the results of calculations of stresses around two openings: one with a value of 1.28 for this parameter and the second for parameter that equals 4.25 for whom results of the experiment are shown in further part of the work. Most important calculation results -from the perspective of the analysis of processes of plastic flow- are depicted in Figs 6, 7, 8 and 9 in the form of maps of distributions of stresses and displacements. Pictures of stress distributions presented in the above Figures relate to the half of the disc

thickness i.e. the lowest surface is the midsurface of the shield.

FEM calculation results show that for the test case (hole Ø20 mm) the derogation from the plane state of stress is very small. This is indicated by very small, although nonzero, the value of stress in the direction perpendicular to the shield shown in Fig. 7. The maximum value of the equivalent stress by hypotheses Huber-Mises-Hencky`s and the Coulomb-Treska-Guest are almost identical and very close to the maximum stress in the direction of the shield stretching. The maximum equivalent stresses occur in the middle surface of the shield where changes along the shield thickness are small.

The calculation of stresses around the hole Ø20 with formulas derived analytically by Howland (Howland 1930) with assumption of a plane stress state, give results very close to the values obtained using finite elements method. Shown in Fig. 8 insignificant σ_z stress value justifies the assumption of plane stress state.

Numerical and analytical calculations lead to the conclusion that in the area of maximum effort of material stresses $\sigma_1 > 0$, $\sigma_2 > 0$, and $\sigma_3 = \sigma_z \cong 0$. In this case, the maximum shear stress in the present work are in a plane passing through the y axis and inclined to the plane of the shield at an angle close to 45º. The above-mentioned maximum shear stress, according to evidence from Nadai research (Nadai, 1950) on the plasticity of steel (confirmed by studies discussed down in (Bucko and Jodłowski 2006, 2009; Jodłowski 2007) plays a decisive role in the launch of plastic slip in steel with a distinct yield point. This is also confirmed in the experiment shown in this study (Fig. 5).

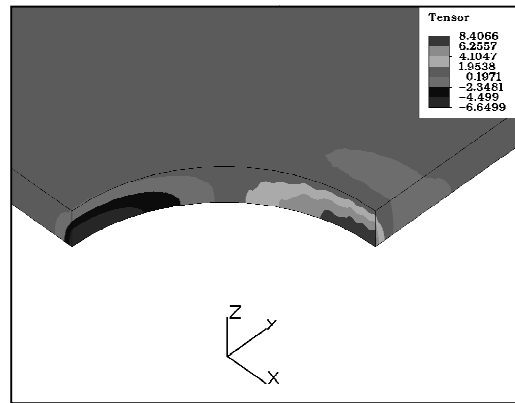The results of FEM calculations for a disk with a hole of 20 mm.

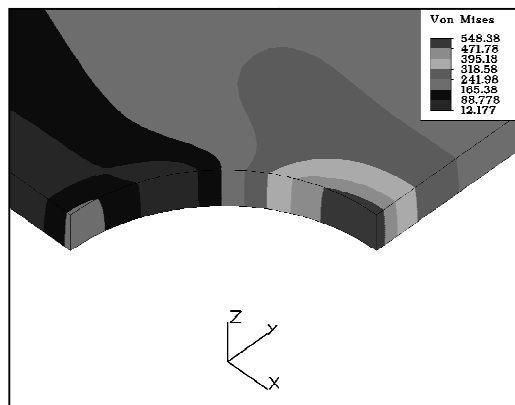

Fig. 8. σ_z stress distribution

Fig. 9. reduced HMH stress distribution
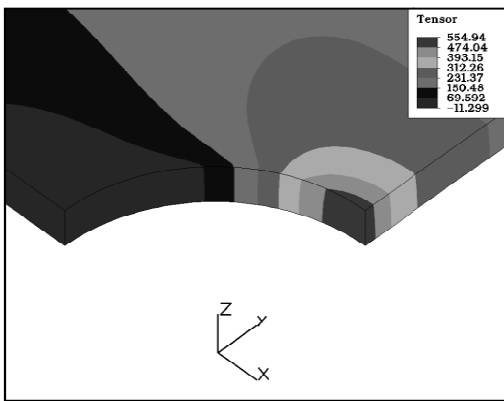
FEM results for the shield with opening of diameter Ø 6 mm
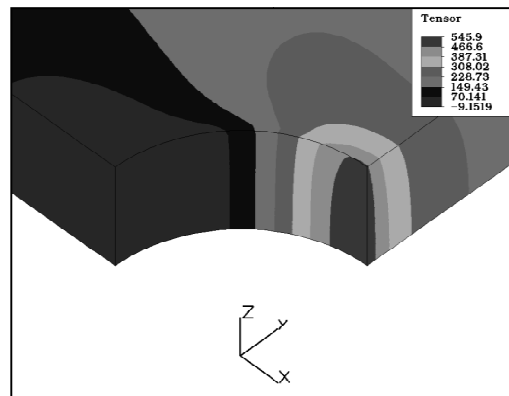

Fig. 6. σ_x stress distribution

Fig. 7. σ_y stress distribution
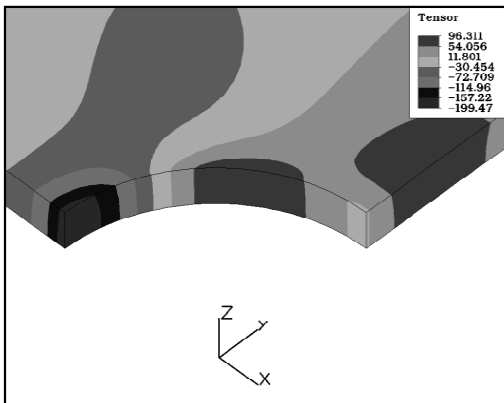
Fig. 10. σ_x stress distribution
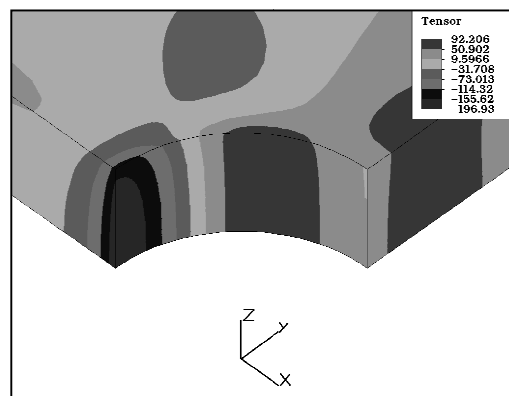

Fig. 11. σ_y stress distribution

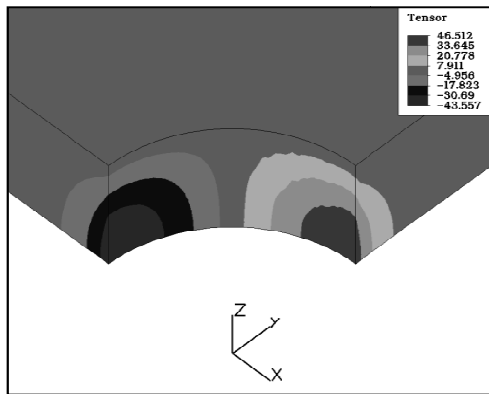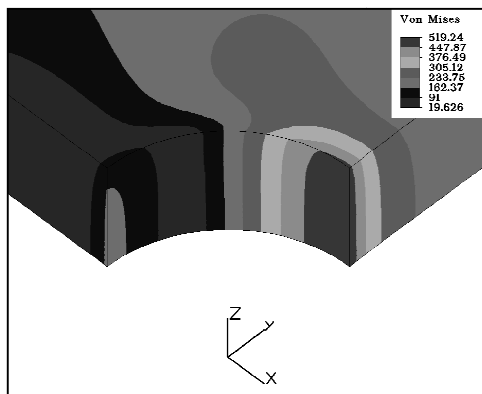**Fig. 12.** σ_z stress distribution

Fig. 13. Reduced HMH stress distribution

As mentioned the calculations of stresses in the disc with a hole diameter of 1.28 times the thickness of the shield (Ø 6 mm) were performed for comparison with earlier results. FEM calculation results indicate that there was a significant departure from the plane state of stress in the zone of the hole. Key results in the form of distributions of stresses in the area of the biggest effort around the hole are shown in Figs. 10, 11, 12 and 13. The σ_z stress valued 8.4% of σ_x stress maximal value occurred in the midsurface of the shield in the zone of the maximal effort. Equivalent stress by hypothesis of Coulomb-Treska-Guest is close to σ_x max and a few percent larger than the equivalent stress by Huber-Mises-Hencky hypothesis. Stress gradient along the shield thickness is clearly larger for the hole Ø 6 than for the hole Ø20.

5. COMPARATIVE ANALYSIS EXPERIMENTAL RESULTS AND CALCULATIONS

Calculation of stresses for the load corresponding to the first plastic strains in the disc with a hole Ø20 mm (signaled by the strain gauge TO and simultaneous of impulsive deformation of interference fringes at the hole edge) were realized with the use of Howland formulas and with the use of FEM program. Both calculation methods base on the assumption of a linear relationship between strains and stress. The maximal stress value obtained with the use of Howland formulas is $\sigma_{Ho} = 1.51 R_{eH}$, the maximum stress value calculated by finite element method is $\sigma_{MES} = 1.52 R_{eH}$, while the stress calculated on the basis of indications of strain gauge TO and Hook's law reached a

value $\sigma_{mo} = 1.462 R_{eH}$. The difference between cited above three stress equals of approximately 4%, what confirms the linearity of the relationship between strains and stresses ie. it confirms elasticity of strains to the stresses exceeding the distinct yield point value by almost 50%. At the same time it confirms the effectiveness of the utility of method of optical interference to the identification of plastic macro-strains in steels with a distinct yield point.

Noteworthy is the shape of plastic zone, i.e. the zone in which there is loss of interference fringes. The Plastic zone is wedge-shaped and extends to the edge of the hole i.e. to place of the largest plastic deformations. The interference fringes behave differently on the both sides of plastic zone during increase of the load (see Fig. 5). Above the plastic zone the number of fringes increases with the load increase, while the in area below the wedge the number of fringes decreases. This indicates the opposite direction of the shield surface displacement perpendicularly to it, on both sides of the plastic zone. This effect confirms the occurrence of slips in the plane of action of maximum shear stress, ie in a plane passing through the axis closely to the y-axis sloped to the shield at an angle close to 45 º.

The results of stress calculations performed by finite element method for hole Ø6 for whom the diameter was comparable to the thickness of the shield, as shown in P.4, justify the conclusion that the patterns of plastic slip for these holes will be different than in cases of large diameter holes such as the hole Ø20 as discussed above. Clarification of the nature of the plastic slides for plates with holes with diameters comparable to the thickness of the disc requires further experimental studies.

REFERENCES

1. **Brzoska Z.** (1972), *Strength of the materials (in polish)*, PWN Warszawa.
2. **Bućko S., Jodłowski H.** (2006), Plastic zones formation in materials with physical plastic limits on the base of new research methods (in polish), *Materiały X Krajowej Konferencji Wytrzymałości i Badania Materiałów*, Kudowa Zdrój.
3. **Bućko S., Jodłowski H.** (2009), Inicjacja odkształceń plastycznych w stali z wyraźną granicą plastyczności w warunkach gradientu naprężeń, *Acta Mechanica et Automatica*, Vol. 3, No. 1.
4. **Durelli A. J., Parks V.J.** (1970), *Moire Analysis of Strain*, Prentice-Hall, Englewood Cliffs, New Jersey 1970.
5. **Howland R.C.J.** (1930), On the Stresses in Neighborhood of a Circular Hole in a Strip Under Tension, *Phil. Trans. Roy. Soc.* (London), A, Vol. 229 (1929-30), 67.
6. **Jodłowski H.** (2007), *Metoda rozpoznawania odkształceń plastycznych w procesie obciążania stali wykazujących niestateczność materiałową*, Praca doktorska, Politechnika Krakowska, Kraków.
7. **Malinin N. N., Rżysko J.** (1981), *Mechanika materiałów*, PWN Warszawa 1981.
8. **Nadai A.** (1950), *Theory of flow and fracture of solids*, t. I, New York 1950, McGraw-Hill.
9. **Theocaris S., Marketos E.** (1964), Elastic-plastic analysis of perforated thin strips of a strain-hardening material, *J. Mech. Phys. Solids.*, 11, 377 – 390.

MACHINING ERROR COMPENSATION
FOR OBJECTS BOUNDED BY CURVILINEAR SURFACES

Lukasz CZERECH*, **Roman KACZYŃSKI***, **Andrzej WERNER***

*Department of Production Engineering, Faculty of Mechanical Engineering, Bialystok University of Technology,
ul. Wiejska 45 C, 15-351 Bialystok, Poland

lukaszczerech@wp.pl, anwer@pb.bialystok.pl, rkgraf@pb.bialystok.pl

Abstract: The paper is devoted to topic related with machining error correction for objects bounded by curvilinear surfaces manufactured on numerically controlled milling machine. Currently it is realized by two techniques. The first of them is called on-line and requires continuous correction of toolpath during the machining process. This approach requires expanded adaptive control systems. The second method called off-line is based on correction of machining control system outside the machine (on the basis of control measurement results). This paper shows methodology of machining shape error correction with off-line technique (with no constant and direct connection to CNC machine tool). This method is based on usage of CAD/CAM systems, numerically controlled milling machine and coordinate measuring machine. Manner of procedure proposed in this paper was verified on the example of ruled surface profile described with NURBS technique. Realization of this proposed methodology of machining error correction has shown significant accuracy correction of manufactured element.

Keywords: CNC Machine Tool, CAD, CAM, Coordinate Measuring Machine, NURBS

1. INTRODUCTION

Manufacturing of elements using numerically controlled machine tools is one of the most popular techniques deployed in modern production processes. Even in case of cold, hot or casting part shaping, many of finishing technological procedures are done by machining. It is caused by noticeable tendency to shorten machining time, the possibility of eliminating other more expensive and time-consuming technological procedures, the possibility of increasing diversity of manufactured products and an increasingly significant role of flexible production. In these cases machining of solid material can be more cost-effective than preparing workpiece by using expensive press tools, dies, molds or casting dies. In many cases thanks to super-efficient tools, with increased wear resistance layers, machining can replace expensive and time-consuming electrical discharge machining (Cichosz, 2006).

Machining of geometric models containing curvilinear geometries is now used in industry for manufacturing different kinds of cams, dies, forming insert for injection moulds, electrodes for electro machining drill and other specialized tools. High accuracy is needed in manufacturing of these elements. Since elements of machines, of which curvilinear surfaces work together, are more common, so they must be in 7,8 accuracy class. Besides accuracy these elements are required of repeatability and high quality of the geometric surface structure.

Factors induced by machining itself, such as thermal and elastic deformations of some elements in kinetic shaping chain, changing the coefficient of friction on surfaces which are used by working units and other loaded with machining forces have essential influence on wrought object accuracy (Chen and Ling, 1996; Lim and Menq, 1997).

1.1. Causes of machining deviations and correction methods

All elements produced on computer controlled machining are burdened with machining errors, which can be grouped according to different genesis.

The first biggest group are geometric errors. They are treated as machining errors, which occur even without mechanical load and basically result from imperfect performance, insufficient stiffness or machining wear. They affect the components mutual compatibility during cooperation, which is their perpendicularity and parallelism. They enlarge severely with increasing machining wear. Okafor and Ertekin in their work (Okafor and Ertekin, 2000) and also Lim, Meng and Yen (Lim et al., 1997) precisely describe causes of that kind of errors.

The second equally important group are deviations resulting from thermal distortion, which can be divided into local and resulting from machine's work environment. These first can come from friction caused by cooperating element's movement, axe's servo drives, other gears and from machining process itself. Engines, bearings, hydraulic systems, ambient temperature and others can be a heat source. The most difficult is to eliminate this group of errors, because they are difficult to predict and estimate. Thermal deformations of machining units are caused by thermal expansion of construction materials which are subjected to impact of changing and different temperatures. Heat sources multiplicity and its complicated transfer mechanism cause the analytical temperature determination of the machining elements is almost impossible. Experimental methods specifying the temperature fields in machining and thermal deformations designation are widely used. These methods, however, are complicated and laborious and the results are similar. Thermal deformations

reflect the workpiece as measure and shape errors. The subject of estimation and thermal deviations errors is widely described in works (Li et al., 1997; Ramesh et al., 2000).

Another very relevant source of errors is machining process itself and phenomenon accompanying. Basically these are forces acting on machining and workpiece, which mainly depend on machine working element's and workpiece weight, machining and inertial forces. This problem was widely described in Raksiria and Parnichkun's works (Raksiria and Parnichkun, 2004) and as well Yaldiz's et al. (2007).

This big quantity of systematic and random errors caused the development of research which eliminate errors components and get the machining of high accuracy. Two methods of error correcting for numerically controlled machining were results of this research. The first of them, off-line method, is based on indirect correction of NC program. The second method of machining errors compensation is on-line, which is characterized by direct correcting during machining.

Analysis of literature connected with machining error correction shows that many approaches towards increasing accuracy of manufacturing have been elaborated. One of them is designing the machining process, in which machining forces are controlled by adjustment of parameters such as feed or the width of machining layer. The result is that the tool is not bending over the specified and permissible limit (Yang and Choi, 1998). Adaptive on-line control approach is developed, which corrects the position of the tool in real time. This approach requires the machining armament with sensors to control permanent merits which have influence on machining preciseness (for example tool banding, dislocation error of machining working unit and others) (Yang and Choi, 1998). Off-line methods are widely used, which include updating of toolpath based on known machining error distribution. It requires the series of machining tests and control measurements which purpose is to appoint modified toolpath (Ryu and Chu, 2005; Lechniak et al., 1998; Lao and Hsiao, 1998).

During realization the technologic program by machine tool, the person who is operating it, has no possibility of compensation these errors, and hence has no influence on machining accuracy. The correction of measurement and the shape of workpiece machined in control program can be entered only after machining, measuring and evaluating the executed object. There are also systems allowing to compensate machining deviations in real time, but these are very complex systems mainly based on neural networks. They allow, in some extent, preliminary evaluation of some machining deviations and minimize them.

2. COMPENSATION METHODOLOGY OF MACHINING DEVIATIONS AT CURVILINEAR PROFILES

Methodology of compensation machining deviations proposed in this article base on off-line method. It can correct summary machining errors, which sources were described in chapter one.

Fig. 1 shows the algorithm of compensation methodology of machining deviation at curvilinear profiles.

This proposed methodology is based on CAD/CAM systems usage, coordinate position measuring technique and CNC milling machines. The initial element is object's geometric model created in CAD module. Based on it, the detail machining program in CAM module is created later on. After manufacturing the object in CNC milling machine, coordinate position control measurements are done. As a result of these measurements

one can get information on values and the distribution of occurring machining deviations. When deviations values meet the needs of executive, the machining process is ended. Error values are corrected when they are too big. First, based on information on values and distribution of observed machining deviations, the shape modification of geometric model of manufactured object is done (CAD). An adjusted geometric model is created that way, which shape takes into account the occurring machining errors. This model is used in generating the adjusted machining program of parts (CAM). After second machining of part, control measurement are done again. Information on effectiveness in methodology of machining errors correction is gathered this way.
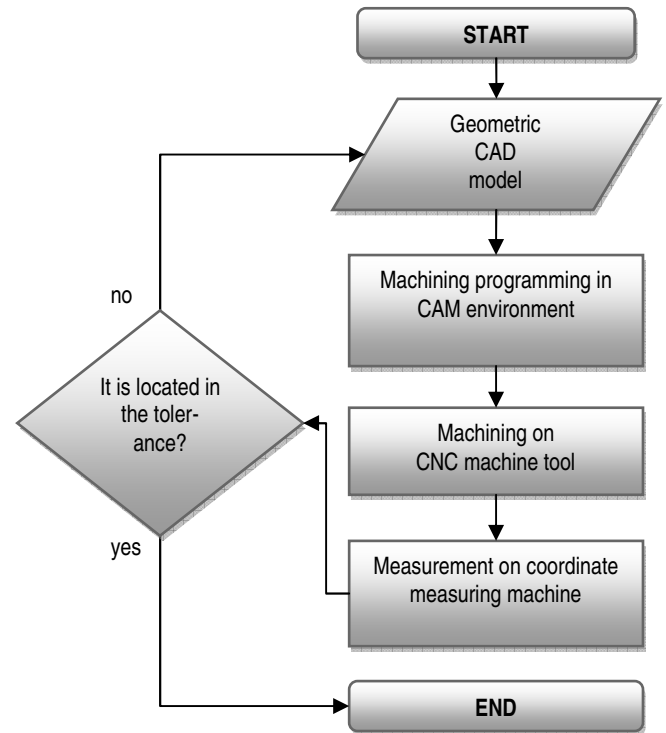
Fig. 1. Algorithm of machining deviations' compensation at curvilinear profiles

In presented methodology the relevant element is value designation and distribution of machining deviations in manufactured profile. The graphic presentation of machining deviation in flat profile is shown in Fig. 2. This is a distance form point observed during measuring to correspondent nominal point on profile (measured in normal direction to profile).
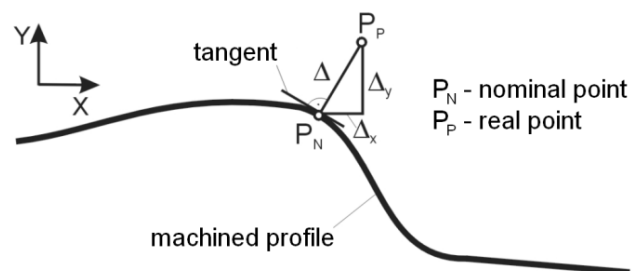
Fig. 2. Graphic interpretation of machining deviation

Deviation values are determined from the following dependence:

$$\Delta = \sqrt{\left(X_P - X_N\right)^2 + \left(Y_P - Y_N\right)^2} \qquad (1)$$

where: Δ – machining deviation, X_P, Y_P – measuring points coordinates, X_N, Y_N – nominal point coordinates.

2.1. Test stand

Test stand consisting of three elements was used in research on effectiveness in compensation deviation method.

First of them was PC computer, equipped with CAD/CAM application used for creating geometric models build of ruled surfaces, which were formed from NURBS curvilinear outlines.

Fig. 3. MasterCAM's environment interface with created geometrical model and programmed path

Fig. 4. Vertical machining centre used to manufacturing elements containing NURBS geometries

Object's geometric modeling was done in MasterCAM X4 MU3 environment. Fig. 3 shows graphic interface of this environment with modeled surface element bonded programmed tool path.

The second element of this environment was numerically controlled vertical machining centre made by AVIA FOP VMC650 with HEIDENHAIN iTNC530 control system (Fig. 4). Producer
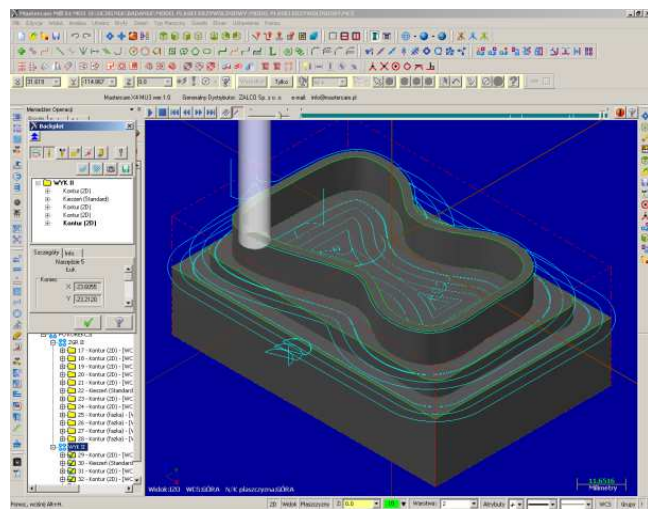
declares +/- 0,005mm of positioning preciousness and repeatability.

This machine tool is used in workshop manufacturing precision tools for making: blanking tools, press tools, dies, forming inserts, injection molds, and other equipment for tools mentioned above. Run time of technological programs on factory components during sample manufacturing was 9000 hrs, and the cumulative operating time of the machining was 17200 hrs.

The last element of the test stand was coordinate measuring machine (CMM). It is combined with PC computer (Fig. 5), with PC-DIMS software installed in MS Windows XP PRO x84 controls the CMM's work.
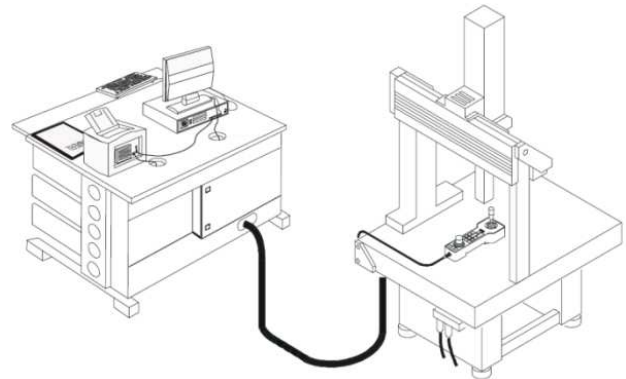
Fig. 5. Equipment used for measuring the element made on CNC machine tool (Lim and Menq, 1997)

Global Performance made by Hexagon Metrology with the producer's declaration of preciousness MPEE = 1.5 + L/333 [µm] is the measuring machine used for coordinate position measurement.

2.2. Experimental studies

Realization of the methodology of compensation machining deviations was mainly based on minimizing differences between the nominal curvilinear NURBS outline modeled in CAD environment and the element manufactured by CNC machine tool.

Firstly, the model consisting NUBRS geometrics was made. Modeling the element was about creating two NURBS curves and drawing them for distance of 10mm with straight drawn surfaces. Extending the surface between curves and the rectangular part that makes the settlement of element easier on coordinate position measuring machine was the next process. The last process was to modeling the base. Geometric model made this way is shown in Fig. 3. This model was used for tool paths programming. The next step was selection of material type, stock size, machining tools and work environment.

Finishing machining of all surfaces taking part in measuring and alignment was done with three flute toroidal end mill with the ø8mm diameter and the 0,5mm fillet radius (picture 6). The tolerance of programmed machining path was 0,015mm. For achieving better quality of surface geometric layer, filtering the arches was used. During machining, besides filtering the arches in MasterCAM environment, filtering in the machining was used, which is done in iTNC530 controller using 'Tolerance' 32 cycle. More fluent tool movement towards machining outline was obtained.

Fig. 6. Analyzed object made on machining centre

The next step after CNC machining was to measure the manufactured element on coordinate measuring machine. After calibration of the measuring head with reference sphere the element was fixed to measuring table. When all the preparative activities were completed, coordinate system orientation of the manufactured object was done. Assignment of the element on the coordinate measuring machine can be divided into following processes:

1. Define the angle between XY plane of the wrought element and the XY plane of the machine.
2. Establishing the coordinate system of fixed element.
3. Define the angle between X axis of the machine and X axis of the element.
4. Establishing the top boundary element's surface.
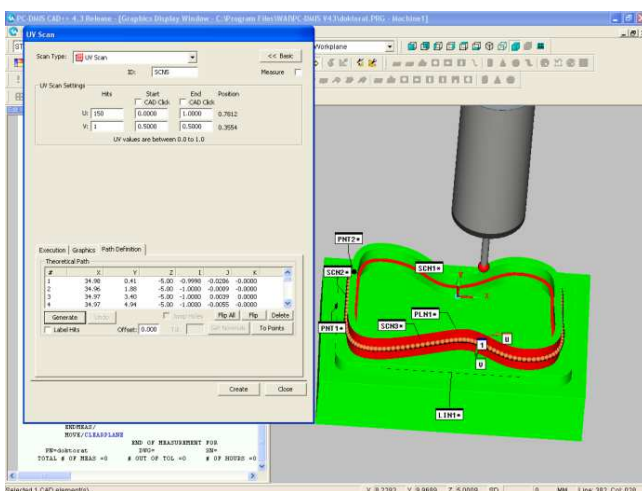5. Fit of the coordinate system in automatic mode (*best fit*).

Fig. 7. Parameters of the measuring program

After analyzing the size and shape of examined profiles, it is accepted that the sampling step during coordinate position meas-

urement will be 2mm. Two profiles of the wrought object were measured. As the result of the measurement, for external profile 113 and for internal profile 106 measuring points were obtained.

As the result of the preliminary elements measurement, the digital equivalent of the geometric model with manufactured deviations was obtained. The given data were imported to the Excel sheet, where manufacturing deviations were separated from nominal values of the object. When the values and distribution of the manufacturing deviations were known, the nominal geometric model was modified and machining program was generated again.
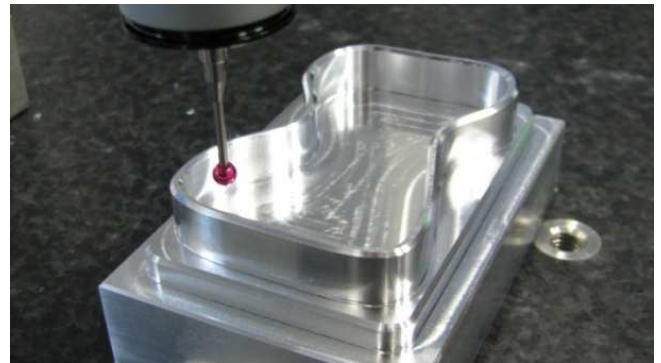
Fig. 8. Measurement of the element
with the coordinate position measuring machine

The next process was to manufacture the element using the corrected machining program. The machining process on machining centre numerically controlled was done using the same machining and technical parameters and in the same work environment. After machining again the measurement was done by coordinate machine (Fig. 8) with the same parameters and according to the same assumptions which were in preliminary controlling measurements.

3. TEST RESULT ANALYSIS

Diagrams in Fig. 9 shows machining deviations values of the external and internal outline. Diagrams show deviations before and after machining errors correction. Significant decrease of deviations maximal values after correction can be seen.

Tab. 1 shows numerical values of appointed machining deviations. 0.025mm is the biggest deviation value for external outline before correction and 0.042mm is the biggest for internal outline. Average deviation value before correction for both external and internal outline was 0.008mm. Note, that after correction of geometric model the maximal deviation values decreased (more accurate projection of the manufactured object was obtained) and were: 0.017mm is the biggest deviation value for external outline and for internal outline the biggest is 0.019mm. Average deviation values after correction were about 0.005mm for external outline and 0.006mm for internal. Reduction of the maximal machining deviations of the external and internal outline was the effect of the correction and was appropriately of 7.4µm and 23.6µm. Reduction of the average deviation values was also obtained and was appropriately of 2.2 and 2.0µm.

Fig. 9. Magnitudes of the deviation values before and after geometric model correction

Tab. 1. Summary of results [μm]

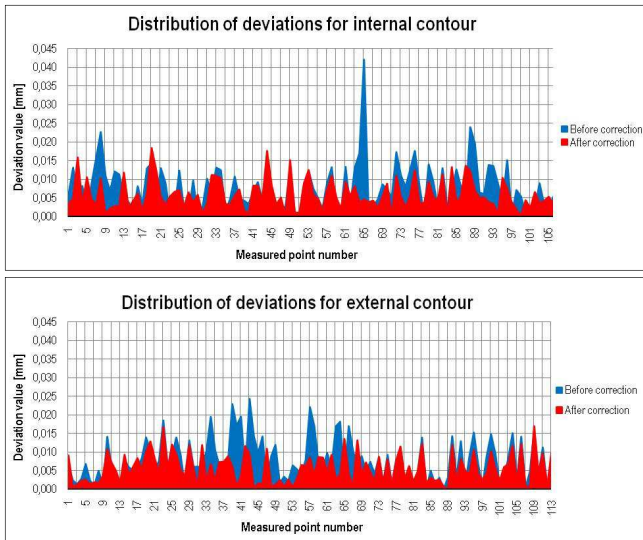|	Before correction		After correction		Correction result	
	out	in	out	in	out	in
Max	24.5	42.1	17.1	18.5	7.4	23.6
Average	7.8	7.9	5.6	5.9	2.2	2.0

4. SUMMARY

The method of deviation compensation is an effective tool, which enables manufacturing elements with high precision. It also enables to minimize deviations for internal outlines (dies) where the wrapping angle is far more bigger than in external outlines (punches). In producing the blanking dies of high precision this method enables obtaining equal clearance on whole length of the cutting contour. It is crucial for aesthetic and dimensional reasons. In the case of molds for plastic it will enable precious fit of the profile forming insets in sockets, where they will be placed, and they will allow for leek proof sealing of the space filled with superficial plastic.

Significant mitigating (for 0.024mm) of the maximal deviation of internal outline is essential and beneficial effect of the correction. Inaccuracy of that size in manufacturing before correction could cause local seizing on cooperating surfaces or could prevent adjustment of two cooperating elements.

Method of the machining deviations' compensation allowed the fast and effective correction of differences between nominal element and the one manufactured by CNC machining.

REFERENCES

1. **Chen J. S., Ling C. C.** (1996), Improving the machine accuracy through machine tool metrology and error correction, *Advanced Manufacturing Technology*, 11, 198-205.
2. **Cichosz P.** (2006), *Narzędzia skrawające*, WNT.
3. **Lechniak Z., Werner A., Skalski K., Kędzior K.** (1988), Methodology of the Off-line Software Compensation for Errors in the Machining Process on the CNC Machine Tool, *Material Processing Technology*, 73, 42-48.
4. **Li S., Zhang Y., Zhang G.** (1997), A study of pre-compensation for thermal errors of NC machine tools, *Machine Tools & Manufacture*, Vol. 37, No. 12, 1715-1719.
5. **Lim E. M., Menq C. H., Yen D. W.** (1997), Integrated planning for precision machining of complex surfaces. Part III: Compensation of dimensional Errors, *Machine Tools & Manufacture*, Vol. 37, No 9, 1313-1326.
6. **Lim E. M., Menq C. H.** (1997), Integrated planning for precision machining of complex surfaces. Part I: Cutting-path and federate optimization, *Machine Tools & Manufacture*, Vol. 37, No 1, 61-75.
7. **Lo C.C., Hsiao C.Y.** (1988), A method of tool path compensation for repeated machining process, *Machine Tools & Manufacture*, 38, 205–213.
8. **Okafor A.C., Ertekin M.** (2000), Derivation of machine tool error models and error compensation procedure for three axes vertical machining center using rigid body kinematics, *Machine Tools & Manufacture,* 40, 1199–1213.
9. **Raksiri C., Parnichkun M.** (2004), Geometric and force errors compensation in a 3-axis CNC milling machine, *Machine Tools & Manufacture*, 44, 1283–1291.
10. **Ramesh R., Mannan M. A., Poo A.N.** (2000), Error compensation in machine tools. Part II: Thermal errors, *Machine Tools & Manufacture*, 40, 1257–1284.
11. **Ryu S. H., Chu C. N.** (2005), The form error reduction in side wall machining using successive down and up milling, *Machine Tools & Manufacture*, 45, 1523–1530.
12. **Yaldiz S., Unsacar F., Saglam H., Isik H**. (2007), Design, development and testing of a four-component milling dynamometer for the measurement of cutting force and torque, *Mechanical Systems and Signal Processing*, 21, 1499–1511.
13. **Yang M.Y., Choi J. G.** (1998), A tool deflection compensation system for end milling accuracy improvement, *ASME J. Manuf. Sci. Eng.*, 120, 222–229.
14. **Yuan J., Ni J. (1988),** The real-time error compensation technique for CNC machining systems, *Mechatronics*, 8, 359-380.

APPLYING RECURRENCE PLOTS TO IDENTIFY BORDERS BETWEEN TWO-PHASE FLOW PATTERNS IN VERTICAL CIRCULAR MINI CHANNEL

Mariusz FASZCZEWSKI[*], **Grzegorz GÓRSKI**[*], **Romuald MOSDORF**[*]

[*]Faculty of Mechanical Engineering, Bialystok University of Technology, ul. Wiejska 45 C, 15-351 Białystok, Poland

mariusz.faszczewski@gmail.com, grzesgor@o2.pl, mosdorf@gmail.com

Abstract: In the paper the method based on recurrence plots has been used for identification of two-phase flow in a vertical, circular mini-channel. The time series obtained from image analysis of high speed video have been used. The method proposed in the present study allows us to define the coefficients which characterize the dynamics of two-phase flow in a mini channel. To identify two-phase flow patterns in a mini channel there has been used the coefficient LAVG which is a measure of an average length of diagonal lines in recurrence plot. The following two-phase flow structures have been considered: bubbly, bubbly-slug and wavy-annular. Obtained results show that method proposed in the paper enables identification of borders between two two-phase flow patterns coexisting in a mini-channel.

Key words: Mini-Channel, Two-Phase Flow, the Method of Recurrence Plots, Nonlinear Analysis, Bubble Pump

1. INTRODUCTION

Numerous experimental studies carried out in recent years in many universities indicate that the two-phase flows in mini-channels are accompanied by fluid behaviors different from those observed in traditional channels (Zhao and Rezkallah, 1993). The flows in mini-channels should be considered taking into account such phenomena as surface tension, liquid pressure oscillation and the reverse flow (Wongwises and Pipathattakul, 2005).

Despite many experimental and theoretical researches, in the literature there is no clear classification of patterns of two-phase flow and types of channels (Chen et al., 2006). Therefore, it is difficult to compare the experimental results, especially when they are carried out for different fluids or different experimental conditions. It is believed that the criterion for distinguishing between types of channels should be based on the channel size and fluid properties (Chen et al., 2006). Usually, the criteria for distinguishing a mini-channel from the traditional channel are based on different numbers of similarities.

Kew and Cornwell proposed the criterion of $Co > 0.5$ (Kew and Cornewll, 1997). Brauner and Moalem-Maron proposed criterion based on the dimensionless numbers of EO. They suggest that when the $EO > 1$, then the surface tension plays an important role in the flow (Brauner and Moal-Maron, 1992). Triplett et. al proposed a criterion in the form of: $EO = 100$ (Triplett et al, 1999). Abkar proposed the criterion in the form of $Bo = 0.3$. The above criteria determine different critical channel diameters which define mini-channels. For air and water channel the critical diameter based on above criterions are in the range from 0.81 to 17.1 mm (Abkar et al., 2003). In the present study the two-phase flow in a vertical, circular channel with a diameter of 4 mm has been analyzed.

Identification of flow patterns in mini-channels often depends on subjective evaluation of the observer and used experimental technique. The flow patterns can change rapidly but usually this change happens slowly and the border between different patterns

is clear. Because of this, the significant scatter in results presented by different researches are observed (Kandlikav, 2002). For parameters characterizing the transition between patterns the two phase flow is usually unsteady. In such situation, the criteria based on average values of the various parameters are not suitable to identify the border between flow patterns. Therefore, the new criterion based on properties of dynamics of two phase flow is required.

In the present paper the method of analysis of video recorded using a high-speed camera has been presented. This method allows us to determine the coefficients characterizing the dynamics of two-phase flows. The recurrence plot method has been used. This method allows us to analyze the dynamics of nonlinear systems with large numbers of freedom degrees. The proposed method was applied to analyze two-phase flows in bubble pump (Benhmidene et al., 2010).

2. METHODS OF EVALUATION OF TWO-PHASE FLOW DYNAMICS

The scheme of experimental stand is shown in Fig.1.

The compressed air generated by the compressor (13), is passing through the tank (12), valve (11), rotameter (10) and a brass nozzle with an inner diameter of 1.1 mm. Air bubbles rising on the nozzle outlet moving in a glass mini-channel (2) with internal diameter of 4 mm and a length of 45 mm, is placed in a glass tank (1) of 400 x 400 x 700 mm filled with distilled water. The movement of air bubbles was recorded by the camera (3) with speed 600 frames/s. Examples of images recorded during the experiment are shown in Fig. 2a. In Fig. 2a the schematic drawing of the flow patterns in mini-channel has been presented.

In the mini-channel the following flow patterns are observed: bubbly, bubbly-slug and wavy-annular. For the flow rate $q < 0.05$ l/min, single bubbles with diameters equal to channel diameter have been observed In the range of $0.05 < q < 0.1$ l/min the flow with long bubbles (Taylor) occurs. In this case a slight variation

of its length and spacing between them was observed (no-observed merger of bubbles). For $q = 0.2$ l/min the process of grouping bubbles in groups of two, three or more bubbles appears. But usually, the line between aggregated bubbles is visible. For $q = 0.3$ l/min bubbles coalesce and form the long slugs, in which the individual bubbles are indistinguishable. The wave-annual flow is formed at $q = 0.4$ l/min.
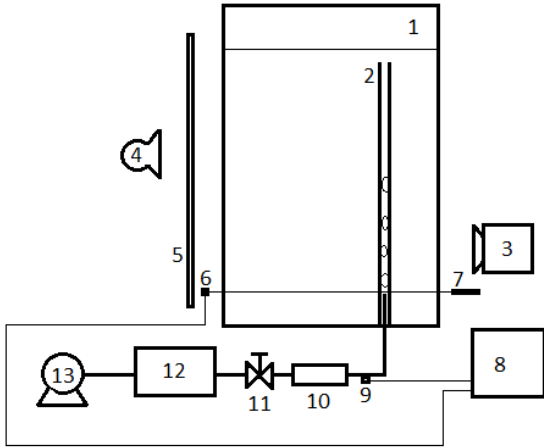

Fig. 1. Scheme of experimental stand: 1 – the water tank,
2 – mini-channel, 3 – Camera Casio EX FX1, 4 – light source,
5 – screen, 6 – phototransistor, 7 – laser, 8 – data acquisition
station (DT9800) 9 – pressure sensor (MPX12DP),
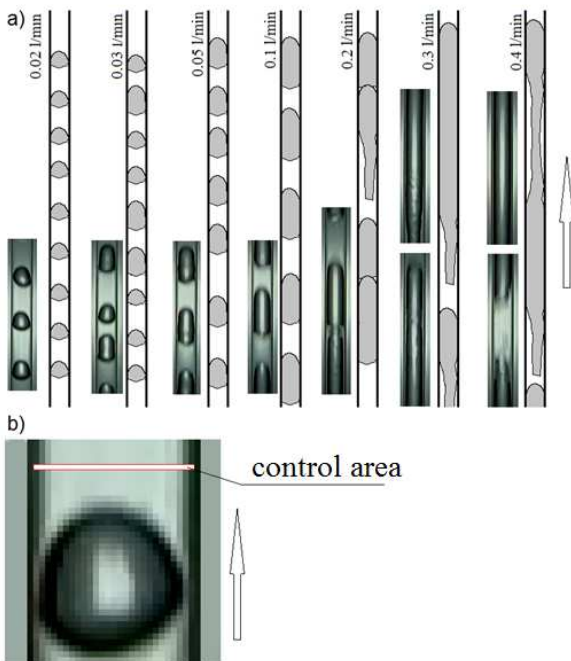10 – rotameter (Kytola OY, A-2k), 11 – valve, 12 – tank of air,
13 – air compressor

Fig. 2. The flow patterns in mini-channel as a function of air volume flow
rate (a). The example of video frame with a selected area
in which the brightness of pixels has been counted (b)

The film made for high speed digital camera (600 frames/s) has been divided into separated color frames. An example of a video frame is shown in Fig.2b. Then, the location of the control area has been determined. In the control area the sum of pixels brightness in each frame has been calculated. The ex-

ample of control area location is shown in Fig.2b. The actual size of the control area is: 0.16 x 4 mm.

Each pixel is characterized by three values of the colour component (RGB). The average brightness of each pixel has been calculated and then, in the control area all brightness values have been summed, according to the relation.

$$x_t = \sum_i \left(\frac{x_R^i + x_G^i + x_B^i}{3} \right)_t \qquad (1)$$

where: i – the number of pixels in the control area, t – number of video frames.

Finally, the time series characterizing the two-phase flow in mini-channel have been obtained. The example of series obtained at different air volume flow rate has been shown in Fig. 3. High values in time series correspond to situations where the control area is filled with water. Low values correspond to situation where the control area is filled with air. In the centre of the air bubble the pixels brightness is low, therefore, in time series the values of x_t are not constant when the bubble passes through the control area. But the beginning and the end of bubble is clearly identified in time series x_t.
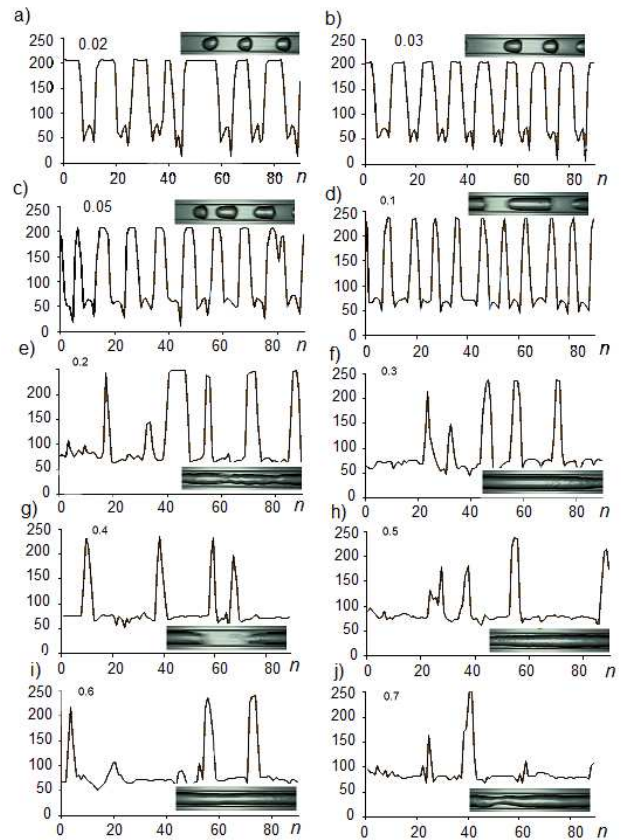
Fig. 3. Time series obtained from the films made by the high speed digital
camera as a function of air volume flow rates. a) $q = 0.02$ l/min,
b) $q = 0.03$ l/min, c) $q = 0.05$ l/min, d) $q = 0.1$ l/min,
e) $q = 0.2$ l/min, f) $q = 0.3$ l/min, g) $q = 0.4$ l/min, h) $q = 0.5$ l/min,
i) $q = 0.6$ l/min, j) $q = 0.7$ l/min

3. DATA ANALYSIS

Identification of the behaviour of dynamic systems based on experimental data proceeds in several steps. The analysis

begins from the reconstruction of the attractor, which is performed in the embedding space, using the so-called time delay method (Schuster, 1993). In this method the coordinates of attractor points are calculated from time series as successive values of time series. The distance between these values (delay time) is equal to τ. The time delay τ is a multiple of time interval Δt between points of time series (Baker and Gollub, 1998). The selection of the appropriate time delay has a significant impact on the reconstruction. There are many methods of determining the optimal values of the time delay. One of them is based on analysis of the autocorrelation function. The optimal value of the time delay is calculated as follows (Baker and Gollub, 1998):

$$C(\tau) \approx \frac{1}{2} C(0) \qquad (2)$$

where: $C(\tau) = \frac{1}{N}\sum_i(x_i - x_{i+\tau})$

Fig. 4 shows the 3D reconstruction of the attractor obtained for the time delay obtained from equation (2).
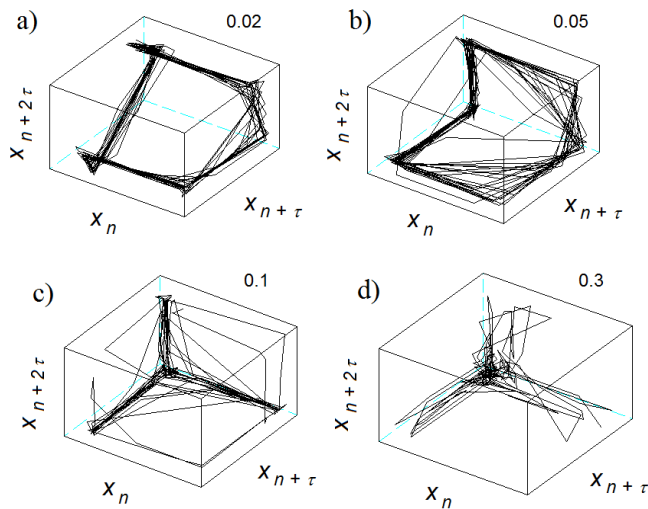

Fig. 4. 3D reconstruction of the attractors for time series shown in Fig. 3.
a) $q = 0.02$ l/min, $\tau = 4$. b) $q = 0.05$ l/min, $\tau = 3$. c) $q = 0.1$ l/min, $\tau = 2$. d) $q = 0.3$ l/min, $\tau = 5$

The values of investigated time series oscillate between two levels. The high level represents the case when the control region (Fig. 2b) is filled with water. Brightness oscillations in this case are small. The low level occurs when in the control area the air bubble occurs. In this case, there are oscillations of brightness due to the changes of the bubble shape. Time intervals in which time series values have small changes (low or high signal level) create these parts of attractor in which the trajectories concentrate. For small q the concentration of trajectories is caused by low and high values of the series (Fig. 4). At high values of q only the low values of time series are responsible for trajectories concentration (Fig. 4d).

The correct embedding dimension in which the attractor should be reconstructed is determined by the correlation dimension. For the experimental data the correlation dimension D_2 can be determined by the following formula (Parker and Chua, 1987; Grassberger and Procacci, 1983):

$$D_2 = \lim_{l \to 0}\frac{1}{\ln r}\ln\sum_i p_i^2 \qquad (3)$$

where: $\sum_i p_i^2 \approx \lim_{N\to\infty}\frac{1}{N^2}\sum_{i,j}\theta(r - |x_i - x_j|) = C_2(r)$,
θ – Heaviside step function.

The quantity C_2, called the correlation integral, determines the probability of finding in the attractor the two points with distance less than r. In order to determine the correlation dimension, the slope of the regression line in linear part of the log plot $\log[C(r)] - \log(r)$ is calculated. Correlation dimension of attractors obtained from recorded time series as a function of air volume flow is shown in Fig. 5.
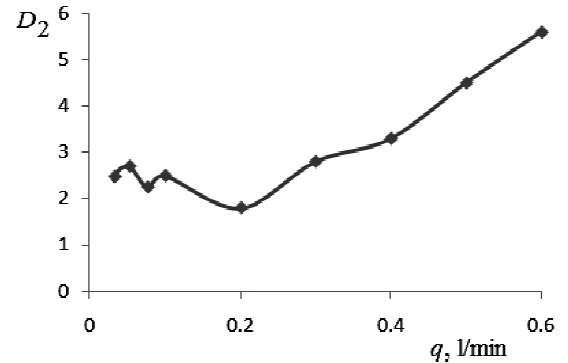
Fig.5. Correlation dimension (D2) of recorded time series vs air volume flow rate

The recurrence plot (RP) is used to evaluate the degree aperiodicity of nonlinear systems. It is also helpful in the analysis of the attractor reconstructed in multidimensional phase space. The recurrence plot is always two-dimensional even though it may represent the system behaviours in the multi-dimensional space. The recurrence plot is described by the relation (Marwan et al., 2007):

$$R_{i,j} = \theta(\varepsilon_i - \|x_i - x_j\|) \qquad (4)$$

where $i, j = 1 ... N$, N number of considered points x_i, ε_i the search radius, $\| \|$ norm, θ Heaviside step function.

Rys. 6. Recurrence plots (RP) obtained for time series shown in Fig. 3., ε_i are equal to 10% of the maximum attractor diameter
a) $q = 0.02$ l/min, $\tau = 4$. b) $q = 0.05$ l/min, $\tau = 3$. c) $q = 0.1$ l/min, $\tau = 2$. d) $q = 0.3$ l/min, $\tau = 5$.

The recurrence plot is defined for attractor immersed in spaces which dimension is the smallest integer number greater than the correlation dimension of attractor. For the air volume flow rate $q \leq 0.3$ l/min the proper embedding dimension is equal to 3. For the larger air volume flow rate the embedding dimension is respectively equal to 4, 5 and 6 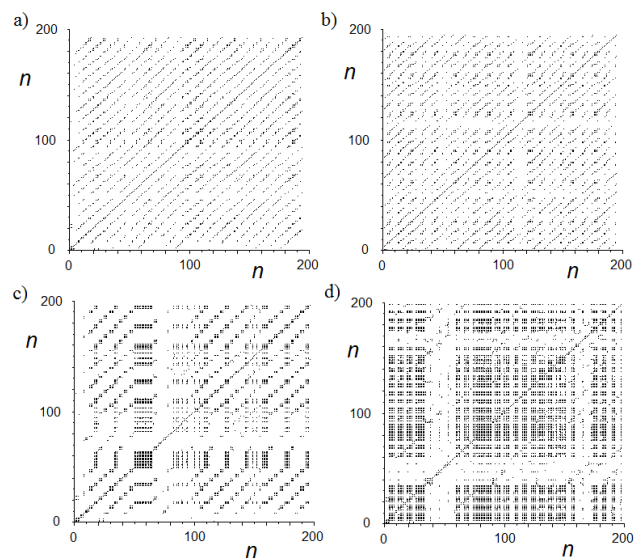(Fig. 5). In Fig. 6 it has been shown the recurrence plots for selected air volume flow rates. For all recurrence plot there has been assumed that threshold ε_i is equal to 10% of the maximum attractor diameter.

Analysis of the shape of the attractor created from measurement data shows that one of characteristic feature of attractor is the area where the attractor trajectories are concentrated. The length of the slug and distance between successive slugs decide on the size of this area. On the other hand, the appearance of those areas is determined by states in which the values of time series vary slightly. Attractor points located in the areas, where attractor trajectories are concentrated, form diagonal and vertical lines on the recurrence plot. The analysis of the length of diagonal lines is carried out, using the coefficient $LAVG$ and $ENTR$, whereas the length of the vertical line describes the coefficient TT.

The average length of diagonal lines, $LAVG$, is defined by the following relation (Marwan et al., 2007):

$$LAVG = \frac{\sum\limits_{l=l_{min}}^{N} lP(l)}{\sum\limits_{l=l_{min}}^{N} P(l)} \tag{5}$$

where $P(n)$ is the number of diagonal lines of length l.

The value of $LAVG$ is a measure of the average time, in which the two segments of the trajectories are close each other (Marwan et al., 2007). In Fig. 7 it has been shown the changes of function $LAVG$ vs air volume flow rate.
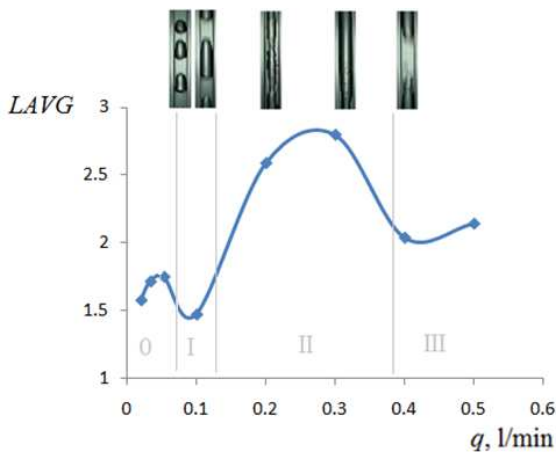

Fig. 7. Changes of $LAVG$ coefficient vs air volume flow rate

In Fig. 7 the range of changes q has been divided into four areas. The bubbly flow appears in the channel in the range marked with symbol "0". With the increase of air volume flow rate the bubble length increases. Such process causes increasing the number of attractor points created by point of time series with a low value. It causes the increase of value of coefficient $LAVG$. Further increase in air volume flow rate leads to decreases of gaps between the bubbles, which leads to decrease of the coefficient $LAVG$. Thus, in the range marked with symbol '0'

(Fig. 7) there is a maximum of function $LAVG(q)$. In this point, the dynamic equilibrium between two processes which determine the bubbly flow mini-channel (the growth of the length of the bubble and reducing the distance between the bubbles) appears.

In the range of q marked with symbol "I" the coefficient $LAVG$ decreases reaching a minimum at $q \sim 0.1$ l/min. The reduction of coefficient $LAVG$ is caused by oscillations of distance between successive bubbles. These oscillations lead to increase of distance between attractor trajectories (Fig.5c). Therefore, the obtained result allows us to divide the range marked with symbol "I" (slug flow) into two sub-ranges:
- in the first sub-range the oscillations of distance between slugs gradually increase. This process leads to drop in the value of the coefficient LAVG,
- in the second sub-range the length of slugs gradually increases. This process leads to increase of values of the coefficient LAVG.

The value of q for which the function $LAVG(q)$ reaches a minimum is a point of dynamic equilibrium between two processes which determine the slug flow in the mini-channel.

In the range "II" the function $LAVG(q)$ reaches a maximum. In the initial part of the range "II" bubble coalescence leads to the formation of long slugs. It causes to increase of the value of the coefficient $LAVG$. In the final phase of region "II" the long slugs are divided into smaller ones due to the flow instability. This process leads to decrease of the value of coefficient $LAVG$. The wave-annual flow is formed at $q = 0.4$ l/min. In this case, the average length of long slugs stabilizes causing small changes of $LAVG$ coefficient with increasing the air volume flow rate. The obtained result allows us to divide the area "II" into two sub-ranges:
- in the first sub-range the process of increasing the average length of joined slugs appears,
- in the second sub-range the average length of long slugs is reduced.

The maximum of function $LAVG(q)$ defines the point of dynamic equilibrium between those two processes.

The coefficient $ENTR$ determines the probability of finding the diagonal line of length l. Its value is related to the Shannon entropy. $ENTR$ is calculated by the following relation (Marwan et al., 2007):

$$ENTR = -\sum\limits_{l=l_{min}}^{N} p(l) \ln p(l) \tag{6}$$

where the probability of finding a line of length is defined as follows (Marwan et a.l, 2007):

$$p(l) = \frac{P(l)}{\sum\limits_{l=l\,min}^{N} P(l)} \tag{7}$$

It is the ratio of the number of diagonal lines with length of l to the sum of all diagonal lines whose length is greater than l_{min}. Fig. 8 shows the changes of the function $ENTR(q)$ for l_{min} equal to 3.

The function $ENTR$ has two maxima and one minimum. The coefficient $ENTR$ increases together with increase of probability of existence of the line with the length greater than l_{min} in RP. It happens when average length of diagonal lines increases (for $q = 0.05$ l/min and $q = 0.3$ l/min, Fig. 7). Thus, the obtained result corresponds to result obtained for coefficient $LAVG$.
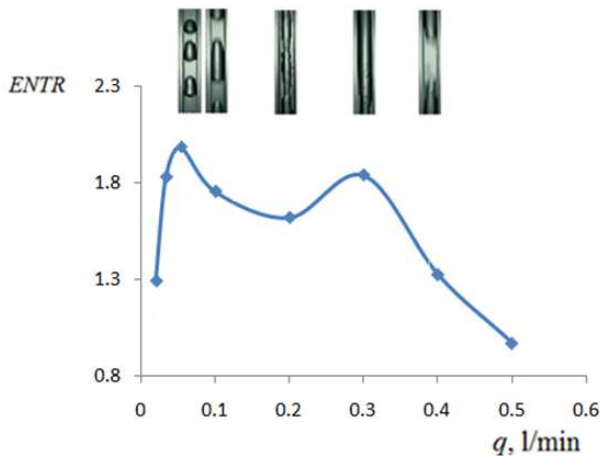
Fig. 8. Changes of coefficient ENTR vs air volume flow rate

The coefficient *TT* (trapping time) determines the average length of the vertical line and is described by the relation (Marwan et al., 2007):

$$TT = \frac{\sum_{v=v_{\min}}^{N} vP(v)}{\sum_{v=v_{\min}}^{N} P(v)} \qquad (8)$$

where $P(v)$ is the number of vertical lines of length v.

The coefficient, *TT*, identifies the average length of the areas on RP, where the state of the system does not change. Fig. 9 shows the changes of *TT* as a function of air volume flow rate.
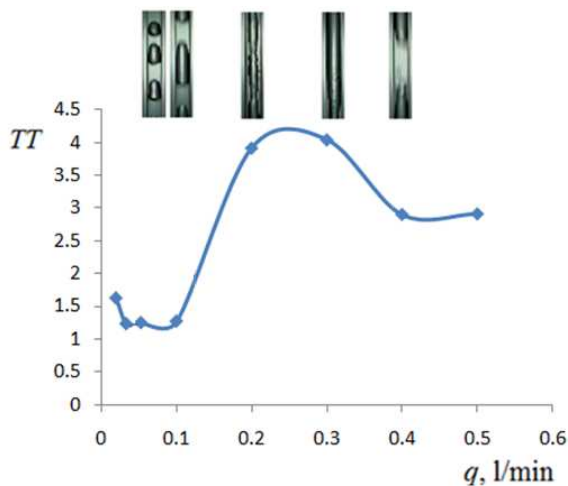
Rys. 9. Changes of the coefficient TT as a function of air volume flow rate

When a slug length is large, the results obtained using the coefficient *TT* are similar to results obtained using the coefficient *LAVG*. The difference occurs for small values of *q* for which there is a small number of vertical lines on the RP.

4. CONSLUSIONS

In the paper, to identify the boundaries between two-phase flow patterns in mini-channel the three coefficients characterizing the structure of recurrence plot have been used:

– coefficient *LAVG* is a measure of the average time in which the trajectories segments are close together;
– coefficient *ENTR* is a measure of entropy of probability of finding the diagonal line of length greater than l_{min} on the RP;
– coefficient *TT* is the average length of the segment of attractor where the state of the system does not change. In this case a large slug passed through the control area.

Obtained results show that using RP allows us to identify borders between dynamically coexisting flow patterns in mini-channel. The coefficient *LAVG* seems to be the most useful in order to identify the borders between different patterns of two-phase flows. Results presented in the paper should be treated as a preliminary once. It is necessary to conduct further research to identify the usefulness of RP for analysing the dynamics of two-phase patterns in mini-channel.

REFERENCES

1. **Akbar M.K., Plummer D.A. and Ghiaasiaan S.M.,** (2003) On gas-liquid two-phase flow regimes in microchannels, *International Journal of Multiphase Flow*, Vol. 29, 855-865,
2. **Baker G.L. , Gollub J.P.** (1998) *A Tutorial of dynamic of chaotic systems (in polish)*, Wydawnictwo Naukowe PWN, Warszawa
3. **Benhmidene, A., B. Chaouachi and S. Gabsi,** (2010). A review of bubble pump technologies. *J. Applied Sci.*, 10: 1806-1813.
4. **Brauner N. and Moalem-Maron D.,** (1992) Identification of the range of small diameter conduits, regarding two-phase flow pattern transitions, *Int. Commun. Heat Mass Transfer*, Vol. 19, 29-39
5. **Chen L., Tian Y.S. and Karayiannis T.G.,** (2006) The effect of tube diameter on vertical two-phase flow regimes in small tubes. *International Journal of Heat and Mass Transfer* 49, 2006, 4220–4230
6. **Grassberger P., Procaccia I.,** (1983) Characterization of Strange Attractors, *Physical Review Letters* 505
7. **Kandlikav S.G.,** Fundamental issues related to flow boiling in minichannels and microchannels, *Experimental thermal and Fluid Science*, Vol. 26, 389-407
8. **Kew P.A. and Cornwell K., (**1997) Correlations for the prediction of boiling heat transfer In small-diameter channel, *Applied Thermal Engineering*, Vol.17, No. 8-10, pp.705-715
9. **Marwan, N.; Romano, M. C.; Thiel, M., Kurths, J**. (2007). Recurrence Plots for the Analysis of Complex Systems, *Physics Reports*, 438(5-6), pp. 237-329. Recurrence Plots And Cross Recurrence Plots (www.recurrence-plot.tk)
10. **Parker T. S, Chua L. O.,** (1987) A Tutorial for Engineers, *Proceedings of The IEEE*, vol. 75, No. 8,
11. **Schuster H.G.** (1993) Chaos deterministyczny – wprowadzenie, Wydawnictwo Naukowe PWN, Warszawa
12. **Triplett K. A., Ghiaasiaan S.M., Abdel-Khalik S.I. and Sadowski D.L.,** (1999) Gas-liquid two-phase flow in microchannels, Part I: Two-phase flow patterns, *International Journal of Multiphase Flow*, Vol. 25., 377-394,
13. **Wongwises S., Pipathattakul M.** (2006) Flow pattern, pressure drop and void fraction of two-phase gas–liquid flow in an inclined narrow annular channel. Experimental Thermal and Fluid Science, 30 (2006) 345-354.
14. **Zhao L., Rezkallah K.S.,** (1993) Gas–liquid flow patterns at microgravity condition, *International Journal Multiphase Flow* 19, 751–763.

EVALUATION OF THE ACCURACY OF THE SOLUTION TO THE HEAT CONDUCTION PROBLEM WITH THE INTERVAL METHOD OF CRANK-NICOLSON TYPE

Małgorzata A. JANKOWSKA, Grażyna SYPNIEWSKA-KAMIŃSKA, Henryk KAMIŃSKI [*]

[*] Institute of Applied Mechanics, Faculty of Mechanical Engineering and Management, Poznan University of Technology
Piotrowo 3, 60-965 Poznań, Poland

malgorzata.jankowska@put.poznan.pl, grazyna.sypniewska-kaminska@put.poznan.pl, henryk.kaminski@put.poznan.pl

Abstract: The paper deals with the interval method of Crank-Nicolson type used for some initial-boundary value problem for the one-dimensional heat conduction equation. The numerical experiments are directed at a short presentation of advantages of the interval solutions obtained in the floating-point interval arithmetic over the approximate ones. It is also shown how we can deal with errors that occur during computations in terms of interval analysis and interval arithmetic.

Key words: Interval Finite Difference Method of Crank-Nicolson Type, Interval Arithmetic, Computational Errors

1. INTRODUCTION

Interval methods belong to a large class of numerical methods first introduced by Sunaga (1958), Moore (1966) and Moore et al. (2009) that enable a result verification. Growing interest in interval methods over a few past decades results from the fact that interval solutions obtained with such methods include the exact solution of the problem. Furthermore, their computer implementation in the floating-point interval arithmetic (Jankowska, 2006, 2009a, b, 2010; Marciniak, 2008, 2009, 2012), together with the representation of the initial data in the form of machine intervals, let us achieve interval solutions that contain all possible numerical errors.

The one-dimensional heat conduction equation considered in the paper belongs to a group of initial-boundary value problems for partial differential equations that occur very often in many scientific fields. For some of such problems the appropriate interval methods were proposed by Jankowska and Marciniak (in press), Manikonda, Berz and Makino (2005), Marciniak (2008), Nakao (2001), Nagatou et al. (2007) and Watanabe et al. (1999).

The paper deals with the interval finite difference method of Crank-Nicolson type. The interval counterpart of the conventional Crank-Nicolson method for the one-dimensional heat conduction equation with the boundary conditions of the first kind were proposed by Marciniak (2012). Jankowska extended his work taking into account the same equation but with the mixed boundary conditions (2012). The interval method proposed enables to include in the interval solutions obtained the local truncation error of the conventional method that is normally neglected. Note that in practice it is not easy to satisfy all the assumptions made in the theoretical formulation of the method given in Jankowska (2012). Nevertheless, the appropriate techniques for the approximation of endpoints of the error term intervals in each step of the method are described in Jankowska (2011). Several numerical tests performed by the author confirmed their effectiveness and usefulness.

The interval method of Crank-Nicolson type described in Jankowska (2011, 2012) is used to solve some initial-boundary value problem for the heat conduction equation formulated in Section 3. The numerical results presented in Section 4 are directed at giving the interval solutions such as they contain the exact solution of the problem. We show how to estimate the errors caused by an inaccuracy of the initial data obtained from the physical experiment, an inexact representation of some real values in a set of all floating-point numbers and the rounding errors that occur during computations. Finally, some conclusions given in Section 5 brings the paper to the end.

2. SOME REMARKS ON INTERVAL METHOD OF CRANK-NICOLSON TYPE

In this section we shortly present the main idea of the interval method of Crank-Nicolson type. Before that it is necessary to introduce fundamentals of interval arithmetic (Moore, 1966; Moore et al., 2009) and its machine implementation (Jankowska, 2009a, b, 2010; Marciniak, 2009). Finally, the well-known sources of errors that can occur during computations are listed and we also explain how to handle them in terms of interval arithmetic.

2.1. Basics of interval arithmetic

A real interval covers the range of real numbers between two bounds and can be defined as follows.

A *real interval* or just an *interval* is a closed and bounded subset of the real numbers R, i.e.

$$X = \left[\underline{x}, \overline{x}\right] := \left\{ x \in \mathbf{R} : \underline{x} \le x \le \overline{x} \right\}, \tag{1}$$

where $\underline{x}$, $\overline{x}$ denote the lower and upper bounds (infimum and supremum) of the interval. The set of all real intervals is denoted by IR.

Degenerate intervals such as $\underline{x} = \overline{x}$ are called thin or point intervals. They are equivalent to real numbers and we may write x instead of X or $[x, x]$.

Since intervals are sets, we can define the standard symbols =, ∈, ⊂, ∩, ∪, /, in the usual sense of set theory. Moreover, we consider the empty set ø as an interval. In this way we ensure that the set of intervals is closed with respect to intersection.

The *diameter* (*width*), *radius* and *midpoint* of an interval *X* are defined as follows:

$$d(X) := \operatorname{diam}(X) = \bar{x} - \underline{x}, \tag{2}$$

$$r(X) := \operatorname{rad}(X) = \frac{\bar{x} - \underline{x}}{2}, \tag{3}$$

$$m(X) := \operatorname{mid}(X) = \frac{\underline{x} + \bar{x}}{2}. \tag{4}$$

The *distance q(X,Y)* between two intervals *X* and *Y* is defined as:

$$q(X,Y) := \max\left\{ \left| \underline{x} - \underline{y} \right|, \left| \bar{x} - \bar{y} \right| \right\}. \tag{5}$$

From the above it follows that the distance equals 0 if and only if *X* = *Y*. It does not depend on the order of its arguments, i.e. *q(X,Y)* = *q(Y,X)*, and the triangle inequality holds. Hence, *q* is a metric and (IR, *q*) is a metric space. Moreover, the concepts of convergence and continuity may be introduced in the usual manner and it can be shown that (IR, *q*) is a complete metric space.

The *interval arithmetic* is an extension of real arithmetic for elements of IR. Let us denote by ∘ one of the following elementary operators +, −, ·, /. Then we define elementary arithmetic operations on intervals by:

$$X \circ Y = \left\{ x \circ y : x \in X, y \in Y \right\}, \tag{6}$$

and we assume that $0 \notin Y$ for the definition of *X/Y*.

The result of an elementary interval operation is the set of real numbers obtained from combining any two numbers in *X* and in *Y*. Since the corresponding real operations are continuous, the right-hand side of (6) is an interval.

Closed intervals can be considered as sets (on which standard set operations apply), or as couples of elements of R on which an arithmetic can be build. Therefore the operations $\circ \in \{+,-,\cdot,/\}$ determined by (6) can be redefined as operations on the bounds of intervals as follows:

$$X + Y = [\underline{x} + \underline{y}, \bar{x} + \bar{y}], \tag{7}$$

$$X - Y = [\underline{x} - \bar{y}, \bar{x} - \underline{y}], \tag{8}$$

$$X \cdot Y = [\min\{\underline{x} \cdot \underline{y}, \underline{x} \cdot \bar{y}, \bar{x} \cdot \underline{y}, \bar{x} \cdot \bar{y}\},$$
$$\max\{\underline{x} \cdot \underline{y}, \underline{x} \cdot \bar{y}, \bar{x} \cdot \underline{y}, \bar{x} \cdot \bar{y}\}], \tag{9}$$

$$X / Y = X \cdot [1/\bar{y}, 1/\underline{y}], \text{ if } 0 \notin Y \tag{10}$$

Note that in terms of the above definition of interval and the way that the interval arithmetic is constructed, a definition of interval function with intervals as variables can be specified. Furthermore, we can build such interval function corresponding to a real-value one in a quite simple way (see e.g. Moore (1966), Moore et al. (2009).

The interval arithmetic can be implemented in most high-level programming languages. However before that some additional definitions of a floating-point interval, a set of all floating-point intervals and basic arithmetic operations on floating-point intervals have to be given.

Let us denote by ʀ the set of all floating-point numbers, i.e. of all real numbers that can be represented in a given real number format.

A *floating-point interval* is a closed and bounded subset of the real numbers R, i.e.

$$X = [\underline{x}, \bar{x}] := \left\{ x \in R : \underline{x} \le x \le \bar{x}, \underline{x}, \bar{x} \in \mathfrak{R} \right\}, \tag{11}$$

whose endpoints are floating-point numbers.

The set ɪʀ of all floating-point intervals over ʀ is denoted by:

$$\text{ɪʀ} = \left\{ [\underline{x}, \bar{x}] : \underline{x} \in \mathfrak{R} \wedge \bar{x} \in \mathfrak{R}, \underline{x} \le \bar{x} \right\}. \tag{12}$$

Let us note that the floating-point interval $[\underline{x}, \bar{x}] \in$ ɪʀ is a connected subset of R, i.e. though $\underline{x}, \bar{x}$ are elements of ʀ, the interval $[\underline{x}, \bar{x}]$ contains not only every floating-point number lying between its bounds, but also every real number within this range.

The rounding ∘ : R → ʀ, which maps a real number to a floating-point number, is defined by the following conditions:

$$\forall_{x \in \mathfrak{R}}, \circ x = x, \tag{13}$$

$$\forall_{x,y \in R}, x \le y \Rightarrow \circ x \le \circ y, \tag{14}$$

where $\circ \in \{\square, \nabla, \Delta\}$, and the symbol □ denotes 'rounding to the nearest', ∇ – 'rounding down' (or 'toward −∞'), and Δ – 'rounding up' (or 'toward +∞').

2.2. Sources of errors during computations

When we are solving a problem in computer we have to be aware that a final result is only an approximation of an exact value. The errors during computations can arise because of three main sources.

First of all, some initial data to a problem can be just experimentally measured quantity that is known only with a limited accuracy. Hence, we use for computations the inexact initial data that can influence the final result very much. Secondly, there are two kinds of errors caused by floating-point arithmetic. Since a set of all floating-point numbers is finite and discrete, some real values (i.e. irrational numbers or real numbers represented by an infinite decimal or binary fraction) cannot be represented exactly in a given floating-point format. If such a real value has to be approximated by a finite fraction, the representation error occurs. On the other hand, even if operands of some arithmetic operator are two. floating-point numbers, the result of operation can be a real value that has to be rounded before it is stored in a given floating-point format. Such errors are called rounding errors and because of complexity of modern computational tasks they are of great importance. Finally, we consider errors of a method applied to solve a problem. If we use a direct method, then after a finite sequence of steps (in absence of rounding errors), we are given an exact solution. On the contrary to an approximate method, that with some necessary simplifications, produces only the approximate solution. An example of approximate methods are finite difference methods for solving an initial-boundary value problems for partial differential equations. An error of these methods is called a truncation error. It is defined as a difference between the partial differential equation and the finite difference approximation to it.

In terms of interval analysis and interval arithmetic we can

deal with the errors considered above. Inexact initial data can be enclosed in an appropriate interval which endpoints depend on the measurement uncertainties. For a real number that cannot be represented exactly in a given floating-point format, we can always find an interval that include such number inside. Furthermore, its left and right endpoints are two neighboring machine numbers. Rounding errors are enclosed in a final interval value, if computations are performed in the floating-point interval arithmetic. Finally, for the interval method we assume that the error term of the conventional method (which is normally neglected) is also included in the final interval solution.

2.3. Interval method of Crank-Nicolson type

The interval finite difference method of Crank-Nicolson type (ICN method) concerns the heat conduction equation with the initial-boundary conditions of the following form:

$$\frac{\partial u}{\partial t}(x,t) - \alpha^2 \frac{\partial^2 u}{\partial x^2}(x,t) = 0, \quad 0 < x < L, \ t > 0, \qquad (15)$$

$$u(x,0) = f(x), \quad 0 \le x \le L, \qquad (16)$$

$$\frac{\partial u}{\partial x}(0,t) - Au(0,t) = \varphi_1(t), \quad t > 0, \qquad (17)$$

$$\frac{\partial u}{\partial x}(L,t) + Bu(L,t) = \varphi_2(t), \quad t > 0. \qquad (18)$$

The ICN method is based on the conventional Crank-Nicolson method (see: Jain (1984), Marciniak et al. (2000)). Its theoretical formulation proposed in Jankowska (2012) assumes that we can enclose values of some partial derivatives of unknown function $u(x, t)$ at midpoints in the appropriate intervals that occur in the error term of the method. With such assumption we can prove that the exact solution of (15) with (16)-(18) at mesh points belongs to the interval solutions obtained. In practice it is impossible to find the endpoints of the intervals considered exactly. We can just approximate them in the best possible way (Jankowska, 2011). The numerical experiments show that such approximation is sufficiently good and the exact solution belongs to the interval solutions obtained.

Let us set the maximum time T_{max} and choose integers n and m. We find the mesh constants h and k such as $h = L/n$ and $k = T_{max}/m$. Hence, the grid points are (x_i, t_j), where $x_i = ih$ for $i = 0, 1, \dots, n$ and $t_j = jk$ for $j = 0, 1, \dots, m$.

For the interval method all initial values, i.e. α, A, B, L, T_{max} should be given in the form of appropriate intervals. Then, for the functions f, φ_1, φ_2, their interval extensions F, Φ_1, Φ_2 are created.

With the interval function F the appropriate interval values of temperature distribution at $t = 0$ are computed. We have:

$$U_{i,0} = F(X_i), \quad i = 0, 1, \dots, n, \qquad (19)$$

where $U_{i,0} = U(x_i, t_0 = 0)$ and $u(x_i, t_0 = 0) \in U_{i,0}$.

The ICN method [8]-[9] is given in the matrix form:

$$CU^{(j+1)} = D^{(j)}U^{(j)} + E^{(j)}, \quad j = 0, 1, \dots, m-1, \qquad (20)$$

where $U^{(j)} = [U_{0,j}, U_{1,j}, \dots, U_{n,j}]^T$, $E^{(j)} = S^{(j)} + R^{(j)}$ is a vector such as a local truncation error of the conventional Crank-Nicolson method at each mesh point is enclosed in $R^{(j)}$,

$R^{(j)} = [R_{0,j}, R_{1,j}, \dots, R_{n,j}]^T$, and C, $D^{(j)}$ and $S^{(j)}$ are matrixes and a vector of coefficients, respectively.

We denote by:

$U_{i,j}$ – an interval value of temperature distribution in (x_i, t_j), $i = 0, 1, \dots, n$, $j = 0, 1, \dots, m$, obtained with the ICN method (20);

$R_{i,j}$ – an interval value which endpoints are appropriate approximations such as a local truncation error $r_{i,j}$ of conventional method is located inside; let us note that we cannot guarantee that:

$$r_{i,j} \in R_{i,j},$$

but numerical experiments confirm that if we consider $R_{i,j}$ in (20), then we have:

$$u(x_i, t_j) \in U_{i,j},$$

$U_{i,j}^C$ – an interval value obtained from the realization of conventional Crank-Nicolson method in interval arithmetic, where all initial data are enclosed in intervals; since the error term of conventional method is neglected, we usually have:

$$u(x_i, t_j) \notin U_{i,j}^C.$$

If we generate $U_{i,j}^C$ in the floating-point interval arithmetic with initial data enclosed in intervals, then their widths provide us information about an influence of errors of inexact input data, rounding errors and representation errors on values of the final result.

3. INITIAL-BOUNDARY VALUE PROBLEM FOR THE HEAT CONDUCTION EQUATION

We consider an infinite plate of thickness L made of the brass (see Fig. 1).
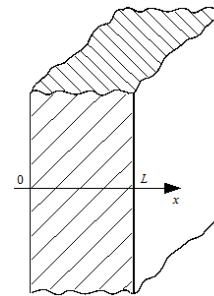

Fig. 1. An infinite plate of thickness L

We assume that it is homogeneous and there is no heat source inside. An initial temperature of the plate is equal to w_0. The external temperatures on the left and right sides of the plate are equal to w_1 and w_2, respectively and they are maintained constant over time.

Under the above assumptions, the distribution of temperature given by a function $w = w(x,t)$ depends on only one spatial variable x. Hence, it is described by the one-dimensional heat conduction equation of the form:

$$\frac{\partial w}{\partial t}(x,t) - \kappa \frac{\partial^2 w}{\partial x^2}(x,t) = 0, \qquad (21)$$

subject to the following initial and boundary conditions:

$$w(x,0) = w_0,$$ (22)

$$\lambda \frac{\partial w}{\partial x}(0,t) = \alpha_1 \left(w(0,t) - w_1 \right),$$ (23)

$$-\lambda \frac{\partial w}{\partial x}(L,t) = \alpha_2 \left(w(L,t) - w_2 \right),$$ (24)

where $\kappa = \lambda/(c\rho)$ [m²/s] is the thermal diffusivity of the material, λ [W/(m·K)] – the thermal conductivity, c [J/(kg·K)] – the specific heat, ρ [kg/m³] – the mass density and α_1, α_2 [W/(m²·K)] – the convection heat transfer coefficients.
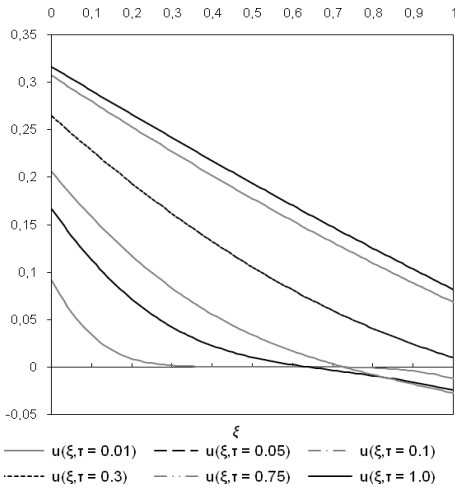

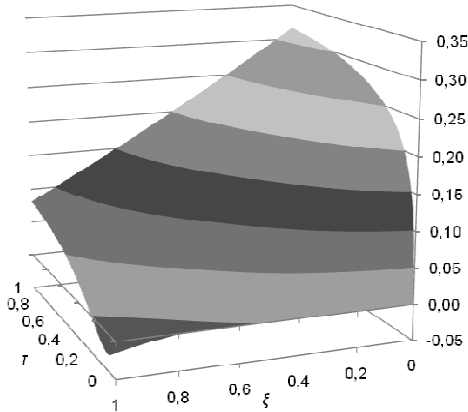**Fig. 2.** Temperature distribution for selected values of time τ

Fig. 3. Temperature distribution for $\tau \in [0,1]$

The initial-boundary problem (21)-(24) can be transformed to the non-dimensional form:

$$\frac{\partial u}{\partial \tau}(\xi,\tau) - \frac{\partial^2 u}{\partial \xi^2}(\xi,\tau) = 0,$$ (25)

subject to the initial and boundary conditions:

$$u(\xi,0) = 0,$$ (26)

$$\frac{\partial u}{\partial \xi}(0,\tau) - \mathrm{Bi}_1 u(0,\tau) = g_1,$$ (27)

$$\frac{\partial u}{\partial \xi}(1,\tau) + \mathrm{Bi}_2 u(1,\tau) = g_2,$$ (28)

where $\xi = x/L$, $\tau = \kappa t/L^2$ and $w(x, t) = w_0\, u(\xi, \tau) + w_0$. The Biot numbers are denoted and defined by $\mathrm{Bi}_1 = (\alpha_1 L)/\lambda$, $\mathrm{Bi}_2 = (\alpha_2 L)/\lambda$. Furthermore, we introduce the notation $g_1 = -\left(w_1/w_0 - 1\right)\mathrm{Bi}_1$ and $g_2 = \left(w_2/w_0 - 1\right)\mathrm{Bi}_2$.

The analytical solution of (25) with (26)-(28) can be derived and is given in the following form:

$$u(\xi,\tau) = f_0(\xi) + 2\sum_{n=1}^{\infty} \frac{f_1(\mu_n,\xi)}{f_2(\mu_n)} \exp\left(-\mu_n^2 \tau\right),$$ (29)

where:

$$f_0(\xi) = \frac{\mathrm{Bi}_2\left(w_2 - w_0\right) + \mathrm{Bi}_1\left(\left(\mathrm{Bi}_2 + 1\right)\left(w_1 - w_0\right) + \mathrm{Bi}_2\left(w_2 - w_1\right)\xi\right)}{\left(\mathrm{Bi}_1 + \mathrm{Bi}_2 + \mathrm{Bi}_1\,\mathrm{Bi}_2\right)w_0},$$ (30)

$$\begin{aligned} f_1(\mu_n,\xi) = {}& \mathrm{Bi}_2\left(w_0 - w_2\right)\mu_n \cos\left(\mu_n \xi\right) \\ &+ \mathrm{Bi}_1\left(\left(w_0 - w_1\right)\mu_n \cos\left(\mu_n - \mu_n\xi\right) + \right. \\ &+ \mathrm{Bi}_2\left(\left(w_0 - w_2\right)\sin\left(\mu_n\xi\right) + \left(w_0 - w_1\right)\sin\left(\mu_n - \mu_n\xi\right)\right), \end{aligned}$$ (31)

$$\begin{aligned} f_2(\mu_n) = {}& w_0\mu_n\left(-\left(\mathrm{Bi}_1 + \mathrm{Bi}_2 + \mathrm{Bi}_1\,\mathrm{Bi}_2 - \mu_n^2\right)\cos\left(\mu_n\right) \right. \\ &+ \left(\mathrm{Bi}_1 + \mathrm{Bi}_2 + 2\right)\mu_n \sin\left(\mu_n\right)\right). \end{aligned}$$ (32)

Note that μ_n, $n = 1, 2, \ldots$ in (29), (31)-(32) are positive roots of the equation:

$$-\arctan\left(\frac{-\mathrm{Bi}_1\,\mathrm{Bi}_2 + \mu_n^2}{\left(\mathrm{Bi}_1 + \mathrm{Bi}_2\right)\mu_n}\right) + \frac{\pi}{2} = \mu_n.$$ (33)

The temperature distribution in the plate given by (29) with (30)-(32) for selected values of time τ is presented in Fig. 2. Similarly, in Fig. 3 we can see $u = u(\xi, \tau)$, $0 \le \xi \le 1$, $0 \le \tau \le 1$.

4. NUMERICAL RESULTS

We take the infinite plate of the thickness $L = 0.05$ [m] and the brass-specific quantities

$$\lambda = 110.6\ [\text{W/(m·K)}],\ c = 377\ [\text{J/(kg·K)}],\ \rho = 8520\ [\text{kg/m}^3].$$ (34)

The initial values of external temperatures and convection heat transfer coefficients are given by exact values or with some tolerance of accuracy depending on the experiment considered.

4.1. Numerical experiment 1

We set

$$w_0 = 280\ [\text{K}],\ w_1 = 400\ [\text{K}],\ w_2 = 250\ [\text{K}],$$ (35)

$$\alpha_1 = 5000\ [\text{W/(m}^2\text{·K)}],\ \alpha_2 = 2500\ [\text{W/(m}^2\text{·K)}].$$ (36)

Hence, the dimensionless quantities g_1, g_2 and the Biot numbers are represented by the intervals given as follows

$g_1 \in [-9.687419271506070\text{E}{-}1, -9.687419271506070\text{E}{-}1]$,
$g_2 \in [-1.210927408938258\text{E}{-}1, -1.210927408938258\text{E}{-}1]$,
$d(g_1) \approx 5.42\text{E}{-}19,\ d(g_2) \approx 1.01\text{E}{-}19,$

$\mathrm{Bi}_1 \in [+2.260397830018083\text{E}{+}0, +2.260397830018083\text{E}{+}0]$,
$\mathrm{Bi}_2 \in [+1.130198915009041\text{E}{+}0, +1.130198915009041\text{E}{+}0]$,
$d(\mathrm{Bi}_1) \approx 6.51\text{E}{-}19,\ d(\mathrm{Bi}_2) \approx 3.25\text{E}{-}19.$

We use the interval realization of the conventional Crank-Nicolson method and the ICN method with h = 1E–2, $k \approx 3.91$E–5.

The widths of interval solutions $U_{i,j}^{C}$ and $U_{i,j}$ at the mesh points (ξ_i, τ_j), $i = 0, 1, \ldots, n$, $j = 1, 2, \ldots, m$ are given in Fig. 4 and Fig. 5. Furthermore, in Fig. 6 the widths of the intervals $R_{i,j}$ of the error term are presented.
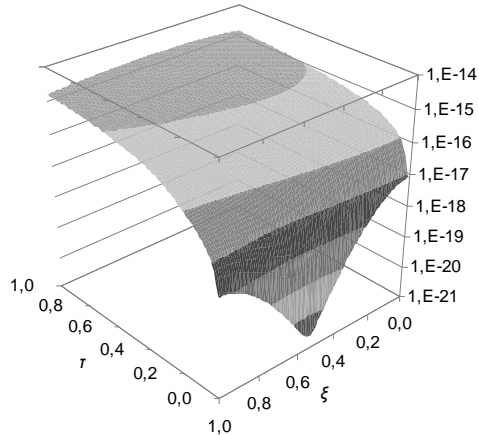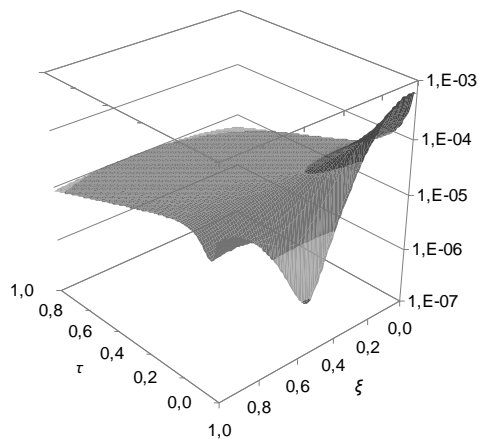

Fig. 4. Widths of the interval solutions $U_{i,j}^{C}$.

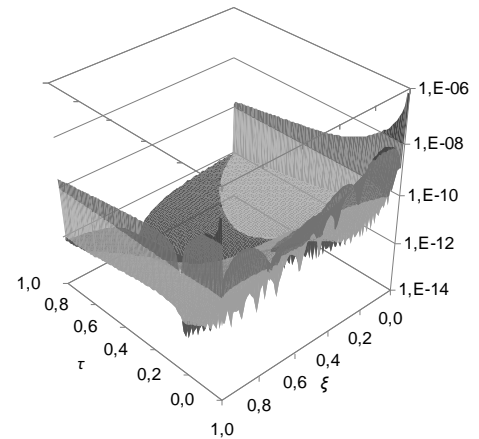**Fig. 5.** Widths of the interval solutions $U_{i,j}$.

Fig. 6. Widths of the intervals $R_{i,j}$ of the error term of the conventional Crank-Nicolson method

In Tab. 1 and Tab. 2 we can also compare the exact solution $u(\xi, \tau)$ with the interval solutions $U^C(\xi, \tau)$ and $U(\xi, \tau)$ computed for $\tau = 1$ and selected values of ξ. Since in the interval solution $U^C(\xi, \tau)$ the local truncation error of the conventional method is neglected, then for all mesh points the exact solution is not included in the interval solution obtained. The difference between the exact solution and the left/right endpoint of the interval solution $U^C(\xi, \tau)$ is presented in Fig. 7.

Tab. 1. Values of the exact and interval solutions $U^C(\xi, \tau = 1)$ obtained with the interval realization of the conventional Crank-Nicolson method for $h = 1$E–2 and $k \approx 3.91$E–5

| ξ	$u(\xi, \tau = 1)$	$U^C(\xi, \tau = 1)$	width
0.0	3.159588E-1	[+3.15958712265990798E-1, +3.15958712265992277E-1]	1.477822E-15
0.1	2.906484E-1	[+2.90648170785494571E-1, +2.90648170785496338E-1]	1.766003E-15
0.2	2.656639E-1	[+2.65663537071720546E-1, +2.65663537071722517E-1]	1.970429E-15
0.3	2.410542E-1	[+2.41053828438518319E-1, +2.41053828438520416E-1]	2.096332E-15
0.4	2.168592E-1	[+2.16858708970163917E-1, +2.16858708970166073E-1]	2.155679E-15
0.5	1.931080E-1	[+1.93107500126792865E-1, +1.93107500126795024E-1]	2.157928E-15
0.6	1.698190E-1	[+1.69818449401430307E-1, +1.69818449401432420E-1]	2.112365E-15
0.7	1.469988E-1	[+1.46998275255881695E-1, +1.46998275255883720E-1]	2.024382E-15
0.8	1.246425E-1	[+1.24641999666420528E-1, +1.24641999666422430E-1]	1.901250E-15
0.9	1.027335E-1	[+1.02733072434454703E-1, +1.02733072434456455E-1]	1.751014E-15
1.0	8.124411E-2	[+8.12437841413371667E-2, +8.12437841413387475E-2]	1.580699E-15
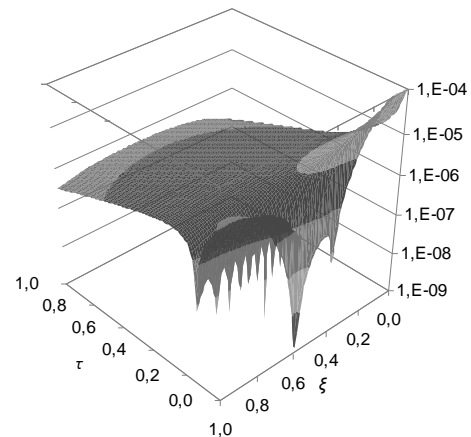
Fig. 7. The difference between the exact solution and the left/right endpoint of the interval solution $U^C(\xi, \tau)$

We can also examine the efficiency of the ICN method applied for solving the problem (25)-(28) with (34)-(36), if we compare widths of the interval solutions obtained for different values of stepsizes h and k. Such comparison is shown in Fig. 8 and Fig. 9. A decrease of stepsizes h and k contributes to the improvement of the interval solutions, i.e. we get the interval solutions of smaller widths. As numerical tests show, a good practice is to adjust the stepsize k in accordance to the stepsize h, such as $k \leq h^2/2$.

Tab. 2. Values of the exact and interval solutions $U(\xi, \tau = 1)$ obtained with the ICN method for $h = 1E-2$ and $k \approx 3.91E-5$

| ξ	$u(\xi, \tau = 1)$	$U(\xi, \tau = 1)$	width
0.0	3.159588E-1	[+3.15954436738475349E-1, +3.15960387416827118E-1]	5.950678E-06
0.1	2.906484E-1	[+2.90643083764027751E-1, +2.90650297636329433E-1]	7.213872E-06
0.2	2.656639E-1	[+2.65657755235743023E-1, +2.65666052507040455E-1]	8,297271E-06
0.3	2.410542E-1	[+2.41047484227741547E-1, +2.41056658209754539E-1]	9,173982E-06
0.4	2.168592E-1	[+2.16851947574807204E-1, +2.16861769802251397E-1]	9,822227E-06
0.5	1.931080E-1	[+1.93100476191670666E-1, +1.93110702112374094E-1]	1,022592E-05
0.6	1.698190E-1	[+1.69811323517989626E-1, +1.69821698582011309E-1]	1,037506E-05
0.7	1.469988E-1	[+1.46991210327409063E-1, +1.47001476310586912E-1]	1,026598E-05
0.8	1.246425E-1	[+1.24635157247229580E-1, +1.24645058613463779E-1]	9,901366E-06
0.9	1.027335E-1	[+1.027726609076264561E-1, +1.027735899317649549E-1]	9,290241E-06
1.0	8.124411E-2	[+8.12378478407702735E-2, +8.12462956141347860E-2]	8,447773E-06
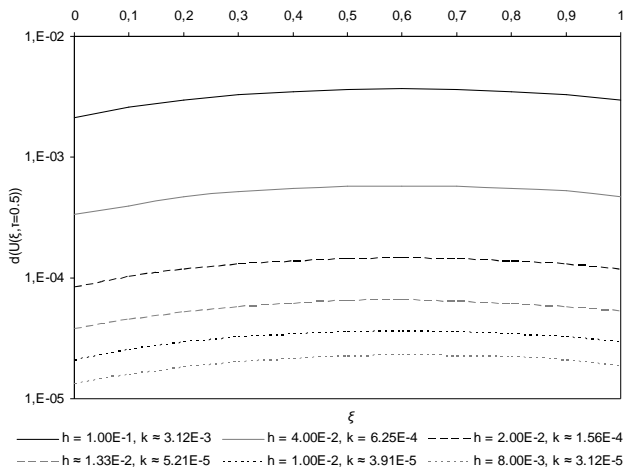
Fig. 8. Widths of the interval solution $U(\xi, \tau = 0.5)$ obtained with the ICN method for different values of stepsizes h and k
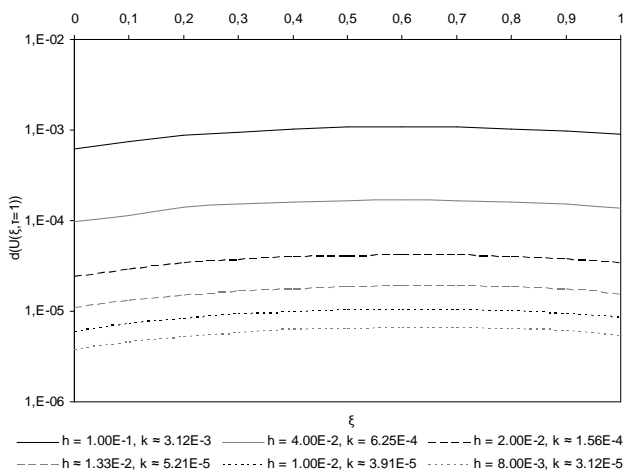

Fig. 9. Widths of the interval solution $U(\xi, \tau = 1)$ obtained with the ICN method for different values of stepsizes h and k

4.2. Numerical experiment 2

We set:

$$w_0 = 280 \text{ [K]}, \quad w_1 = 400 \pm 2 \text{ [K]}, \quad w_2 = 250 \pm 2 \text{ [K]}, \qquad (37)$$

$$\alpha_1 = 5000 \text{ [W/(m}^2\cdot\text{K)]}, \quad \alpha_2 = 2500 \text{ [W/(m}^2\cdot\text{K)]}. \qquad (38)$$

Hence, we take:

$w_1 \in [398.0, 402.0], \quad d(w_1) = 4.0,$
$w_2 \in [248.0, 252.0], \quad d(w_2) = 4.0,$

The dimensionless quantities g_1, g_2 and the Biot numbers are represented by the intervals given as follows:

$g_1 \in [-9.848876259364505E-1, -9.525962283647636E-1],$
$g_2 \in [-1.291655902867476E-1, -1.130198915009041E-1],$
$d(g_1) \approx 3.22E-02, \quad d(g_2) \approx 1.61E-02,$

$Bi_1 \in [+2.2603978300180831E+0, +2.2603978300180831E+0],$
$Bi_2 \in [+1.1301989150090415E+0, +1.1301989150090416E+0],$
$d(Bi_1) \approx 6.51E-19, \quad d(Bi_2) \approx 3.25E-19.$

We use the interval realization of the conventional Crank-Nicolson method and the ICN method with $h = 1E-2$, $k \approx 3.91E-5$. Fig. 10, Fig. 11 and Tab.3 present the results of computations.
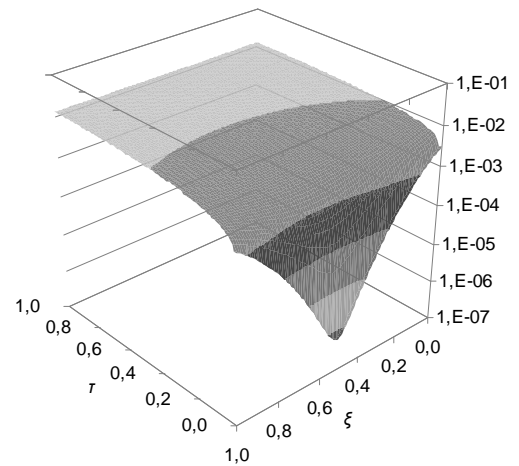

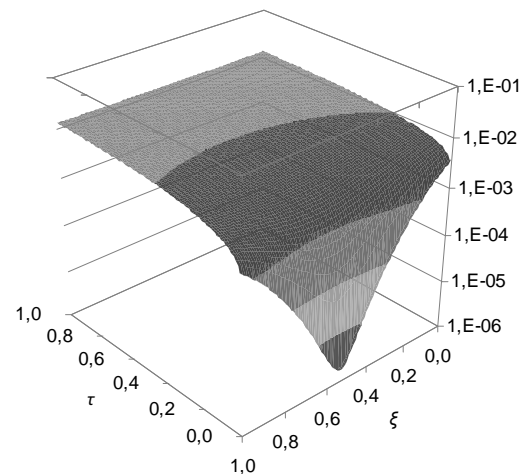**Fig. 10.** Widths of the interval solutions $U_{i,j}^C$

Fig. 11. Widths of the interval solutions $U_{i,j}$

Tab. 3. Values of the exact and interval solutions $U(\xi, \tau = 1)$ obtained with the ICN method for $h = 1\text{E-}2$ and $k \approx 3.91\text{E-}5$

ξ	$u(\xi, \tau = 1)$	$U(\xi, \tau = 1)$	width
0.0	3.159588E-1	[+3.09184783437008590E-1, +3.22730040718293928E-1]	1.354526E-02
0.1	2.906484E-1	[+2.83952786874633136E-1, +2.97340594525724109E-1]	1.338781E-02
0.2	2.656639E-1	[+2.59035525184234897E-1, +2.72288282558548651E-1]	1.325276E-02
0.3	2.410542E-1	[+2.34480333446458798E-1, +2.47623808991037363E-1]	1.314348E-02
0.4	2.168592E-1	[+2.10325514492529920E-1, +2.23388202884528759E-1]	1.306269E-02
0.5	1.931080E-1	[+1.86599383498977412E-1, +1.99611794805067427E-1]	1.301241E-02
0.6	1.698190E-1	[+1.63319561770483399E-1, +1.76313460329517616E-1]	1.299390E-02
0.7	1.469988E-1	[+1.40492537317271714E-1, +1.53500149320724339E-1]	1.300761E-02
0.8	1.246425E-1	[+1.18113503180345723E-1, +1.31166712680347713E-1]	1.305321E-02
0.9	1.027335E-1	[+9.61664774474748486E-2, +1.09296030946439333E-1]	1.312955E-02
1.0	8.124411E-2	[+7.46247020072574241E-2, +8.78594414476476994E-2]	1.323474E-02

4.3. Numerical experiment 3

We set:

$$w_0 = 280 \text{ [K]}, \quad w_1 = 400 \text{ [K]}, \quad w_2 = 250 \text{ [K]}, \tag{39}$$

$$\alpha_1 = 5000 \pm 250 \text{ [W/(m}^2\cdot\text{K)]}, \quad \alpha_2 = 2500 \pm 250 \text{ [W/(m}^2\cdot\text{K)]}, \tag{40}$$

and hence, we take:

$\alpha_1 \in [4750.0, 5250.0], \quad d(\alpha_1) = 500.0,$
$\alpha_2 \in [2250.0, 2750.0], \quad d(\alpha_2) = 500.0,$

The dimensionless quantities g_1, g_2 and the Biot numbers are represented by the intervals given as follows:

$g_1 \in [-1.017179023508137\text{E}+0, -9.203048307930767\text{E}-1],$
$g_2 \in [-1.332020149832084\text{E}-1, -1.089834668044432\text{E}-1],$
$d(g_1) \approx 9.68\text{E-}02, \quad d(g_2) \approx 2.42\text{E-}02,$

$Bi_1 \in [+2.1473779385171792\text{E}+0, +2.373417721518987\text{E}+0],$
$Bi_2 \in [+1.0171790235081374\text{E}+0, +1.2432188065099457\text{E}+0],$
$d(Bi_1) \approx 2.26\text{E-}1, \quad d(Bi_2) \approx 2.26\text{E-}1.$
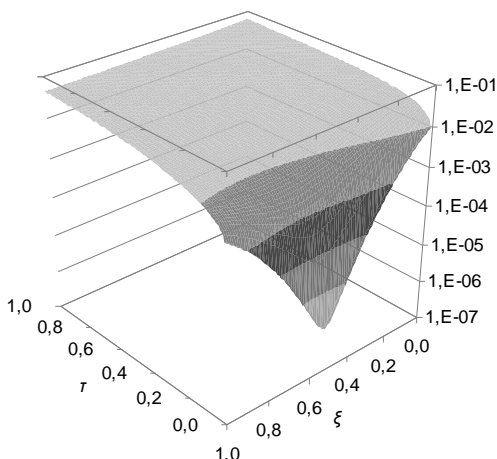

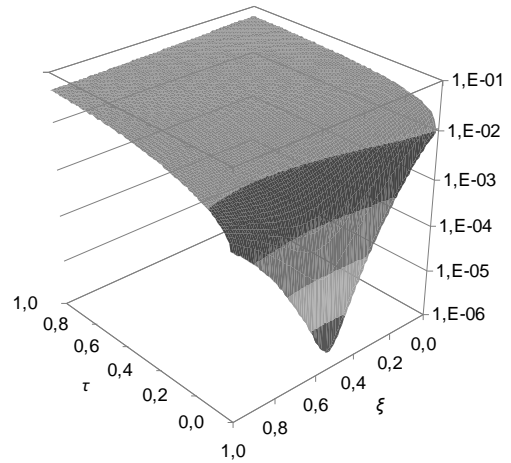**Fig. 12.** Widths of the interval solutions $U_{i,j}^C$

Fig. 13. Widths of the interval solutions $U_{i,j}$

Tab. 4. Values of the exact and interval solutions $U(\xi, \tau = 1)$ obtained with the ICN method for $h = 1\text{E-}2$ and $k \approx 3.91\text{E-}5$

ξ	$u(\xi, \tau = 1)$	$U(\xi, \tau = 1)$	width
0.0	3.159588E-1	[+2.85981889581640435E-1, +3.48735827509592245E-1]	6.275394E-02
0.1	2.906484E-1	[+2.61941715297462713E-1, +3.22087348519591537E-1]	6.014563E-02
0.2	2.656639E-1	[+2.38161863649265124E-1, +2.95848727684306683E-1]	5.768686E-02
0.3	2.410542E-1	[+2.14682974454601979E-1, +2.70079238878866673E-1]	5.539626E-02
0.4	2.168592E-1	[+1.91537766753450941E-1, +2.44827119587005676E-1]	5.328935E-02
0.5	1.931080E-1	[+1.68750177753681014E-1, +2.20128436301078798E-1]	5.137826E-02
0.6	1.698190E-1	[+1.46334732916635882E-1, +1.96006236264017843E-1]	4.967150E-02
0.7	1.469988E-1	[+1.24296163758492568E-1, +1.72470005509110585E-1]	4.817384E-02
0.8	1.246425E-1	[+1.02629283427895288E-1, +1.49515445902885899E-1]	4.688616E-02
0.9	1.027335E-1	[+8.13191232548695133E-2, +1.27124576470833617E-1]	4.580545E-02
1.0	8.124411E-2	[+6.03413267279543483E-2, +1.05266156532657562E-1]	4.492483E-02

Similarly, as in the previous numerical experiments, we use the interval realization of the conventional Crank-Nicolson method and the ICN method with $h = 1\text{E-}2$ and $k \approx 3.91\text{E-}5$. The results of computations are presented in Fig. 12, Fig. 13 and Tab. 4.

4.4. Discussion of results

In Section 4.1 we assumed that all input data, i.e. the material specific quantities, the temperatures and the convection heat transfer coefficients are known exactly. Hence, we only had to deal with the representation errors, rounding errors and the error of the conventional method. In Fig. 4 we see the widths of the interval solutions $U^C(\xi_i, \tau_j)$. The influence of rounding errors and the representation errors on the final results is not significant. It could be significant if we continue computations for greater values of time τ. On the other hand more important is in this case the contribution of the error term of the conventional method enclosed in $R_{i,j}$ (see Fig. 6) to the final intervals $U(\xi_i, \tau_j)$ obtained with the ICN method (see Fig. 5).

In Section 4.2 and 4.3 we introduced some kind of uncertainty in values of the external temperatures and the convection heat transfer coefficients, respectively. Fig. 10 and Fig. 12 show that the influence of inexactness of the initial values that are enclosed in intervals is probably greater (see also Fig. 4) then the rounding errors (for a given time τ). Furthermore, if we compare Fig. 10 with Fig. 11 (and Fig. 12 with Fig. 13), we conclude that the influence of the errors of the initial data together with rounding errors is greater than the error of the method.

In all example experiments the approximation of the endpoints of intervals $R_{i,j}$ that should include the error of the conventional method is good enough. Hence, as we see in Tab. 2, Tab. 3, Tab. 4, the exact solution belongs to the interval solutions $U(\xi_i, \tau_j)$ obtained with the ICN method.

The accuracy of the interval results in the first example experiment (see Tab. 2) is of order 1E–6. Its further improvement is possible if we set smaller stepsizes h and k. The numerical tests carried out in Section 4.2 and 4.3 indicate that due to the inexactness of some input quantities to the heat conduction problem, the accuracy of the interval solution is of order 1E–2.

5. CONCLUSIONS

The numerical experiments presented in Section 4 are conceived to show some advantages of the interval method of Crank-Nicolson type for solving the initial-boundary value problem for the heat conduction equation. Such interval method gives interval solutions that with a good approximation of the error term of the conventional Crank-Nicolson method include the exact solution of the problem. Furthermore, the implementation of the interval method considered in the floating-point interval arithmetic leads to the interval values that also contain errors of the inexact initial data, errors of representation and rounding errors.

REFERENCES

1. **Anderson D.A., Tannehill J.C., Pletcher R.H.** (1984), *Computational Fluid Mechanics and Heat Transfer*, Hemisphere Publishing Corporation, New York.
2. **Jain M.K.** (1984), *Numerical Solution of Differential Equations - 2nd edition*, John Wiley & Sons (Asia) Pte Ltd.
3. **Jankowska M.A.** (2006), Interval Multistep Methods of Adams type and their Implementation in the C++ Language, Ph.D. Thesis, Poznan University of Technology, Poznań.
4. **Jankowska M.A.** (2009a), *C++ Library for Floating-Point Conversions*. User and Reference Guide, Poznan University of Technology. Last updated 2009, available in *Software* at http://www.mjank.user.icpnet.pl/.
5. **Jankowska M.A.** (2009b), *C++ Library for Floating-Point Interval Arithmetic*. User and Reference Guide, Poznan University of Technology. Last updated 2009, available in *Software* at http://www.mjank.user.icpnet.pl/.
6. **Jankowska M.A.** (2010), Remarks on Algorithms Implemented in Some C++ Libraries for Floating-Point Conversions and Interval Arithmetic, *Lecture Notes in Computer Science* 6068, 436-445.
7. **Jankowska M.A.**, **Marciniak A.**, An Interval Finite Difference Method for Solving the One-Dimensional Heat Conduction Equation, *Lecture Notes in Computer Science* (accepted).
8. **Jankowska M.A.** (2012), An Interval Finite Difference Method of Crank-Nicolson Type for Solving the One-Dimensional Heat Conduction Equation with Mixed Boundary Conditions, *Lecture Notes in Computer Science* 7133, 157-167.
9. **Jankowska M.A.** (2011), Some Kind of the Error Term Approximation in Interval Method of Crank-Nicolson Type, *Dynamical Systems. Nonlinear Dynamics and Control, Proceedings of DSTA 2011 – 11th Conference on Dynamical Systems – Theory and Applications*, Łódź, Poland, 297-304.
10. **Kamiński H., Stefaniak J., Sypniewska-Kamińska G.** (2004), Some remarks on the method of fictitious of direct and inverse problems of heat conduction, *Proceedings of the International Symposium on Trends in Continuum Physics*, TRECOP 2004, 163-175.
11. **Manikonda S., Berz M., Makino K.** (2005), High-order verified solutions of the 3D Laplace equation, *WSEAS Transactions on Computers* 4 (11), 1604-1610.
12. **Marciniak A.** (2009), *Selected Interval Methods for Solving the Initial Value Problem*, Publishing House of Poznan University of Technology, Poznan.
13. **Marciniak A.** (2008), An Interval Difference Method for Solving the Poisson Equation - the First Approach, *Pro Dialog 24*, 49-61.
14. **Marciniak A.** (2012), An Interval Version of the Crank-Nicolson Method - the First Approach, *Lecture Notes in Computer Science* 7133, 120-126.
15. **Marciniak A., Gregulec D., Kaczmarek J.** (2000), *The basic numerical procedures in Turbo pascal language (in polish)*, Wydawnictwo Nakom, Poznań.
16. **Moore R.E.** (1966), *Interval Analysis*, Prentice-Hall, Englewood Cliffs, NJ.
17. **Moore R.E., Kearfott R.B., Cloud M.J.** (2009), *Introduction to Interval Analysis*, SIAM Philadelphia.
18. **Nakao M.T.** (2001), Numerical verification methods for solutions of ordinary and partial differential equations, *Numerical Functional Analysis and Optimization* 22 (3-4), 321-356.
19. **Nagatou K., Hashimoto K., Nakao M.T.** (2007), Numerical verification of stationary solutions for Navier-Stokes problems, *Journal of Computational and Applied Mathematics* 199 (2), 445-451.
20. **Press W.H., Teukolsky S.A., Vetterling W.T., Flannery B.P.** (2007), *Numerical Recipes 3rd Edition: The Art of Scientific Computing*, Cambridge University Press.
21. **Sunaga T.** (1958), *Theory of interval algebra and its application to numerical analysis*, in: Research Association of Applied Geometry (RAAG) Memoirs, Ggujutsu Bunken Fukuykai. Tokyo, Japan, 1958, Vol. 2, pp. 29-46 (547-564).
22. **Watanabe Y., Yamamoto N., Nakao M.T.** (1999), A Numerical Verification Method of Solutions for the Navier-Stokes Equations, *Reliable Computing* 5 (3), 347-357.

PREMISES OF PARAMETRICAL ASSESSMENT OF TURBOJET ENGINE IN FLIGHT REGULATION CONDITION DURING GROUND TEST

Paweł LINDSTEDT*, **Karol GOLAK***

*Faculty of Mechanical Engineering, Bialystok University of Technology, ul. Wiejska 45 C, 15-351 Bialystok, Poland

p.lindstedt@poczta.pb.edu.pl, karolgolak@gmail.com

Abstract: The article presents the theoretical bases of new parametrical method of turbojet engine technical condition assessment. In this method, engine technical condition is described by one (in other methods four are used) comprehensive model (binding engine input – signals p_2 and m_p and engine output - n and p_4 signals) with unique feature, that engine operation quality during ground tests will provide necessary data on its performance in flight. The changes occurring in turbojet engine during its exploitation will be measurable by comparison of standard model with parameters obtained from experiment (ground test).

Key words: Regulation, Computer Simulation, Turbine Jet Engine, Parametric Diagnostics, Ground Tests

1. INTRODUCTION

Proper regulation of turbine turbojet engines as well as other objects is a necessary condition for safe usage admission. Currently, in process of engine performance signals courses and their quality indicators values are researched in precisely determined moments during ground tests. Such method of engine performance assessment is unreliable due to differences between environment (temperature, pressure) influencing engine during ground tests and in flight as well as impossibility to imitate noises, usually unknown, affecting engine in flight during ground tests. This may cause a situation where proper regulation during ground tests may not provide sufficient utilitarian value for engine in flight. Hence the necessity of finding new researching method allowing engine performance determined during ground tests to provide data on its performance in flight. One of such methods is comprehensive (simultaneous analysis of four basic signals resulting from engine operation), parametrical (engine performance is described by 32 parameters) method of turbojet engine regulation condition assessment.

2. THEORETICAL BASIS OF PARAMETRICAL ASSESSMENT OF AIRCRAFT ENGINE REGULATION CONDITION DURING GROUND TESTS REFLECTING ITS STATE IN FLIGHT

Currently, during aircraft regulation condition assessment, quality indicators of engine signals courses determined during ground tests are of major significance. However these are often inadequate to in flight indicators due to noise and environment changes. Hence the need occurred to supplement the quality indicators of signals courses determined during ground tests with additional parameter – regulation potential, obtained from equation of state binding system operation quality and its technical condition. (Balicki and Szczeciński, 2001; Gosiewski and Paszkowski, 1995; Lindstedt 2002, 2009). Noticeably, this problem may

be solved by transforming signals into system parameters such as amplification coefficients, time constants. Obtained parameters allow to assess the value of other, unknown parameters that occur in flight.

Simplified diagram of engine rotational speed regulation system is presented on Fig. 1.
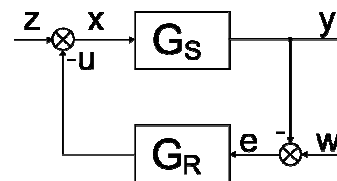

Fig. 1. Simplified diagram of aircraft engine regulation system: G_S- engine transfer function, G_R – regulator trans function, w – input function, u – signal of influence of regulator onto object, z – interference, y – applied signal (e.g. rotational speed), x – object incentive signal, e – deviation signal

In order to assess the engine operation, transfer functions of closed-loop system for an input function H_W (1) (ground tests) and of closed-loop system for interference H_Z (2) in flight tests (Pełczewski, 1980; Piety, 1998):

$$H_W = \frac{y}{w} = \frac{G_S G_R}{1+G_S G_R} \tag{1}$$

$$H_Z = \frac{y}{z} = \frac{G_S}{1+G_S G_R} \tag{2}$$

Noticeably system ground test transfer function may be multiplied by controller transfer function reciprocal G_R of given test, and thus, by transfer functions determined during ground tests, obtain the transfer function describing engine in flight.

$$H_Z = H_Z \cdot \frac{1}{G_R} \tag{3}$$

This gives base for assessment of regulation conditions of turbine turbojet engine in flight based on its ground tests (Lindstedt 2002, 2009).

3. THEORETICAL FUNDAMENTALS FOR JOINT CONSIDERATION OF ENGINE REGULATION CONDITION ASSESSMENT MODELS

Four basic signals n – rotational speed, p_2 – pressure behind the compressor, m_p- mass intensity of fuel flow, p_4 – pressure in engine nozzle, are considered in process of engine regulation condition assessment (Fig. 2) (Lindstedt, 2009; Staniszewski, 1980; Szczeciński, 1965; Szevjakow, 1970).
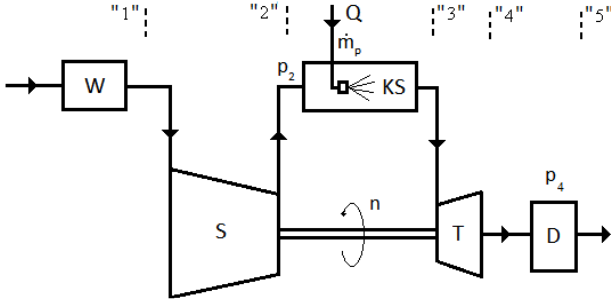

Fig. 2. Engine regulation diagram (where W – intake, S – compressor, KS – combustion chamber, T – turbine, D – nozzle, outlet, 1,2,3,4,5 – characteristic sections)

Each relation between main signal, described by following transfer functions, are researched in order to assess engine performance (Balicki, Szczeciński, 2001, Lindstedt, 2002):

$$G_{1m_p} = \frac{\Delta n}{\Delta m_p} \tag{4}$$

$$G_{1p_2} = \frac{\Delta n}{\Delta p_2} \tag{5}$$

$$G_{2m_p} = \frac{\Delta p_4}{\Delta m_p} \tag{6}$$

$$G_{2p_2} = \frac{\Delta p_4}{\Delta p_2} \tag{7}$$

Assumingly, model in form of four transfer functions might be reduced to one comprehensive model with desired feature that allows engine performance determined during ground tests to provide data on its quality in flight.

After removing output signals Δn and Δp_4 from equations (4)÷(7), the following is obtained:

$$G_{1m_p1p_2} = \frac{\Delta p_2}{\Delta m_p} \tag{8}$$

$$G_{2m_p2p_2} = \frac{\Delta p_2}{\Delta m_p} \tag{9}$$

Subsequently, input signals Δm_p and Δp_2 are removed and the following is obtained from equations (4)÷(7) as well:

$$G_{1n1p_4} = \frac{\Delta n}{\Delta p_4} \tag{10}$$

$$G_{2n2p_4} = \frac{\Delta n}{\Delta p_4} \tag{11}$$

In the end, model is created in form of quotient of relations of output signals transform to relation of input signals transform:

$$G_{kompleks}(s) = \frac{G_{1n1p_4}}{G_{1m_p1p_2}} = \frac{G_{2n2p_4}}{G_{2m_p2p_2}} \tag{12}$$

Taking dependences (10) and (12) into consideration, the following is obtained:

$$G_{kompleks}(s) = \frac{\frac{\Delta n}{\Delta p_4}}{\frac{\Delta m_p}{\Delta p_2}} \tag{13}$$

Using inverse Laplace transform following is determined: (Osiowski, 1981; Szabatin, 2000).

$$g_{kompleks}(t) * \Delta p_4 * \Delta p_2 = \Delta n * \Delta m_p \tag{14}$$

As seen from dependences (13), (14), one comprehensive engine model exists that corresponding to 4 classical models applied hitherto in engine regulation condition assessment process. This model is a transfer function (13) or dependence of courses n and m_p tangle (14). Tangle model (14) is difficult to solve. Model (13) is more suitable for further analysis. In case of adopting model in form of transfer function (13), transition can be made from space of variable s to space of frequency ω, hence obtaining ability to analyze signals basing on power densities and cross power densities for signals recorded during engine test.

Transfer function $G_{kompleks}(j\omega)$ argument may be determined from dependence (13):

$$ArgG_{kompleks}(j\omega) = \Delta\varphi_{np_4p_2m_p} = \Delta\varphi_{np_4} - \Delta\varphi_{p_2m_p} \tag{15a}$$

$$ArgG_{kompleks}(j\omega) = Arg\frac{\frac{S_{np_4}}{S_{p_4p_4}}}{\frac{S_{p_2m_p}}{S_{m_pm_p}}} \tag{15b}$$

Subsequently, transfer function $G_{kompleks}(j\omega)$ modulus square may be determined:

$$|G_{kompleks}(j\omega)|^2 = \frac{\frac{S_{nn}}{S_{p_4p_4}}}{\frac{S_{p_2p_2}}{S_{m_pm_p}}} = \frac{A^2_{nnp_4p_4}}{A^2_{p_2p_2m_pm_p}} \tag{16}$$

where: S – power spectral density or cross power spectral density, $A^2(\omega)$ – amplification square, $\varphi(\omega)$ – phase shift.

Signals power S spectral density functions is determined basing on their correlation functions with Fourier transform applied. Therefore, when courses $n(t)$, $p_4(t)$, $p_2(t)$ and $m_p(t)$ are known, determination of their correlation and cross correlation functions and, subsequently, power spectral densities and cross power spectral densities should prove no difficulty. In the end, transfer function $G_{kompleks}(j\omega)$ and, then, signals amplification square $|G_{kompleks}(j\omega)|^2$ might be determined. Similarly, basing on cross power spectral density, phase shift $\Delta\varphi_{np_4p_2m_p}$ is determined ($A^2_{nnp_4p_4}$ and $\Delta\varphi_{np_4p_2m_p}$ being values physically interpretable). (Osiowski, 1981; Szabatin, 2000).

4. COMPREHENSIVE, PARAMETRICAL ANALYSIS OF ENGINE REGULATION CONDITION BASING ON ENGINE EXPLOITATION RESEARCH

Recorded courses of input and output signals of turbojet engine are shown in Fig. 3. and Fig. 4. (Pawlak et al., 1996).

Additionally, assumption is made that *DProb* course corresponds with signal m_p course, signal *P4* with signal p_4, signal *N* with signal n and *P2* with signal p_2.

Ranges for determination of amplification value $|G_{kompleks}(j\omega)|^2$, as well as phase shift $\Delta\varphi_{np_4p_2m_p}$ were determined dividing signal N onto sections as seen in Fig. 5. and Tab. 1.

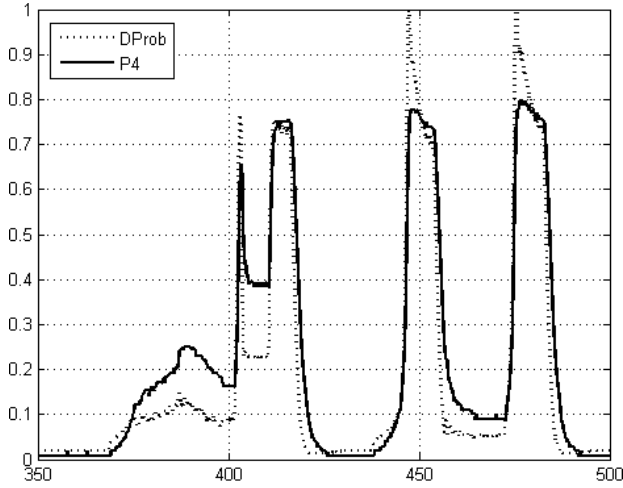**Fig. 3.** Courses of normalized engine input signals
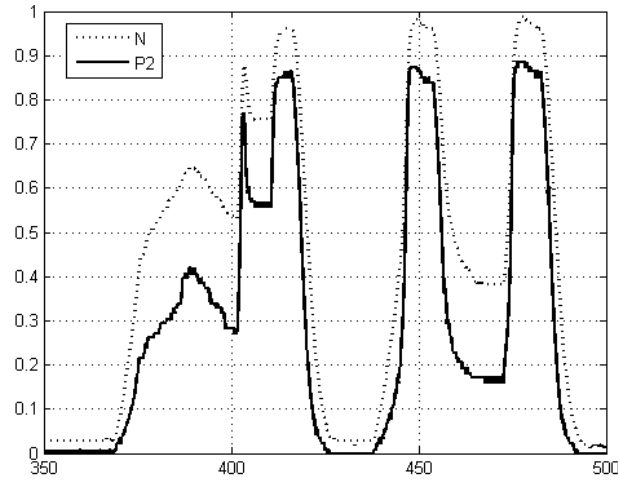(signal observation time 350 – 500 [s])

Fig. 4. Courses of normalized engine output signals
(signal observation time 350 – 500 [s])

Tab. 1. Signal n ranges for beginning and end of signal course types

Signal n range for the beginning of signal	Signal n range for the end of signal	Signal type
<0,0.33>	(0.33,0.67>	1
<0,0.33>	(0.67,1>	2
(0.33,0.67>	<0,0.33>	3
(0.33,0.67>	(0.67,1>	4
(0.67,1>	<0,0.33>	5
(0.67,1>	(0.33,0.67>	6

Recorded characteristics of basic signals $n(t)$, $p_4(t)$, $p_2(t)$ i $m_p(t)$ were divided onto sections according to assumptions presented in table 1. Hanning window was put on each of obtained sections. For obtained signal courses autocorrelations and cross correlations of signals n and p_4 as well as p_2 and mp were calculated. Obtained charts of autocorrelations and cross-correlations were approximated with precision of $R^2>0.995$ (described by determination coefficient) using 4 degree polynomials in general form of:

$$R_{xy}(\tau) = l_4\tau^4 + l_3\tau^3 + l_2\tau^2 + l_1\tau + l_0 \qquad (17)$$

$$R_{yy}(\tau) = k_4\tau^4 + k_3\tau^3 + k_2\tau^2 + k_1\tau + k_0 \qquad (18)$$

In order to determine function spectral power from obtained autocorrelation and cross-correlation functions, bilateral Fourier transform was used. Subsequently engine models in form of amplification $|G_{kompleks}(j\omega)|^2$ and phase shift $\Delta\varphi_{np_4p_2m_P}$ during ground test were determined in general form of:

$$|G_{kompleks}(j\omega)|_i^2 =$$
$$\frac{a_{i8}s^8+a_{i7}s^7+a_{i6}s^6+a_{i5}s^5+a_{i4}s^4+a_{i3}s^3+a_{i2}s^2+a_{i1}s+a_{i0}}{b_{i8}s^8+ba_{i7}s^7+b_{i6}s^6+b_{i5}s^5+b_{i4}s^4+b_{i3}s^3+b_{i2}s^2+b_{i1}s+1} \qquad (19)$$

$$\Delta\varphi_{np_4p_2m_P}|_i =$$
$$Arg\left(\frac{c_{i8}s^8+c_{i7}s^7+c_{i6}s^6+c_{i5}s^5+a_{i4}s^4+a_{i3}s^3+a_{i2}s^2+a_{i1}s+a_{i0}}{b_{i8}s^8+ba_{i7}s^7+b_{i6}s^6+b_{i5}s^5+b_{i4}s^4+b_{i3}s^3+b_{i2}s^2+b_{i1}s+1}\right) \qquad (20)$$
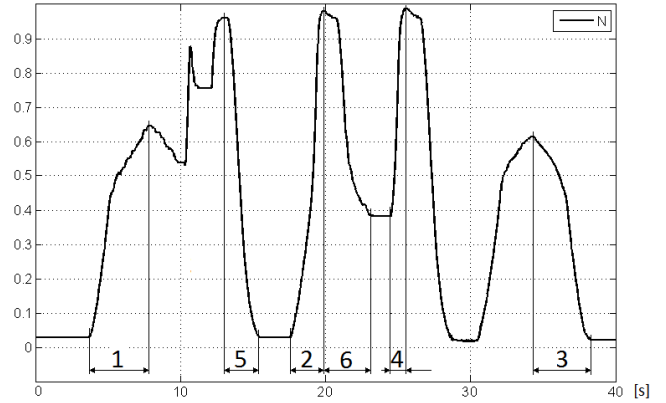

Fig. 5. Courses of normalized engine output signals
(signal observation time 350 – 500 [s])

Changes occurring in engine during its exploitation may be determined by determining percentage values of each δ parameter (24) deviation from approximate μ (21) for each signal course types (Fig. 4.) and comparing them to variability coefficient v (22) presented as a percentage and calculated for standard deviations σ(23), 2σ and 3σ.

$$\mu_l = \frac{\sum_{i=1}^n x_{il}}{n} \qquad (21)$$

$$v_l = \frac{\sigma_l}{\mu_l} \cdot 100\% \qquad (22)$$

$$\sigma_l = \sqrt{(x_{il} - \mu_l)^2} \qquad (23)$$

$$\delta_{il} = \frac{x_{il} - \mu_l}{\mu_l} \cdot 100\% \qquad (24)$$

where: x – parameter a, b, c or d; l – parameter number.
Results are presented as percentage of regulation potential ϑ for each parameter.

$$\vartheta_{il} = \frac{v_l - \delta_l}{v_l} \cdot 100\% \qquad (25)$$

Results of undertaken research in form of regulation potential ϑ of parameters from 5 tests for each of six signal types are presented in Tab. 2. for amplification as well as in Tab. 3. for phase shift.

Engine condition is described by 34 parameters with specific value. For various courses, different configurations and parameter values are obtained. During consecutive tests with identical program, parameters values should remain unchanged. Regulation changes applied during engine ground test, expressed as change of regulator transfer function reciprocal $1/GR$ may be introduced into model and ultimately allow determination of engine parameters in flight.

Tab. 2. *A² model parameters*

type	nr	a0	a1	a2	a3	a4	a5	a6	a7	a8	b1	b2	b3	b4	b5	b6	b7	b8
1	1	43	158	40	166	16	195	104	18	247	2	184	46	81	218	-59	82	237
	2	128	59	160	9	249	-67	50	250	-43	0	220	-50	291	-74	139	292	-55
	3	86	114	85	118	71	145	95	69	149	63	129	85	86	150	42	82	156
	4	271	-64	253	-33	180	187	-27	179	29	245	-37	219	34	64	233	35	41
	5	-29	234	-38	240	-15	40	277	-16	118	190	4	201	8	143	145	9	121
2	1	297	-97	297	-93	286	-84	234	284	-94	193	45	64	261	-92	276	276	-94
	2	62	153	27	195	-3	169	186	-6	149	223	-43	263	-15	148	136	0	147
	3	40	152	60	117	113	73	99	117	104	9	200	0	152	98	49	134	105
	4	77	121	79	126	52	183	-28	49	173	109	72	164	10	179	51	15	176
	5	24	171	37	154	52	159	9	56	168	-34	226	10	93	167	-12	75	167
3	1	110	85	117	86	69	178	57	65	199	60	138	71	86	205	37	79	200
	2	-14	222	-27	227	25	-76	261	27	-71	249	-47	240	7	-69	270	15	-72
	3	24	174	29	169	38	51	157	43	79	182	17	186	5	88	159	14	83
	4	276	-72	268	-70	297	171	-31	298	90	-21	225	-37	278	77	12	287	89
	5	103	90	114	87	72	176	56	67	202	30	167	40	123	199	22	106	200
4	1	299	-98	291	-68	188	191	-57	173	-15	202	3	188	37	39	242	35	2
	2	42	150	64	110	146	-13	125	150	54	18	184	14	190	19	34	184	44
	3	38	173	11	212	-36	201	186	-34	260	141	55	153	25	244	96	25	258
	4	58	126	100	59	205	-28	33	216	34	-51	251	-51	249	1	-43	253	19
	5	64	149	35	187	-4	149	214	-4	168	191	7	196	-1	196	171	3	177
5	1	152	48	152	49	151	151	49	151	49	130	62	144	53	149	50	151	49
	2	154	46	154	46	155	150	47	153	48	96	81	134	57	149	48	152	48
	3	149	51	149	51	149	150	51	149	51	157	45	153	48	150	50	149	51
	4	-100	300	-100	300	-100	-100	300	-100	300	-87	295	-99	300	-100	300	-100	300
	5	146	54	146	55	145	149	53	147	52	204	16	168	42	151	52	148	52
6	1	57	181	0	205	30	-90	259	19	-81	255	-53	246	47	-84	272	20	-81
	2	45	137	76	119	60	178	71	69	172	45	154	48	116	168	37	130	167
	3	124	103	77	137	49	88	144	44	63	177	20	188	-49	71	154	-40	64
	4	282	-92	292	-91	299	158	-46	296	171	-14	215	-20	253	175	5	245	181
	5	-8	172	55	130	62	165	73	71	175	37	163	39	133	170	32	144	169

Tab. 3. Regulation potential for $\Delta\phi$ model

type	nr	a0	a1	a2	a3	a4	a5	a6	a7	a8	b1	b2	b3	b4	b5	b6	b7	b8
1	1	27	178	15	188	18	172	70	25	179	89	99	125	34	179	39	39	179
	2	95	84	152	-4	247	-29	67	269	-5	-26	249	-84	292	-18	102	296	-12
	3	111	85	115	101	51	207	-35	46	190	71	115	115	30	193	21	36	193
	4	279	-69	250	-17	190	-13	270	158	-39	282	-66	221	105	-26	293	88	-32
	5	-12	222	-32	233	-6	163	128	2	175	85	102	122	39	173	45	41	172
2	1	300	-100	300	-100	300	-100	262	300	-100	257	111	-87	299	-100	276	300	-100
	2	54	150	44	161	40	153	172	44	151	174	-84	209	33	152	142	44	151
	3	47	151	53	142	61	142	19	58	145	-7	215	100	68	143	5	59	145
	4	54	146	54	147	51	152	28	49	151	56	102	147	49	152	56	48	152
	5	46	153	48	150	49	153	19	49	152	20	155	131	51	154	21	49	152
3	1	100	94	109	94	64	180	58	62	191	69	125	89	52	192	41	47	190
	2	-15	228	-37	237	20	-93	280	24	-81	248	-42	222	87	-81	284	92	-82
	3	45	150	54	144	47	103	119	49	128	176	20	192	-15	136	129	-2	129
	4	283	-76	271	-71	297	141	-18	298	75	-32	240	-57	285	71	17	290	77
	5	87	104	103	96	72	169	61	68	187	39	157	55	91	183	30	74	186
4	1	300	-98	284	-44	169	91	114	121	-44	241	-39	233	-10	22	263	-4	-14
	2	54	134	85	84	150	32	33	162	90	22	179	19	184	40	34	176	75
	3	42	174	4	219	-31	251	177	-23	248	127	70	138	38	261	95	36	255
	4	43	132	108	36	219	-36	-52	242	43	-43	244	-46	251	4	-32	258	14
	5	61	157	19	204	-7	162	228	-2	164	153	46	156	36	172	139	34	169
5	1	60	141	58	144	56	52	148	86	111	43	156	45	153	49	150	86	112
	2	69	130	71	127	90	47	139	90	109	11	180	30	161	48	145	88	110
	3	43	156	45	155	46	47	153	85	113	56	146	52	149	50	151	85	113
	4	298	-98	298	-98	294	300	-100	155	53	292	-96	298	-99	300	-100	158	50
	5	29	171	29	173	14	53	159	83	114	97	114	75	137	54	154	83	115
6	1	64	181	-5	213	14	-79	259	0	-76	237	-33	219	145	-78	263	130	-76
	2	34	141	75	118	60	174	67	72	170	87	110	104	-12	175	51	8	166
	3	93	129	58	150	46	59	154	43	52	179	18	188	10	56	164	-11	52
	4	293	-97	291	-85	295	178	-36	289	178	-47	250	-59	265	176	-11	269	187
	5	16	145	81	105	84	169	56	96	175	44	156	48	91	170	33	104	170

5. SUMMARY

Comprehensive model for turbojet engine regulation condition assessment was executed. This model allows calculating amplification $|G_{kompleks}(j\omega)|^2$ and phase Shift $\Delta\varphi_{np_4p_2m_P}$, that may be physically interpreted. Engine condition is described by 34 parameters of specific value, assuming various configurations for different ground tests signal courses. Obtained parameters present regulation condition of turbojet engine. Changes in engine occurring during its exploitation are expressed as parameters $|G_{kompleks}(j\omega)|^2$ and $\Delta\varphi_{np_4p_2m_P}$ changes and by changes of regulator adjustment. Parameters of ground model and regulations may be the basis to determine engine in flight model according to dependence $H_Z = H_W \cdot 1/G_R$.

REFERENCES

1. **Balicki W., Szczeciński S.** (2001), *Diagnostics of jet aircraft engines (in Polish)*, Scientific Library of the Institute of Aviation, Warsaw.
2. **Bendat J. S., Piersol A. G.** (1976), *Metody analizy i pomiaru sygnałów losowych*, PWN, Warszawa.
3. **Gosiewski Z., Paszkowski M.** (1995), Globalny wskaźnik diagnostyczny turbinowego silnika odrzutowego, *III Krajowa Konferencja Diagnostyka techniczna urządzeń i systemów nr 328/95*, Wyd. ITWL, Warszawa.
4. **Lindstedt P.** (2002), *Practical diagnostics of machines and its theoretical foundations (in Polish)*, Scientific Library ASKON, Warsaw.
5. **Lindstedt P.** (2009), Possibilities of assessment of the potential of Aircraft Engines, *Solid State Phenomena*, Vols 147-149/2009, Trans Tech Publications, Switzerland.
6. **Osiowski J.** (1981), *Zarys rachunku operatorowego*, WNT, Warszawa.
7. **Pawlak W. I., Wiklik K., Morawski J. M.** (1996), *Synteza i badanie układów sterowania lotniczych silników turbinowych metodami symulacji komputerowej*, Wyd. Nauk. Instytutu Lotnictwa, Warszawa.
8. **Pełczewski W.** (1980), *Teoria sterowania*, WNT, Warszawa.
9. **Piety K. R.** (1998), *Method for determining rotational speed from machine vibration data*, United States Patent no. 5,744,723, US.
10. **Staniszewski R.** (1980*), Sterowanie zespołów napędowych*, WKŁ, Warszawa.
11. **Szabatin J.** (2000), *Fundamentals of signal theory (in Polish)*, WKŁ, Warszawa.
12. **Szczeciński S.** (1965), *Lotnicze silniki turbinowe*, MON, Warszawa.
13. **Szevjakow A.** (1970), *Awtomatika awiacionnych i rakietnych siłowych ustanowok*, Maszinostrojenije, Moskwa.

NUMERICAL-EXPERIMENTAL INVESTIGATION OF SQUARED-BASED METAL PYRAMIDS LOADED WITH A BLAST WAVE FROM A SMALL EXPLOSIVES CHARGE

**Robert PANOWICZ[*], Wiesław BARNAT[*], Tadeusz NIEZGODA[*],
Leszek SZYMAŃCZYK[**], Julian GRZYMKOWSKI[*]**

[*]Department of Mechanics and Applied Computer Science, Faculty of Mechanical Engineering,
Military University of Technology, 2 Gen. Kaliski Str., 00-908 Warsaw 49
[**]Institute of Chemistry, Faculty of New Technologies and Chemistry,
Military University of Technology, 2 Gen. Kaliski Str., 00-908 Warsaw 49

rpanowicz@wat.edu.pl, wbarnat@wat.edu.pl, Tadeusz.Niezgoda@wat.edu.pl, lszymanczyk@wat.edu.pl, julian.grzymkowski@gmail.com

Abstract: The paper presents the results of computer simulation and experimental investigation of blast wave action arising from a small explosive charge on a metal pyramid with a square base. The explicit finite element method has been used to perform numerical analyses. This method is included in the Ls-Dyna software for modelling the behaviour of the pyramid exposed to the action of a pressure wave arising from the detonation of an explosive charge. The detonation process was described in programming burn approximation. The fluid–structure interaction was used to describe an influence of a blast wave on the structure.

Key: FEM, Blast Wave, Blast Wave Interaction with Structure, Fluid Structure Interaction

1. INTRODUCTION

Threats in the form of terrorist attacks during actions of Polish Army in Chad, Iraq and Afghanistan revealed the necessity of improving mine resistance and shrapnel resistance of different of military equipment.

The works on different solutions allowing meeting the requirements included in various documents and standards, for example in STANAG 4569, are carried out worldwide.

One of typical elements, which can be utilized in new solutions for dispersion of explosion energy, are metal pyramids. A simple construction of geometrical energy absorbents can assure the maximum protection at relatively low costs. The main advantage of this solution is using the streamlined shape of the construction and energy dispersion through great system deformations.

2. EXPERIMENTAL INVESTIGATIONS

In the initial part of investigations, the basic parameters characterizing mechanical properties of the applied material were determined. A universal strength machine INSTRON was used for the investigations. In order to obtain information about the boundary strength, plasticity boundary Re and strength Rm, the manufactured oblong samples were cut out of the examined pyramids. Part of the samples were subjected to the examination till the moment of breaking. The remaining samples were used to determine Young modulus and Poisson ratio.

The strength characteristic of the examined steel, presented in Fig. 1, was also obtained from the tensile stress test. The below characteristic was initially simplified to the form of the multi-linear one, possible to be used in LS-DYNA software (a thin line in Fig. 1).

The graph of a tensile stress static test does not have a clear

moment in which the material undergoes breaking (Fig. 1), what is characteristic for, among others, constructional steel. The examined material did not undergo failure till the end of the test. Deformations were recorded till the moment when stress reached the value of 0 MPa. This situation occurred at deformation $\varepsilon = 0.624$. In the presented Fig., only the change of the stress-deformation curve course at deformation $\varepsilon = 0.58$ is observed.

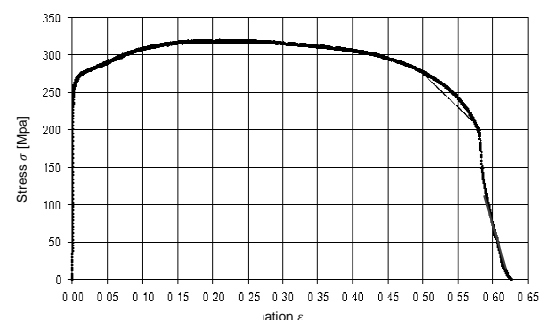The collected data describing the examined material are presented in Tab. 1.

Fig. 1. Graph of dependencies of stresses from deformations in static tensile stress test along with simplified numerical multi-linear characteristic (a thin line)

In the further part of tests, a metal pyramid was loaded with the use of a pressure wave coming from detonation of an explosive charge. The scheme of the utilized experimental testing stand is presented in Fig. 2. The metal pyramid was set freely, below the explosive charge, on the thick flat plate selected so as not to undergo permanent deformation resulting from explosion. The explosive charge in the shape of cylinder was freely and symmetrically hung over the examined element.

Tab. 1. Properties of the examined steel

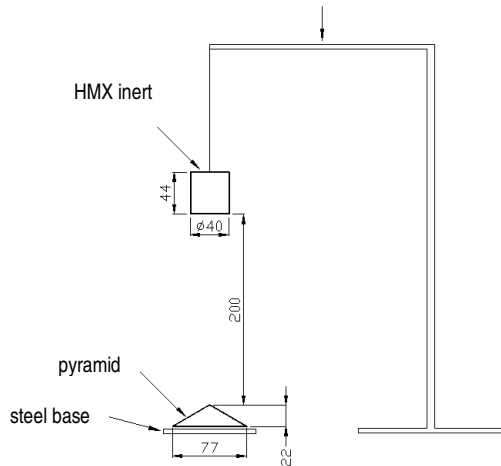| properties	low-carbon steel
density, ρ [kg/m3]	7865
Young's modulus, E [GPa]	94.62
Poisson ratio, ν	0.284
yield point, R_e [MPa]	253
ultimate tensile strength, R_m [MPa]	319.4
stress at fracture, [MPa]	200
strain failure, ε_f [mm/mm]	0.58

Fig. 2. Scheme of the experimental testing stand (dimensions in mm)

HMX inert, which properties are presented in Tab. 1, was used for the examinations.

Tab. 2. Properties of HMX inert [3 ÷ 7]

HMX inert $C_4H_8N_8O_8$	
explosion energy [kJ/cm³]	16.23
Chapman – Jouguet pressure [GPa]	38.6
detonation velocity V_{det} [km/s]	9.12
density corresponding to V_{det} [g/cm³]	1.894
detonation temperature[° C]	279
gas products volume[cm³/g]	755
equivalent of TNT according to Berthelot approximation	1.73
JWL coefficients for HMX inert	
A [GPa]	858.08
B [GPa]	7.55
R_1	4.306
R_2	0.80
ω	0.30

As a result of the conducted experiment, the metal pyramid underwent permanent deformation and its height was reduced from 22 mm to 12 mm. Changes of the dimensions of the base are possible to be ignored due to their size. The deformed pyramid is presented in Figs. 3 and 4.

Despite the symmetric structure of the pyramid before explosion, its deformations are asymmetric. One of the edges was "pushed" under the vertex, where the rest three edges meet.

The opposite edge, especially its end, stuck up significantly higher, at the height of approximately 5 mm, than the others. It can results from imperfections in manufacturing and setting the pyramid, or result from the fact that during the process of the pyramid extrusion, the material underwent strengthening to a different degree.

Fig. 3. Side view on undeformed and deformed pyramid

Fig. 4. Top view on deformed and undeformed pyramid

3. NUMERICAL INVESTIGATION

In order to reproduce accurately the experimental research consisting in loading the metal pyramid with a pressure wave coming from detonation of explosive material, the 3D model was developed (Fig. 5).

The following assumption and simplifications were applied in respect to the conducted experiment:

– it was assumed that the system was symmetric, what allowed modelling of only the one quarter of the whole system. It enabled over threefold shortening of calculations time with simultaneous maintenance of very good agreement with the results of the conducted experiment,
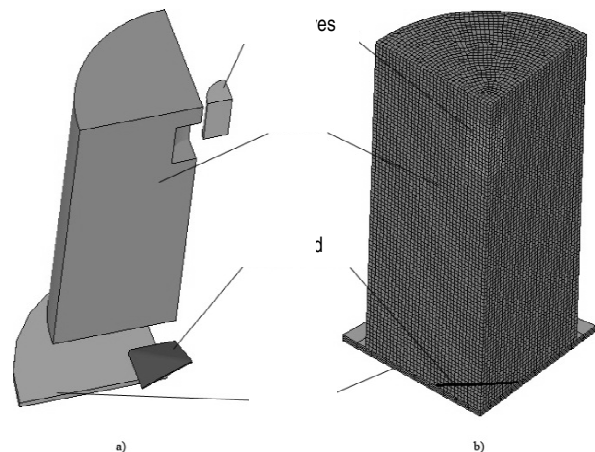

Fig. 5. Full model in decomposed view (a) and in state ready to conduct simulation, along with superimposed mesh (b)

– behaviour of the examined element was described with properties of an isotropic body. Any effects of material strengthening on the edges, caused by plastic deformation of the steel plate during formation of the pyramid were ignored. Its behaviour was described with the multi-linear model,

– the air was described with the use of equation of perfect gas,

– approximation of detonative optics was used to describe detonation (Jach et al., 2001),

– behaviour of detonation products was described with JWL equation (Włodarczyk, 1994),

– in this case, to model the influence of a pressure wave on the structure, the algorithm included in LS-Dyna software was applied.

Based on the obtained results, it is possible to distinct three stages of the described phenomenon:

– stage I (0-35 μs): detonation of explosive material and expansion of gas explosion products until the moment of reaching the pyramid by the front of the pressure wave;

– stage II (35–50 μs): interaction of the wave with the structure (pyramid) (Fig. 6). The characteristic feature of this stage is the phenomenon of originating of the wave reflected from the pyramid with the intensity significantly greater than intensity of an incident wave. The value of the pressure at the front of a reflected wave is possible to be higher even eighth times than the pressure of an incident wave. After approximately 15 μs from the moment of reaching the pyramid vertex by a blast wave, deformations in the examined object start to be visible;

– stage III (50–250 μs): structure deformation. The pressure of the reflected wave decreases quickly and progressive deformation of the element occurs only as an effect of interaction of inertia forces (Fig. 7).

Owing to the character of the conducted examinations, it is only possible to compare the final shapes of the considered elements. The final form of the element deformation obtained through the experiment and numerical calculations is presented in Figs. 8 and 9. A very good agreement of calculations and the experiment was obtained. The difference in the final form of deformation was amounted to less than 7.5 %.
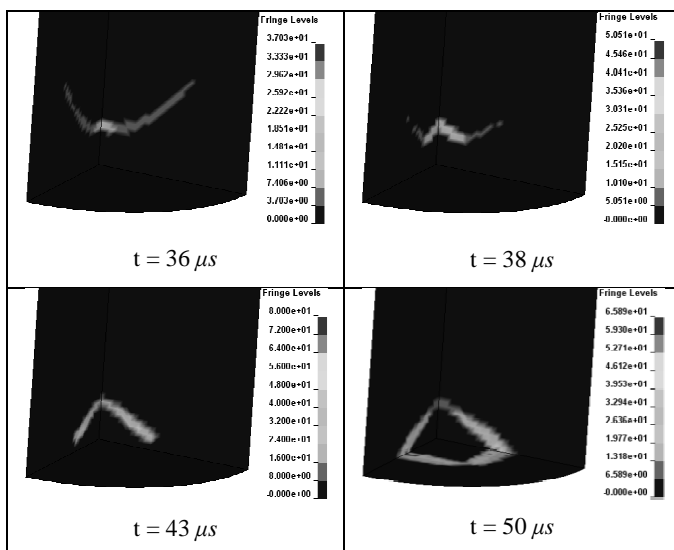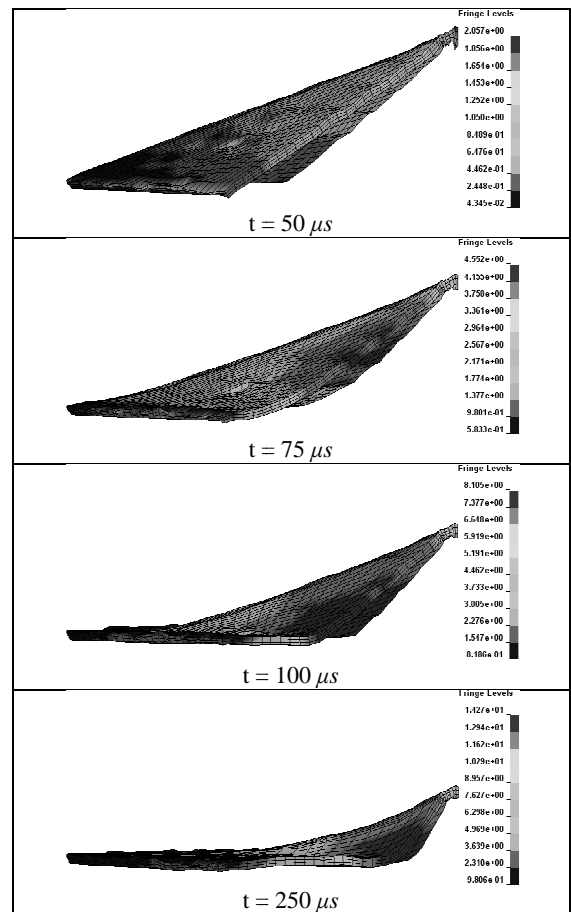

Fig. 7. The course of deformation process of the object (deformations in mm)
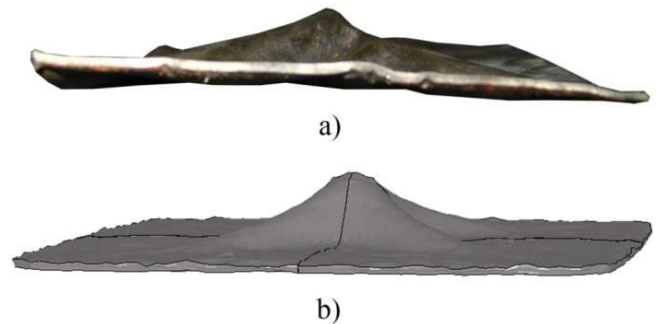

Fig. 8. Comparison of deformed pyramid from the experimental research (a) with the result obtained in full simulation of influence of pressure wave on the element (b) – side view

Fig. 6. The course of process of pressure wave reflection from the considered object (pressure values in MPa)

Fig. 9. Comparison of deformed pyramid from the experimental research (a) with the result obtained in full simulation of influence of pressure wave on the element (b) – top view

Comparing visually both of the models, it is possible to observe mainly the difference in the form of the edge between the pyramid walls. In the real model they are maintained on the whole length – from the pyramid vertex to the corners of the base. In the numerical model, the edges between the pyramid walls are maintained more or less to the half length, viewing from the vertex, and subsequently they undergo complete flattening. It results, first of all, from ignoring the material strengthening effect at the edges.

4. SUMMARY AND CONCLUSIONS

The paper presents the numerical-experimental results of research of dynamic loading the constructional element in the form of a metal pyramid with a square base with the pressure wave (coming from detonation of explosive material). A very good agreement between numerical calculations and the experiment was obtained in the aspect of the final form of deformation of the considered objects. The calculated intensity of the falling and reflected pressure wave corresponds to literature data. There was depicted the course of deformation in the examined element during the course of the considered phenomenon.

The presented constructional element is possible to be applied in energy absorbing panels. Due to their mass, such panels can be used for protection of stationary objects, not the mobile ones. They can be used particularly for protection of objects of critical infrastructure.

The paper presents the narrow part of a wide range of work on the problem of energy absorption and impact energy dispersion carried out by the Department of Mechanics and Applied Computer Science, Military University of Technology.

REFERENCES

1. **Hallquist J. O.** (2005), *Ls-Dyna Theory Manual, Livermore Sotware Technology Corporation*, Livermore, CA.
2. **Jach K. et al.** (2001), *Komputerowe modelowanie dynamicznych oddziaływań metodą punktów swobodnych*, PWN, Warszawa.
3. **Suceska M.** (1999), Evaluation of Detonation Energy from EXPLO5 Computer Code Results, Propellants, Explosives, *Pyrotechnics*, 24.
4. **Włodarczyk E.** (1994), *Mechanics of explosion (in polish)*, PWN, Warszawa.
5. http://www.globalsecurity.org/military/systems/ munitions/explosives-nitramines.htm.
6. Calculation of detonation pressures of condensed CHNO explosives, *Journal of the Chinese Institute of Engineers*, 29, 2006, tom 1.
7. http://stason.org/TULARC/science-engineering/chemistry/13-8-What-is-the-chemical-structure-of-common-explosives.html.

THE INFLUENCE OF A MAGNETIC FIELD ON VIBRATION PARAMETERS
OF A CANTILEVER BEAM FILLED WITH MR FLUID

Bogdan SAPIŃSKI*, **Jacek SNAMINA***, **Mateusz ROMASZKO***

*AGH University of Science and Technology, Faculty of Mechanical Engineering and Robotics,
Department of Process Control, al. A. Mickiewicza 30, 30-059 Kraków, Poland

deep@agh.edu.pl, snamina@agh.edu.pl, matek@agh.edu.pl

Abstract: The paper investigates a magnetic field acting on a three-layer sandwich beam filled with MR fluid, the field being generated by an electromagnet. The FEM approach is applied to determine the magnetic field strength and magnetic flux density in the area between the poles and in the MR fluid layer. The results are utilised to establish the relationship between the magnetic flux density and parameters of the assumed model of the MR fluid layer.

Key words: Cantilever Beam, MR Fluid, Magnetic Field

1. INTRODUCTION

Beams, plates and shell elements are widely used as structural components in vehicles, aircraft and various installations. Their operation, however, gives rise to some undesired phenomena, such as vibrations. Such vibrations can be reduced by the use of active and semiactive control methods.

Recently, semiactive methods using smart materials e.g. magnetorheological (MR) fluids have received a great deal of attention. MR fluids properties are varied under the action of a magnetic field. The stiffness and damping characteristics of the structure incorporating MR fluid are modified, too. These changes occur within a very short time and that is why MR fluids can be well applied in highly dynamic systems (Sun et al., 2003; Yalcinitias et al., 2004; Sapiński et al., 2009; Lara-Prieto et al., 2010; US Patent 5547049). Through varying the magnetic field strength, we are able to control mechanical parameters of the structure. Development of the magnetic field is crucial to functioning of the structures with MR fluid.

Magnetic field generated by an electromagnet and acting on a cantilever beam filled with MR fluid is investigated. The FEM model (Vector Fields Ltd 2007) developed in the Opera-2D environment (version 12) is used to determine the magnetic field strength and magnetic induction in the MR fluid layer. The influence of the beam's static deflection on the magnetic field distribution is investigated, too. The relationship is found between the Kelvin-Voigt model parameters of the MR fluid layer and magnetic flux density.

2. BEAM AND ELECTROMAGNET STRUCTURE

Schematic diagrams of the beam and the electromagnet are shown in Fig. 1 and 2. The beam shown schematically in Fig. 1 is made of two outer layers made of aluminium 400 mm long, 30 mm wide and 2 mm high. The space between the two layers is sealed with silicone rubber 2 mm thick and 1.5 mm wide and the beam interior is filled with MR fluid of the type 132DG,

manufactured by Lord Corporation (US Patent 5547049). The beam is placed centrally in the gap of the electromagnet and fixed on one end, so that the electromagnet can be moved smoothly.
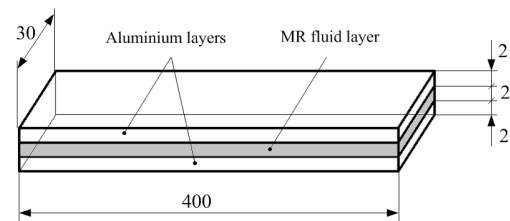

Fig. 1. Three-layer sandwich beam

The electromagnet (Fig. 2) is made of steel. The distance δ between the poles (gap) can be varied in the range 20-30 mm by moving the upper arm of the electromagnet, fixed on bolts. Each arm of the electromagnet has 370 wound turns of copper wire 1.4 mm in diameter.
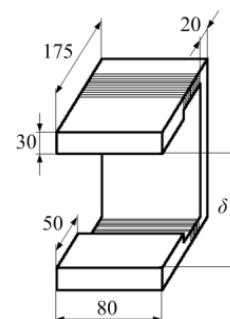

Fig. 2. Schematic diagram of the electromagnet

3. MODEL OF THE ELECTROMAGNET–BEAM STRUCTURE

The model of the electromagnet and the beam is developed in the Opera-2D environment. It is a 2D model contained

in the plane *x-z* (Fig 3). The symbol *I* stands for the current flowing through the electromagnet coil, z_u denotes the distance of the beam's cross section from the equilibrium position. Further, the area in which magnetic field is determined is bounded by a rectangle 220 x 180 mm. The model comprises 870389 finite elements and 174854 nodes.
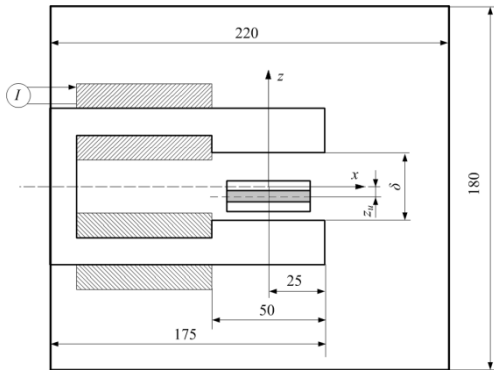

Fig. 3. Schematic diagram of the 2D beam-electromagnet model in the coordinate system *x–z*

Magnetic properties of MR fluid and of the electromagnet core are described by relevant magnetisation characteristics based on the catalogue data (Fig. 4). Relative permeability of aluminium layers is taken to be constant and equal to 1.
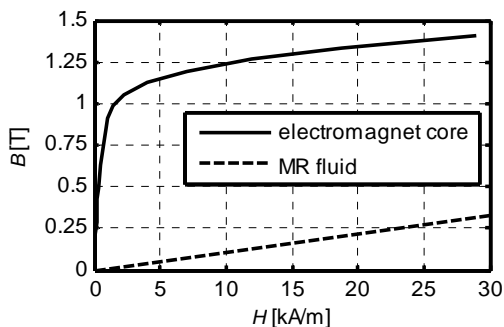
Fig. 4. Magnetisation characteristic of MR fluid and the electromagnet core

4. CALCULATION RESULTS

The calculation procedure is applied to obtain the magnetic flux density *B* and magnetic field strength inside the MR fluid layer. First the magnetic flux density is determined in the area between the electromagnet poles, without the beam present. Simulation results are then compared with measurement data. The measurements consist in varying the current *I* in the electromagnet coil from 1 to 10 A, with the step 0.5 A. In each case the magnetic flux density *B* is measured for three gaps *δ*: 20, 25, 30 mm. Registered values are then used to derive the static characteristic of the electromagnet. Fig. 5 shows the experimental data (continuous line) against the simulation results (broken line) for the air gap *δ*=20 mm (black) and *δ*=30 mm (grey). It appears that the proposed model sufficiently well emulates the behaviour of the real system. The discrepancies may be attributable to certain inadequacies of *B–H* characteristics of the electromagnet core. For example, all the details relative to connecting the electromag-

net arms are left out from the modelling procedure and a 2D model can only approximate any real system. 2D models take into account the magnetic flux distribution in two directions only, that is why the calculation results seem to be overestimated in relation to measurement data.
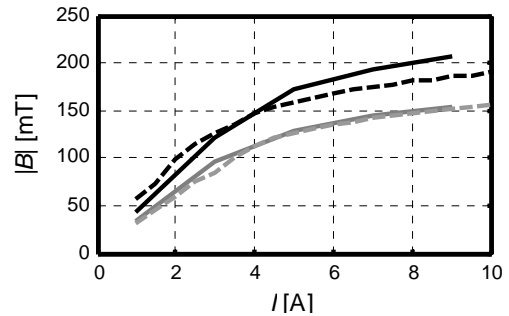

Fig. 5. Magnetic flux density *B* in the gap vs. current *I*

The experimental procedure is applied in which the MR beam is placed centrally in the gap of the electromagnet *δ*=20 mm (Fig 3). Magnetic properties of MR fluid are duly taken into account in the context of the magnetisation characteristics (Fig 4). The distribution of magnetic flux density *B* and magnetic field strength *H* in the middle of the MR fluid layer for the beam placed symmetrical z_u=0 mm (no static deflection) and for three selected currents *I* are shown in Fig. 6 and 7 (*I*=1 A – dashed line, *I*=5 A – continuous line, *I*=9 A – dotted line). It is apparent that flux density assumes higher values in the middle of the MR fluid layer (for *x* in the range from -15 to 15 mm), and decreases beyond the MR fluid. In the case of magnetic field strength, however, the situation is just the opposite.
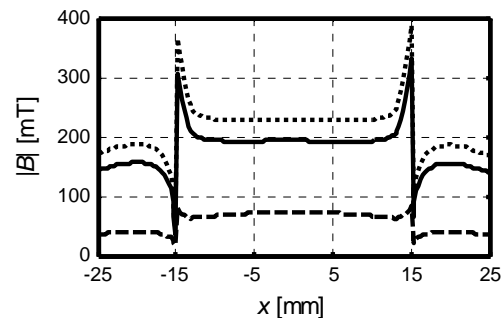

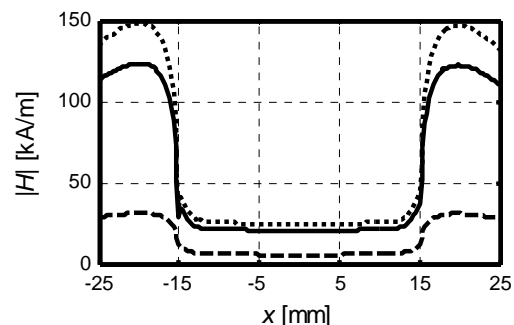**Fig. 6.** Distribution of magnetic flux density *B* along the *x*–axis; z_u=0 mm

Fig. 7. Magnetic field strength *H* along the *x*–axis; z_u=0 mm

The further step of the calculation procedure is applied to investigate the flux density distribution in the middle of the MR fluid

layer in the case when the beam's cross-section is displaced by z_u=2 and 5 mm, the electromagnet gap being δ=20 mm. Vertical displacement of the beam's cross-section is associated with static deflection or the beam' movements during vibration. Results are shown in Fig. 8 and 9, line designations as in Fig. 6. Apparently the flux density distributions for the two values of z_u are nearly identical and follow the same pattern. Higher values of B are registered in the middle of the MR layer (for x ranging from -15 to 15 mm) than beyond the beam. Flux density distributions for two beam positions: z_u=0 mm and z_u=5 mm are compared in Fig. 10.
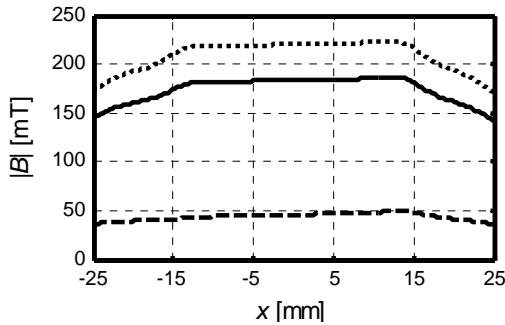
Fig. 8. Flux density distribution B along the x–axis; z_u=2 mm
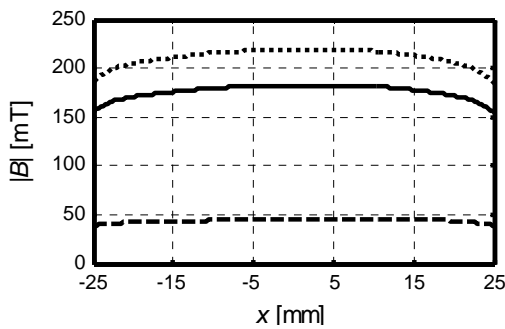
Fig. 9. Flux density distribution B along the x–axis; z_u=5 mm
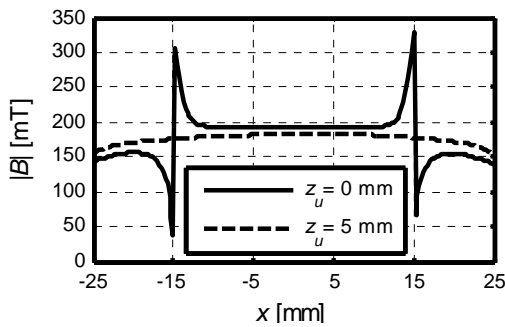

Fig. 10. Flux density distribution B along the x–axis; I= 5 A
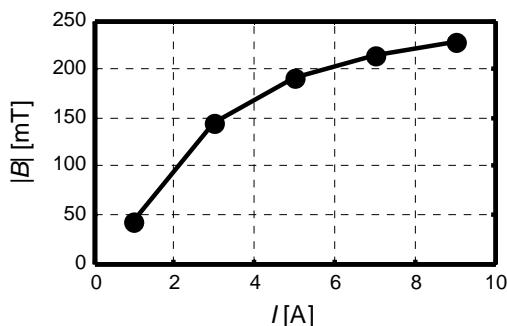

Fig. 11. Flux density B in the middle of MR layer vs. current I

The flux density distribution shown in Fig. 10 reveals major differences on the beam edges only, for x=–15 mm and x=15 mm. In quantitative terms, the flux density in the MR fluid layer and outside the beam is quite similar.

Further, the distribution of magnetic flux density B in MR fluid is obtained in the function of current I. Results are summarised in Fig. 11, for the applied current levels I: 1, 3, 5, 7, 9 A, revealing the pattern of flux density variations in the middle part of the MR fluid layer with current I. MR fluid contains a ferromagnetic material, that is why an increase of the external magnetic field strength H at the certain point reaches the state of saturation.

The works (Sapiński et al., 2010; Snamina et al., 2010) focus on the developed FEM model of a cantilever sandwich beam (Fig. 2) and identification of its parameters. The MR layer is modelled in terms of the Kelvin-Voigt rheological model, comprising a spring and a viscous damper connected in parallel. Its schematic diagram is shown in Fig. 12. The spring stiffness is expressed by the parameter k_p, whilst c_p is the damping coefficient.

Parameters k_p and c_p are identified by comparing the computed first natural frequency f_o and the modal damping coefficient ζ with experimental data. The relationship between those parameters and magnetic flux density B in the middle section of the MR layer is shown in Fig. 13 and 14, revealing a similar variability pattern of these two parameters. In qualitative terms, that agrees well with research data provided in the work (Sun et al., 2003). The authors relied on the loss coefficient G'' when defining the energy dispersion level whilst the coefficient G' applies to energy conservation.
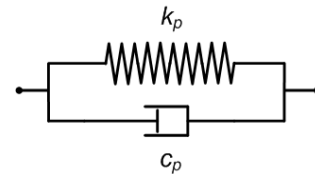

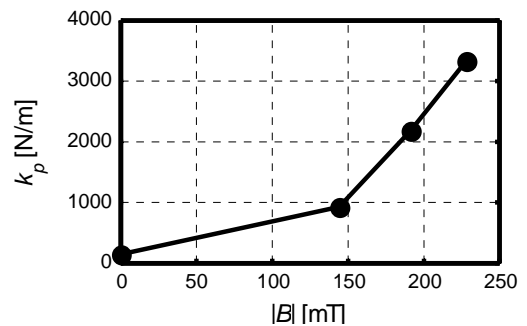**Fig. 12.** Kelvin-Voigt rheological model

Fig. 13. Stiffness k_p of the MR fluid model vs. magnetic flux density B
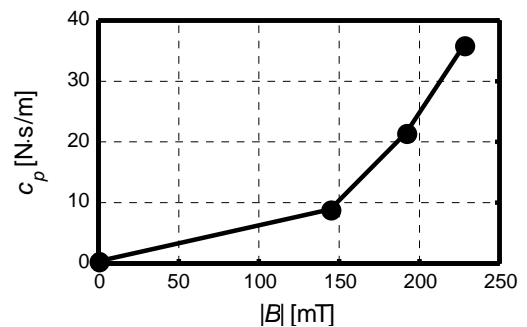

Fig. 14. Damping c_p of the MR fluid model vs. magnetic flux density B

Simulation results illustrate the influence of magnetic field on vibration parameters of the beam. Investigated parameters describing the beam vibration are: the first natural frequency f_o and the modal damping coefficient ζ. The values of f_o and ζ are obtained by investigating the beam's free vibration in the test rig designed specifically for the purpose of the research program (Sapiński et al., 2010).

The influence the electromagnet configuration y_m and magnetic flux density B on the first natural frequency fundamental free vibration frequency f_o is illustrated in Fig. 15. Magnetic flux density B in the MR layer is varied by changing the current level I in the electromagnet coils. It appears that as the electromagnet moves farther from the fixed end of the beam (y_m increased to 80 mm) and magnetic flux density B increases, the first natural frequency of the beam will increase, too and the beam stiffening effect is observed in the range $y_m<80$ mm. Moving the electromagnet any further $y_m>80$ mm enhances the non-uniformity of magnetic field acting upon the vibrating beam. As the result, the first natural frequency f_o will decrease. The value of the first natural frequency with no magnetic field is 8.92 Hz.
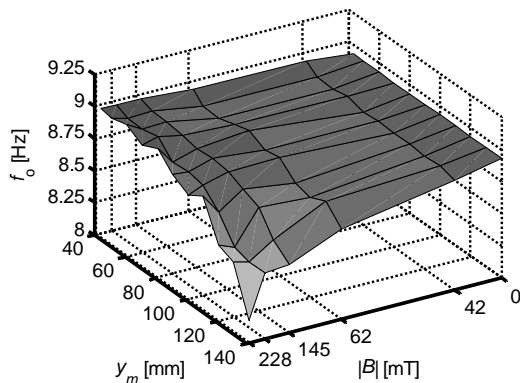

Fig. 15. Free vibration frequency f_o of the beam vs. the electromagnet position y_m and flux density B; δ=20 mm

The influence of the electromagnet position y_m and magnetic flux density B on the modal damping coefficient ζ is shown in Fig. 16. In qualitative terms, the distribution of the damping coefficient is similar to that of the natural frequency. As the electromagnet is moved farther from the fixed end of the beam (y_m increased to 80 mm) and magnetic flux density B increases, the value of the dimensionless damping ratio will increase, too, and the damping performance of the sandwich MR beam increases relatively fast. The value of the modal damping coefficient in the absence of magnetic field is 0.009.
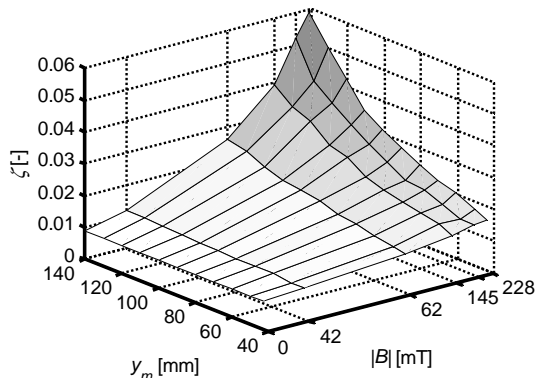

Fig. 16. Modal damping coefficient ζ vs. the electromagnet position y_m and flux density B; δ=20 mm

5. CONCLUSIONS

Underlying the 2D model of the beam-electromagnet system is the FEM approach supported by the Opera-2d software. The electromagnet is used as a source of magnetic field to interact with the MR fluid layer embedded in the sandwich beam. The model enables us to find the magnetic field distribution in the gap of the electromagnet- when empty and with the beam placed there. The study also investigates the influence of the MR fluid layer position with respect to the electromagnet poles. The change in the MR fluid layer position is due to either static deflection or beam vibrations.

Calculated parameters of magnetic field are used to establish the relationship between magnetic flux density and parameters of the adopted Kelvin-Voigt rheological model, emulating the properties of the MR fluid layer (Sapiński et al., 2010; Snamina et al., 2010). In qualitative terms, the results obtained by the authors agree well with research data reported in literature (Sun et al., 2003).

Finally, the study investigates the influence of the magnetic flux density in the middle part of the MR fluid layer on the value of the modal damping coefficient and the first natural frequency.

Research work is now underway to develop a 3D model of the beam-electromagnet system, using the Comsol Multiphysics software.

REFERENCES

1. **Lara-Prieto V., Parkin R., Jackson M., Siberschmidt V., Kęsy Z.** (2010), Vibration characteristics of MR cantilever sandwich beams experimental study, *Smart Materials and Structures*, 19, 1–9.
2. **Sapiński B., Snamina J., Romaszko M.** (2010), Identification of model parameters of a sandwich beam incorporating magnetorheological fluid, *Vibration in Physical Systems*, 24, 349-354.
3. **Sapiński B., Snamina J.** (2009), Vibration of a beam with magnetorheological fluid in non-homogenous magnetic field, *Modelowanie Inżynierskie*, 6, 241-248.
4. **Snamina J., Sapiński B., Romaszko M.** (2010), Modelowanie belki z cieczą magnetoreologiczną metodą elementów skończonych, *Modelowanie Inżynierskie*, 8,185-192.
5. **Sun Q., Zhou J., Zhang L.** (2003), An adaptive beam model and dynamic characteristics of magnetorheological materials, *Journal of Sound and Vibration*, 261, 465-481.
6. **US Patent** 5547049 Magnetorheological Fluid Composite Structure.
7. **Vector Fields Ltd.**(2007), Opera-2d version 12, User Guide.
8. **Yalcinitas M., Dai H.** (2004), Vibration suppression capabilities of magneto-rheological materials based adaptive structures, *Smart Materials and Structures*, 13, 1–11.

ASSESSMENT OF CUTTING EDGE DEFECTS USING A VISION METHOD

Andrzej SIOMA*

*AGH University of Science and Technology, Faculty of Mechanical Engineering and Robotics,
Department of Process Control, Al. Mickiewicza 30, 30-059 Kraków, Poland

andrzej.sioma@agh.edu.pl

Abstract: The paper discusses a vision method of assessment of laser cutting edges and surfaces of metals. It presents an analysis of the defects that occur at the edges and surfaces of components cut out in laser technology. It discusses in detail examples of defects, their causes, and methods of preventing their occurrence in the cutting process. The paper presents a vision method for the identification and assessment of defects based on selected examples. It also discusses a method of constructing a three-dimensional image of a product, issues related to the resolution of the vision system and the resolution of laser beam analysis, and methods of image analysis.

Key words: 3D Vision System, Image Processing, Surface Defects, Process Control, Quality Control

1. INTRODUCTION

The purpose of this paper is to present methods for the identification and evaluation of surface and edge defects formed during laser cutting. The process of detection and identification of defects that occur during cutting is part of the control carried out on production lines usually by humans. The method of automating the control process discussed in this article was developed for a selected technological process. i.e. laser cutting, based on studies of defects that occur during the machining of metals. A method for constructing a three-dimensional image of the product and an image processing algorithm that allows observation and evaluation of the defect are discussed (Kowal and Sioma, 2009,2010; Gawlik and Sioma, 2004). Such an image contains information about the actual dimensional parameters of the product and allows their control immediately after technological operations. These days, in the conditions prevailing on the production line in mass production, statistical control is used in order to evaluate product parameters (Sioma, 2011a, b). Accurate measurements are also performed at random, in measurement laboratories. The solution presented in this work allows monitoring of all products leaving the process and practical application of the "zero defects" method. It also allows the use of feedback information about possible defects in the product in the process of controlling the technological parameters of the process.

The machining tools used in the industry are equipped with control systems capable of carrying out technological operations in accordance with a developed programme, including quality control of its implementation. However, there may still occur manufacturing defects associated with the type of workpiece material, programmers' errors, operators' technique, and characteristics of the machining method employed in the technological process (Sioma and Struzikiewicz, 2011; Oczoś and Liubimov, 2003; Pawlus, 2006).

The paper presents typical defects that occur in the cutting of metals with the use of a laser. The advantages of this method of machining include: precision of the cut, quality of the edges obtained, cutting speed, and a narrow range of temperature impact. In addition, the following pros should be mentioned: material savings resulting from the small dimensions of the gap, a wide range of workpiece materials, and non-contact machining. Technological practice, however, shows that laser metal cutting produces defects also on the machined surfaces and edges. Defects can be created as a result of damage to the components of the machine (laser cutter) or a bad choice of parameters in the process.

One of the causes may be the wear of laser head nozzle or damage to the nozzle in contact with the workpiece material. The operating conditions of a laser cutter are defined by its boundary parameters, such as data regarding the range of laser power or the thickness of the workpiece material. Prior to starting work, the operator selects process parameters on the basis of technology tables implemented into the control system of the machining tool. Technology tables together with the available labour rules allow the operator to prepare a programme for the implementation of the cutting process. At this stage, the operator must pay attention to the parameters which affect correct execution of the cutting process, such as contour cutting sequence, direction of cutting, burn-through, entry positions, type of contour, corners, collisions between the machined pieces and the head, and arrangement of the table ribs.

For example, the position of a burn-through point is changed if the operator decides that the programme had arranged them too close to the cutting edge. However, if the burn-through point is moved too far away from the edge, the process will become longer and create additional costs, which, in turn, increases the price of the product itself. Workmanship of the cutting edge also depends on the knowledge and experience of operators. Many experienced operators build their own technology tables based on observation of the results produced by their machine. On the basis of work carried out in the industry, a description of the typical defects that occur on the edges and surfaces of cut-out pieces has been prepared.

The defects shown in the figures are described, along with their causes as well as methods of preventing their occurrence in the cutting process. The most basic and common geo-

metric shape cut with laser machines are circles. Cutting circles is mostly intended to eliminate the need for additional technological operations such as routing, drilling or reaming. However, the technological capabilities of the cutter and the required tolerances of the hole must be noted. One of the principles used in laser cutters when it comes to cutting holes is to verify whether the hole diameter is greater than or equal to the thickness of the material (Fig. 1):

$$\varnothing \geq g \qquad\qquad\qquad\qquad (1)$$

where: $\varnothing$ – hole diameter, g – thickness of material.
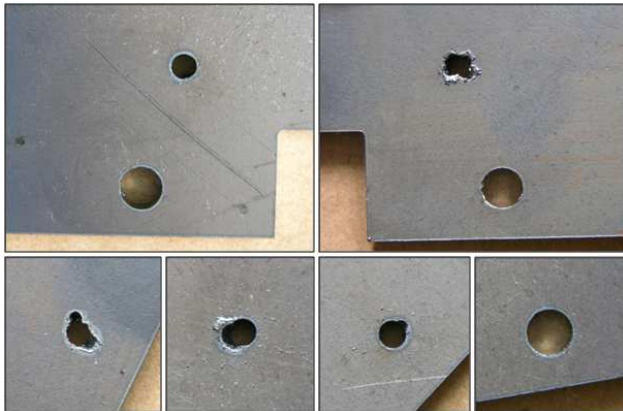
Fig. 1. View of holes made in steel

Depending on both the thickness and type of material used to manufacture a product, that principle may be abandoned and a test cut performed instead. However, failure to apply that rule leads to deterioration of the edge of the hole, which, in turn, leads to deformation of the hole.
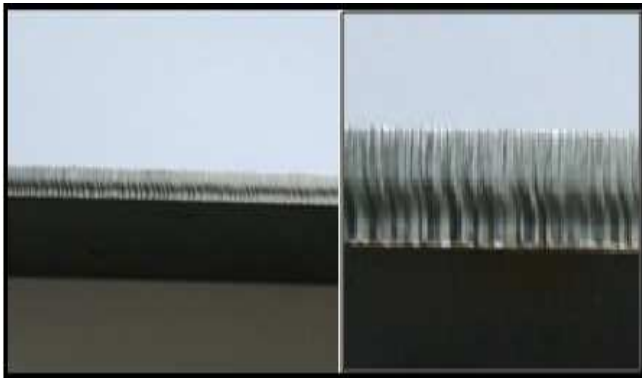

Fig. 2. Example of a defect on a cutting edge

Another example is the quality of a cutting edge. If the pieces are made of thin sheet metal, the edges are sufficiently accurate, which makes it possible to omit additional finishing operations such as grinding.

However, as thickness of the material increases, quality of the edge decreases, which also is closely related to the type and grade of the material machined. An example of a defect on an edge is shown in Fig. 2.

Another disadvantage observed during machining in the formation of welds, teeth, and, consequently, the lack of proper cutting of the material. Such a defect appears on the surface of the material in case of wrong selection of laser power. An example of such a defect is the edge in Fig. 3. That defect also occurs when the working gas pressure drops or in case of an error in the setting of the laser beam focus. This requires additional repair process and adjustment of laser power.

Fig. 3. A defective cutting edge

Another example of defects are those caused by poor preparation of the laser work programme. A cut-out piece may be held by the grid in such a position in which it is damaged as a result of the laser cutting of successive pieces.

Fig. 4. Damage to the surface of the piece

Another defect that occurs during cutting is the formation of burr on the cutting edge. Burr is the presence of roughness on the edge. The causes of this defect are usually insufficient laser power, insufficient gas pressure, or incorrect focusing of the laser beam.

Fig. 5. Burr on cutting edges

In conclusion, the causes of defects on the edges and surfaces of the material being cut in laser technology usually include: dirty lens of the head, poorly chosen technology table, incorrect position of the laser beam focus, erroneously selected cutting speed, incorrectly chosen laser power, and worn or damaged table ribs.

Methods for improving the quality of edges and surfaces made by laser cutting include: proper selection of technology tables, laser lens cleaning, cutting head speed control, laser power control and adjustment of the laser beam focus, replacement of damaged ribbing of the table, cleaning of the surface of the material, and proper mounting of the material.

2. CONSTRUCTION OF PRODUCT IMAGE

The paper presents a method that enables automatic quality control of laser cut pieces. Quality control of the edges and assessment of the defects formed on surfaces was carried out using a specialized vision system. The construction of a vision system requires several steps, as a result of which successive parameters of the system's operation are chosen (Bednarczyk and Sioma, 2011; Tytko and Sioma, 2011; Sioma, 2010).

The first stage is the selection of the geometry of the system, i.e. camera and laser arrangement relative to the surface of the workpiece. The paper discusses a geometry in which the sensor of the vision system is set at angle α relative to the surface of the measuring table. For the selected geometry, a method for determining the measuring resolution of the vision system is presented. It should be noted that in the selection of a vision system for specific measurement requirements, such as the measurement resolution recommended in the assessment of surface defects, selection of an appropriate optical system, i.e. focal length and type of the lens, and of an appropriate resolution of the vision system sensor, will also be necessary. In the presented geometry, the optical axis of the camera is not perpendicular to the surface of the measuring table and the plane of the test object's base (Fig. 6a).
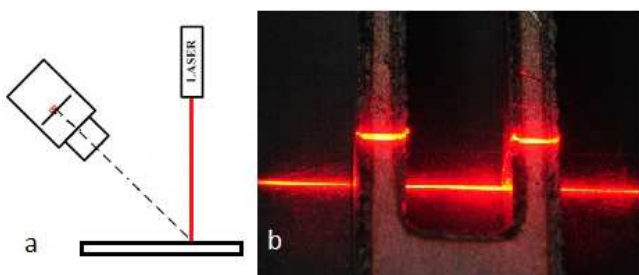

Fig. 6. Geometry of a vision system - camera and laser cooperation

For the presented geometry of vision system settings, the cross-section of the workpiece viewed in the camera and effected by the laser beam is parallel to axis Z in the coordinate system of the measuring table. It is also parallel to the plane of the laser displayed on the test object. That cross-section is observed by the vision system at a certain angle that had been chosen for this task (Fig. 6b). As a result, mathematical processing is required to enable conversion of the geometry of the cross-section in the image created by the laser beam in order to obtain an actual cross-section and then construct a three-dimensional image of the tested object. In the next stage of vision system

configuration, it is necessary to set the vision system resolution in the adopted configuration. As a result of change in object height, the laser line image moves on the CMOS camera sensor. Designation of vision system resolution consists in determining such minimum change in object height, described by the ΔZ parameter, at which the laser image is observed to move exactly by one row of pixels on the camera sensor (Fig. 7).
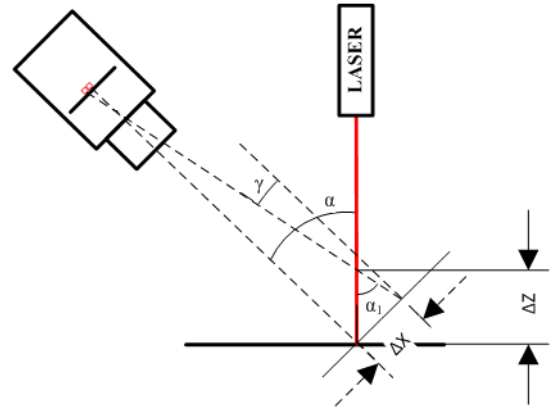

Fig. 7. Determination of resolution in axis Z

On the plane parallel to the sensor plane, resolution ΔX in axis X is then determined based on the dimensions of the field of view and sensor resolution given in pixels. Resolution ΔY in axis Y is defined as the distance between the acquisition of an image of the successive height profiles of the test object. When calculating the resolution in the configuration presented, an approximation is used where we assume that angle α is equal to angle α_1. In fact, angle α_1 is equal to:

$$\alpha_1 = \alpha - \gamma \qquad (2)$$

However, when determining resolution based on the formula below, the following is assumed for calculation purposes: $\alpha_1 = \alpha$. As a result, such a simplification does not significantly affect the outcome of resolution in axis Z.

$$\Delta Z \approx \Delta X / \sin(\alpha) \qquad (3)$$

where: ΔZ – resolution in axis Z, ΔX – resolution in axis X, α – the angle between the axis of symmetry of the laser and the optical axis of the camera.

Resolution in axis X and axis Z is determined in millimetres per pixel. If sub-pixels image processing is to be conducted, then the value calculated per pixel should be divided by the value of pixel division coefficient. Then, it is possible to determine movement of the line on a screen with the resolution of e.g. ½ pixel, ¼ pixel or any other. Using a 1536x512 pixel sensor and a lens for the vision system allowing observation of a 64 mm wide object (FOV = 64mm), resolution in axis X and Z was determined for the test object.

$$\Delta X = 64mm / 1536\,pixels = 0.041[mm / pixel] \qquad (4)$$

$$\Delta Z \approx 0.041 / \sin(45°) = 0.058[mm / pixel] \qquad (5)$$

On the plane parallel to the plane of the sensor, with the resolution ΔX in axis X known, resolution in the axis perpendicular to X is also taken to be ΔX. Resolution in axis Y of the coordinate system is dependent on the shift of the table between the successive image acquisitions by the vision system. Assuming that in the

object displacement measurement system there is an encoder sending 1600 pulses per 1 mm of table displacement for an image acquired every 160 pulses, resolution in the direction of axis Y is

$$\Delta Y = 160 [imp/scan]/1600[imp/mm] = 0,1[mm/scan] \qquad (6)$$

A three-dimensional image of the object is built from profiles collected during object movement in the direction of axis Y of the test station. The vision system captures a profile image each time after the object moves by 0.1 [mm], i.e. 160 pulses. In axis X, the resolution is 0.041 [mm] and it is the distance between successive measuring points on that axis without sub-pixel processing. Resolution in axis Z is equal to 0.058 [mm]. In case of sub-pixel image processing, the resolution in axis X and Z takes into account the coefficient resulting from the pixel division algorithm.

After acquiring the image, a procedure is carried out to translate the laser line visible on the sensor into profile height in each of sensor column. The most important element of this analysis is precise definition of the position of the centre of the laser line as seen by the vision system. Each column of the image is presented as a function of intensity $f(x)$, where the argument is the number of a pixel in the column. Then, for each column, the position of laser line centre is determined, and thus complete information about line position needed to calculate the height of the profile point is obtained. For each sensor column (Fig. 8b), a value of the change in intensity along the pixels forming the column is determined (Fig. 8a). Then, the centre of the laser line is determined.
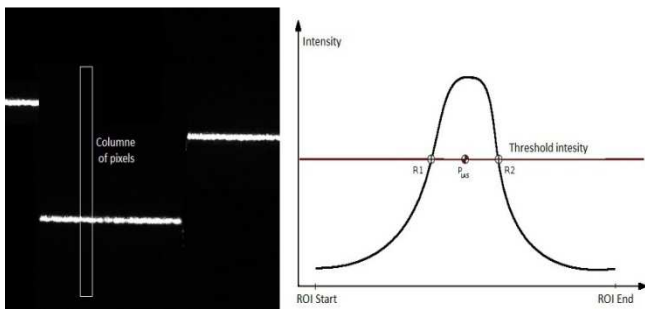

Fig. 8. Algorithm to determine the position of laser line in the successive sensor columns
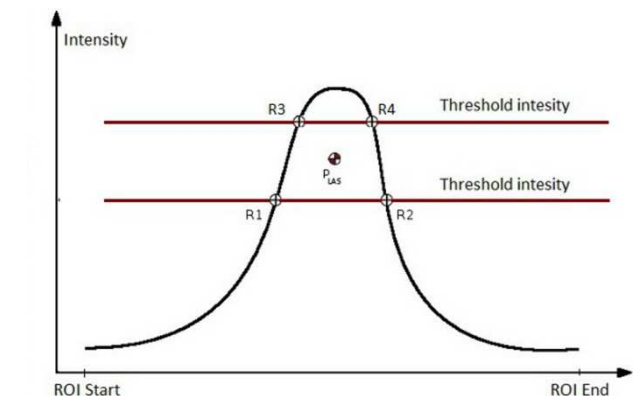

Fig. 9. Determination of laser line centre using double intensity threshold

To determine the centre of the laser line, the method of threshold intensity definition is used. In that method, an intensity threshold defined by the user is put in. If there is no interference and the threshold was well chosen, it intersects the intensity diagram at two points (R1 and R2). The centre of the laser line

is determined as the arithmetic mean of pixel positions where the diagram intersected with the threshold. Analysis of intensity in a column, using an intensity threshold, allows obtaining resolution of ½ pixel. In order to increase the resolution of laser line centre determination, two intensity thresholds should be used. In such case, four points describing the intensity function are available and laser line centre is determined as the arithmetic mean of the positions of those points. The use of two intensity thresholds allows obtaining resolution of ¼ pixel (Fig. 9).

$$x_{LAS} = \frac{x_{R1} + x_{R2} + x_{R3} + x_{R4}}{4} \qquad (1)$$

3. OBJECT MEASUREMENTS ON 3D IMAGE

The vision system observes an image of the given piece in the manner shown in Fig. 10a. Parameters of the vision system are chosen in such a way that the image shows only a trace of the laser line. It is also important that in the event of accidental reflection of laser light from other surfaces of the object, the trace of that reflection is not visible on the image. The impression of the tested object is removed from the image. Based on the sequence of images collected, height profiles of the tested object are determined in the successive cross-sections. Figs. 10a and 10b show an image and a profile of an incorrect edge. Fig. 10c shows a profile of a correct edge.
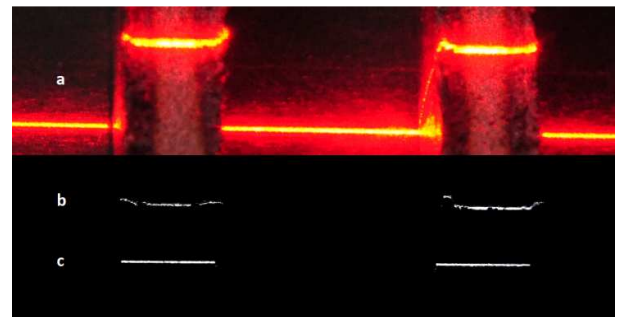

Fig. 10. Laser beam illuminating the object

On the basis of the prepared height profiles that form the successive cross-sections, a three-dimensional image of the object is constructed. View of a piece with correct cutting edges is presented in Fig. 11a. Fig. 11b shows edges with visible cutting defects (burr).
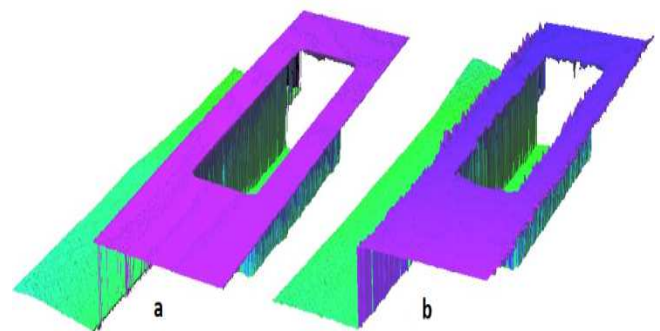

Fig. 11. 3D image of a product:
a – correct, b – with defects on cutting edges

Both in the case of the profile and the 3D image, there are distortions of the image resulting from both the geometry of the system as well as from the laser light reflected from the surface of the object. As a result of occlusion, the three-dimensional image does not show the portions of the object which the laser light does not reach. Such an image must be filtered prior to the implementation of a control procedure. Fig. 12 shows an image after smoothing filtering using a structural element – a 3x3 sensor. However, it should be noted that in the course of smoothing, the height of "peaks" appearing in the image will have an impact on the value of points in their vicinity.

After performing image transformations, as a result of which noise is removed from the image, an analysis of the quality of cutting may be performed for a selected edge of the object. That analysis should be performed using assessment of the height profile along the tested edge of the object (Fig. 12).
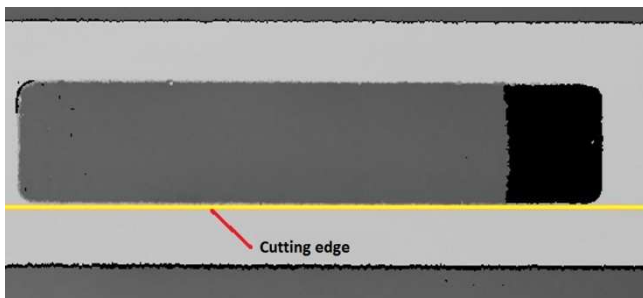

Fig. 12. An edge along which the height profile has been determined

For the tested profile, a comparative analysis was carried out of the height of unevenness in a correct edge and in an edge with a visible defect. The incorrect edge and its three-dimensional image are shown in Fig. 5 and 11b respectively.
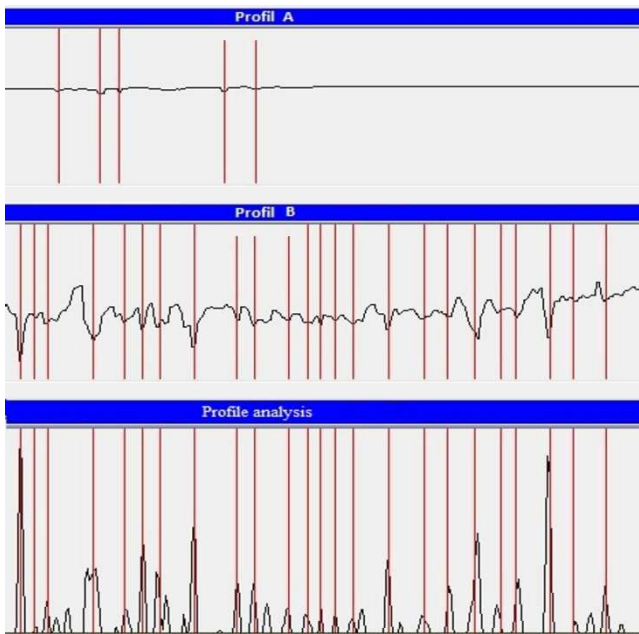

Fig. 13. Measurement of edge defect

A height profile of a proper edge is described in Fig. 13 as "Profile A". Small interferences (chipping) can be seen marked with 5 vertical lines. Quality of the edge was assessed by measur-

ing the deviation of the height of the cutting edge from the nominal profile. The nominal profile is determined based on an assessment of the height of the surface of the material outside the cutting edge.

A defective cutting edge is described as "Profile B" (Fig. 13). The height of profile unevenness shows visible distortions in relation to the proper edge. The values of such deviations from the nominal profile at selected points described for an incorrect edges are shown in the bottom part of Fig. 13 and are identified as "Height of profile unevenness". Those heights are determined at the resolution specified in this paper. Based on such information, the algorithm implemented into the video system enables measurement and assessment of the product on selected edges and planes.

Another method of measuring edge defects is the assessment of edge shape in relation to a reference plane. The reference plane was determined on the basis of analysis of points spaced around the edge of the object (Fig. 14). The figure shows a three-dimensional image of edges above the reference plane. During the research, the volume of edges was measured in relation to the plane and were thus a quantitative parameter describing the defective edge was obtained. In the case of proper edges, the volume should be close to zero.
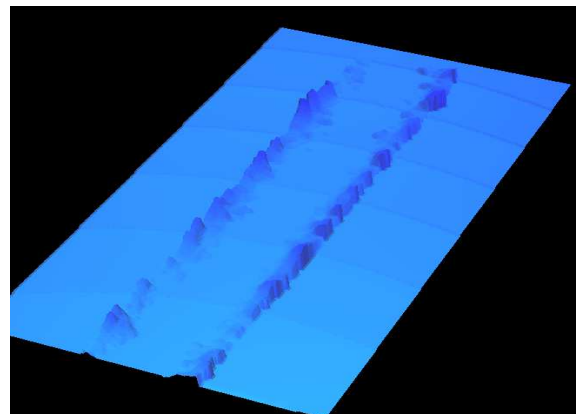

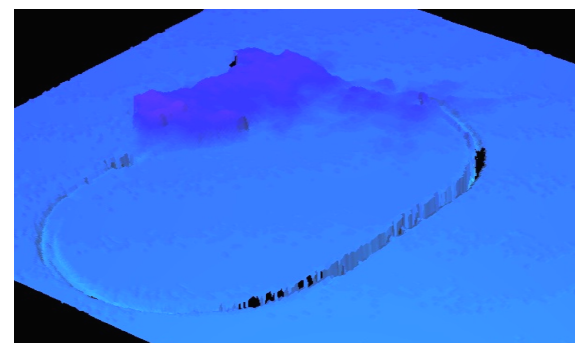**Fig. 14.** Measuring the volume of material visible above the reference plane

Fig. 15. Measuring the volume of material visible above the reference plane

Similar algorithms were also applied to the assessment of defects described in the first part of the paper. Profile height measurements combined with volume measurements and hole dimension measurements allow unambiguous assessment of the presence of a hole and its defects. Figure 15 shows an incorrect hole from which material has not been removed.

4. SUMMARY

In the course of research, algorithms for the detection and assessment of defects generated during laser cutting were developed. Those algorithms, developed and tested on products, confirmed the effectiveness of the vision method for assessing defects. A significant advantage of the solution is the possibility of controlling the product on all edges and surfaces simultaneously within about 1 s. That enables precise control of all products leaving the production line. As a result of the analysis, identifying presence of the material in an opening and presence of burr on the cutting edge was made possible. Also, detection of a defect in a three-dimensional image of the product makes it possible to send feedback information to both the operator of the technological line and to the machine control system. It is crucial information that prevent the manufacturing of defects in the process.

REFERENCES

1. **Bednarczyk J., Sioma A.** (2011), Application of a visual measurement technique to the assessment of electrodynamic stamping, *Solid State Phenomena*; Control engineering in materials processing, Vol. 177, 1–9, 20.

2. **Gawlik J., Ryniewicz A., Sioma A.** (2004), The strategies and methods of measurement in multifunctional quality inspection, *8th International Symposium on Measurement and Quality Control in Production*, Erlangen, MEASURE AND QUALITY CONTROL IN PRODUCTION Book Series: VDI BERICHTE Vol. 1860, 649-662.

3. **Kowal J., Sioma A.** (2009), Active vision system for 3D product inspection: Learn how to construct three-dimensional vision applications by reviewing the measurements procedures, *Control Engineering* USA, Vol. 56, 46-48.

4. **Kowal J., Sioma A.** (2010), Metoda budowy obrazu 3D produktu z wykorzystaniem systemu wizyjnego [Construction of a 3D image of a product using a vision system], *Acta Mechanica et Automatica*, Vol. 4. No. 1, 48–51.

5. **Oczoś K., Liubimow V.** (2003), *Struktura geometryczna powierzchni* [*The geometric structure of surfaces*], Oficyna Wydawnicza Politechniki Rzeszowskiej, Rzeszów.

6. **Pawlus P.** (2006), *Topografia powierzchni* [*Surface topography*], Oficyna Wydawnicza Politechniki Rzeszowskiej, Rzeszów.

7. **Sioma A.** (2010), Zastosowanie systemów wizyjnych 3D w kontroli jakości wykonania elementów pneumatyki i hydrauliki [Using 3D vision systems in the quality inspection of pneumatic and hydraulic components], *Pneumatyka*, No. 1, 27–30.

8. **Sioma A.** (2011a), Modelowanie i symulacja realizacji procesu technologicznego [Modelling and simulation of processes], *Mechanik* miesięcznik naukowo-techniczny, No. 12, 990.

9. **Sioma A.** (2011b), Projektowanie CAD z wykorzystaniem danych z systemu wizyjnego [CAD design using data from a vision system], *Mechanik* miesięcznik naukowo-techniczny, No. 12, 990.

10. **Sioma A., Struzikiewicz G.** (2011), Pomiary głowicy frezowej z wykorzystaniem systemu wizyjnego [Milling head measurements using a vision system], *Świat Obrabiarek*, No. 9-10, 8-10.

11. **Tytko A., Sioma A.** (2011,) Evaluation of the operational parameters of ropes, *Solid State Phenomena*, Control engineering in materials processing, Vol. 177, 125–134.

VISION METHODS FOR ASSESSING THE GEOMETRICAL PARAMETERS OF STEEL ROPES

Andrzej SIOMA*, Andrzej TYTKO**

* AGH University of Science and Technology, Faculty of Mechanical Engineering and Robotics, Department of Process Control,
Al. A. Mickiewicza 30, 30-059 Kraków, Poland
** AGH University of Science and Technology, Faculty of Mechanical Engineering and Robotics, Department of Rope Transport,
Al. A. Mickiewicza 30, 30-059 Kraków, Poland

andrzej.sioma@agh.edu.pl, tytko@agh.edu.pl

Abstract: This article discusses a vision method of measuring the geometric parameters of ropes and evaluating their wear based on measurements made in a three-dimensional rope image. The article discusses the method of construction of a three-dimensional image based on mapping of the actual dimensions of the rope and on algorithms that allow determination of the parameters describing its basic geometrical dimensions and surface condition. The article discusses issues related to resolution of the vision system, resolution of laser beam analysis, and resolution relating to the measurement of the height profile on the surface of the rope. Based on the image constructed in such a way, measurements are presented in order to assess the dimensional parameters and surface defects in sample rope structures. Based on tests and analyses of the three-dimensional image, a range of inspection tasks using 3D vision systems is indicated.

Key words: 3D Vision System, Rope Defects, Rope Diagnostics, Rope Model Resolution

1. INTRODUCTION

Steel wire ropes are the fundamental element crucial to the safety of operation of all devices in which they are used. They include a very broad range of machines: cable railways, mine shaft hoists, passenger and cargo lifts, cranes, gantry cranes, winches, off-shore equipment, and many more. Steel wire ropes are popular because their wear characteristics and methods of determining service life are well-known (Tytko and Sioma, 2011). All ropes used as intended are taken out of service In accordance with one of three principles: service life to replacement results from an arbitrarily adopted value, service life to replacement is determined by the amount of work done by the rope, or (most commonly) numerical criteria for discarding as a result of identified actual level of wear or degree of weakening are provided for in relevant regulations (Kowalski et al., 2009).

In most countries, supervision of the safety of operation of ropes and the associated equipment is mandatory and is stipulated by law. The rule of three parties is applied. The user is legally responsible for the operational safety a rope device and is obliged to prove that the condition of the device, including the rope, is good, i.e. fulfils the requirements of relevant regulations. Ropes are tested with non-destructive methods by certified staff, usually external companies. In the case of ropes, two main methods, which are prevalent in various ways, are used: magnetic rope testing (MRT) and visual testing (VT). The third party has inherent legal competence to permit further use of the device based on evidence in the form of certificates or expert opinions on the condition of the device. Procedures, measurement methods, certification of NDT staff, and criteria for discarding ropes are usually regulated by local laws, but also, for example, in the case of cable railways in European Union countries, by laws or regulations at national level and by normative acts.

For the last several years, users of rope transport devices and

ropes researchers have been witnessing constantly improving quality of ropes, especially in new structures. Therefore, the existing measuring methods for assessment of the degree of wear applicable to many applications of ropes are not sufficient any more. An example might be the visual testing method, which, in addition to visual inspection, measures the basic geometric parameters of the rope, i.e. diameter and length of the pitch. Those parameters or, more specifically, changes thereof with respect to the standard values determined during routine testing of ropes can be the basis for assessing the degree of wear. Fig. 1 shows an example of correct and incorrect measurement of rope diameter using that method (Tytko, 2003; Tytko and Sioma, 2011). Measurement of rope diameter using the presented method has also other limitations. It is inherently random and feasible in very few places (cross-sections of the rope). Even more difficult and less precise is measurement of the pitch length of a working rope.
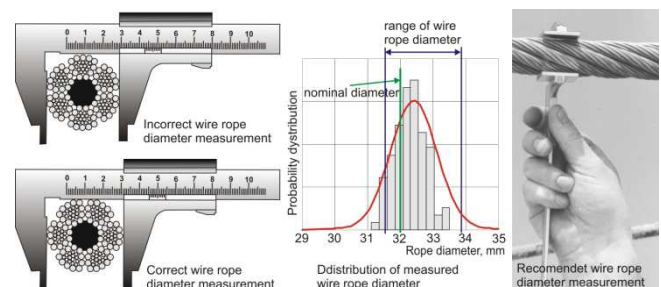

Fig. 1. Correct and incorrect method of rope diameter measurement

Typically, a measuring tape is used. There are also methods of determining pitch length on the basis of signal frequency analysis in magnetic rope testing (MRT), but such methods do not allow simultaneous instrument-aided measurement of the diameter

(Kowalski et al., 2009; Tytko, 2003). To date, there has not been a good and simple measuring method which would enable continuous and simultaneous measurement of stroke length and diameter of the rope. A method of continuous measurement of those two parameters that is simple to interpret, in addition to diagnostic applications, is of great operational significance. Both parameters significantly affect the durability and service life of ropes and associated components. This is illustrated in Fig. 2, which shows the effect of changing the diameter of the rope on its fatigue life in the context of dimensions of the collaborating rollers and pulleys. Monitoring of rope diameter would allow rational use of ropes working in pulley systems.
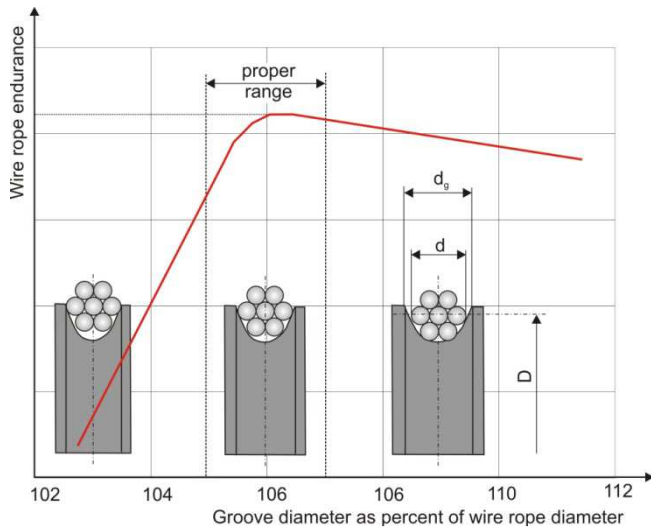

Fig. 2. The effect of rope diameter on its fatigue life

As outlined above, there is a reasonable need to supplement the non-destructive testing methods with new ones, allowing continuous measurement of the diameter and pitch length. Among the many possible concepts, methods based on spatial visualization (model construction) of the rope seem to be most promising. Below, such a method and its advantages are presented. From the viewpoint of diagnosing steel wire ropes, it is a totally new concept because it allows not only to obtain an image of the external surface of the rope, but also to determine the diameter and pitch length of the rope on the basis thereof.

That method certainly belongs to visual testing (VT) methods and would complement the magnetic rope testing (MRT) method, especially where the latter is ineffective. This applies to steel wire ropes that do not reveal wear processes in the form of massive losses (corrosion, fretting and abrasion) and fatigue, and to a very large class of ropes made of artificial and natural fibres. That class of ropes is becoming more frequently used in areas where only steel wire cables were used previously. The presented method is currently the only proposed instrument-aided method for the evaluation of fibre ropes, in addition to the classic method of visual assessment.

2. CONFIGURATION AND RESOLUTION OF THE 3D VISION SYSTEM

Construction of a three-dimensional model requires proper configuration of the vision system and structural lighting to enable

separation and reading of the data about the height of the profile of the tested rope components on the image in the camera. In order to conduct that task, a number of operating parameters of the checkpoint and of the vision system itself need to be determined (Kowal and Sioma, 2010, 2011; Gawlik et al., 2004). Measurement and evaluation of rope parameters should be carried out continuously along the entire length of the rope. This will enable assessment of the changeability in the determined parameters along the length of the rope and make it possible to assess changes in the selected parameters during operation of the rope.
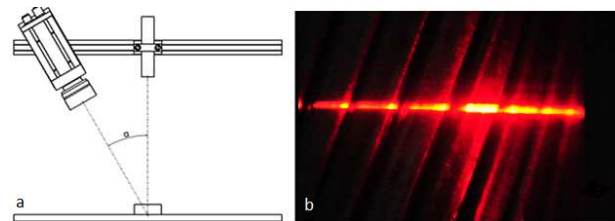

Fig. 3. Sample geometry of a 3D vision system and view of the laser line illuminating the rope

An example of 3D vision system geometry may be such an arrangement, as shown in Fig. 3, in which the laser plane is perpendicular to the axis of the rope. Optical axis of the camera is then inclined at angle α to the plane of the laser. Optical axis is the straight line passing through the centre of a camera's optical components and sensor (e.g. CCD) (Sioma, 2010, 2011a, b; Sioma and Struzikiewicz, 2011).

As a result of using such geometry, the plane of the cross-section of the object seen in the camera and produced by the laser beam is parallel to axis "Z" in the coordinate system of the test station, i.e. laser axis. Such a profile requires conversion of the geometry of the cross-section in the image created by the laser beam in order to obtain an actual three-dimensional cross-section, and then a three-dimensional image of the tested object.

In the next stage of vision system configuration, it is necessary to set the vision system resolution in the adopted configuration. As a result of change in object height, the laser line image moves on the CMOS camera sensor. Designation of vision system resolution consists in determining such minimum change in object height at which the laser image moves exactly by one row of pixels on the sensor. This is shown in Fig. 4.
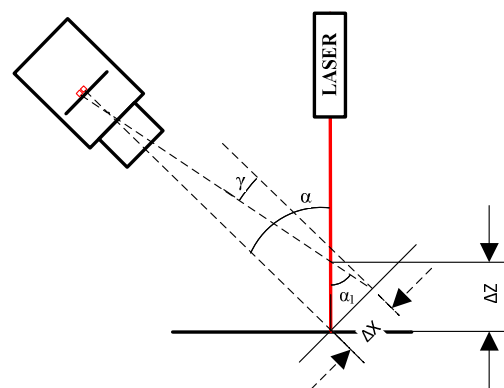

Fig. 4. Designation of the resolution of a vision system

Resolution ΔX in a plane parallel to the plane of the the sensor is determined based on the dimensions of the field of view and sensor resolution given in pixels in axis X. Resolution ΔY in axis Y is defined as the distance between the successive height profiles acquired on rope surface.

3. MEASUREMENT OF SELECTED ROPE PARAMETERS

For the inspection of selected rope parameters, a vision system was prepared to allow testing both in laboratory and typical working conditions. View of the station is shown in Fig. 5.
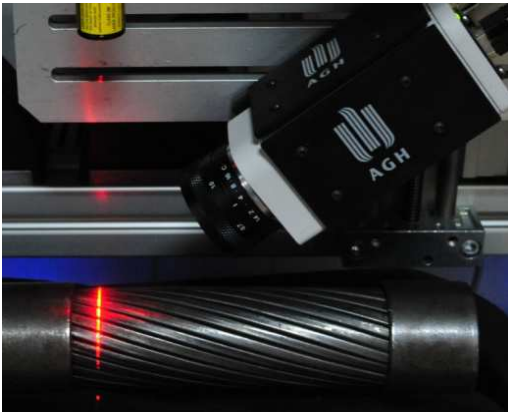

Fig. 5. View of the test station

The vision system receives an image on a monochrome CMOS sensor. Based on the sequence of images collected, height profiles of the tested object are determined in the successive cross-sections in accordance with the above-described resolution. Parameters of the vision system and the optical system are chosen in such a way that the image shows a trace of the laser line. It is also important that in the event of accidental reflection of laser light from rope surface, the trace of that reflection is not visible on the image. Based on parameters selected in such a way, successive images are acquired. Then, they are translated into a height profile to create successive cross-sections of the three-dimensional image.
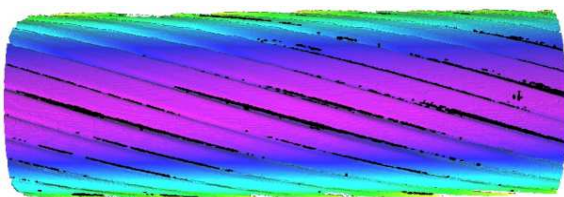

Fig. 6. 3D image of a locked-wire rope with "Z" wires in the outer layer

Both in the case of 3D profile and 3D image, there are distortions of the image resulting from both the geometry of the system as well as from the improper laser light reflection from the surface of the rope. This is shown by the example in Fig. 6. As a result of occlusion, the value of some of the points forming the 3D model of the object is equal to 0. As a result of laser light reflection from the edge of the object, the image shows interferences in the form of "height profile peak". Such an image must be pre-processed prior to any measurement procedures. The purpose is to remove any "false" measurement points. Fig. 7 shows an image after

smoothing filtering using a structural element – a 3x3 sensor. However, it should be pointed out that in case of using the smoothing procedure, the height of "peaks" appearing in the image has an impact on the value of points in their vicinity. In addition, the plane passing through its axis was determined for the image of the rope. That plane is used as a reference plane in the measurements made on the image.
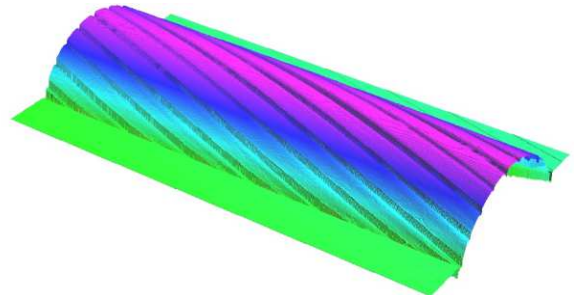

Fig. 7. Rope image after filtering

The presented method was used to measure the pitch length of the outer layer of a sample rope. Three-dimensional image was processed to determine the edges of strands forming the surface of the rope (Fig. 8a). The measurement was made by determining the distance between the edge of the same strand in the outer layer of that rope. The entire procedure was conducted for a twisted locked-wire rope with 23 wires in the outer layer. Pitch length was assessed on a continuous basis in order to determine the maximum, minimum and average length of the pitch along the rope.
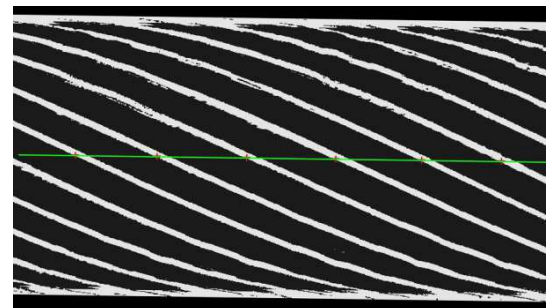

Fig. 8. Measurement of rope pitch length using an image of the edges of rope strands

The system is also equipped with a HMI, shown in Fig. 9, which enables presentation of the results of measurements and collection of measurement history for the purposes of follow-up documentation. Successive measurements of the pitch length of the outer layer of the rope are stored in a database and then processed and presented to the operator.

Fig. 9. Presentation of the result of rope pitch length measurements

Another parameter determined in the three-dimensional image of the rope is the diameter, as shown in Fig.10.
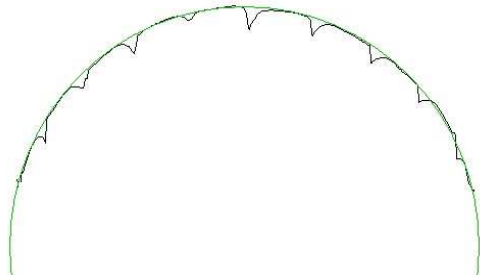

Fig. 10. Image of the cross-section of a locked-wire rope with "Z" wires in the outer layer

The diameter is measured in cross-sections spaced along the rope at distances of about 5 mm. On such a cross-section, a set of radii distributed over the profile every 1° was determined. Next, the maximum, minimum and average radius was determined for the tested cross-section. Rope diameter is determined as the diameter of the circle circumscribed on the profile shape and is calculated using the maximum radius. An image of the cross-section shows the shape of the outer layer of the rope and a circle representing the diameter determined.

Analysis of measurements allows determination of the average, maximum and minimum value for the tested ropes. It is also possible to promptly locate points on the rope that show a deviation from the limit values (e.g. permissible diameter tolerances) adopted for that type of rope.
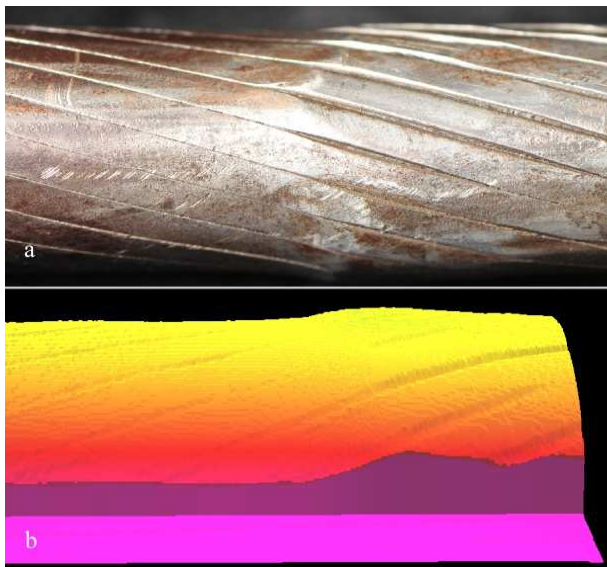

Fig. 11. View of rope section where a change in diameter was detected: a) view of rope, b) 3D image of rope surface

In the course of the study, an algorithm to detect defects on the surface of ropes was also developed. Some of the defects can be detected by measuring the diameter. A change in the diameter describes rope wear as presented in Fig. 11. However, defects associated with wire cracks should be controlled in a different way. For the purpose of such tests, an algorithm was prepared to detect continuity of the components making up the rope. Fig. 12 shows an example of a detected defect in the form of ruptured wire.
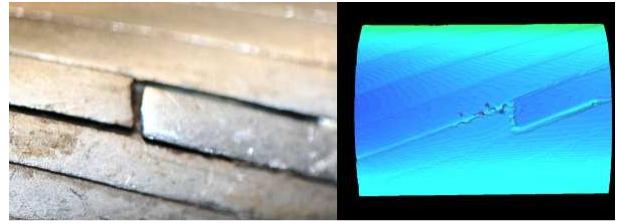

Fig. 12. View of ruptured wire in the outer layer of a FLCR-type locked-wire rope

4. SUMMARY

The above method, apparatus, and algorithm used for three-dimensional rope surface imaging with a laser warrants the following conclusions:
- it is possible to measure the length of rope pitch on any section of the rope;
- it is possible to measure the diameter on any section of the rope;
- the rope surface images obtained and the algorithms developed allow automatic identification of certain forms of damage and wear occurring on the surface of the rope;
- a sequence of diameter and pitch length values as measured along the rope allows for their registration as two additional diagnostic signals;
- recording of the results in computer memory or other storage media allows comparison of the individual parameters and changes therein in the rope service life function;
- the results of measurements obtained so far indicate that their accuracy is much higher than the accuracy of the current visual methods of measuring the geometrical characteristics of steel ropes.

It is expected that industrial implementation of a device for laser imaging of rope surface using a 3D method would allow the use of such a method as a supplement to the currently used magnetic rope testing and visual testing in the following applications:
- assessment of rope condition in hard-to-reach pulley systems, working port cranes, mining machines, off-shore equipment, etc.;
- replacement of visual assessment of the carrying ropes of cable railways with instrument-aided assessment using 3D imaging methods;
- supplementation of magnetic rope testing of all ropes with continuous measurement of diameter and pitch length;
- application of the 3D imaging method to assessment of the condition of ropes made of synthetic and natural fibres.

REFERENCES

1. **Bednarczyk J., Sioma A.** (2011), Application of a visual measurement technique to the assessment of electrodynamic stamping, *Solid State Phenomena*; Control engineering in materials processing, Vol. 177, 1–9, 20.

2. **Gawlik J., Ryniewicz A., Sioma A.** (2004), The strategies and methods of measurement in multifunctional quality inspection, *8th In-*

ternational Symposium on Measurement and Quality Control in Production, Erlangen, MEASURE AND QUALITY CONTROL IN PRODUCTION Book Series: VDI BERICHTE Vol. 1860, 649-662.

3. **Kowal J., Sioma A.** (2009), Active vision system for 3D product inspection: Learn how to construct three-dimensional vision applications by reviewing the measurements procedures, *Control Engineering* USA, Vol. 56, 46-48.

4. **Kowal J., Sioma A.** (2010), Metoda budowy obrazu 3D produktu z wykorzystaniem systemu wizyjnego [Construction of a 3D image of a product using a vision system], *Acta Mechanica et Automatica*, Vol. 4. No. 1, 48–51.

5. **Kowalski J., Nowacki J., Tytko A.** (2009), *Discard criteria for modern ropes in some applications*, OIPEEC Conference, Stuttgart.

6. **Sioma A.** (2010), Zastosowanie systemów wizyjnych 3D w kontroli jakości wykonania elementów pneumatyki i hydrauliki [Using 3D vision systems in the quality inspection of pneumatic and hydraulic components], *Pneumatyka*, No. 1, 27–30.

7. **Sioma A.** (2011a), Modelowanie i symulacja realizacji procesu technologicznego [Modelling and simulation of processes], *Mechanik* miesięcznik naukowo-techniczny, No. 12, 990.

8. **Sioma A.** (2011b), Projektowanie CAD z wykorzystaniem danych z systemu wizyjnego [CAD design using data from a vision system], *Mechanik* miesięcznik naukowo-techniczny, No. 12, 990.

9. **Sioma A., Struzikiewicz G.** (2011), Pomiary głowicy frezowej z wykorzystaniem systemu wizyjnego [Milling head measurements using a vision system], *Świat Obrabiarek*, No. 9-10, 8-10.

10. **Tytko A.** (2003), *Eksploatacja lin stalowych* [Utilization of steel wire ropes]. Wydawnictwo Naukowe „Śląsk", Katowice – Warszawa 2003.

11. **Tytko A., Sioma A.** (2011), Evaluation of the operational parameters of ropes, *Solid State Phenomena*, Control engineering in materials processing, Vol. 177, 125–134.

ADAPTATION OF CLASSIC COMBUSTION ENGINES TO COMPRESSED AIR SUPPLY

Wojciech SZOKA[*], Dariusz SZPICA[**]

[*]Phd student, Department of Machine Construction, Department of Mechanical Engineering,
Bialystok University of Technology, ul. Wiejska 45 C, 15-351 Białystok, Poland
[**]Department of Machine Construction, Department of Mechanical Engineering,
Bialystok University of Technology, ul. Wiejska 45 C, 15-351 Białystok, Poland

wojt1983@wp.pl dszpica@pb.edu.pl

Abstract: This paper presents the issue of the construction and operation of the pneumatic piston engines. We analyzed different options for design solutions, as well as their applicability. It proposes its own solutions based on reciprocating internal combustion engines JAWA 50 and FIAT 126P, which was obtained during the adaptation of two-stroke engines air. The first attempts were successful operation. We showed the process of adaptation each of engines, their specifications and set the scope for further work related to the improvement of operational characteristics, as well as guidelines for developing a mathematical model of action.

Key words: Mechanical, Compressed Air Engine, the Design

1. INTRODUCTION

Declining resources of the fuel in the ground, tend to search for new fuels or new design of internal combustion engines, which will use the existing fuel liquids, gases or solid fuels.

On the other hand, the gradual reduction of the emission levels of harmful emissions emitted by internal combustion engines, forced the designers to increase the efficiency of energy conversion resulting from combustion into mechanical work, the use of all types of treatment systems as well as the composition of hybrid systems (1999/125/EC.OJ L40, No 2000/303/EC.OJ L100).

In hybrid systems (drive line system, where are working together two different power sources), classically used in internal combustion engines connected to electric generators, which in effect are able to power the electric motors placed on the wheels of the vehicle. At present, internal combustion engines are used independently to generate electricity only, without direct participation in the generation of torque to the wheels (www.elektroenergetyka.org/6/46.pdf).

Hybrid systems can also use the energy contained in compressed air, which through an appropriate system will be processed on the torque driving of the generator. The simplest way to use compressed air is to use the classic internal combustion engine with modifications. The essence of this solution is that the compression of air outside of the external compressor, could occur during vehicle braking by compressor system mounted in the vehicle (recuperation).

2. REVIEW OF EXISTING CRANK SYSTEMS

There are many coverage about use of the working medium which is compressed air. A very large part in this area are structures designed for drive models, especially flying. There are also more advanced constructs used to drive small cars, trucks and small sports vehicles. Below are some constructions of pneumatic engines differ in construction, as well as the degree of sophistication.

2.1. Classic Layout of Crank System

In solutions used in models (Fig. 1), the working medium from source of gas is supplied by ball valve into the cylinder. Conversion of the energy to power is done by work carried out is using classical cranks. In this case, the engine can be considered two-stroke. The advantage is simplicity of construction, disadvantage and the portion of the work lost for combustion residues in air after departure.
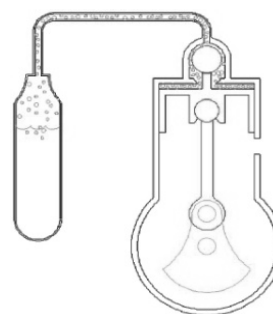

Fig. 1. Classic crank system (www.darmowa-energia.eko.org.pl/pliki/ekoauto/spr_pow.html)

Adaptation of the classic cranks system have got the need to take account of the less energy density at which the compressed air supplies engine, through the ball valve with the specified bandwidth in relation to energy density resulting from the combustion of a combustible mixture inside the cylinder.

Based on the construction shown in Fig. 1, we can duplicate the solution to consecutive cylinders, resulting in the formation for example of the design of 4-cylinder engine, covering smaller fluctuations of speed (Fig. 2).
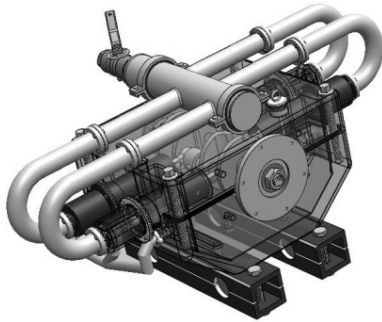

Fig. 2. The boxer engine (Gosk, 2008)

2.2. The Layout with the Split Crankshaft Made by MDI

Because of the considerable differences in the density of energy both sources, which is the compressed air and combustible mixture, constructors attempted to extend time of piston being in "out-crank" position, to enable it to increase the degree of filling the cylinder with compressed air, which is directly converted to work (with minor losses at expansion in relation to the classical crank layout).

The latest solution used in pneumatic piston engines, is the system with split crank made by company MDI also known as Nègre engine (Fig. 3), which provides momentary stop of the piston in the upper extreme point. Drawback of this solution is that the piston and crankshaft doesn't lie in one plane, which increases the size of the engine and problems with mounting it in cars with small space. Another problem is the presence of significant accelerations during expansion and compression stroke, and thus inertia forces, not leaving without effect on the consumptions cooperating pairs and strength of construction.
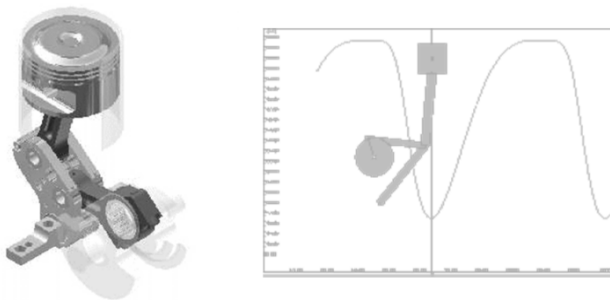

Fig. 3. The layout with the split crankshaft
(www.engineair.com.au/development.htm)

MDI company constructed engine in such a way, that it can work in the opposite direction, as a compressor, because the is engine-alternator mounted on gearbox. Composite tanks can be filled by air in two ways: either from the station where is previously compressed air-refuelling is only about 3 minutes, or by plugging the car into electric plug in your wall – then engine-alternator is working as an electric motor and drives pneumatic engine of the car, which is working as a compressor. Such a way of fuelling

to full is about 4 h, but this vehicle is not totally dependent on the station with compressed air.

2.3 Angelo Di Pietro Engine

His own concept of pneumatic Wankel engine developed Angelo Di Pietro. The engine he design (Fig. 4) reminds one of the many developed by F. Wankel, except that the working factor here is compressed air, that moves the blade. Originally Wankel foresaw it as internal combustion engine.
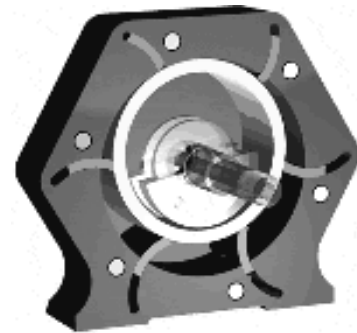

Fig. 4. Angelo Di Pietro engine (www.rexresearch.com/pietro/pietro.htm)

The modernization included also inlet and outlet channels. Di Pietro engine demonstrated significantly less use of components, because there is no combustion and there is less demand for the working factor (compressed air).

2.4. Modified Wankel Engine

In order to adapt the Wankel engine to work on compressed air, the timing system has been redesigned by modifying valve timing and inlet and outlet valve profile (Fig. 5). Presented solution is only a concept that require construction of the prototype and experimental studies.

Opening of the first exhaust window is 6° before closing the intake (Fig. 5e). The chamber is connected to the exhaust channels including by 226° rotation of the engine crankshaft. At the end of the exhaust phase, there is again 5° cover phases of filling and emptying by second outlet window. Exhaust phase was divided in to two parts due to the need to strengthen the head of the engine.
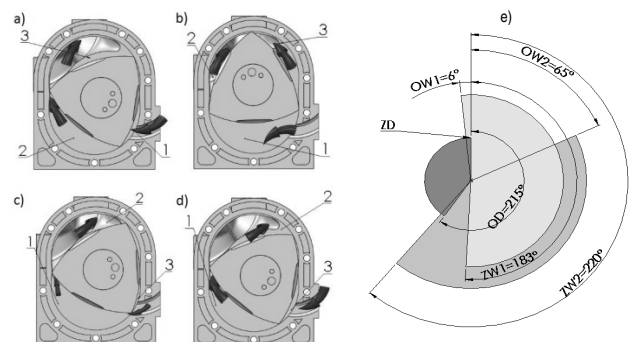

Fig. 5. Modified Wankel engine: a, b, c, i d – phases of load Exchange, e – circular graph of timing phases (Mejlun et al., 2011)

2.5. Crankshaft System with Elongated Expansion Stroke

Another proposal is the design of the engine with elongated expansion stroke (Fig. 6). Its construction is based on the prototype crankshaft system providing temporary immobilization of piston in the upper extreme point, which in the case of using it as energy source of compressed air, it boosts the efficiency of the engine.
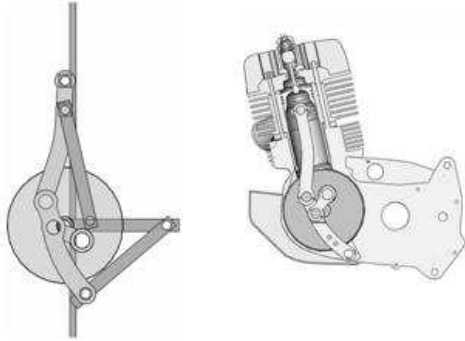

Fig. 6. Crankshaft system with elongated expansion stroke, comparison passes of specific values of concept and classical engine (Jaszuk, 2008)
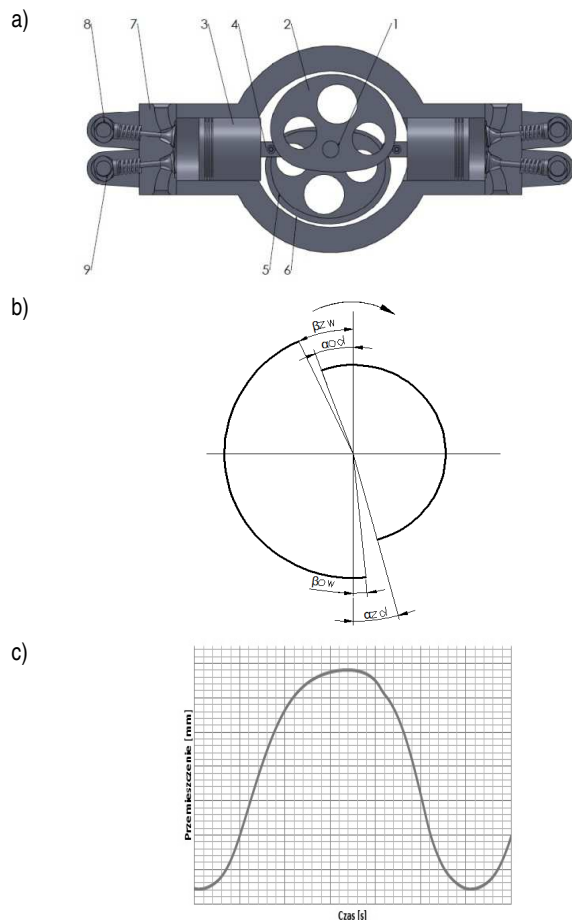
2.6. Cam Engine

Fig. 7. The concept of cam engine: a – construction schema, b – timing phases: $\alpha_{od}=20^o$ – open angle of intake, $\alpha_{zd}=15^o$ – close angle of exhaust valve, $\beta_{ow}=5^o$ – open angle of exhaust valve, $\beta_{zw}=25^o$ – close angle of exhaust valve; c – piston movement at function of time (Mejlun et al., 2011)

In the cam engine crankshaft system is replaced by twin-roller cam with the pusher. Similarly, as the Nègre engine (in this case, through appropriate relief camshaft) it is possible to temporary immobilization of piston in the upper extreme point (Fig. 7c).

The conceptual solution (Fig. 7a) is a four-cylinder, double-breasted engine and cylinders in opposite position, where the classic crankshaft was replaced by the shaft with cams (1). Cam (2) drives the special design piston coupled with crankshaft (3) through double-breasted pusher (4). Cam is built with two cams (internal (5) and external (6)), on which roller of pusher moves. Both cams have been designated with different equations. That's because of unchanging position of rollers relative to each other while working. Over the head (7) are camshafts, intake (8) and exhaust ports (9) of cams with different work angle. Such arrangement will be working according to the timing phases shown in Fig. 7b.

3. TECHNICAL CHARACTERISTICS OF THE OBJECTS OF ANALYSIS

In the first place two stroke engine from JAWA 50 has been adapted to work on compressed air. Directory data of engine JAWA 50 is shown in Tab. 1.

The design required a modification of the timing, where in place of the original solution of slot-piston system, appeared intake controlled by ball valve developed within the original devices of the spark plug.

The next design is based on the four stroke engine from the FIAT 126P 650. Technical data is shown in Tab. 2.

Tab. 1. Technical characteristics of the base engine and the modified JAWA 50

Parameter/Indicator	Base	After adaptation
Engine	Two stroke. one cylinder	
Engine capacity	49.9 cm³	
Compression ratio	9:1	-
Maximum power	2.6 BHP	b.d.
Cooling	a free flow of air	
Diameter of cylinder	38mm	
Travel of the piston	44mm	
Rotational speed of idling	1100 rpm	300 rpm
Camshaft system	Slot-piston	Slot-piston + cams

Tab. 2. Technical characteristics of the base engine and a modified FIAT 126P 650

Parameter/Indicator	Base	After adaptation
Engine capacity	652 ccm³	
Operating cycle	4-stroke with spark ignition	2-stroke
Number of cylinder	2	
Diameter of cylinder	77 mm	
Ravel of the piston	70 mm	
Compression ratio	8:1	-
Maximum power	24 BHP	bd
Rotational Speer of idling	850 rpm	120 rpm
Camshaft system	Uppercam system, camshaft mounted In engine block, chain drive	

4. DESCRIPTION OF THE NECESSARY MODIFICATIONS AND EFFECTS

4.1 Adaptation of JAWA 50 Engine

As a base was taken the engine blocked with clutch and gearbox from JAWA 50 engine. Maintained without change gearbox, engine shaft with bearings mounted in gearbox block and connecting rod and cylinder.

Fig. 8. Modified head of JAWA 50 engine: 1 – middle part, 2 – base, 3 - cover

In the course of modification, the fundamental change is the head of the engine (Fig. 8) with innovative timing layout, which, in the lower part is matched to the original cylinder of JAWA 50 engine. At the top there is a socket for a steel ball, acting together with the valve controls the intake of compressed air. The middle part (1) is a tray for compressed air just before returning it to the cylinder. There is also a spring which pushes the ball to the base (2). Spring has its mainstay in the basis (2) and the cover (3). In addition, there is universal connector mounted to the lid (3) to the power cord.
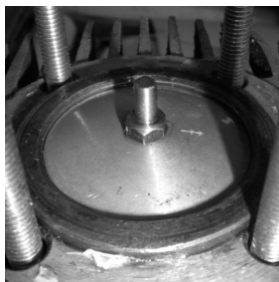

Fig. 9. Modified piston from JAWA 50 engine

The original piston have been modified (Fig. 9). In the center of the piston now there is the spindle, which during filling, raises a steel ball and the compressed air is injected into the cylinder to perform work.

The cycles of this one cylinder JAWA engine is shown by using the model engine (Fig. 10).

When the piston is at the top position (Fig. 10a) its spindle opens the ball valve, the compressed air fills the space of cylinder. The air exerts pressure on surface of the piston, causing its movement down and rotate the crankshaft (Fig. 10b). The valve closes when piston is moving down, but the air is still expanding and exerts a force on the piston. In the lower turning point (Fig. 10c) piston is opening outlet window and releasing air outside. The shaft is starting to move by inertia (Fig. 10d) then pushes the piston to the top and closing the off window. In the cylinder

are small amounts of air, so the piston moves upwards until it will again open the ball valve and the cycle repeats.
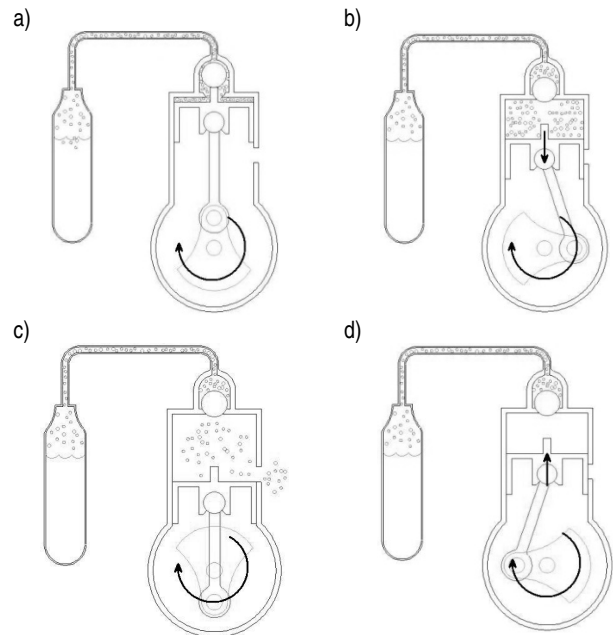

Fig. 10. Work of the model pneumatic engine (www.darmowa-energia. eko.org.pl/pliki/ekoauto/spr_pow.html)

After the prototype was made, there were few initial starts of an engine, which ended successfully. When air pressure approx. 4 bars, there were noticeable sounds of air escaping between the individual parts of the head, which require additional seals. It needed also regulation eject of mandrel mounted on top of piston. After the fixes and reconnecting compressed air, there were achieved speeds in a wide range of work, less vibration against a variant of combustion engine resulting from the absence of cyclic explosions in the combustion chamber.

4.2 Adaptation of FIAT 126P 650 Engine

As the base of the next adaptation was used the engine from the FIAT 126P with engine capacity of 650cm ^{3} (Fig. 11).

Fig. 11. The modified engine FIAT 126 650cm³

Many of serial parts has been dismantled, making the engine lighter and smaller. It was necessary to make a modifications in key parts of the engine. In the engine, circulation of the compressed-air was inverted, outlet channels became the inlet and inlet channels became outlet ones. Also camshaft has to be changed (Fig. 12). The angle between the axis of the inlet and outlet cam in the serial camshaft is 120°. In the compressed-air engine inlet and outlet cam are placed opposite each other, so the angle between them is 180°.

Fig. 12. The modified camshaft with cams placed opposite

As a result of the modifications, it was necessary to transit the cycle of engine from 4-stroke to only two-stroke, hence the use of 1:1 ratios in the drive shaft timing (Fig. 13).
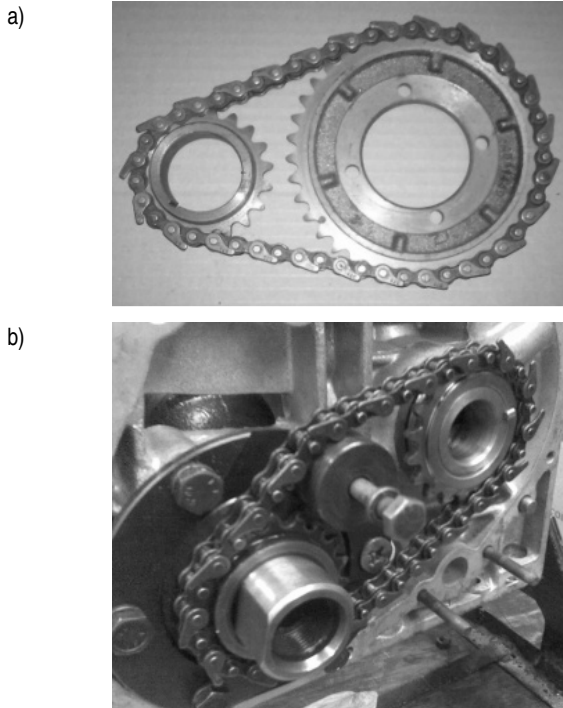
a)

b)

Fig. 13. Drive shaft timing system: (a) original, (b) modified

The operating cycle of the modified engine FIAT 126 is following. Compressed air through the open intake valve (originally outlet) is filling cylinder and pushes the piston down, doing the work. At the end of work stroke air goes out through the outlet valves (originally inlet) on the outside of the engine.

The first tests have shown that the engine is running from the air pressure of 2 bars. Maximum air pressure on which engine worked was 8 bars. Rotating speed of crankshaft, in this case, as like in JAWA engine is regulated by ball valve for regulating flow of mass air to intake. Engine oil system remained unchanged. Interesting is the fact that in the case of compressed-air engine it's possible to get the air conditioning system based on process of expansion in air from the exhaust and the associated pressure drop.

5. APPLY OF THE MODIFY FIAT 126P 650 ENGINE

The first vehicle, in which the modified FIAT 126 engine was provided to be assembly is the tube type vehicle SAM (Fig. 14).

The first tests have shown that the modifications was correct. There are works going on with mounting tank with compressed air and the necessary equipment in the vehicle.

After the tests and road trials will be completed, the engine will be dismantled and its parts taken to verification in order to designate their consumption. This will allow further modifications to increase the usage possibilities.

Further provides for the examination of the engine on rolling road (or dynamometer) to determine the values of the external indicators at variable pressure, indicating the area of the modification phases of timing.
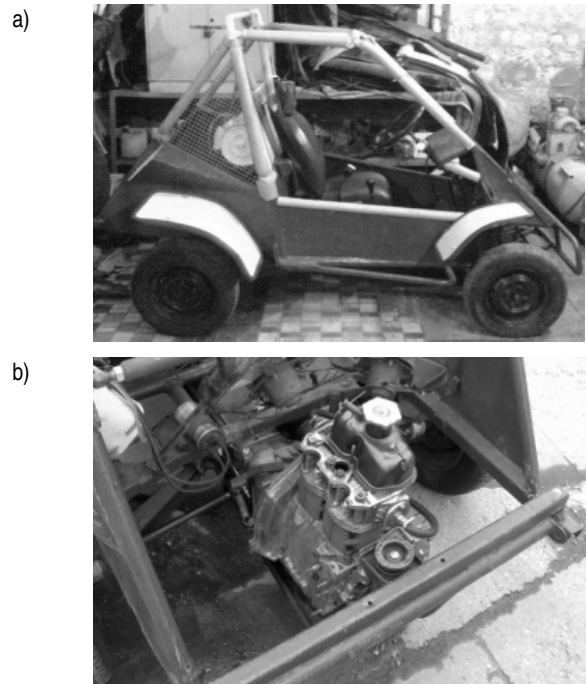
a)

b)

Fig. 14. Vehicle type Buggy in which will be mounted an engine on the compressed air

In parallel with the experimental, will be build a mathematical model of functioning pneumatic engine in Matlab-Simulink. During process of modeling will be used finite element method proposed by Miatluk and Avtuszko (1980) and have been successfully used with modeling of pneumatic braking systems (Miatluk, 2003), and air supply systems of internal combustion engines (Szpica, 2008; Szpica, 2009). To describe the phenomena will be used the descriptions set out in (Bossel, 2010), and verification will be a function of flow Miatluka-Avtuszko against the commonly-used.

As the end result is planned to verify the mathematical model with the results of the experimental in the pressure area changes in the cylinder in different conditions of loads.

6. APPLICATIONS

By making the necessary modifications it is possible, as it has been shown in the article, to adopt classic engines to work in the

two-stroke cycle on compressed air. In addition, the use of compressed air as a source of energy, due to the absence of explosions of combustible mixture, as it's in the combustion engine, results in smaller vibrations power unit, which however would reflect negatively on the values of generated torque. Proposed guidelines for the construction of a mathematical model describing work of the pneumatic engine, which intends to be present in subsequent publications.

REFERENCES

1. **Bossel U.** (2010), *Thermodynamic Analysis of Compressed Air Vehicle Propulsion*, European Fuel Cell Forum, Morgenacherstrasse 2F, CH-5452 Oberrohrdorf/Switzerland.
2. **Gosk M.** (2008), *Konstrukcja silnika pneumatycznego*, praca inżynierska pod kierunkiem pod kierunkiem D. Szpicy, Politechnika Białostocka, Białystok, 2008.
3. **Jaszczuk B.** (2008), *Projekt silnika napędzanego sprężonym powietrzem*, praca magisterska pod kierunkiem D. Szpicy, Politechnika Białostocka, Białystok.
4. **Mejlun M., Jaworski B., Szpica D.** (2011), *Adaptacja nietypowych rozwiązań silników spalinowych do zasilania sprężonym powietrzem*, XXX Seminarium Kół Naukowych "Mechaników", Warszawa, 52.
5. **Miatluk M. F., Avtuszko W. P.** (1980), *Dynamika pnievmatičeskich i gidravličeskich privodov avtomobiliej*, Izd – wo Maszinostrojenije, Moskva.
6. **Miatluk M., Kamiński Z., Czaban J.** (2003), Characteristic features of the airflow of pneumatic elements of agricultural vehicles, *Commission of Motorization and Power Industry in Agriculture*, Vol. 3, 174-181.
7. **Szpica D.** (2009), Flows tests of an air controlling throttle body in a spark ignition engine, *Combustion Engines*, Nr 2, 12-18.
8. **Szpica D.** (2008), The assessment of the influence of temperature differences in individual ducts of an intake manifold on the unevennes of air filling in a cylinder of a combustion engine, *Combustion Engines*, Nr 2, 44-53.
9. **EU Directives** No 1999/125/EC.OJ L40 i No 2000/303/EC.OJ L100.
10. www.darmowa-energia.eko.org.pl/pliki/ekoauto/spr_pow.html
11. www.engineair.com.au/development.htm
12. www.rexresearch.com/pietro/pietro.htm
13. www.elektroenergetyka.org/6/46.pdf

THE INFLUENCE OF RIVETING PROCESS ON SHEETS FATIGUE LIFE – THE STRESS STATE ANALYSIS

Elżbieta SZYMCZYK[*], Jan GODZIMIRSKI[**]

* Department of Mechanics and Applied Computer Science, Faculty of Mechanical Engineering
** Institute of Aviation Technology, Faculty of Mechatronics and Aeronautical
Military University of Technology, ul. Kaliskiego 2, 00-908 Warszawa, Poland

eszymczyk@wat.edu.pl, jgodzimirski@wat.edu.pl

Abstract: The paper deals with estimation of a stress concentration factor in the hole area during tensile loading. The load carrying capacity and fatigue performance of sheet samples (made of 2024 aluminium alloy) with open and riveted holes are compared. Tests confirm the insignificant influence of riveting on ultimate strength, however, it strongly affects fatigue life. The material cold working around the hole causes a decrease in maximum principal stress values as well as stress concentration moves away a few millimetres (about half a rivet radius length) from the hole. During tensile loading the maximum stress values increase slower around the riveted hole than at the open one and consequently in the former case the yield stress is achieved later.

Key Words: Riveted Joints, Residual Stress States, FEM Analysis

1. INTRODUCTION

The object of analysis are riveted joints used in aircraft structures to fasten skins with the frame. High-strength aluminium alloys 2xxx (with copper) or 7xxx (with zinc) are thought of as the aircraft alloy because of their strength and excellent fatigue resistance however the copper content makes them extremely difficult to weld. The tens or even hundreds of thousands rivets used in a typical aircraft structure have a significant influence on the service life and this is the reason of the last decades research concerning fatigue performance improvement.

The load carrying capacity and fatigue resistance of riveted joints depends on many structural, manufacturing and material factors (Szulżenko and Mostowoj, 1970; Godzimirski, 2008; Matwijenko, 1994; Jachimowicz and Wronicz, 2008) like: connection type (overlap or butt, symmetric or asymmetric), size, rivet pitch and spacing (distance between rivets and rivet rows), sheet thickness, diameter of rivet shank and rivet type (i.e. universal, mushroom or countersunk). The most advantageous stress states occur for symmetric joints (where uniaxial or biaxial tension is dominant). Unfortunately, they can be rarely used in practice. The non-symmetric joint is very unfavourable because of eccentric tension (secondary bending). The secondary bending influence is estimated by comparing maximum bending stress in the concentration area with the nominal stress in the reduced section or with local tension stress. In the paper a uniaxial tension of the sheet with an open and riveted hole are analysed. The values and fields of principal stress obtained for this case provide a base of more accurate evaluation of the other factors (e.g. secondary bending) influence on fatigue life.

The manufacturing factors include mainly: a method and quality of riveting (hole drilling, finishing the edges, concentricity of holes in joining sheets and rivet squeezing) (Gruchelski et al., 1969; Godzimirski, 1998; Szymczyk and Jachimowicz, 2007; Szymczyk, 2010; Deng and Hutchinson, 1998; Muller, 1995; Rans, 2007). Static cold riveting (with a press) or dynamic (with a pneumatic hammer) are used to assemble components of an aircraft fuselage. A residual stress state in the joint results from the riveting process. Despite local exceeding of the yield stress, it has a profitable influence on fatigue performance. In this paper the influence of residual stress (regarding the various magnitude of squeezing force) on the stress fields during tensile loading is analysed.

The calculations are performed for sheets with open holes and riveted ones. Two types of the hole shape are analysed: cylindrical one and with a conical socket for a countersunk (flush) rivet. Countersunk rivets are used for external surfaces of an aircraft, which airspeed is higher than 300 km/h, in order to reduce aerodynamic resistance. The theoretical case of symmetric squeezing is analysed for the sheet with a cylindrical hole to obtain the most profitable - uniform stress distribution around the hole (Abibow, 1982). The actual stress state is nonuniform; higher values of stress are in the sheet on the driven rivet head side (Szymczyk, 2010; Rans, 2007).

For an aircraft purpose sheets of thickness from 0.6 mm to 4 mm are used. In the paper a sheet of 2 mm thickness and rivet of 4mm diameter (mushroom and countersunk) are analysed. Aluminium alloys 2024T4 for sheets and PA24 (corresponding to 2117) for rivets, widely used in aircraft industry, are undertaken in the paper. The load carrying capacity of sheets depends on rolling direction (the difference can reach 5%). This condition is not concerned in numerical models where isotropic materials are assumed.

Riveted joints are areas of stress concentrations where crack initiation of an aircraft fuselage is likely/tends to start (Rans, 2007; Kocańda et al., 2007; Howland, 1930; Hartman, 1961). The aim of this paper is analysis of stress state around the hole in the sheet with regard to rivet type and residual stresses and their influence on fatigue performance of sheets. Stress concentration magnitude is estimated in the hole area during tensile loading as a result of the numerical calculations.

2. EXPERIMENTAL TESTS

The static tension test of 2024T4 aluminium alloy used in aircraft fuselages is carried out to obtain the stress-strain curve (Fig. 1). Yield strength is of 330 MPa. The values of real stress are calculated using the experimental data (with respect to the decreasing of specimen cross section during tension) and the following well known formula: $\sigma_{rz} = \sigma(1+\varepsilon)$.
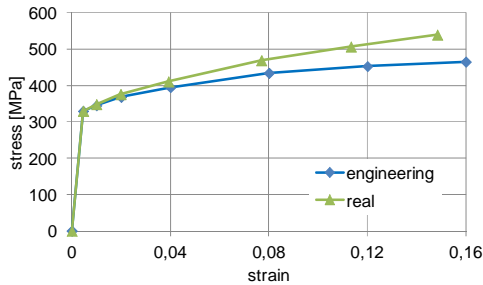

Fig. 1. Stress-strain curves for aluminium alloy 2024T4

Afterward, the sheet samples of 2mm thickness, 30 mm width and 170 mm length with centrally localised hole of 4 mm diameter are made of 2024T4 alloy. Some samples are prepared for countersunk rivets with angle of 90º [BN 70/1121-03] using a spotting drill. The load carrying capacity of such samples is estimated and compared with ultimate tensile strength of a sample without a hole. The applied tensile stress and the nominal stress in the reduced cross section for cylindrical and countersunk holes are compared in Tab. 1.

Tab. 1. The load carrying capacity for samples of 1.99 mm thickness

specimen type	without hole	cylindrical hole	hole with socket
applied stress [MPa]	445 ± 6	336 ± 12	327 ± 11
nominal stress [MPa]	445	388	394

Tab. 2. Fatigue life of samples with open holes for applied stress range of 134 MPa

sample number	hole type	number of cycles
p1	cylindrical	65 296
p2	cylindrical	77 773
p3	cylindrical	72 306
p4	with socket	63 992
p5	with socket	56 452
p6	with socket	61 264

The samples with holes are subjected to cyclic tension with an applied stress range from 3 to 134 MPa and frequency of 20 Hz. Fatigue life (number of cycles to damage) is presented in Tab. 2.

Subsequently, the samples with holes riveted using mushroom or countersunk rivets are prepared and subjected to fatigue load (Tab. 3). For all samples with mushroom rivets the crack initiation starts in a full cross section at some distance from the hole (Fig. 2). Fatigue life for samples with countersunk rivets is over three times lower than for mushroom ones, however, nearly two times higher than for samples with open holes. The cracks propagate through the reduced section in the latter cases.

Tab. 3. Fatigue life of samples with riveted holes

nr	rivet type	applied stress [MPa]	nominal stress [MPa]	number of cycles
n1	mushroom	3 … 134 3 … 200	155 232	340 000 + 255 176
n2	mushroom	3 … 167 3 … 200	193 232	276 000 + 109 883
n3	mushroom	3 … 200	232	422 000
n4	countersunk	3 … 200	242	131 046
n5	countersunk	3 … 200	242	100 680
n6	countersunk	3 … 200	242	117 863

Fig. 2. Fatigue crack of the sheet with a hole riveted with mushroom rivet

The influence of rivet squeezing on the load carrying capacity of the sheet with a hole is also examined. The results of the test are presented in Tab. 4. It is possible to observe that squeezing of the rivet has no effect on ultimate tensile strength but increases the fatigue performance of such sheets.

Tab. 4. The load carrying capacity of riveted sheets

Sample type	with mushroom rivet	with countersunk rivet
applied stress [MPa]	336 ± 8	328 ± 14
nominal stress [MPa]	388	396

3. NUMERICAL MODELS

3D numerical models of the samples described in the previous section are prepared using Patran. Finite element meshes of the rivet neighbourhood in the sheets for countersunk and cylindrical holes are presented in Fig. 3. The case of theoretical symmetric riveting is considered for a cylindrical hole to achieve the most beneficial uniform stress field in the sheet. One half of the sheet is modelled due to plane symmetry with respect to its middle surface. The rivet and sheets models consist of eight-noded, isoparametric solid elements with a tri-linear interpolation function and eight integration points. A rounded mesh shape and small elements close to the rivet holes and larger elements a bit further from the rivet region are taken into account. The calculations are carried out with Nastran and Marc codes.

The specimens are made of aluminium alloy 2024T3 used in aircraft structures and rivets are made of PA24 alloy (corresponding to 2117). The nonlinear elasto-plastic material models are taken into consideration. The stress-strain curves (obtained from a compression test of the rivet sample and tension of the

sheet one) are shown in Fig. 4. The yield value for the multiaxial state is calculated using the von Mises criterion.
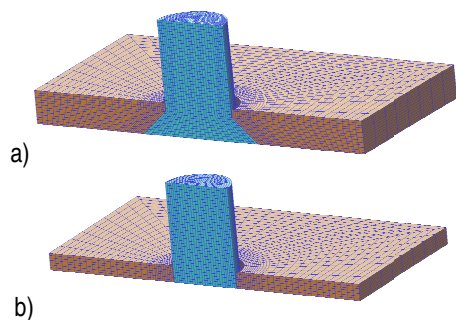

Fig. 3. Models of rivet neighbourhoods: a) countersunk hole, b) cylindrical one.
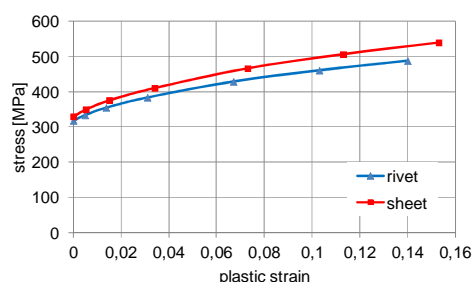

Fig. 4. Material stress-strain curves

The classical updated Lagrange formulation (with large strain plasticity option) for elastic–plastic materials is used due to large geometrical and material nonlinearities.

The riveting tools (bucking bar and punch/riveter) are described using rigid elements. Contact with friction is defined between the mating parts of the joint. The Coulomb model with trial friction coefficient $\mu = 0.2$ is used. The penalty method is applied to implement numerically the contact constraints. The contact stiffness is proportional to stiffness of mating elements and their sizes.

The iterative penetration checking approach allows changing

of the contact condition within the Newton-Raphson iteration loop. Using this procedure, the iteration process is done simultaneously to satisfy both the contact constraints and global equilibrium.

Degrees of freedom, corresponding to grip condition in the testing machine, are fixed on each end of the sheets. Additionally, in the latter model (with cylindrical hole), degrees of freedom related to the plane symmetry are fixed in normal direction.

Two steps of loading are carried out. In the first step, corresponding to the rivet squeezing, the bucking bar is fixed and punch is driving to achieve shop (driven head) diameter according to riveting standards. Afterwards, the riveting tools are removed. In the second step the sample is tensile loaded. In the case of samples with open holes only the latter step is done.

4. NUMERICAL ANALYSIS

The aim of the paper is to explain the influence of riveting on the fatigue life of the sample with a hole. The rivet affects it in two ways. The rivet as a rigid element filling the hole restricts its deformations and, as a result, limits the decreasing capacity of the diameter. Moreover, during riveting the sheet material around the hole is squeezed (cold worked) what leads to its hardening (the yield stress increase in cyclic loading). The numerical FE analysis is performed for the sheets with mushroom and countersunk rivets in order to estimate the influence of these factors on the growth in fatigue life of the sample. The material effort in terms of fatigue life is better described by the 1st principal stress than Huber-Mises equivalent stress.

In the first step, the analysis of the sheet with a cylindrical hole is performed. The comparison of a stress state for an open hole and a hole with a rivet shank set inside, both loaded with 184 MPa, is shown in Fig. 5. The calculations confirmed that filling the hole with a rivet shank (without squeezing) has a negligible influence on the maximum stress level at the rivet hole. Otherwise, material cold working around the rivet hole causes about 20% reduction of the principal stress maximum value in this area. Stress concentration still occurs in the reduced hole cross section, however, no longer takes place exactly/strictly at the hole edge.
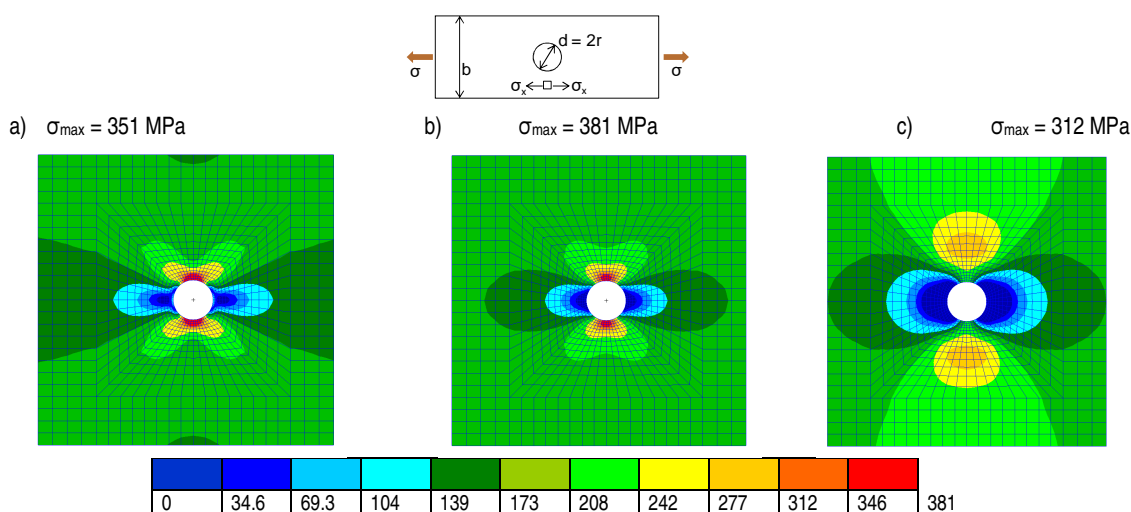

Fig. 5. Principal stress fields close to the rivet hole: a) sheet with an open hole b) with a rivet shank set inside the hole (without squeezing) c) with an upset rivet and with consideration of material hardening (residual stress state due to riveting)
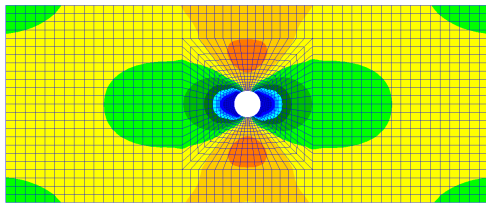
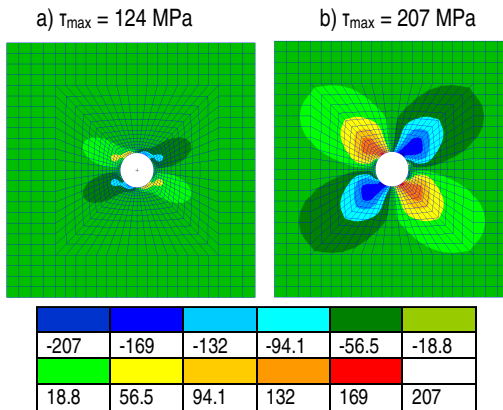**Fig. 6.** The σ_I stress field in the sample with an upset rivet (the same scale as in Fig. 5)

a) τ_{max} = 124 MPa b) τ_{max} = 207 MPa

-207	-169	-132	-94.1	-56.5	-18.8
18.8	56.5	94.1	132	169	207

Fig. 7. The shear stress fields: a) sample with an open hole b) sample with an upset rivet

a) σ_{max} = 510 MPa b) σ_{max} = 524 MPa

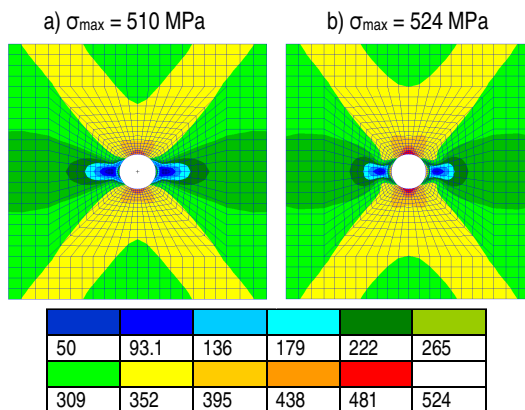| 50	93.1	136	179	222	265
309	352	395	438	481	524

Fig. 8. Equivalent stress fields: a) specimen with an open hole b) specimen with a riveted hole

The principal stress values (334 MPa) exceed the yield stress as a result of increasing applied stress to 244 MPa, whereas the stress distribution (Fig. 6) remains nearly the same as in elastic range (Fig. 5c).

The shear stress fields in the sample with the open hole and with the riveted one (for an applied stress 184 MPa) are shown in Fig. 7. Analysis of the principal and shear stress states presented in Fig. 6 and 7, respectively, leads to the conclusion that a crack tends to initiate from the specimen free edge (in the area showed in Fig. 2), especially if an existence of positive normal stresses in this area of the sample edged by milling is considered.

There are not observed any important differences in equivalent stress states between the sample with the open hole and the riveted one subjected to ultimate stress equal to 360 MPa (Fig. 8). This result is in good accordance with tests during which load carrying capacity of both samples (with an open and riveted hole) is determined to be at the same level.

The aim of the above stress analysis for the selected load levels is qualitative explaining of the increase in fatigue life of riveted samples in comparison to samples with open holes but first of all pointing out the reason of crack initiation movement from the reduced cross section.

Secondly, quantitative analysis of changes in principal stress (equal to σ_x component in load direction) is performed during tension of the sample with an open and riveted cylindrical hole. The normalised stress values (related to sheet yield stress R_e) are presented in the below figures to simplify the comparison among various models. The comparison of stress values as well as places of their concentration in the hole cross section are marked in Fig. 9.
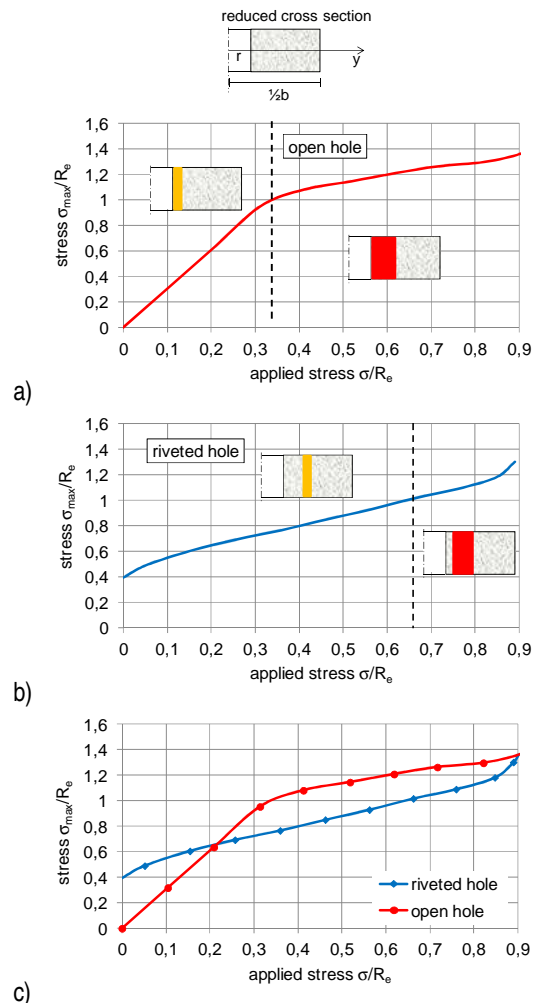

Fig. 9. Principal stress graph vs. applied stress in sheet with cylindrical hole: a) open hole c) riveted hole c) comparison
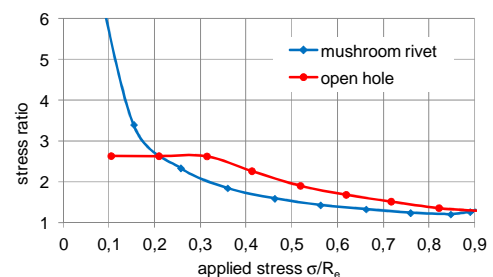

Fig. 10. Stress concentration graph for sheet with cylindrical hole vs. applied stress

The maximum principal stress values for the sheet with an open hole exceed the yield stress for applied stress of 33% R_e, while for the sheet with a riveted hole, due to residual stresses, the increase in principal stress values is remarkably slower (over seven times slower than for an open hole sample). Consequently, the yield stress is obtained for the applied stress level of 66% R_e (two times greater than in former case). The increase in maximum principal stress values (for the sheet with riveted hole) is uniform in almost the whole range of loading. The exceeding of the yield stress has no effect on the maximum stress growth rate. Only in the last stage of loading, when the hole cross section is in the plastic state (nominal stress values in this section reach the yield stress level), principal stresses change faster.

a)

b)

Fig. 11. Principal stress graph vs. thickness distance and applied stress for riveted sample: a) 4 mm from hole axis b) at the edge of the hole

Fig. 12. Principal stress graphs vs. tensile load and distance from the hole axis for riveted sample

In the elastic stage of tensioning the stress concentration (maximum stress value related to nominal stresses in reduced section) for the sheet with an open hole is equal to 2.64 and for

assumed dimensions of sheets is in very good accordance with the analytical value (Howland, 1930). After exceeding the yield stress value of the coefficient gradually decreases. The initial stress concentration value approaches infinity for a riveted sample since the nominal applied stress value is equal to zero while residual principal stress is greater than zero. The stress concentration magnitude decreases rapidly while the load increase and for applied stress of 20% R_e reaches the same value as for an open hole, then it still decreases and remains below the corresponding value for an open hole.

During tensile loading in the stress concentration area the principal stress axis is the same as load direction therefore the maximum principal stress (σ_I) is equal to σ_x component.

The principal stress (σ_x component) values for symmetrical riveting are practically constant in the whole reduced section (Fig. 11a). Small distortions only occur at the edge of the hole.

The maximum residual stress (after squeezing) occurs not at the edge of the hole but inside the sheet material, at half the radius length from the edge approximately. During tensile loading the distance from the edge to the stress concentration area even increases (Fig. 12). The stress graph on the outer surface (section AB) changes similarly to those on the middle one (section CD) but under a driven head is less regular.
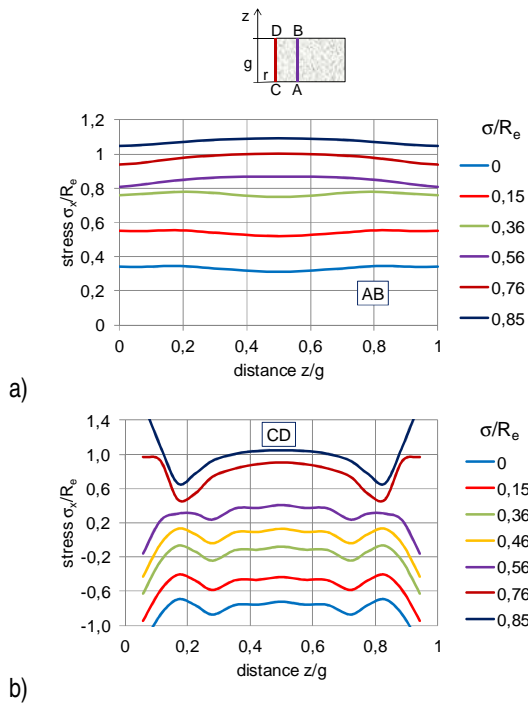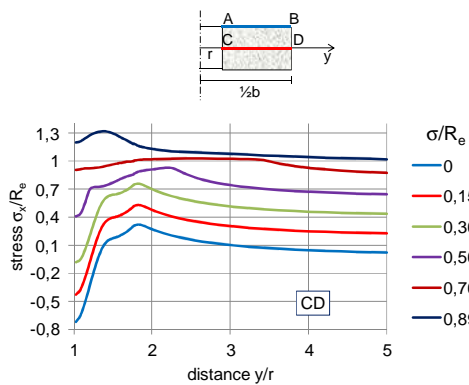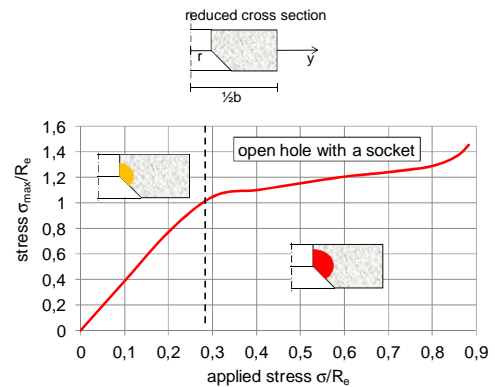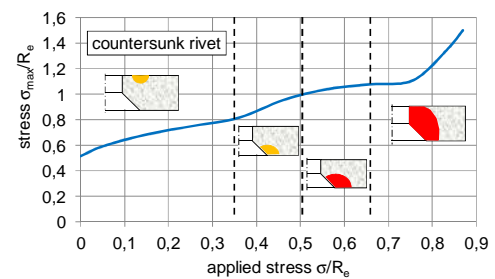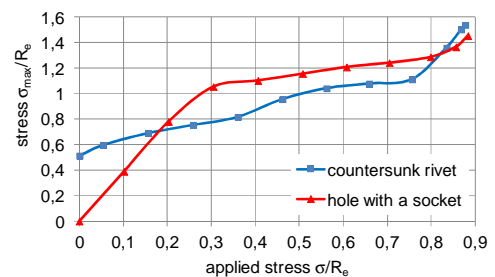

a)

b)

c)

Fig. 13. Principal stress graph vs. applied stress in sheet with countersunk hole: a) an open hole c) riveted hole c) comparison

At the next stage, the calculations for a sheet with a countersunk hole are performed to make a comparison with a cylindrical one. The Maximum principal stress diagrams versus applied load for a sheet with a countersunk hole (open and riveted) are shown in Fig. 13. Principal stress for a sheet with an open hole exceeded yield stress for applied stress of 27% R_e. The growth of principal stresses for the riveted hole (due to residual stresses) is much slower (seven times than for an open one) and, as a result, the yield stress is reached for applied stress of 50% R_e (almost two times greater than in former case). Stress concentration occurs at the edge of the hole in the area where a cylindrical part turns into a conical one (Fig. 13a). The growth of maximum principal stress for the sheet with a riveted hole is relatively uniform almost in the whole analysed load range but for applied stress between 34% R_e and 66% R_e graph becomes slightly irregular what is connected with the change of the stress field in the reduced cross section (the stress concentration area moves from the sheet surface on the driven head side to the outer edge of the conical part of the hole) (Fig. 13b).

The coefficient of stress concentration (Fig. 14) for the sheet with a countersunk riveted hole is lower than a corresponding value for an open hole (practically in the whole load range) what is similar to results obtained for a cylindrical hole.
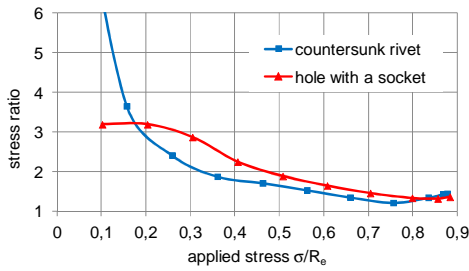

Fig. 14. Stress concentration graph for sheet with countersunk hole vs. applied stress
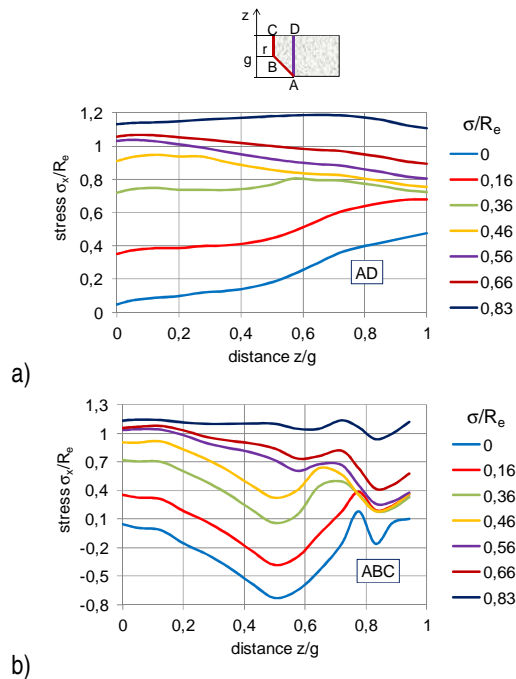

Fig. 15. Principal stress graph vs. thickness distance and applied stress for a riveted sample: a) 3.5 mm from the hole axis b) at the edge of the countersunk hole
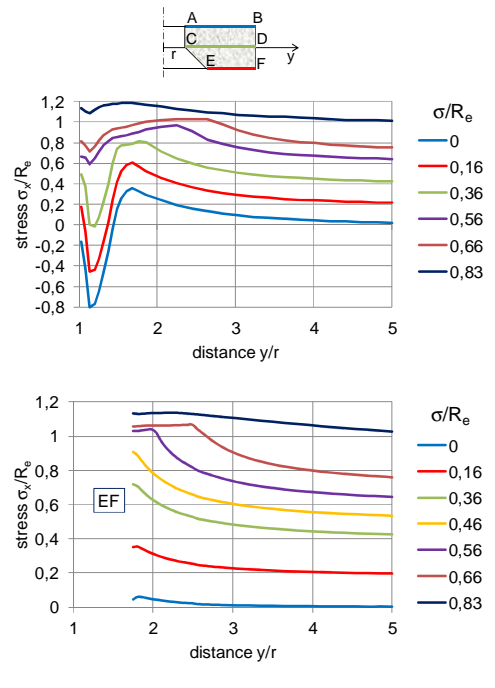

Fig. 16. Principal stress graphs vs. distance from the hole axis and applied stress for riveted sample (countersunk rivet)
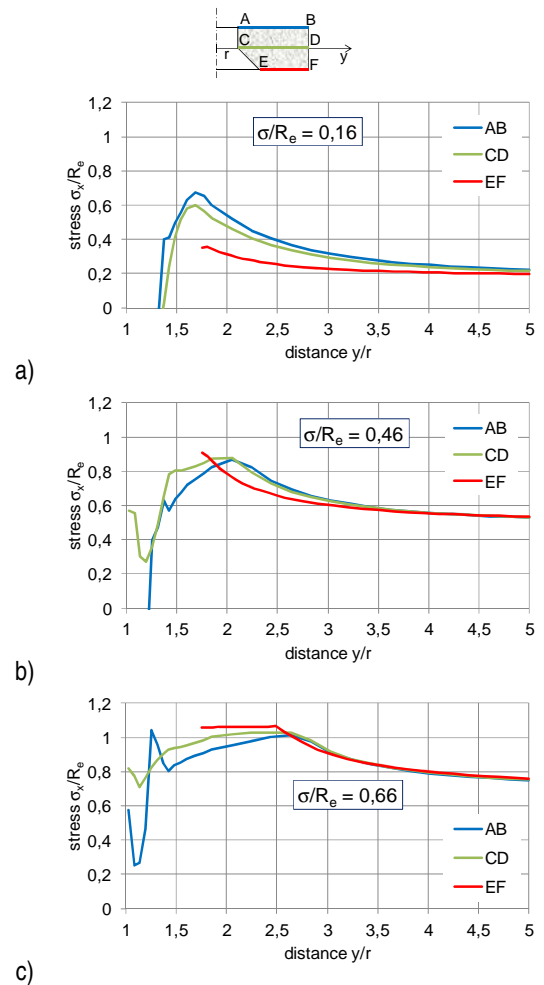

Fig. 17. Principal stress graphs vs. distance from the hole axis for riveted sample (countersunk rivet) for selected applied stress levels: a) 16% R_e, b) 46% R_e, c) 66% R_e

A conical shape of the socket in the hole has an important influence on the principal stress state (Fig. 15). After squeezing, the stress concentration occurs on the sheet surface on the driven head side (D point). During tensile loading (for applied stress of 36% Re) a change in stress field appears. The stress concentration area is being moved to a conical part of the hole (A point). The most irregular stress state is recognised at the edge of the hole under the driven head (Fig. 15b)

Similarly as for a cylindrical hole, the stress concentration occurs not at the edge of the hole but inside material approximately at half the radius length from the cylindrical edge (Fig. 16a). During tensile loading the stress concentration area is being moved to the conical part of the hole (Fig. 16b and 17). Stress values on the outer surface of the sheet (section AB) change similarly as on the middle surface (section CD) but under a driven rivet head (point A) negative stress values (compression) are nearly two times larger.

The comparison of principal stress values for the cylindrical hole and for the hole with a socket is shown in Fig. 18. In the elastic range maximum values of principal stress are a few percent higher for the hole with a socket, what is a result of a smaller area of the reduced cross section. The principal stress values over the yield stress for an open hole are practically independent on the shape of the hole. However, for a riveted hole the corresponding curves are almost parallel in the whole load range. Slight irregularities can be observed for applied stress from 35% to 65% of the yield stress, in this scope for the hole with a socket the change in stress state occurs - the stress concentration appears at the edge of the hole in the conical part (Fig. 13).
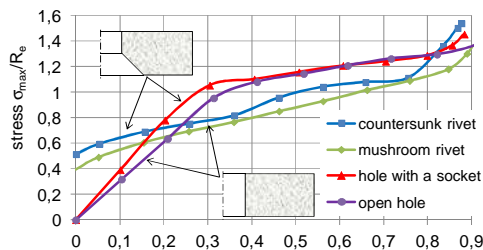

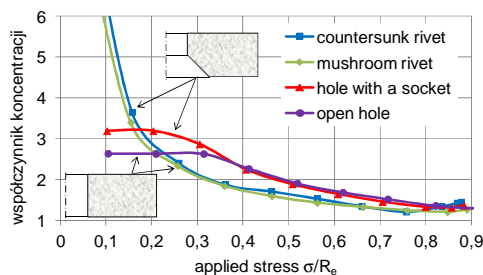**Fig. 18.** The comparison of principal stress for samples with cylindrical and countersunk hole

Fig. 19. The comparison of stress concentration for samples with cylindrical and countersunk hole

The stress concentration (Fig. 19) for riveted holes only slightly depends on the shape of the hole while for the hole with a socket is a bit higher (about 1%). The concentration coefficient for the sheet with an open hole within the elastic range is about 20% higher for the hole with the socket. However, it is almost at the same level for both the hole types over the yield stress.

The analysis of the stress concentration coefficient (Fig. 19)

does not provide a sufficient information about the state of a riveted joint with regard to the results of fatigue tests (presented in chapter two). Much more information can be obtained from the principal stress graph (Fig. 18). It seems to be especially important to compare these values with the yield stress, but only analysis of stress fields for a selected applied stress level can be used for a deeper insight on fatigue performance.

Fatigue tests of sheets with open holes are carried out at applied stress of 40% R_e. The maximum principal stress for a cylindrical hole and a hole with a socket at this load level are practically the same and over the yield stress (110% R_e). This is the reason for comparable low fatigue life of this sheets. It can be observed in Fig. 18 that for applied stress of 30% R_e fatigue life of the sheet with a cylindrical hole should remarkably increase.

Tests for sheets with riveted holes are performed at applied stress of 40% R_e. According to Fig. 18, it leads to maximal principal stress lower than the yield stress – 80% R_e, what suggests high cycle fatigue strength confirmed in tests. Secondly, tests at applied stress of 60% R_e are performed causing damage of samples with countersunk rivets. The maximum principal stress for this load level is above the yield stress (106% R_e) as it can be read in Fig. 18 and stress concentration appears at the hole surface (Fig. 13b) what suggests slightly higher fatigue life than for a sheet with an open hole (in experiments almost two times higher). The damage character for samples with a mushroom rivet is different than for other cases. The failure does not appear in the reduced section. In this case the maximum principal stress level is about 96% R_e (lower than yield stress) as it can be observed in Fig. 18, however, it seems to be more important that stress concentration occurs inside sheet material at a remarkable distance from the hole (longer than hole radius).

The residual stress state is a significant feature of a riveted sheet. It depends on squeezing force (and driven head diameter). Accordingly to riveting standards the driven head diameter should be equal to 1.5d with tolerance of 0.1d, where d is a rivet shank diameter. The diagram of maximum principal stress (for a driven head diameter of 1.4d ,1.5d and 1.6d) during tension tests is shown in Fig. 20. The increase in squeezing force, estimated from a driven head diameter, leads to the increase in residual stress nevertheless the higher residual stress values the increase rate of principal stresses is slower. As a result, with the increase of driven head diameter (from 1.4d to 1.6d) principal stress values reach the yield stress level at applied stress of 44 % R_e ,50% R_e and 60% R_e, respectively. At the first stage of tensile loading, the maximum principal stress values increase with the increase of a driven head diameter. The situation is entirely opposite for the applied stress of 30% R_e and higher. As assumed, the maximum residual stresses (corresponding to the driven head diameter of 1.6d) proved to be the most advantageous.
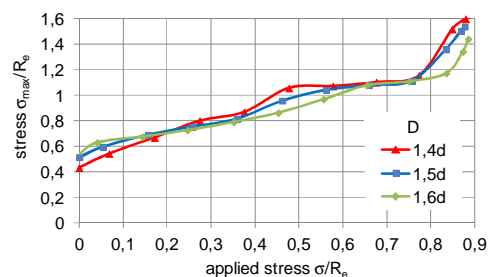

Fig. 20. Principal stress graph vs. driven rivet head diameter (squeezing force)

5. CONCLUSIONS

Filling the hole with a squeezed rivet has no effect on the ultimate strength of the sheet with a hole, however, it remarkably increases its fatigue life.

The material cold working as a result of riveting is the main reason for the fatigue life growth of riveted samples. The performed tests and calculations allow the conclusion that the localization of the crack initiation at the sheet edge is not only a result of the stress state, but also depends on sheet width and most of all on existence of a free surface at the edge of the sheet.

Numerical calculations allow the estimation of maximum stress values close to the notch and consequently the stress concentration magnitude (which is the base of fatigue life estimation of parts with notches [3,9]) for various stress amplitudes of a fatigue cycle.

The material effort in terms of fatigue life is better described by the 1st principal stress than by Huber-Mises equivalent stress. The analysis of the maximum principal stress values during tensile loading allows the evaluation of the influence of different factors (like shape of the hole, residual stress state, applied load) on fatigue life of the sheets.

The equivalent residual stress values in the hole neighbourhood obtained from squeezing exceed the yield stress. On the other hand, the 1st principal stress magnitudes are at the level 50-60% R_e and what is more important they are moved from the hole surface inside material volume. During tensile loading, the growth of the maximum principal stress values is considerably slower for the sheet with a riveted hole and consequently they reach the yield stress level later (for higher applied load).

The 1st principal stress graph versus the applied stress provides more information than the graph of the stress concentration magnitude, however, only the stress state analysis for selected levels of applied load allow the localization of the crack initiation point and a deeper insight on fatigue performance.

REFERENCES

1. **Abibow A.Ł.** (1982), *Technołogia samoletostrojenia*, Moskwa Maszinostrojenie.
2. **Deng X., Hutchinson J.W.** (1998), The clamping stress in a cold driven rivet. *Int. J. Mech. Sci.,* 40, 7, 683-694.
3. **Godzimirski J.** (1998), *Naprawa płatowców*, WAT Warszawa.
4. **Godzimirski J.** (2008), *Lotnicze materiały konstrukcyjne*, Warszawa WAT.
5. **Gruchelski B., Szumielewicz K., Wanad T.** (1969), Przegląd i naprawa sprzętu lotniczego, *Wydawnictwo Komunikacji i Łączności* Warszawa.
6. **Hartman A.** (1961), *Some tests on the effect of fatigue loading on the friction in riveted light alloy specimens*, NLR M2008, NLR, Amsterdam.
7. **Hartman A., Schijve J.** (1969) *The effect of secondary bending on the fatigue strength of 2024-T3 Alclad riveted joints.* NLR TR 69116U, NLR, Amsterdam.
8. **Howland R.C.J.** (1930), On the stress in the neighbourhood of a circulair hole in a strip under tension, *Phil. Trans. of the Roy. Soc.*, Series A (229), London, 49–86.
9. **Jachimowicz J., Wronicz W.** (2008), Wybrane problemy modelowania nitowych lotniczych struktur cienkościennych, *Przegląd Mechaniczny* LXVIII nr 5.
10. **Kocańda D., Hutsaylyuk V., Hlado V.** (2007), Analiza rozwoju małych pęknięć zmęczeniowych od otworu oraz mikromechanizm pękania platerowanej blachy ze stopu 20024-T3, *Biul. WAT* Vol. LVI Nr 4.
11. **Matwijenko W.A.** (1994), Wpływ czynników konstrukcyjno-technologicznych na wytrzymałość zmęczeniową połączeń klejowo-nitowych, *Technologia i Automatyzacja Montażu* Nr 2.
12. **Muller R.** (1995), *An experimental and numerical investigation on the fatigue behaviour of fuselage riveted lap joints*, Doctoral Dissertation, Delft University of Technology.
13. **Rans C.D.** (2007), *The Role of Rivet Installation on the Fatigue Performance of Riveted Lap Joints*, Department of Mechanical and Aerospace Engineering Carleton University.
14. **Rijck J.** (2005), *Stress Analysis of Fatigue Cracks in Mechanically Fastened Joints*, Doctoral Dissertation, Delft University of Technology
15. **Szulżenko M.N., Mostowoj A.S.** (1970), Konstrukcja samolotów, *Wydawnictwo Komunikacji i Łączności*, Warszawa.
16. **Szymczyk E.** (2010), Numeryczna analiza deformacji nitu grzybkowego i otworu nitowego w procesie zakuwania, *Biuletyn WAT* 4.
17. **Szymczyk E., Jachimowicz J.** (2007), Analiza powierzchni kontaktu w połączeniu nitowym, *Biul. WAT* Vol. LVI Nr 4.
18. **Szymczyk E., Orzyłowski M.** (2010), Numerical modelling of a selected part of the airplane fuselage, Journal of KONES, Vol. 17, nr 2, 459-465, *European Science Society of Powertrain and Transport Publication*, Warszawa.

INFLUENCE OF CHOSEN PROCESS-MATERIAL PARAMETERS ON THE QUALITY OF SAND-LIME BRICK

Wojciech TARASIUK [*], **Leon DEMIANIUK** [**]

[*] Department of Mechanics and Applied Computer Science, Faculty of Mechanical Engineering,
Bialystok University of Technology, Wiejska 45 C, 15-351 Białystok, Poland
[**] Department of Machine Design and Maintenance, Faculty of Mechanical Engineering,
Bialystok University of Technology, Wiejska 45 C, 15-351 Białystok, Poland

w.tarasiuk@pb.edu.pl, demleon@pb.edu.pl

Abstract: The results of experimental studies on the influence of process and material parameters on quality of a lime-sand product. The quality is determined on the basis of compressive strength in the direction of compaction of the finished product. The obtained results can be helpful in choosing granulometric composition of lime-sand mixture and determining compaction pressure for products with specific quality requirements.

Key words: Compaction, Lime-Sand Mixture, Quality of a Lime-Sand Product

1. INTRODUCTION

Silicate products form a large percentage of building materials manufactured nowadays. They are made of the lime-sand mixture, which is a mixture of siliceous sand, lime and water. During mixing of these ingredients in silos or reactors the lime is slaked (Skalamowski, 1973). So prepared mixture is thickened in the moulding machines at fixed pressure (Królikowski, 2006), and then autoclaved (Wolfke, 1986). The process, called product hardening, consists of exposing the molded product to water vapour at a pressure of 1.6 MPa and a temperature of 203° C (Wolfke, 1986).

In order to increase the competitiveness of silicate products their quality improvement is required. The main parameters by which the quality was determined were compressive strength RC and the density of the product. They depend on both material and process factors. The material factor which was examined was the granulometric composition of sand-lime mixture. Its influence on the quality of the finished product is described in the literature on compacting materials of plant origin (Demianiuk, 2011) and compacting sand-lime mixture with the pigment addition (Tarasiuk and Krupicz, 2009). The investigated process factor was the value of pressure per area unit of the moulding piston, which is referred as the compaction pressure further in the article.

The desirable result is a product of low density and high compressive strength R_C.

2. LIME-SAND MIXTURE

In order to verify the assumptions made in the introduction part, the experiment was carried out according to a given schedule. The realisation plan of the experiment is shown in Fig. 1.

The mixture used in the experiment was obtained from factory "Silikaty-Białystok". It was collected on the day of experiment directly from the production line, after the process of lime slaking. It was subjected to the sieve analysis where granulometric composition of each fraction was determined. The average percentage of each fraction and the standard deviation of 5 sample analyses presents Fig. 2.
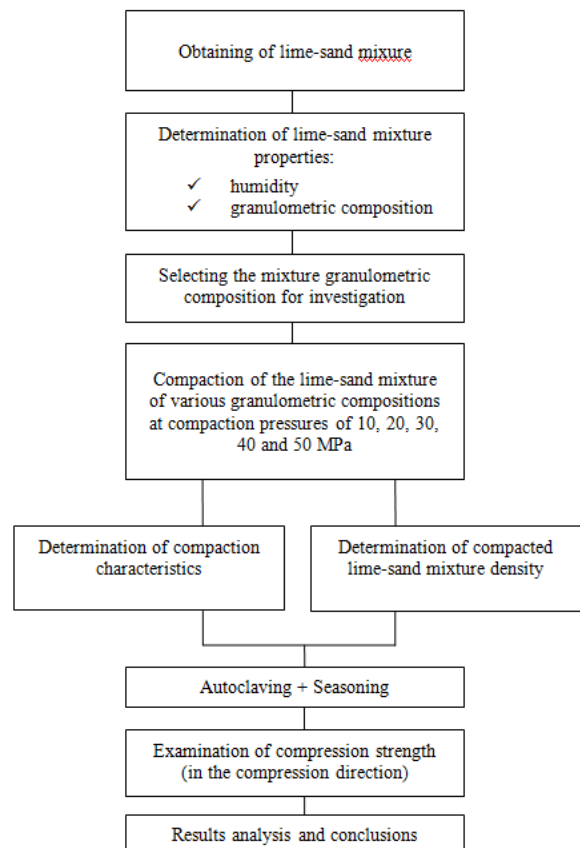

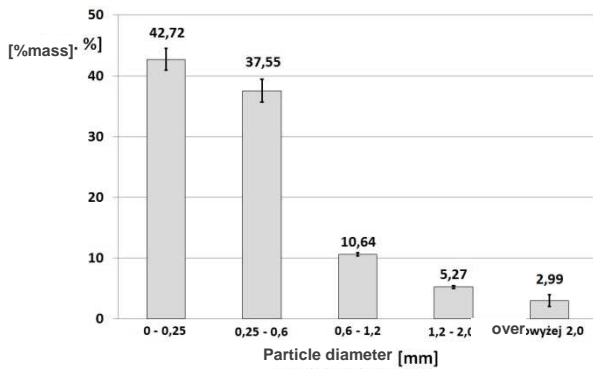**Fig. 1.** Layout of the conducted research

Fig. 2. Sieve analysis of the base mixture

Mass of the mixture used in each analysis was 0.5 kg. Three granulometric compositions were chosen on the basis of analyses results. The first composition was the original one of the lime-sand mixture taken directly from the production line. The next two were the results of the separation of mixtures characterized by the particle size within the range 0 – 0.6 mm and 0 – 1.2 mm. The percentage of each granulometric fraction in the mixtures shown in Tab. 1.

Tab. 1. Granulometric composition of mixtures used in the experiment

Particle size [mm]	Base mixture	0 – 0.6 mm	0 – 1.2 mm
	Fraction content [% weight]		
0 – 0.25	42.9 %	52.8 %	47 %
0.25 – 0.6	37.8 %	47.2 %	41.3 %
0.6 – 1.2	10.8 %	-	11.7 %
1.2 – 2.0	5.5 %	-	-
2.0 – 4.0	3 %	-	-

The analyzed process parameter was the compaction pressure P_a. In the experiment $P_a = 10$, 20, 30, 40 and 50 MPa was applied. During the compaction process the moisture content of analyzed mixture was approximately 5%.

3. DENSIFICATION

Compaction of selected lime-sand mixtures was carried out on MTS 322 universal testing machine (Fig. 3), which allowed the recording of compaction force and the height of the sample.

Fig. 3. The materials testing machine MTS 322

Samples for compressive strength tests were prepared in a steel mould. The photo and schematic diagram with basic dimensions are shown in Fig. 4a and b.
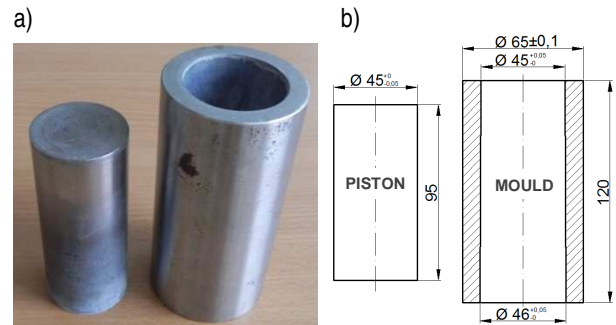
a)

b)

Fig. 4. Mould and piston used in sand-lime mortar compaction

Each sample was prepared from 200 g of the mixture. Compaction force increased at a rate of 2 kN/sec. The parameters needed for the determination of compaction characteristics were recorded. On the bases of collected data the compaction curve was obtained for each sample. The compaction curve for the base mixture is presented, as an example, in Fig. 5.
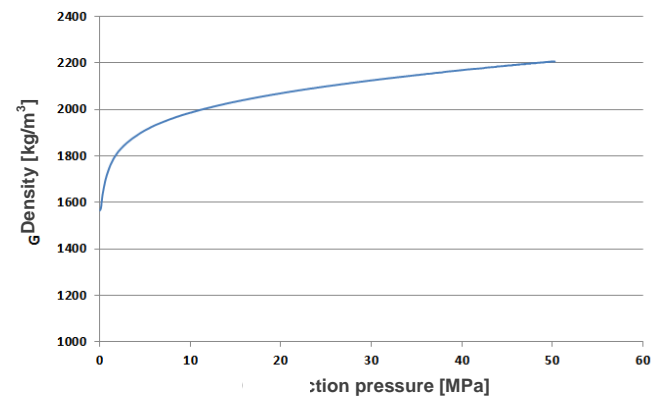

Fig. 5. Compaction characteristics of the base compound

4. COMPRESSIVE STRENGTH

Compacted samples were subjected to autoclaving and seasoning (7 days). After that a compressive strength test was conducted. The test was carried out on the MTS 322 universal testing machine with the head (Fig. 6) that enabled a parallel arrangement of sample and head surfaces.

Fig. 6. The head used during the compression tests

5. RESULTS

The outcome of the experiment were average density values of selected mixture samples at various compaction pressures. The results are shown in the following order:
- base mixture - Fig. 7;
- mixture of particle size 0 – 0.6 - Fig. 8;
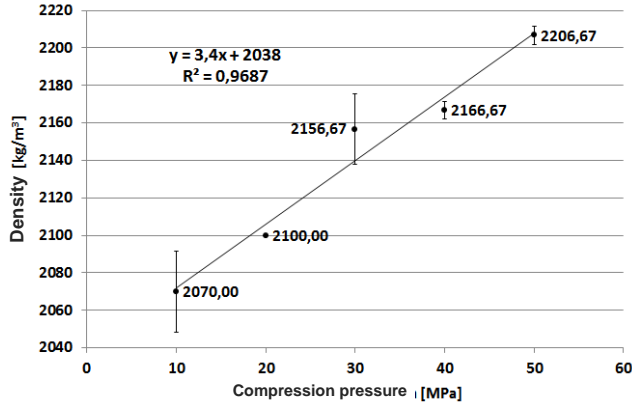- mixture of particle size 0 – 1.2 - Fig. 9.

The mixture of particle size 0 – 0.6 mm was found to be the one of the lowest density, but only at low compaction pressures (P_a = 10 i 20 MPa). At higher pressures, the same mixture had the highest density among all the investigated mixtures.

The results regarding compressive strength R_C are shown in graphs:
- base mixture - Fig. 10;
- mixture of particle size 0 – 0.6 - Fig. 11;
- mixture of particle size 0 – 1.2 - Fig. 12.

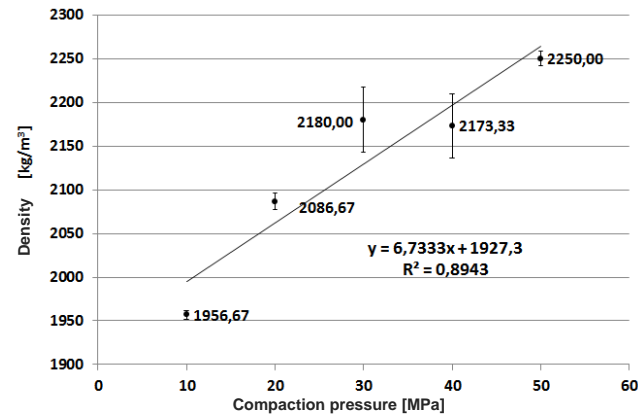**Fig. 7.** The density dependence on the compaction pressure P_a for the base mixture
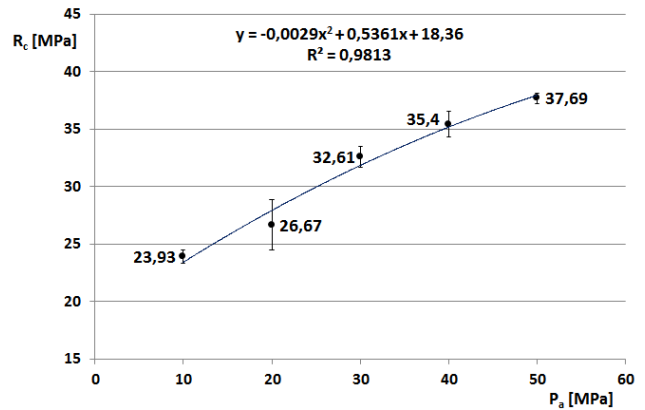
Fig. 10. The compressive strength R_C dependence on compaction pressure P_a for base mixture

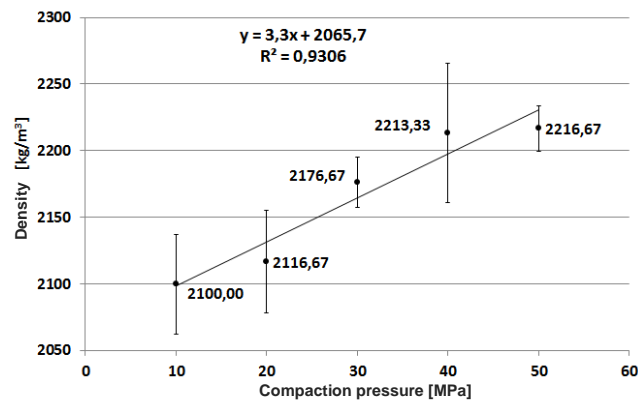**Fig. 8.** The density dependence on the compaction pressure P_a for the mixture of particle size 0 – 0.6 mm

Fig. 11. The compressive strength R_C dependence on compaction pressure P_a for the mixture of particle size 0 – 0.6 mm

Fig. 9. The density dependence on the compaction pressure P_a for the mixture of particle size 0 – 1.2 mm

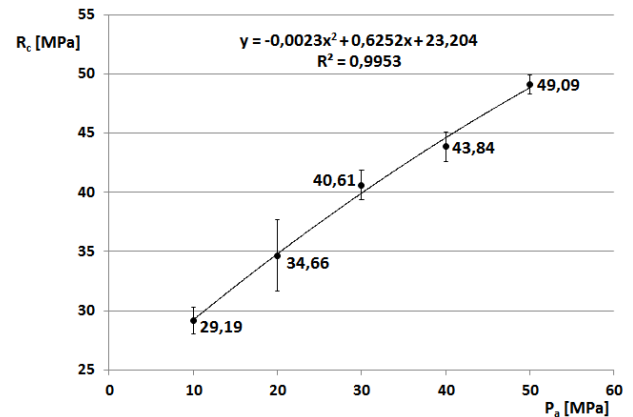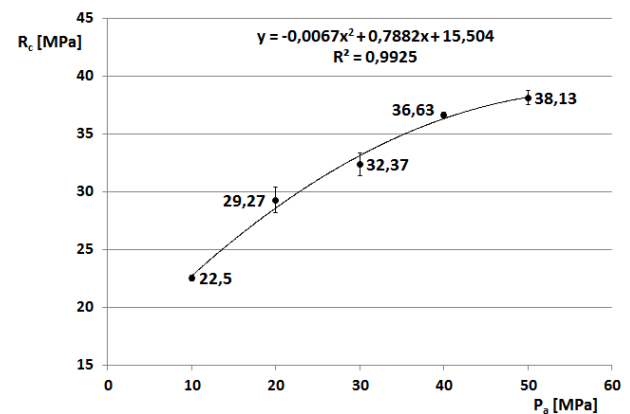**Fig. 12.** The compressive strength R_C dependence on compaction pressure P_a for the mixture of particle size 0 – 1.2 mm
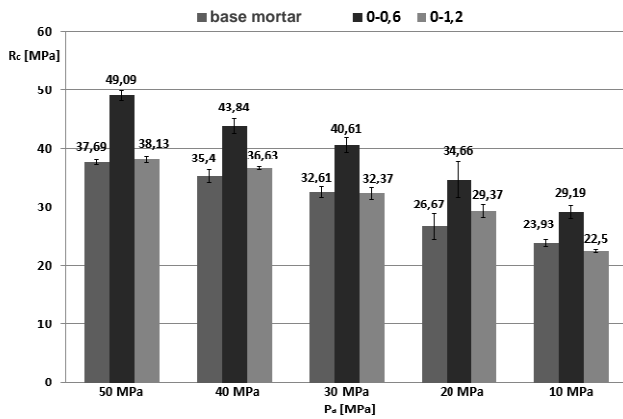
Fig. 13. Comparison of compressive strength R_C correlation with the compaction pressure P_a

The sample of a particle size 0 - 0.6 mm was characterised by the highest strength. For P_a = 50 MPa, this difference in this value exceeded 20% in relation to the other mixtures (Fig. 13).

6. CONCLUSIONS

The results indicate that:
− increase in compaction pressure P_a within the range of 10 MPa to 50 MPa causes an increase in the compressive strength of calcium silicate,
− the mixture of particle size 0 – 0.6 mm has the highest compressive strength the whole range of compacting pressures applied in the experiment,
− the mixture of particle size 0 – 0.6 mm at a compaction pressure P_a = 10 MPa has the lowest density with maximum compression strength R_C,
− a proper choice of the mixture granulometric composition allows to obtain a finished product with a lower weight and higher compressive strength.

REFERENCES

1. **Demianiuk L.** (2011), Reseach on the miscanthus giganteus compaction process (in Polish), *Acta Agrophysica*, Vol. 17, Nr 1, 43-53.
2. **Królikowski M.** (2006), *Technological regime of silicate manufacture* (in Polish), 13-14.
3. **Skalamowski W.** (1973), *Technology of building materials* (in Polish), vol. II, Arkady, Warszawa, 306-307.
4. **Tarasiuk W., Krupicz B.** (2009), Analysis of friction forces in the lime-sand mixture compaction process (in Polish), *Tribologia*, Nr 3, 273-283.
5. **Wolfke S.** (1986), *Technology of lime-sand products* (in Polish), Arkady, Warszawa 1986.

SELECTION OF THE BEST METHOD FOR ASSESSMENT OF THE FATIGUE LIFE OF ALUMINIUM ALLOYS BASED ON THE ROOT OF THE SCATTER MEAN-SQUARE VALUE

Karolina WALAT*

*Department of Mechanics and Machine Design, Faculty of Mechanical Engineering,
Opole University of Technology, Mikołajczyka 5 Street, 45-271 Opole

k.walat@po.opole.pl

Abstract: The paper presents comparison of three methods of fatigue life assessment related to aluminium alloys. One of these methods is a new way of statistical interpretation of the fatigue test results by means of the root of the mean-square value of the error expressing a half of scatter of the calculated fatigue life. The results of fatigue tests of specimens, and different geometries of welded joints made of aluminium alloys were considered. The calculated fatigue lives were obtained with use of critical plane orientations determined according to the variance of normal and shear stresses, and the covariance of normal and shear stresses.

Key words: Aluminium Alloys, Critical Plane, Fatigue Life

1. INTRODUCTION

Estimation of the fatigue life of elements of machines and structures is a complex process and it can be performed according to many known mathematical models, depending on the material applied and geometry of the element. However, it is difficult to find in literature standards informing how to compare different models in order to select the best one. Some proposals can be found in papers by Berger et al. (2002), Bracessi et al. (2005), Eibel et al. (2003), Karolczuk, Macha (2004). However, they cannot be applied in all the cases. There is no one model precisely comparing different models of fatigue life estimation ad allowing to distinguish the best one.

This paper presents three methods of estimation of the fatigue life of elements made of aluminium alloys, compared by means of a new way of statistical interpretation of fatigue test results.

2. ANALYSIS OF FATIGUE TEST RESULTS

Analyzing fatigue life scatters, we usually use logarithms of ratios of experimental and calculated lives determined according to the following expression:

$$E = log\ \frac{N_{\exp}}{N_{cal}} = \log N_{\exp} - \log N_{cal}, \tag{1}$$

(see the paper by Li et al. (2009)).

The mean value of the considered magnitude can be defined as:

$$\overline{E} = \frac{1}{n}\sum_{i=1}^{n} E_i\ , \tag{2}$$

where n is a number of measurements.

Variance is determined from the following formula:

$$s^2 = \frac{1}{n-1}\sum_{i=1}^{n}\left(E_i - \overline{E}\right)^2\ , \tag{3}$$

and standard deviation is defined from:

$$s = \sqrt{s^2}\ . \tag{4}$$

Finally, the mean scatter is determined from the formula:

$$\overline{T}_N = 10^{\overline{E}}\ , \tag{5}$$

in the scatter band of the scatter coefficient T_N given by the formula:

$$T_N = 10^{t_{n-1}\alpha/2\cdot s}\ . \tag{6}$$

Thus, we obtain parameters (2) and (6), in case of which explicit interpretation is not possible. Karolczuk and Macha (2004) proposed their following connection:

$$E_s = \sqrt{\overline{E}^2 + s^2}\ . \tag{7}$$

There are no theoretical foundations for application of the proposed models. However, another method can be proposed, namely we can determine a root from the mean-square error value as:

$$E_{RMS} = \sqrt{\frac{\sum_{i=1}^{n} \log^2 \frac{N_{\exp i}}{N_{cali}}}{n}}\ , \tag{8}$$

so finally the obtained scatter value is:

$$T_{RMS} = 10^{E_{RMS}}\ . \tag{9}$$

3. EXPERIMENTS

The results of own tests and tests from literature were analyzed. The considered results concerned some selected aluminium alloys and welded joints of those alloys under combined bending with torsion.

Specimens made of the aluminium alloy 2017A, known as PA6 were subjected to pure bending, pure torsion, cyclic and

random proportional and non-proportional combinations of bending with torsion (Walat, 2010).

The proposed method was also verified with use of the results of cyclic tests obtained by Kueppers and Sonsino (2001, 2003) for aluminium welded joints of tube-tube and tube-flange types, made of aluminium-magnesium-silicon for plastic working, AlSiMgMn T6, which present numerical notation is EN AW-6082 T6. Experiments were realized for pure bending, pure torsion and combined proportional and non-proportional bending with torsion.

Results of fatigue tests of duralumin D-30 realized by Nishihara and Kawamoto (1941) were also analyzed. Specimens made of D-30 were subjected to the same loadings as those tested by Kueppers and Sonsino.

The calculated fatigue lives were obtained with use of orientations of critical planes determined according to variance of normal stresses μ_σ, shear stresses μ_τ and covariance of normal and shear stresses $\mu_{\sigma\tau}$.

The method of maximum variance of normal stresses can be written as:

$$\mu_\sigma = \frac{1}{T_0} \int_0^{T_0} \sigma_\eta(t) \sigma_\eta(t) dt ,$$ (10)

where T_0 observation time, $\sigma_\eta(t)$ is history of normal stress oriented at the angle of α in relation to stress $\sigma_{xx}(t)$ for combination of bending with torsion, where σn(t) is assumed as:

$$\sigma_n(t) = \cos^2 \alpha \sigma_{xx}(t) + \sin 2\alpha \tau_{xy}(t).$$ (11)

The method of maximum variance of shear stress is expressed by the following formula:

$$\mu_\tau = \frac{1}{T_0} \int_0^{T_0} \tau_{\eta s}(t) \tau_{\eta s}(t) dt,$$ (12)

where $\tau_{\eta s}(t)$ is history of shear stress at the angle of α in relation to stress $\sigma_{xx}(t)$ for combination of bending with torsion can be written as:

$$\tau_{\eta s}(t) = -\frac{1}{2} \sin 2\alpha \sigma_{xx}(t) + \cos 2\alpha \tau_{xy}(t).$$ (13)

Another method including variations of both normal stresses and shear stresses is the method of covariance of normal and shear stresses written as:

$$\mu_{\sigma,\tau} = \frac{1}{T_0} \int_0^{T_0} \sigma_n(t) \tau_{\eta s}(t) dt.$$ (14)

Figs. 1÷6 present mean-square errors obtained with use of the proposed Eq. (9) for successive considered tests according to three analyzed models. The numerous tests of aluminium alloy 2017 A were realized in laboratories of Opole University of Technology, and the results were shown in three separate figures. Fig. 1 shows the test results for loadings under in-phase combination of bending with torsion, and in Fig. 2 presents the results of tests under the phase shift. Fig. 3 presents the scatters for combination of in-phase and out-of-phase loadings. From the figures it appears that the maximum scatters occur always in the case of application of the criterion on the critical plane defined by variance of normal stresses μ_σ (the mean-square

scatter for all the tests equals 6.5), and the minimum scatters occur for the criterion defined by covariance of normal and shear stresses $\mu_{\sigma,\tau}$ (the mean-square scatter for all the tests is 1.5). In the case of the criterion defined by variance of shear stresses μ_τ the mean-square scatter for all the tests is 4.7. The mean-square scatters for variable-amplitude loadings are 2.103.

Fig. 1. Root of the mean-square error of scatters for specimens made of 2017A under in-phase loadings
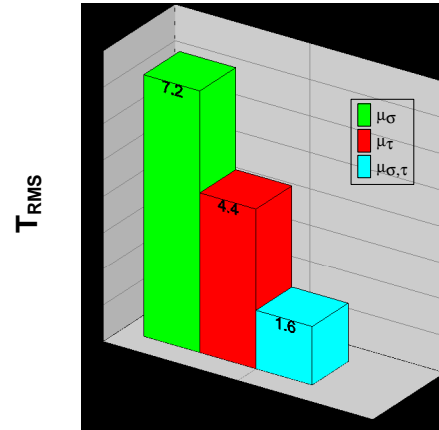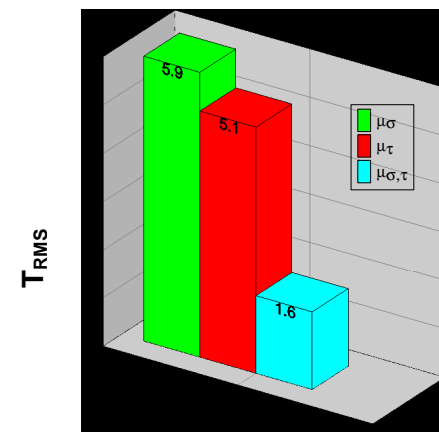

Fig. 2 Root of the mean-square error of scatters for specimens made of 2017A under out-of-phase loadings
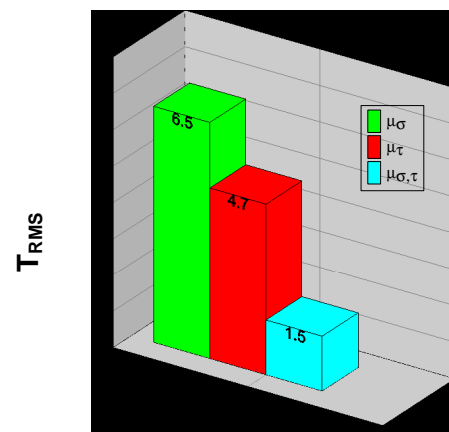

Fig. 3. Root of the mean-square error of scatters for specimens made of 2017A under in-phase and out-of-phase loadings

Fig. 4 presents the test results obtained for specimens made of the aluminium alloy D-30. The maximum scatters were obtained

for the criterion on the critical plane defined by variance of normal stresses (the mean-square scatter for all the tests was 12.6). The minimum scatters were obtained for the criterion defined by covariance of normal and shear stresses (the mean-square scatter for all the tests was 1.2). Thus, the results are similar as those obtained for the aluminium alloy 2017A. When the criterion defined by variance of shear stresses was applied, the mean-square scatter was 4.4 for all the tests.
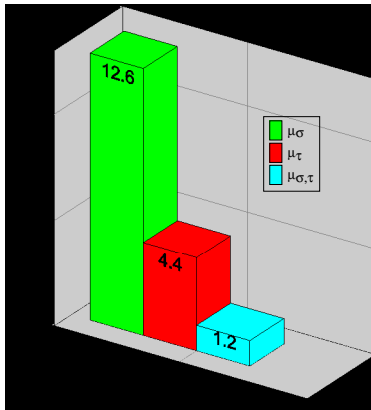

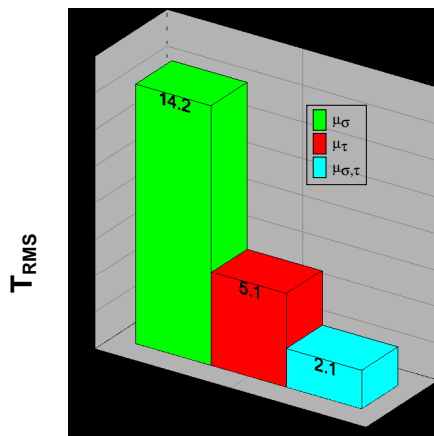**Fig. 4.** Root of the mean-square error of scatters for specimens made of D-30

Fig. 5. Root of the mean-square error of scatters for specimens made as tube-flange welded joints of AlSi1MgMn-T6
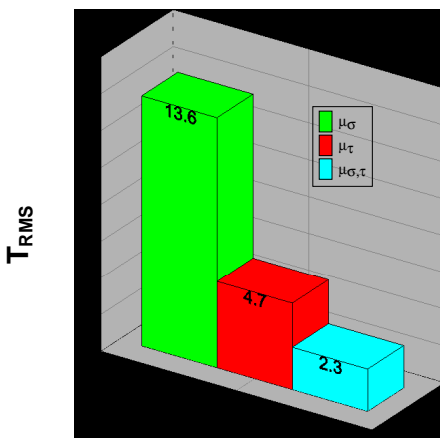

Fig. 6. Root of the mean-square error of scatters for specimens made of tube-tube welded joints of AlSi1MgMn-T6

Fig. 5 shows the test results for specimens made as tube-flange welded joints of AlSi1MgMn-T6. Fig. 6 presents the test results for tube-tube specimens made of the same material. From the figures it appears that each time the greatest scatters are obtained in the case of application of the criterion on the critical plane defined by variance of normal stresses (the mean-square scatter is 14.2 and 13.6). The minimum scatters are obtained for criterion of covariance of normal and shear stresses (the mean-square scatters are 2.1 and 2.3), like in the case of fatigue tests for aluminium alloys 2017A and D30. When the criterion defined by variance of shear stresses is applied, the mean-square scatter is 5.1 and 4.7 for all the tests.

4. CONCLUSIONS

The method of statistical interpretation of the fatigue test results by means of the root of mean-square error is an universal method for comparison of fatigue lives obtained by different methods (fatigue criteria). It allows to select the best method, giving the best conformity between the calculated and experimental results.

REFERENCES

1. **Berger C**., **Eulitz K.G., Heuler P**., **Kotte K.L., Naundorf H., Schuetz W., Sonsino C.M., Wimmer A., Zenner H**. (2002), Betriebsfestigkeit in Germany – an overview, *Int. J. Fatigue*, Vol. 24, 603-625
2. **Braccesi C., Cianetti F., Lori G., Pioli D**.(2005), Fatigue behaviour analysis of mechanical components subject to random bimodal stress process: frequency domain approach, *Int. J. Fatigue*, Vol. 27, 335-345
3. **Eibel M., Sonsino C.M., Kaufmann H., Zhang G**.(2003), Fatigue assessment of laser welded thin sheet aluminium, *International Journal Fatigue*, Vol.25, 719-731
4. **Karolczuk A., Macha E**.(2004), *Płaszczyzny krytyczne w modelach wieloosiowego zmęczenia materiałów. Wieloosiowe zmęczenie losowe elementów Maszyn i konstrukcji*-część IV. Studia i Monografie, Politechnika Opolska, Opole
5. **Kueppers M., Sonsino C.M**.(2003), Critical plane approach for the assessment of the fatigue behaviour of welded aluminium under multiaxial loading, *Fatigue Fract. Engng. Mater. Struct.*, Vol. 26, 507-513
6. **Kueppers M.,Sonsino C. M**.(2001), *Festigkeitsverhalten von Aluminiumschweiss verbindungen unter mehrachsigen Spannungszuständen*, AiF-No. 10731N, LBF-Report No 280542, Fraunhofer-Insitut für Betriebfestigkeit (LBF), Darmstadt
7. **Li J., Zhang Z., Sun Q., Qiao Y**.(2009), A new multiaxial fatigue damage model for various metallic materials under the combination of tension and torsion loadings, *International Journal of Fatigue*, No. 31, 776-781
8. **Nishihara T., Kawamoto M.**(1941), *The Strength of Metals under Combined Alternating Bending and Torsion with Phase Difference, Memoirs of the College of Ingineering*, Kyoto Imperial University, Vol. 10, No.6, 117-122
9. **Walat K**.(2010), *Wpływ kowariancji naprężeń w płaszczyźnie krytycznej na trwałość zmęczeniową elementów maszyn*, Rozprawa doktorska, Politechnika Opolska, Opole
10. **Walat K., Łagoda T**.(2010a), Trwałość zmęczeniowa aluminiowych złączy spawanych według kryteriów opartych na położeniu płaszczyzny krytycznej wyznaczanych trzema metodami, *Transport przemysłowy i maszynowy* 2(8)/2010, 68-72

ABSTRACTS

Jacek Mateusz Bajkowski

Design, Analysis and Performance Evaluation of the Linear, Magnetorheological Damper

The paper issues the design and analysis of the linear, magnetorheological damper. Basic information concerning the characteristics of the typical magnetorheological fluid and the damper incorporating it, were presented with the short description of the applied fluid MRF-132 DG. Basing on the computations, the prototype damper T-MR SIMR 132 DG was designed, manufactured, and tested under different operating conditions. Presented calculations were verified with the experimental results and their accuracy was evaluated. The conclusions and observations from the research were compiled in the summary.

Wiesław Barnat, Robert Panowicz, Tadeusz Niezgoda, Paweł Dybcio

Numerical Analysis of IED Detonation Effect on Steel Plate

The article presents the results of initial works on protection of vehicles crews against improvised explosive mechanisms (charges) IED. The presented coupled problem of explosion and interaction of pressure impulse coming from detonation was described in available standard documents. The presented results are the introduction to works on composed protective layers applied in vehicles.

Wiesław Barnat, Robert Panowicz, Tadeusz Niezgoda

Numerical and Experimental Comparison of Combined Multilayer Protective Panels

The paper presents numerical and experimental analysis of combined multilayer protective panels. The developed structures are prospective solutions for enhancing protection of military vehicles and crucial elements of pipelines especially in places like river crossings.

Jarosław Bieniaś, Monika Ostapiuk, Barbara Surowska

Fractography and Damage Analysis of Carbon/Epoxy Composites Under Static and Dynamic Loading at Elevated Temperatures

This paper presents the microstructural and fractographic analysis of damage in carbon/epoxy composites after static and fatigue strength (shear) tests at elevated temperature. The microstructural tests and fractographic analysis confirmed the complexity of degradation process and degradation mechanisms in composite structure. Multiple cracks, delaminations and interface degradation between fibre and matrix have been observed. The fracture analysis indicate the occurrence of characteristic failure area: matrix river lines, matrix rollers, fractures and reinforcing fibres imprints. The interface, except of the type of components and their features, is the principal factor determining the properties of composite material. The quality of the bonding between the reinforcing phase and matrix, mechanism of composite cracking as a whole as well as cracks of individual components are directly affected by the interface.

Stefan Bućko, Henryk Jodłowski, Marcin Trzebicki

Numerical-Experimental Analysis of Plastic Flow Beginning Phase Round the Hole in the Thin Shield Under Tension

The method of recognition of plastic strains with the use of optical interference was characterized in the work. The idea of the method was shown on the example test for 15HM steel tension. The results of experimental testing of plastic strains initiation in the thin shield with opening of Ø20 diameter under tension, especially considering round the hole zone were presented in further part of the work. The experiment was carried out with the use of method mentioned above. In the experiment the stresses initializing plastic deformations and the shape of plastic zone were determined. The stress state analysis in the hole zone in the specimen under tension was realized with the use of finite element method. The calculations were done for two significantly different hole diameters. The results of FEM calculations allow for certification that for the holes of diameters significantly bigger than the shield thickness round the hole plane stress state occurs.

Łukasz Czerech, Roman Kaczyński, Andrzej Werner

Machining Error Compensation for Objects Bounded by Curvilinear Surfaces

The paper is devoted to topic related with machining error correction for objects bounded by curvilinear surfaces manufactured on numerically controlled milling machine. Currently it is realized by two techniques. The first of them is called on-line and requires continuous correction of toolpath during the machining process. This approach requires expanded adaptive control systems. The second method called off-line is based on correction of machining control system outside the machine (on the basis of control measurement results). This paper shows methodology of machining shape error correction with off-line technique (with no constant and direct connection to CNC machine tool). This method is based on usage of CAD/CAM systems, numerically controlled milling machine and coordinate measuring machine. Manner of procedure proposed in this paper was verified on the example of ruled surface profile described with NURBS technique. Realization of this proposed methodology of machining error correction has shown significant accuracy correction of manufactured element.

Mariusz Faszczewski, Grzegorz Górski, Romuald Mosdorf

Applying Recurrence Plots to Identify Borders Between Two-Phase Flow Patterns in Vertical Circular Mini Channel

In the paper the method based on recurrence plots has been used for identification of two-phase flow in a vertical, circular mini-channel. The time series obtained from image analysis of high speed video have been used. The method proposed in the present study allows us to define the coefficients which characterize the dynamics of two-phase flow in a mini channel. To identify two-phase flow patterns in a mini channel there has been used the coefficient LAVG which is a measure of an average length of diagonal lines in recurrence plot. The following two-phase flow structures have been considered: bubbly, bubbly-slug and wavy-annular. Obtained results show that method proposed in the paper enables identification of borders between two two-phase flow patterns coexisting in a mini-channel.

Małgorzata A. Jankowska, Grażyna Sypniewska-Kamińska, Henryk Kamiński

Evaluation of the Accuracy of the Solution to the Heat Conduction Problem with the Interval Method of Crank-Nicolson Type

The paper deals with the interval method of Crank-Nicolson type used for some initial-boundary value problem for the one-dimensional heat conduction equation. The numerical experiments are directed at a short presentation of advantages of the interval solutions obtained in the floating-point interval arithmetic over the approximate ones. It is also shown how we can deal with errors that occur during computations in terms of interval analysis and interval arithmetic.

Paweł Lindstedt, Karol Golak

Premises of Parametrical Assessment of Turbojet Engine in Flight Regulation Condition During Ground Test

The article presents the theoretical bases of new parametrical method of turbojet engine technical condition assessment. In this method, engine technical condition is described by one (in other methods four are used) comprehensive model (binding engine input – signals p_2 and m_p and engine output – n i p_4 signals) with unique feature, that engine operation quality during ground tests will provide necessary data on its performance in flight. The changes occurring in turbojet engine during its exploitation will be measurable by comparison of standard model with parameters obtained from experiment (ground test).

Robert Panowicz, Wiesław Barnat, Tadeusz Niezgoda, Leszek Szymańczyk, Julian Grzymkowski

Numerical-Experimental Investigation of Squared-Based Metal Pyramids Loaded with A Blast Wave From A Small Explosives Charge

The paper presents the results of computer simulation and experimental investigation of blast wave action arising from a small explosive charge on a metal pyramid with a square base. The explicit finite element method has been used to perform numerical analyses. This method is included in the Ls-Dyna software for modelling the behaviour of the pyramid exposed to the action of a pressure wave arising from the detonation of an explosive charge. The detonation process was described in programming burn approximation. The fluid–structure interaction was used to describe an influence of a blast wave on the structure.

Bogdan Sapiński, Jacek Snamina, Mateusz Romaszko

The Influence of a Magnetic Field on Vibration Parameters of a Cantilever Sandwich Beam with Embedded MR Fluid

The paper investigates a magnetic field acting on a three-layer sandwich beam filled with MR fluid, the field being generated by an electromagnet. The FEM approach is applied to determine the magnetic field strength and magnetic flux density in the area between the poles and in the MR fluid layer. The results are utilised to establish the relationship between the magnetic flux density and parameters of the assumed model of the MR fluid layer.

Andrzej Sioma

Assessment of Cutting Edge Defects Using a Vision Method

The paper discusses a vision method of assessment of laser cutting edges and surfaces of metals. It presents an analysis of the defects that occur at the edges and surfaces of components cut out in laser technology. It discusses in detail examples of defects, their causes, and methods of preventing their occurrence in the cutting process. The paper presents a vision method for the identification and assessment of defects based on selected examples. It also discusses a method of constructing a three-dimensional image of a product, issues related to the resolution of the vision system and the resolution of laser beam analysis, and methods of image analysis.

Andrzej Sioma, Andrzej Tytko

Evaluation of the Operational Parameters Of Ropes

This article discusses a vision method of measuring the geometric parameters of ropes and evaluating their wear based on measurements made in a three-dimensional rope image. The article discusses the method of construction of a three-dimensional image based on mapping of the actual dimensions of the rope and on algorithms that allow determination of the parameters describing its basic geometrical dimensions and surface condition. The article discusses issues related to resolution of the vision system, resolution of laser beam analysis, and resolution relating to the measurement of the height profile on the surface of the rope. Based on the image constructed in such a way, measurements are presented in order to assess the dimensional parameters and surface defects in sample rope structures. Based on tests and analyses of the three-dimensional image, a range of inspection tasks using 3D vision systems is indicated.

Wojciech Szoka, Dariusz Szpica

Adaptation of Classic Combustion Engines To Compressed Air Supply

This paper presents the issue of the construction and operation of the pneumatic piston engines. We analyzed different options for design solutions, as well as their applicability. It proposes its own solutions based on reciprocating internal combustion engines JAWA 50 and FIAT 126P, which was obtained during the adaptation of two-stroke engines air. The first attempts were successful operation. We showed the process of adaptation each of engines, their specifications and set the scope for further work related to the improvement of operational characteristics, as well as guidelines for developing a mathematical model of action.

Elżbieta Szymczyk, Jan Godzimirski

The Influence of Riveting Process on Sheets Fatigue Life – the Stress State Analysis

The paper deals with estimation of a stress concentration factor in the hole area during tensile loading. The load carrying capacity and fatigue performance of sheet samples (made of 2024 aluminium alloy) with open and riveted holes are compared. Tests confirm the insignificant influence of riveting on ultimate strength, however, it strongly affects fatigue life. The material cold working around the hole causes a decrease in maximum principal stress values as well as stress concentration moves away a few millimetres (about half a rivet radius length) from the hole. During tensile loading the maximum stress values increase slower around the riveted hole than at the open one and consequently in the former case the yield stress is achieved later.

Wojciech Tarasiuk, Leon Demianiuk

Influence of Chosen Process and Material Parameters on the Quality of Silicate Product

The results of experimental studies on the influence of process and material parameters on quality of a lime-sand product. The quality is determined on the basis of compressive strength in the direction of compaction of the finished product. The obtained results can be helpful in choosing granulometric composition of lime-sand mixture and determining compaction pressure for products with specific quality requirements.

Karolina Walat

Selection of the Best Method for Assessment of the Fatigue Life of Aluminium Alloys Based on the Root of the Scatter Mean-Square Value

The paper presents comparison of three methods of fatigue life assessment related to aluminium alloys. One of these methods is a new way of statistical interpretation of the fatigue test results by means of the root of the mean-square value of the error expressing a half of scatter of the calculated fatigue life. The results of fatigue tests of specimens, and different geometries of welded joints made of aluminium alloys were considered. The calculated fatigue lives were obtained with use of critical plane orientations determined according to the variance of normal and shear stresses, and the covariance of normal and shear stresses.